

Technische Universität München

Max-Planck-Institut für Physik
(Werner-Heisenberg-Institut)

Automated evaluation of one-loop scattering amplitudes

Hans van Deurzen

Vollständiger Abdruck der von der Fakultät für Physik
der Technischen Universität München zur Erlangung des akademischen Grades eines
Doktors der Naturwissenschaften (Dr. rer. nat.)
genehmigten Dissertation.

Vorsitzender: Univ.-Prof. Dr. L. Oberauer
Prüfer der Dissertation: 1. Hon.-Prof. Dr. W. F. L. Hollik
2. Priv.-Doz. Dr. A. Vairo

Die Dissertation wurde am 18.05.2015
bei der Technische Universität München eingereicht und
durch die Fakultät für Physik am 07.07.2015 angenommen.

Publications

This dissertation is based on the author's work conducted at the Max Planck Institute for Physics (Werner-Heisenberg Institut) in Munich. Parts of this work have already been published or are in preparation for publication:

Articles

- [1] G. Cullen, H. van Deurzen, N. Greiner, G. Heinrich, G. Luisoni, P. Mastrolia, E. Mirabella, G. Ossola, T. Peraro, J. Schlenk, J.F. von Soden-Fraunhofen, F. Tramontano, *GoSam-2.0: a tool for automated one-loop calculations within the Standard Model and beyond*, Eur.Phys.J. C74 (2014) 8, 3001
- [2] H. van Deurzen, G. Luisoni, P. Mastrolia, E. Mirabella, G. Ossola, T. Peraro, *Multi-leg One-loop Massive Amplitudes from Integrand Reduction via Laurent Expansion*, JHEP 1403 (2014) 115
- [3] H. van Deurzen, G. Luisoni, P. Mastrolia, E. Mirabella, G. Ossola, T. Peraro, *NLO Corrections to Higgs boson production in association with a top quark pair and a jet*, Phys.Rev.Lett. 111 (2013) 171801
- [4] G. Cullen, H. van Deurzen, N. Greiner, G. Luisoni, P. Mastrolia, E. Mirabella, G. Ossola, T. Peraro, F. Tramontano, *NLO QCD corrections to Higgs boson plus three jets in gluon fusion*, Phys.Rev.Lett. 111 (2013) 131801
- [5] H. van Deurzen, N. Greiner, G. Luisoni, P. Mastrolia, E. Mirabella, G. Ossola, T. Peraro, J.F. von Soden-Fraunhofen, F. Tramontano, *NLO QCD corrections to the production of Higgs plus two jets at the LHC*, Phys.Lett. B721 (2013) 74-81

In preparation

- [6] H. van Deurzen, R. Frederix, V. Hirschi, G. Luisoni, P. Mastrolia, G. Ossola, GOSAM + MADGRAPH5_AMC@NLO, *a complete NLO event generator*, in preparation (2015)

Reports

- [7] J. Butterworth, G. Dissertori, et al., *Les Houches 2013: Physics at TeV colliders: Standard Model Working group report*, arXiv:hep-ph/1405.1067
- [8] S. Alioli, S. Badger, et al., *Update of the Binoth Les Houches Accord for a standard interface between Monte Carlo tools and one-loop programs*, Comput.Phys.Commun. 185 (2014) 560-571
- [9] S. Heinemeyer, C. Mariotti, et al., *Handbook of LHC Higgs Cross sections: 3. Higgs Properties*, arXiv:hep-ph/1307.1347 (2013)

Proceedings

- [10] H. van Deurzen, N. Greiner et al., *Recent progress in higher order computations for the physics of the Higgs boson*, PoS LL2014 (2014) 038
- [11] H. van Deurzen, N. Greiner et al., *Automated one-loop calculations with GoSam2.0*, PoS LL2014 (2014) 021
- [12] H. van Deurzen, *Associated Higgs production at NLO with GoSam*, Acta Physica Polonica B44 (2013) 11 2223-2230
- [13] G. Cullen, H. van Deurzen et al., *GoSam @ LHC: algorithms and applications to Higgs production*, PoS RADCOR2013 (2013) 029
- [14] H. van Deurzen, G. Luisoni et al., *Multi-loop Integrand Reduction via Multivariate Polynomial Division*, PoS RADCOR2013 (2013) 012
- [15] G. Cullen, H. van Deurzen et al., *NLO QCD Production of Higgs boson plus jets with GoSam*, PoS EPS-HEP2013:446 (2013)
- [16] G. Cullen, H. van Deurzen, et al., *GoSam applications for automated NLO calculations*, J.Phys.Conf.Ser., 523:012056 (2014)
- [17] P. Mastrolia, E. Mirabella, G. Ossola, T. Peraro, H. van Deurzen, *The integrand reduction of One- and Two-Loop scattering Amplitudes*, PoS LL2012 (2012) 028

Abstract

To assess the properties of the recently discovered Higgs boson, as well as to search for possible physics beyond the Standard Model, very precise theoretical predictions of both signal and background processes are warranted. Leading-order calculations in perturbation theory have shown to be insufficient to reach the required precision, which necessitates shifting to next-to-leading order (NLO), where loop diagrams appear. Furthermore, with the larger center-of-mass energy at the Large Hadron Collider, the multiplicity of the particles produced and the kinematic probability of creating massive particles will increase as well. Especially at these multi-particle processes, the number of loop diagrams will be of a magnitude that makes automation of these calculations imperative. In this dissertation the developments toward fully automated evaluation of one-loop scattering amplitudes at hadron colliders will be presented.

Several techniques have been developed in recent years to simplify the computation of one-loop diagrams. Particularly successful was the integrand reduction algorithm as implemented in the code SAMURAI, which decomposes the integrand of the loop integral into a sum of fundamental contributions and extracts the coefficients of this decomposition, which can then be used to write the amplitude as a linear combination of scalar master integrals. The loop integration is effectively replaced by the much simpler task of fitting the coefficients of a multivariate polynomial in the loop momentum. SAMURAI was however unable to process so-called higher-rank integrands, which appear in the calculation of processes involving effective couplings. The expansion of the integrand reduction algorithm to include higher-rank diagrams was implemented in the extended code XSAMURAI.

XSAMURAI is incorporated in GOSAM, a framework for the automated evaluation of one-loop scattering amplitudes. This framework has in recent years been enhanced with a number of new features and improvements in speed, stability and accuracy. These improvements and the extension to higher-rank capability allowed GOSAM to compute three of the most important Higgs boson production processes at LHC: Higgs boson production in association with jets in vector boson fusion ($pp \rightarrow H + \text{jets}$ in VBF), in association with a top anti-top pair and a jet ($pp \rightarrow H t \bar{t} j$) and Higgs production in gluon fusion in association with up to three jets ($pp \rightarrow H + 3j$ in GF). Currently, because of the extension to higher rank, GOSAM is the only code able to calculate this last process.

For full NLO calculations, one-loop calculations are just one ingredient and Monte Carlo programs are needed to provide the others. For this reason, an interface between GOSAM and the Monte Carlo program MADGRAPH5_AMC@NLO was constructed, yielding a powerful framework that will be capable of computing any process at NLO precision needed in the LHC era.

Contents

1. Introduction	1
2. Collider physics	7
2.1. Parton Distribution Functions	7
2.2. NLO calculations	8
2.3. Jet algorithms	11
2.4. Photon isolation	13
3. Standard Model	15
3.1. Electroweak sector	15
3.1.1. Higgs mechanism	16
3.1.2. Yang-Mills Lagrangian	17
3.1.3. Fermions	18
3.1.4. Yukawa couplings and fermion masses	18
3.2. Quantum chromodynamics	19
3.2.1. Asymptotic freedom	20
3.2.2. Scale dependence at NLO	21
4. One-loop calculations in Quantum Field Theory	23
4.1. Regularization	23
4.2. Tensor reduction	24
4.2.1. Passarino-Veltman reduction	25
4.2.2. Singular kinematic regions	29
4.3. Rational terms	30
4.3.1. Structure of rational terms	31
4.3.2. R_2 rational terms from effective rules	32
4.4. Construction of a massless basis	33
4.5. d -dimensional integrand decomposition	36
4.6. Parametric form of the numerators	38
4.6.1. Five-point contributions	38
4.6.2. Four-point contributions	38
4.6.3. Three-point contributions	39
4.6.4. Two-point contributions	40
4.6.5. One-point contributions	40
4.7. Integrand reduction algorithm	40

5. Extended d-dimensional integrand reduction	43
5.1. Samurai: d -dimensional integrand reduction	43
5.1.1. Discrete Fourier Transformation (DFT)	43
5.1.2. Quintuple cut	44
5.1.3. Quadruple cut	47
5.1.4. Triple cut	49
5.1.5. Double cut	50
5.1.6. Single cut	52
5.2. Xsamurai: Higher rank integrand reduction	53
5.2.1. Parametric form of the higher-rank residues	54
5.2.2. Quintuple and quadruple cut at higher rank	55
5.2.3. Triple cut at higher rank	55
5.2.4. Double cut at higher rank	56
5.2.5. Single cut at higher rank	59
5.2.6. Numerical considerations	59
5.2.7. XSAMURAI	60
6. Automation of one-loop calculations	63
6.1. The GOSAM framework	63
6.1.1. Overview	63
6.1.2. Amplitudes convention	65
6.1.3. Integrand reduction programs	67
6.1.4. GOSAM-2.0	68
6.2. Stability test and rescue system	71
6.2.1. Precision tests	71
6.2.2. Rescue system in GOSAM	72
6.2.3. Precision tests on massive high-multiplicity processes	73
6.3. Binoth Les Houches Accord	75
6.3.1. BLHA1	76
6.3.2. BLHA2	78
7. Higgs boson phenomenology	81
7.1. Higgs boson plus jets production in Vector Boson Fusion	82
7.1.1. Diagram selection	83
7.1.2. Higgs boson plus two jets in VBF	84
7.1.3. Higgs boson plus three jets in VBF	86
7.2. Higgs boson plus jets production in Gluon Fusion	88
7.2.1. Effective Field Theory	88
7.2.2. Higgs boson plus two jets in GF	89
7.2.3. Higgs boson plus three jets in GF	94
7.2.4. H+2j and H+3j with ATLAS setup	98
7.3. Higgs boson production in association with a $t\bar{t}$ pair and a jet	98
7.3.1. $pp \rightarrow Ht\bar{t}j$	100
7.3.2. Renormalization of the Yukawa coupling	101
7.3.3. Setup and parameters	101
7.3.4. Results	103

8. Framework for fully automatic NLO calculations	105
8.1. Overview MadGraph5_aMCatNLO	105
8.2. Description of the interface	105
8.3. Benchmark processes	106
8.4. Production of a top anti-top pair in association with two photons	108
8.4.1. Setup	109
8.4.2. Comparison with Sherpa and MadLoop	109
8.4.3. Phenomenological results	111
9. Conclusions	115
A. Feynman rules	117
A.1. Electroweak sector	117
A.2. Quantum Chromodynamics	119
A.3. Effective Higgs boson vertices	121
B. One-loop integrals	123
B.1. Higher dimensional integrals	123
B.1.1. $I_{ij}[\mu^2]$	124
B.1.2. $I_{ijk}[\mu^2]$	124
B.2. Higher rank integrals	125
C. Spinor helicity formalism	127
D. Residues	129
D.1. Five-point contributions	129
D.1.1. Normal rank	129
D.1.2. Higher rank	129
D.2. Four-point contributions	129
D.2.1. Normal rank	129
D.2.2. Higher rank	129
D.3. Three-point contributions	130
D.3.1. Normal rank	130
D.3.2. Higher rank	130
D.4. Two-point contributions	130
D.4.1. Normal rank	130
D.4.2. Higher rank	131
D.5. One-point contributions	131
D.5.1. Normal rank	131
D.5.2. Higher rank	131
E. GOSAM example	133
F. Benchmark phase space points	135
F.1. SAMURAI and Ninja $pp \rightarrow H + 3j$ in VBF	135
F.2. Ninja $Zt\bar{t}$	137
F.2.1. $u\bar{u} \rightarrow t\bar{t}e^+e^-$	137
F.2.2. $g\bar{g} \rightarrow t\bar{t}e^+e^-$	137

Contents

F.3. Ninja $Zt\bar{t}j$	138
F.3.1. $u\bar{u} \rightarrow t\bar{t}e^+e^-g$	138
F.3.2. $gg \rightarrow t\bar{t}e^+e^-g$	138
F.4. SAMURAI $pp \rightarrow H + 2j$ in GF	139
F.5. SAMURAI $pp \rightarrow H + 3j$ in GF	140
F.6. Ninja $pp \rightarrow Ht\bar{t}j$	141

Acknowledgments	153
------------------------	------------

1 ■ Introduction

On the 4th of July 2012, ATLAS and CMS, two experiments at the *Large Hadron Collider* (LHC) at the particle physics laboratory CERN, together announced the discovery of a new boson [18,19], which was later confirmed to be consistent with the Higgs boson of the Standard Model. The Nobel prize 2013, a mere fifteen months later, was awarded to François Englert and Peter Higgs who were among the first to postulate a particle like this had to exist, in the context of the Brout-Englert-Higgs mechanism [20–25]. These two events mark the triumphant conclusion of a search that has been ongoing for almost half a century since the original set of papers appeared in 1964. With its last missing predicted building block now discovered, the Standard Model has been confirmed as our most accurate description of elementary particles at present. It has been validated over the course of decades by a great number of experiments, leading to some of the most accurate measurements in physics.

Nevertheless, there are numerous indications that the Standard Model cannot be the ultimate theory of nature. Regardless of its great success, the Standard Model suffers from a list of shortcomings. It has no explanation for Dark Matter and Dark Energy, nor for the extreme difference in strength between the weak force and the gravitational force, neutrino oscillations or the observed excess of matter over anti-matter in the universe. Apart from these unexplained phenomena in nature, there are also indications from the theoretical side. The Standard Model does not include a description of gravity at the quantum level, and there is no explanation for the large variety in masses appearing in the Standard Model. The Higgs boson mass acquires quantum corrections that require the Standard Model to have an extreme amount of fine-tuning of its parameters, known as the *hierarchy problem*. Over the years, a large number of theories have been developed to account for these problems, which are collectively known as *Beyond the Standard Model* (BSM) theories. Now that the Higgs boson has been found, the focus of the LHC will shift to searching for indications of BSM physics.

Both precise measurements of the Higgs properties and searches for BSM physics are plagued by enormous SM backgrounds. At hadron colliders in particular, these will predominantly be dictated by *Quantum Chromodynamics* (QCD). QCD is an asymptotically free theory, meaning that its coupling α_s becomes small for high energies, allowing for a perturbative treatment, whereas at low energies the coupling becomes large and the validity of perturbation theory breaks down. At this energy regime the partons cluster into hadrons. This is a challenging property for measurements at hadron colliders, because at the high energies of the collision the constituents of the proton, the quarks and gluons, behave like free particles, whereas the detectors operate in the low energy limit where only bound states occur. The main task of particle physics phenomenology is to translate theoretical models into experimentally measurable predictions. In particular for the QCD induced processes at hadron colliders, the

phenomenological approach is to factorize events based on the energy scales at which they operate. Events at hadron colliders are quite involved, primarily because in general both the initial and final state are not precisely known. Contrary to the situation at e^+e^- colliders like the *Large Electron-Positron Collider* (LEP), which operated between 1989 and 2000 at CERN, at hadron colliders the colliding particles are not well-defined point-like particles. Hadrons comprise a number of valence quarks, three in the case of baryons. At higher energies, they contain also an infinite sea of light quark anti-quark pairs and gluons. Probing a hadron at energy Q^2 allows for sea quarks with masses $m_q \ll Q$. *Parton Distribution Functions* (PDFs) give the probability of finding a parton when probing a hadron with a certain energy, hence they govern which partons participate in the hard interaction. The hard interaction is the high energy part of the event that can be calculated perturbatively. The QCD evolution from the hard interaction down to hadronization scale, which is typically around $\Lambda_{QCD} = 1 \text{ GeV}$, is achieved through emission of quarks and gluons in what is known as a *parton shower*. The resulting hadrons will often still decay into the particles that can be observed by the detector. The beam remnants can have a secondary interactions, leading to a further complication in disentangling the event. Figure 1.1 gives an overview of an event at a hadron collider.

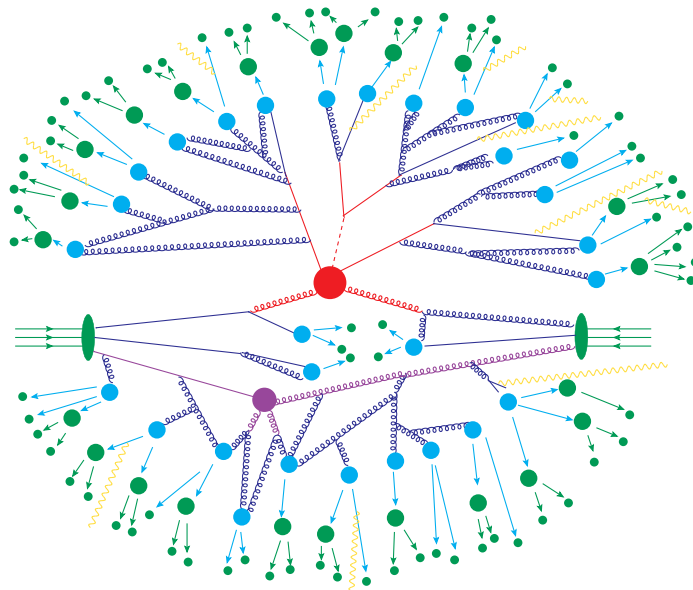


Figure 1.1.: An illustration of an event at hadron colliders, inspired by a similar picture by the SHERPA collaboration [26]. The event can be factorized in different energy scales. The hard interaction, which can be calculated perturbatively, is shown in red. The incoming hadrons contain gluons, sea quarks and three valence quarks. Which of those participate in the hard interaction is governed by the PDFs. The produced partons will radiate, shown in dark blue. These partons are evolved by a parton shower, until they reach the hadronization scale, shown in light blue. The particles that form at this stage can be stable or unstable, in the latter case decaying into even more particles. Photons, shown in yellow, can be radiated at any stage. Apart from the primary hard interaction, there can be secondary interactions at high energy scales, shown in purple.

In order to confirm the new boson is indeed the Standard Model Higgs boson, several of its properties have to be measured. These include its spin, its CP -properties and its couplings to

other particles. To determine these properties as accurate as possible, very precise theoretical predictions are necessary. Furthermore, precise theoretical predictions and accurate modelling of the background are needed to constrain the model parameters of any new physics that may be found. In general, searching for new particles in colliders requires ever higher center-of-mass energies to probe new physics regimes. These high energy scales have two important effects on the final state of the hard interaction: There is an increase both in multiplicity of the final state and in the kinematic probability of creating massive particles.

Hence, there has been an increasing need for precise theoretical predictions of massive multi-particle processes. In fact, over recent years, theoretical precision has only just managed to keep up with its experimental counterpart. Central to theoretical predictions for the hard interaction is the computation of *scattering amplitudes*, which describe the probability of particles interacting. Exact computations of observables are not realistic in a quantum field theory like the Standard Model and therefore resorting to *perturbation theory* is required. Aiming at higher precision then means going to higher orders in perturbation theory, which complexifies the computation since it requires the calculation of loop diagrams. Calculations at *leading order* (LO) in perturbation theory, very commonly used until recently for almost all relevant processes, have become insufficient and the standard has shifted to *next-to-leading order* (NLO) calculations.

Theoretical uncertainties originate from two different sources. Firstly, there are *parametric uncertainties*, which are caused by the uncertainty on the input parameters, such as the uncertainty on the precise value of the top mass. Secondly, there is the *truncation uncertainty*, which is the uncertainty that is caused by truncating the perturbative expansion. A common approach to estimate the truncation uncertainty is to assess the dependence on the renormalization and factorization scale. These scales are unphysical, hence at infinite order observables are expected to be independent of the choice of this scale. LO calculations however show a strong dependence on these scales. Increasing the order of the calculation therefore makes the calculated quantity less dependent on the scale, thereby reducing the uncertainty of the calculation, which is nicely illustrated in Figures 1.2 and 1.3.

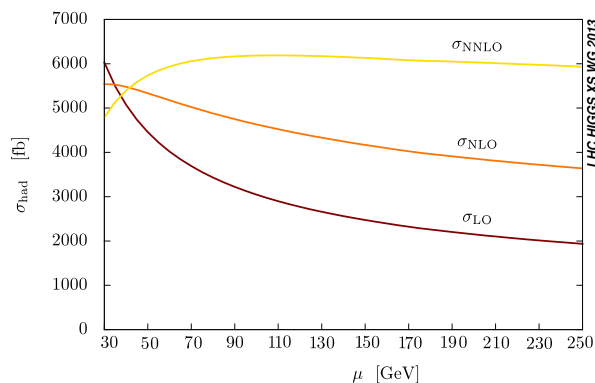


Figure 1.2.: Example of the effect of going to higher-order calculations. Shown is the dependence on the renormalization and factorization scale μ of the total cross section of the process $pp \rightarrow Hj$, at Leading Order (LO), Next-to-Leading Order (NLO) and Next-to-Next-to-Leading Order (NNLO) [7, 27].

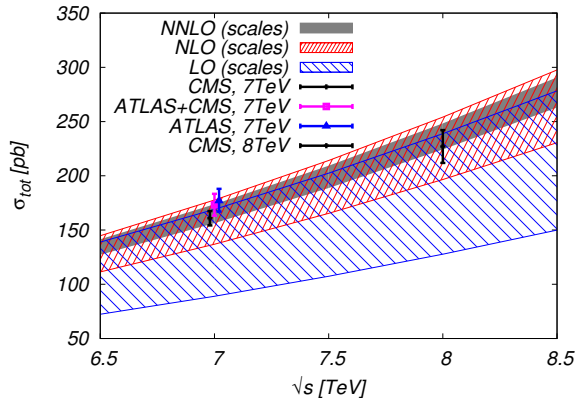


Figure 1.3.: Example of the effect of including higher-order contributions on the uncertainty of a calculation. Shown is the dependence on the center-of-mass energy \sqrt{s} of the total cross section of the process $pp \rightarrow t\bar{t}$, at Leading Order (LO), Next-to-Leading Order (NLO) and Next-to-Next-to-Leading Order (NNLO) [28], together with the measurements of ATLAS and CMS at $\sqrt{s} = 7$ TeV and $\sqrt{s} = 8$ TeV. The error bands are obtained by varying the renormalization and factorization scale.

For NLO calculations, in particular the one-loop contributions used to be a bottleneck. This motivated the development of novel techniques and dedicated programs for one-loop calculations. The methods based on *unitarity* have been particularly influential. Unitarity, in essence just a statement about conservation of probability, leads to the *optical theorem*, relating the total cross section to the imaginary part of the scattering amplitude. This can be used to show that an amplitude factorizes into lower-point amplitudes when one *cuts*, *i.e.* puts on-shell, a set of internal propagators. These techniques stimulated the development of concepts which have been explored systematically in the framework of *generalized unitarity* [29,30]. From the traditional approach to the calculation of one-loop diagrams, known as *Passarino-Veltman reduction* [31], it naturally follows that any one-loop integral can be decomposed into a basis of scalar *master integrals*, with up to four legs. The calculation then simplifies to the task of determining the coefficients of this decomposition, which is what methods such as generalized unitarity and improved tensor reduction [32] aim to do. An important element leading to the development of further sophisticated numerical methods was the universal decomposition in four dimensions of the numerator of a one-loop integrand, known as *integrand decomposition* [33–36]. Combined with generalized unitarity, it was realized that the coefficients of the master integrals can be extracted by using the knowledge of the mathematical structure of the integrands. The integrands of Feynman diagrams are rational functions of the components of the loop momentum, with numerators that are polynomial in these components and as many quadratic denominators as there are external legs, coming from the propagators inside the loop. Any integrand can be expressed as a linear combination of fundamental contributions, which are expressions with numerators that are *irreducible polynomial residues*. The so-called *multiple cut conditions*, in which the propagators are put on-shell simultaneously, then function as projectors to isolate the corresponding residues. These residues have a form that is process independent, whereas the actual values of the coefficients are process dependent. A subset of the coefficients obtained in this way can then be identified with the ones multiplying the master integrals. In this way, the complicated task of loop integration is reduced to

the much simpler task of fitting the coefficients of a (multivariate) polynomial. This method was later generalized to full *d-dimensional integrand-reduction* as implemented in the code SAMURAI [37], which revealed a richer polynomial structure of the residues.

Driven by the development of these new techniques, over the last couple of years, one could witness a surge in NLO calculations, sometimes referred to as the *NLO revolution*. This name was mainly motivated by the remarkable increase in the final state multiplicity of the available processes. In the 1990s, NLO calculations were available for $2 \rightarrow 2$ processes at most. This increased to $2 \rightarrow 3$ in the early years of the 21st century. At the dawn of the second decade, this suddenly rose within a few years to $2 \rightarrow 6$ processes with the calculation in 2013 of $pp \rightarrow W + 5j$ at NLO [38]. This spectacular increase was in fact very much needed: The list of processes for which theoretical NLO prediction are warranted at LHC energy scales are often $2 \rightarrow 4$ or even higher final state multiplicity. This effectively means that the sheer number of loop diagrams to be calculated, frequently in the order of $\mathcal{O}(10^3 - 10^4)$, poses a practical problem on its own. For a long time NLO calculations were done on a process-by-process basis, often requiring the effort of a large number of people for a long time, in recent years the focus therefore has been forced to shift to the automation of NLO calculations.

The GOSAM framework [1, 39] for the automated computation of one-loop diagrams was designed with this automation as primary motivation. The name of the framework originates from its original constituents GOLEM95C [40–43], a program based on tensor reduction, and the before mentioned SAMURAI. Later NINJA [44, 45] was added as third reduction procedure.

The developments in the context of the work performed for this dissertation were focused around this framework. The code SAMURAI was originally not designed with the capability of calculating processes with so-called *higher-rank numerators*. These kind of numerators appear in particular in one-loop calculations in which the Higgs boson is produced through effective gluon-Higgs boson couplings, a production channel known as *gluon fusion*. Therefore, to be able to calculate processes involving gluon fusion, SAMURAI was extended to include higher-rank functionality. This extended code, named XSAMURAI [12], is a generic reduction library that can be interfaced to any code. The deeper understanding of the structure of the residue, combined with the implementation in XSAMURAI allowed for the calculation of Higgs boson production in gluon fusion in association with jets at full NLO in QCD. This calculation was performed in association with two [5] and three jets [4, 7, 9]. The latter calculation, a six-point process with over thirteen thousand one-loop diagrams, pushed the computational capability of the original GOSAM framework to its limit. This sparked the need for several improvements, which eventually together with a variety of new features were collected in an updated version of the code, which was released in [1]. An important contribution to the development of this new version were the tests performed on the stability of the code, which were presented originally in [2]. Among other improvements, the new features also included the possibility to have massive gauge bosons inside the loop. As an illustration to the usefulness of this capability, the NLO QCD virtual corrections to the production of a Higgs boson in *vector boson fusion* in association with up to three jets were calculated. The GOSAM framework was also used to calculate the production of a Higgs boson in association with a top anti-top pair and an additional jet at NLO in QCD [3]. This process is phenomenologically important to measure the relevant properties of the Higgs boson, but was considered very difficult because of the massive particles in the loop and the appearance of two mass scales.

Besides the virtual corrections given by the one-loop diagrams, several other ingredients are needed for full NLO calculations. These are provided by *Monte Carlo programs*, which also take care of the other elements depicted in Figure 1.1: The use of PDFs, the matching to parton showers and any decays of the final state particles. In order to facilitate the communication between Monte Carlo programs and *one-loop providers* like GOSAM, a standardized interface was designed, known as the *Binoth-Les-Houches-Accord* [8, 46]. This standard was used to build an interface [6] between the Monte Carlo program `MADGRAPH5_AMC@NLO` [47] and GOSAM2.0. The resulting powerful framework, harnessing the strengths of both codes, promises to be able to calculate virtually any phenomenologically relevant full NLO process.

The structure of this dissertation is given in the following outline. A review of the collider physics relevant for this work will be given in Chapter 2, followed by a brief introduction to the Standard Model in Chapter 3. In Chapter 4, the *Passarino-Veltman reduction* and the *d-dimensional integrand decomposition algorithm* will be discussed in detail.

After setting these theoretical preliminaries, the developments in the context of the work performed for this dissertation will be explored. In Chapter 5, the implementation of the *d-dimensional integrand decomposition algorithm* in SAMURAI will be presented and we will focus specifically on XSAMURAI.

Chapter 6 will then cover the automation of one-loop calculations. It will give an overview of the GOSAM framework and its improvements collected in GOSAM2.0, as well as discuss the tests on the stability of the code presented in [2]. The details of the Binoth-Les-Houches Accord, which was used in combination with GOSAM for the calculation of several important processes, will be discussed here as well. In particular the improvements of the update presented in [8] and implemented in GOSAM2.0 will be explained.

The novel techniques and their automation as presented in these two chapters lead to a very strong tool which was exploited in the calculation of three of the most important Higgs boson production channels at the LHC. The results of these three Higgs boson phenomenology projects are collected in Chapter 7. Firstly, the NLO QCD corrections to Higgs boson production in vector boson fusion in association with up to three jets ($pp \rightarrow H + 3j$ in VBF) will be discussed. Secondly, the results of the full NLO QCD calculation of the production of a Higgs boson in *gluon fusion* in association with jets ($pp \rightarrow H + \text{jets}$ in GF) will be presented. Thirdly, the full NLO QCD calculation of Higgs boson production in association with a top anti-top pair and an additional jet ($pp \rightarrow Ht\bar{t}j$) is presented.

Finally, in Chapter 8, the details of the work on the interface between GOSAM and the Monte Carlo program `MADGRAPH5_AMC@NLO` will be discussed. As an illustration, we will focus on the full NLO QCD calculation of the production of a top anti-top pair in association with two photons.

2 ■ Collider physics

The goal of particle physics is to develop a mathematical theory which describes the dynamics of the fundamental building blocks of matter. This theory should allow to make predictions for quantities and observables which can be measured directly in experiments. In quantum mechanics, the probability of measuring a final state $|f\rangle$ starting from an initial state $|i\rangle$ is described by the unitary S -matrix,

$$\mathcal{P}(i \rightarrow f) = |\langle f|S|i\rangle|^2. \quad (2.1)$$

The S -matrix can be split in a noninteracting part, which is simply the identity operator, and the part that is caused by interactions, which is known as the T -matrix,

$$S = 1 + iT. \quad (2.2)$$

The conservation of momentum can be written explicitly by splitting off a delta-function,

$$\langle f|iT|i\rangle = (2\pi)^4 \delta^{(4)}(k_i - k_f) \cdot i\mathcal{M}(i \rightarrow f), \quad (2.3)$$

where k_i and k_f are the momenta of the incoming and outgoing particles respectively and where the *invariant matrix element* \mathcal{M} was introduced. The total cross section also includes the integration over the available phase space of the final state particles and dividing by the incoming flux. Hence, the cross section for a $2 \rightarrow n$ scattering process with momenta $\{k_i^\mu\}$ is given by

$$d\sigma = \frac{1}{2E_1 E_2 |v_1 - v_2|} \prod_{j=3}^{n+2} \frac{d^3 k_j}{(2\pi)^2 2E_j} \delta^{(4)}(k_1 + k_2 - \sum_{j=3}^{n+2} k_j) |\mathcal{M}|^2, \quad (2.4)$$

with E_j denoting the energy of a particle and $|v_1 - v_2|$ being the relative velocity of the colliding beams in the laboratory frame. In this way, the details of the interaction, the *dynamics*, contained in the matrix element \mathcal{M} , are separated from the elements that do not, the *kinematics*.

2.1. Parton Distribution Functions

The calculation of cross sections becomes more complicated when the initial state particles are hadrons, as is the case at Tevatron and LHC. Considering a hard scattering process of two hadrons with momenta P_1 and P_2 , the cross section can be written as

$$\sigma(P_1 P_2 \rightarrow X) = \sum_{ij} \int_0^1 dx_1 \int_0^1 dx_2 f_i(x_1, \mu_F^2) f_j(x_2, \mu_F^2) \int d\hat{\sigma}_{ij}(x_1 P_1, x_2 P_2, \alpha_s(\mu_F^2), Q^2/\mu_F^2). \quad (2.5)$$

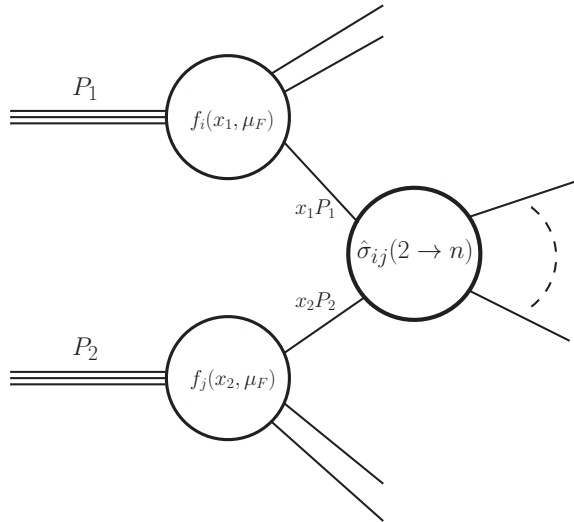


Figure 2.1.: Pictorial representation of a hadronic interaction. The colliding hadrons have momenta P_1 and P_2 . The parton distribution functions f_i and f_j at factorization scale μ_F govern which constituents participate in the partonic interaction $\hat{\sigma}_{ij}$ and with which momentum fractions. The partonic interaction is then calculated using 2.4.

The summation is over all possible initial state partons i and j . The momenta of the incoming partons, which are assumed massless, participating in the hard interaction are $p_1 = x_1 P_1$ and $p_2 = x_2 P_2$. Q is the characteristic scale of the hard interaction. The functions $f_i(x_1, \mu_F^2)$ and $f_j(x_2, \mu_F^2)$ are the parton distribution functions (PDFs), which parametrize the probability of quarks and gluons from the hadron participating in the hard interaction. The partonic cross section σ_{ij} is then again given by equation (2.4). A pictorial representation is given in Figure 2.1.

QCD makes no predictions on the parton content of hadrons, therefore the only way to determine the shape of the PDFs is to fit the data of experiments. The usual procedure is to start with non-perturbative PDFs at low scale and fit to experimental data, which can be for example data from *Deep Inelastic Scattering* (DIS) experiments. The DGLAP equations [48–51], which express how a PDF changes as a function of the energy scale at which they are probed, are then used to evolve to the wanted scale. The final result then still depends on a variety of parameters, among which the order in perturbative QCD at which the calculation is performed, which input data is used, how the heavy quarks are treated and which assumptions are made about the PDFs. In Figure 2.2 the PDF set MSTW2008 [52] is shown as an example.

2.2. NLO calculations

Computations in particle physics are performed in a perturbative expansion of a coupling constant. This is possible when the expansion parameter is sufficiently small in the energy regime that is being considered. For example, a cross section in perturbative *quantum chromodynam-*

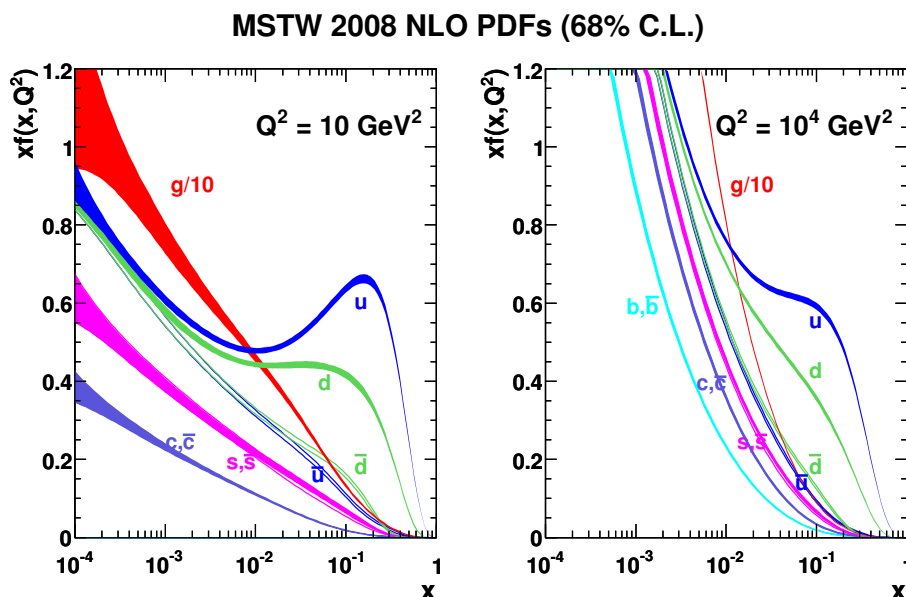


Figure 2.2.: The NLO PDF set MSTW2008 [52] at two different energy scales $Q^2 = 10 \text{ GeV}^2$ and $Q^2 = 10^4 \text{ GeV}^2$. Shown is the probability density for finding a parton with transverse momentum fraction x . The uncertainty bands are at 68% confidence level.

ics (see Section 3.2) can be written as an expansion in the strong coupling constant α_s ,

$$\sigma = \alpha_s^b \left[\sigma^{(0)} + \frac{\alpha_s}{2\pi} \sigma^{(1)} + \left(\frac{\alpha_s}{2\pi} \right)^2 \sigma^{(2)} + \dots \right]. \quad (2.6)$$

The *Leading Order* (LO) contribution, $\sigma^{(0)}$, contains only the so-called *tree-level diagrams*, which contain no loops or additional radiation. The contribution to the cross section is given by the sum over all coherently interfering tree-level diagrams, which we denote by \mathcal{A}_0 ,

$$\sigma^{(0)} \propto \sum |\mathcal{M}|_{\text{tree}}^2 = \sum \mathcal{A}_0^\dagger \mathcal{A}_0. \quad (2.7)$$

One order higher, there are two types of contributions. The *real contribution* is given by diagrams which feature additional radiation, denoted by $\mathcal{A}_{0,1}$, interfered with themselves,

$$\sigma_R \propto \sum |\mathcal{M}|_{\text{radiation}}^2 = \sum \mathcal{A}_{0,1}^\dagger \mathcal{A}_{0,1}. \quad (2.8)$$

The *virtual contribution* is given by diagrams which contain a loop, denoted by \mathcal{A}_1 , interfered with the tree level-diagrams,

$$\sigma_V \propto \sum |\mathcal{M}|_{1\text{-loop}}^2 = \sum \mathcal{A}_1^\dagger \mathcal{A}_0 + \mathcal{A}_0^\dagger \mathcal{A}_1. \quad (2.9)$$

The next order in the expansion is then given by the sum of the two,

$$\sigma^{(1)} = \sigma_V + \sigma_R. \quad (2.10)$$

One-loop diagrams can be *UV divergent*. UV divergences arise through integrating over internal loop-momenta, as we will show in Chapter 4. These divergences need to be regularized, *i.e.*

made visible in a consistent way, through a *regularization method*. One often used method is *dimensional regularization*, because it preserves Lorentz and gauge invariance. In this method loop-calculations are performed in $d = 4 - 2\epsilon$ dimensions and at the end the limit $\epsilon \rightarrow 0$ is taken. Commonly used varieties are conventional dimensional regularization (CDR), 't Hooft-Veltman regularization (tHV) [53] and dimensional reduction (DRED) [54]. See [55–57] for a discussion on the different schemes.

Using dimensional regularization, UV divergences appear as poles $1/\epsilon$, which can then be absorbed in a redefinition of the fields and parameters, a procedure known as *renormalization*. This is accomplished by adding *counterterms* to the Lagrangian that exactly cancel the divergent parts of the Lagrangian. These counterterms do not only make the final result finite, but also redefine the meaning of the input parameters. The form of the finite parts, as well as the exact meaning of the parameters that remain, depend on the renormalization conditions given by the chosen renormalization scheme. Two often used schemes are the minimal subtraction scheme (MS -scheme) and the modified minimal subtraction scheme (\overline{MS} -scheme), which differ by the finite terms that are absorbed in the counter-terms.

A full *Next-to-Leading-Order* (NLO) calculation then consists of the three ingredients mentioned above. However, both of the two types of corrections, σ_V and σ_R , can be *infrared divergent*. IR divergences arise if an emitted gluon from a quark line is either soft (vanishing energy) or collinear (vanishing angle between two particles).

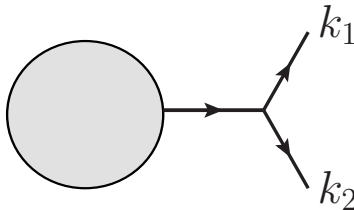


Figure 2.3.: Infrared divergences can occur if an external parton splits into two massless particles.

Consider a general process where an external massless particle splits into two massless particles. This could be a parton emitting a gluon or a gluon splitting into a quark pair. The internal propagator is given by

$$\frac{1}{(k_1 + k_2)^2} = \frac{1}{2E_1 E_2 (1 - \cos \theta_{12})}. \quad (2.11)$$

where E_1 and E_2 are the energies of the two particles and θ_{12} is the angle between them. This expression diverges for either $E_1 \rightarrow 0$, $E_2 \rightarrow 0$ or $\theta_{12} \rightarrow 0$. Similarly, loop-diagrams exhibit IR divergences when the loop momentum becomes arbitrarily small or collinear to an external massless particle. Since from quantum mechanics it is known that all indistinguishable processes with the same final state have to be summed together, real radiation contributions where a particle becomes unresolved and the corresponding virtual contributions have to be added together. Upon summation, all divergences cancel at every order in perturbation theory. This is a consequence of the Bloch-Nordsieck [58] and Kinoshita-Lee-Naunberg theorems [59, 60], which state that observable transition probabilities are free from soft and collinear divergences.

In order not to spoil the cancellation of the divergences, an observable J_m which depends on m final state momenta k_1, \dots, k_m should be *infrared safe*, *i.e.* it has to fulfill the following two requirements:

$$\begin{aligned} J_{m+1}(\dots, k_i, \dots, k_j, \dots) &\longrightarrow J_m(\dots, k_i + k_j, \dots), & \text{if } k_i \parallel k_j, \\ J_{m+1}(\dots, k_i, \dots) &\longrightarrow J_m(\dots, k_{i-1}, k_{i+1}, \dots), & \text{if } k_i \rightarrow 0. \end{aligned} \quad (2.12)$$

When performing a numerical phase space integral, the presence of IR divergences is still a problem, since they become explicit only after integration. One then needs a *subtraction scheme* to regulate these infinities at the integrand level. In this method a term is subtracted from the $(m+1)$ -particle integral, and is added back to the m -particle integral, while integrating over the phase space of the additional particle. In summary, the full NLO cross section is given by

$$\sigma^{NLO} = \int_m \left[d^{(4)}\sigma^B + \int_{loop} d^{(d)}\sigma^V + \int_1 d^{(d)}\sigma^S \right] + \int_{m+1} \left[d^{(4)}\sigma^R - d^{(4)}\sigma^S \right]. \quad (2.13)$$

where the integrals outside the brackets are over the m - and $(m+1)$ -particle phase space, and the ones inside the brackets over the internal loop momentum and the additional single particle phase space. The m - and $(m+1)$ -particle integrals are now IR finite on their own.

There are several subtraction schemes available. One that is very often used is the *Catani-Seymour dipole formalism* [61, 62]. Other subtraction methods are the *antenna subtraction method* [63, 64] and the *FKS approach* [65]. Calculating subtraction terms is numerically time consuming and only necessary in the vicinity of a collinear and/or soft limit. Therefore, in [66, 67], a slightly modified version of Catani-Seymour dipole subtraction was proposed, which introduced the α *parameter* with $\alpha \in (0, 1]$. This parametrizes the region for which subtraction terms are non-zero, with at $\alpha = 1$ the full Catani-Seymour dipole subtraction. The α parameter is not only useful in restricting the phase space for which subtraction terms need to be calculated, but can also be used as a test of the numerical stability of a result: The full correction should be independent of slightly varying the α parameter.

2.3. Jet algorithms

The calculations in perturbative QCD work with final states that can include partons. However, whenever these particles are produced, they will immediately start radiating off more partons until they have reached the hadronization energy scale, a process known as *parton showering*. At the end of the partons shower the partons cluster into hadrons, which can subsequently decay into even more particles. What in the end hits the detector is a large collection of hadrons. The clustering of these particles into *jets* that are defined in an unambiguous way is far from trivial. A jet is defined in a set of rules that govern how to cluster particles and how to assign a momentum to the resulting jet. The first jet algorithm was developed in the late 1970s by Stermann and Weinberg [68]. It defined an event as having two jets when a fraction $1 - \epsilon$ of the energy of the event was contained in two cones that had an opening half-angle of δ , which is an example of a *cone algorithm*. Cone algorithms today are still being used in hadron colliders, even though they have evolved substantially. Many

cone algorithms now make use of *iterative cones*, in which a seed particle i is taken for an initial direction and the momenta of all particles j within a cone of radius R around i , with azimuthal angle ϕ and rapidity y (or pseudo-rapidity η),

$$\Delta R_{ij}^2 \equiv (y_i - y_j)^2 + (\phi_i - \phi_j)^2 < R^2, \quad (2.14)$$

where the rapidity y or pseudorapidity η are defined as

$$y = \frac{1}{2} \ln \frac{E + p_z}{E - p_z}, \quad \eta = -\ln \tan \frac{\theta}{2}, \quad (2.15)$$

in terms of energy and momentum in the direction of the beam axis, and longitudinal angle θ . The dimensionless parameter R^2 is called the jet radius. The particles in the jet are then summed and the resulting vector is used as a new seed i in this iterative algorithm. The algorithm stops when a stable configuration for the cone is reached.

Another class of algorithms are the *sequential recombination algorithms*, which define a measurement of distance between two particles and order the particles into jets from the bottom up. The k_t algorithm, first described in [69], for example defines (in e^+e^- collisions)

$$y_{ij} = \frac{2\min(E_i^2, E_j^2)(1 - \cos \theta_{ij})}{Q^2}, \quad (2.16)$$

with Q^2 the total energy of the event, E_i and E_j the energies of the particles i and j respectively, and θ_{ij} the longitudinal angle between them. The algorithm then proceeds by searching for the smallest instance of y_{ij} . If this is below a certain threshold then i and j are combined into a new particle and the procedure is repeated with this new set of particles. When there are no particle pairs left with y_{ij} below the threshold, all remaining are declared jets. In the collinear limit $\theta_{ij} \ll 1$, y_{ij} reduces to the squared transverse momentum of i with respect to j , which is the reason behind the name of the algorithm. When the incoming particles are hadrons, the algorithm is a bit more complicated [70, 71]. Instead of the dimensionless y_{ij} , two dimensionful distances d_{ij} and d_{iB} are defined as

$$d_{ij} = \min((p_t^i)^2, (p_t^j)^2) \frac{\Delta R_{ij}^2}{R^2}, \quad d_{iB} = (p_t^i)^2, \quad (2.17)$$

with ΔR_{ij} as defined in equation (2.14) and p_t^i and p_t^j the transverse momentum with respect to the beam axis. The algorithm then searches for the minimal value in the combined sets of d_{ij} and d_{iB} . The particles are combined into a new particle if the minimum value is a d_{ij} . If the minimum value is a d_{iB} , it is declared a jet and removed from the list. The algorithm stops when there are no particles left. This version of the k_t algorithm has a new parameter R , which plays a similar role as the R in cone algorithms.

If one generalizes the k_t algorithm to allow for any power p of transverse momenta,

$$d_{ij} = \min((p_t^i)^{2p}, (p_t^j)^{2p}) \frac{\Delta R_{ij}^2}{R^2}, \quad d_{iB} = (p_t^i)^{2p}, \quad (2.18)$$

with $p = 1$ for the k_t algorithm, other possible choices become apparent. The algorithm with $p = 0$ is known as the *Cambridge/Aachen algorithm* [72], and particularly the choice $p = -1$, introduced as the *anti- k_t algorithm* in [73], has been used very frequently in recent calculations.

2.4. Photon isolation

Similarly as in the case of additional gluon radiation, also additional photons in the final state have to be treated with care to ensure IR safety. Photons can appear in the final state through two mechanisms. They are either produced in the hard scattering process, which can be calculated using perturbative QCD, or they appear in the fragmentation process of the parton shower. The *Frixione isolation procedure* [74] is a method to isolate photons in an infrared safe way. Given a photon and a hadron i , in this method one first calculates the angular distance $R_{i\gamma}$, which in the case of hadronic collisions is given by

$$R_{i\gamma} = \sqrt{(\eta_i - \eta_\gamma)^2 + (\phi_i - \phi_\gamma)^2}, \quad (2.19)$$

with η and ϕ being the pseudorapidity and azimuthal angle respectively. The event is rejected if the following condition is not fulfilled,

$$\sum_i E_i^T \theta(\delta - R_{i\gamma}) \leq \mathcal{X}(\delta) \quad \text{for all } \delta \leq \delta_0, \quad (2.20)$$

where E_i^T is the transverse energy of the hadron and δ_0 is the radius of isolation one has to set in advance. The function $\mathcal{X}(\delta)$ has to vanish as $\delta \rightarrow 0$. In the Frixione isolation procedure, it is given by

$$\mathcal{X}(\delta) = E_\gamma^T \epsilon_\gamma \left(\frac{1 - \cos \delta}{1 - \cos \delta_0} \right)^n, \quad (2.21)$$

with E_γ^T being the transverse energy of the photon. Often the choice $\epsilon_\gamma = n = 1$ is made.

3 ■ Standard Model

All calculations in this work are processes that are allowed in the Standard Model (SM) of particle physics. The essential parts of this model will be discussed in this chapter, leading to a set of Feynman rules as building blocks collected in Appendix A. The standard model is a quantum field theory in which the interactions can be derived from local symmetries called gauge symmetries. The most often used formulation is the Lagrange formalism, where all kinematic, mass and interaction terms are presented in a functional called the *Lagrangian*. By performing a four-dimensional integration over this functional the action of the theory can be obtained. The full Lagrangian of the Standard Model (SM) consists of the following different parts,

$$\mathcal{L}_{SM} = \mathcal{L}_{YM} + \mathcal{L}_{ferm} + \mathcal{L}_H + \mathcal{L}_{Yuk} + \mathcal{L}_{gf} + \mathcal{L}_{gh}, \quad (3.1)$$

where the subscript text indicate respectively the *Yang-Mills* part, the *fermionic* part, the *Higgs* part, the *Yukawa* part, the *gauge-fixing* part and the *Faddeev-Popov ghost* part, which will be discussed below.

The Lagrangian of the Standard Model is invariant under transformations of the symmetry group $SU(3)_C \otimes SU(2)_w \otimes U(1)_Y$,

$$U(\theta_s, \theta_w, \theta_Y) = \exp \left\{ ig_s T^a \theta_s^a + ig I_w^i \theta_w^i - ig' \frac{Y_w}{2} \theta_Y \right\} \equiv U(\theta_s) U(\theta_w) U(\theta_Y), \quad (3.2)$$

where θ_s , θ_w and θ_Y are arbitrary real parameters and g_s , g' and g are the couplings of their respective gauge groups. T_c^a ($a = 1, \dots, 8$), I_w^i ($i = 1, \dots, 3$) and Y_w are the generators of the gauge groups. The fundamental representations most often used for them are $T^a = \lambda^a/2$ and $I^i = \sigma^i/2$, with the Gell-Mann matrices λ^a and Pauli matrices σ^i . When going from global to local gauge invariance, the Lagrangian only stays invariant if the normal space-time derivative is replaced with a covariant derivative,

$$\partial_\mu \rightarrow D_\mu = \partial_\mu + ig_s T_c^a F_\mu^a + ig I_w^i W_\mu^i + ig' \frac{Y_w}{2} B_\mu, \quad (3.3)$$

where the new fields F_μ^a , W_μ^i and B_μ are called gauge fields.

3.1. Electroweak sector

We will focus first on the electroweak (EW) sector of the SM, which is realized through spontaneous symmetry breaking of the $SU(2)_w \otimes U(1)_Y$ part of the SM gauge symmetry. The mechanism behind this is known as the *Higgs mechanism*. Since we will not consider higher-order EW processes in this work, the gauge fixing and ghost parts of the Lagrangian will be ignored in this section.

3.1.1. Higgs mechanism

Explicit mass terms for the gauge bosons in the Lagrangian, for example proportional to $W_\mu^i W_i^\mu$ for the W-bosons, would lead to violation of gauge invariance. The Higgs mechanism is a way to give gauge boson a mass through the introduction of a new scalar field in the Lagrangian. This is the third term in equation (3.1),

$$\mathcal{L}_H = (D_\mu \Phi)^\dagger (D^\mu \Phi) - V(\Phi), \quad (3.4)$$

with the potential

$$V(\Phi) = -\mu^2 (\Phi^\dagger \Phi) + \frac{\lambda}{4} (\Phi^\dagger \Phi)^2. \quad (3.5)$$

Φ transforms as a complex scalar doublet of $SU(2)_w$ with weak hypercharge $Y_\Phi = 1$,

$$\Phi = \begin{pmatrix} \phi^+ \\ \phi^0 \end{pmatrix}. \quad (3.6)$$

In order to have vacuum stability, λ needs to be positive. μ^2 needs to be positive to get a nonzero vacuum expectation value (VEV) Φ_0 of Φ . Minimizing the potential gives

$$\Phi_0^\dagger \Phi_0 = \frac{v^2}{2}, \quad v = 2\sqrt{\frac{\mu^2}{\lambda}}. \quad (3.7)$$

If the vacuum expectation value needs to be electrically neutral, the upper component of Φ_0 has to be zero. Φ_0 is then fixed up to a phase, with the common choice of $\Phi_0 = (0, v/\sqrt{2})^T$. This freedom of choice for Φ_0 is the spontaneous breaking of the $SU(2)_w \otimes U(1)_Y$ symmetry down to the electromagnetic $U(1)_{em}$ symmetry. Splitting off the vacuum expectation value, we can reparametrize Φ in terms of the physical real Higgs field H and the unphysical Goldstone boson fields ϕ^+ and χ by

$$\Phi = \begin{pmatrix} \phi^+ \\ \phi^0 \end{pmatrix}, \quad \text{with} \quad \phi^0 = \frac{1}{\sqrt{2}}(v + H + i\chi). \quad (3.8)$$

The simplest choice is the unitary gauge, in which ϕ^+ and χ vanish. The mass eigenstates can be obtained by diagonalizing the mass matrix arising in the Lagrangian. The photon field A_μ and the Z-boson field Z_μ are given by the rotation

$$\begin{pmatrix} Z_\mu \\ A_\mu \end{pmatrix} = \begin{pmatrix} c_w & -s_w \\ s_w & c_w \end{pmatrix} \begin{pmatrix} W_\mu^3 \\ B_\mu \end{pmatrix}, \quad (3.9)$$

with

$$\begin{aligned} c_w &= \cos \theta_w = \frac{g}{\sqrt{g^2 + (g')^2}}, \\ s_w &= \sin \theta_w = \sqrt{1 - c_w^2}. \end{aligned} \quad (3.10)$$

The angle θ_w is called the weak mixing angle. The electric unit charge is then given by

$$e = \frac{gg'}{\sqrt{g^2 + (g')^2}}. \quad (3.11)$$

Recombining the two remaining fields to the charge eigenstates,

$$W_\mu^\pm = \frac{1}{\sqrt{2}}(W_\mu^1 \mp iW_\mu^2), \quad (3.12)$$

gives the charged weak gauge bosons of positive and negative charge e , the W-bosons.

Inserting equation (3.8) in the original Lagrangian (3.4), we get in the unitary gauge,

$$\mathcal{L}_{H,u.gauge} = \frac{1}{2}(\partial H)^2 + \frac{g^2}{4}(v+H)W_\mu^+W^{-\mu} + \frac{g^2}{8c_w^2}(v+H)^2Z_\mu Z^\mu + \frac{\mu^2}{2}(v+H)^2 - \frac{\lambda}{16}(v+H)^2. \quad (3.13)$$

Defining

$$M_W = \frac{gv}{2}, \quad M_Z = \frac{M_W}{c_w}, \quad M_H = \sqrt{2\mu^2}, \quad (3.14)$$

we can substitute the parameters λ , μ^2 and v for the masses of the bosons,

$$\begin{aligned} \mathcal{L}_{H,u.gauge} &= \frac{1}{2}(\partial H)^2 + \frac{1}{2}M_H^2H^2 + M_W^2W_\mu^+W^{-\mu} + \frac{1}{2}M_Z^2Z_\mu Z^\mu \\ &+ gM_WHW_\mu^+W^{-\mu} + \frac{g^2}{4}H^2W_\mu^+W^{-\mu} + \frac{gM_Z}{2c_w}HZ_\mu Z^\mu + \frac{g^2}{4c_w^2}H^2Z_\mu Z^\mu \\ &- \frac{gm_H^2}{4M_W}H^3 - \frac{g^2M_H^2}{32M_W^2}H^4 + \text{constant}. \end{aligned} \quad (3.15)$$

We now have explicit mass terms for the gauge bosons, as well as a number of interaction terms, which lead to the Feynman rules collected in Appendix A.

3.1.2. Yang-Mills Lagrangian

The first two terms in the Lagrangian of equation (3.1) describe the gauge bosons and fermions before symmetry breaking. The Yang-Mills part, \mathcal{L}_{YM} , describes the free propagators and the interactions of the gauge fields,

$$\mathcal{L}_{YM} = -\frac{1}{4}W_{\mu\nu}^iW_i^{\mu\nu} - \frac{1}{4}B_{\mu\nu}B^{\mu\nu} - \frac{1}{4}F_{\mu\nu}^aF_a^{\mu\nu}, \quad (3.16)$$

with the field strength tensors

$$\begin{aligned} W_{\mu\nu}^i &= \partial_\mu W_\nu^i - \partial_\nu W_\mu^i - g\epsilon^{ijk}W_\mu^jW_\nu^k, \quad i = 1, 2, 3, \\ B_{\mu\nu} &= \partial_\mu B_\nu - \partial_\nu B_\mu, \\ F_{\mu\nu}^a &= \partial_\mu A_\nu^a - \partial_\nu A_\mu^a - g_s f^{abc}A_\mu^bA_\nu^c, \quad a, b = 1, \dots, 8. \end{aligned} \quad (3.17)$$

ϵ^{ijk} and f^{abc} are the usual structure constants of the $SU(2)$ and $SU(3)$ group. The QCD part will be covered in the next section. The EW interaction terms can be derived through writing out $W_{\mu\nu}W^{\mu\nu}$ and $B_{\mu\nu}B^{\mu\nu}$,

$$\begin{aligned} -\frac{1}{4}W_{\mu\nu}^iW_i^{\mu\nu} &= -g(\partial_\mu W_\nu^1 - \partial_\nu W_\mu^1)W^{\mu 2}W^{\nu 3} \\ &+ g(\partial_\mu W_\nu^2 - \partial_\nu W_\mu^2)W^{\mu 1}W^{\nu 3} - g(\partial_\mu W_\nu^3 - \partial_\nu W_\mu^3)W^{\mu 1}W^{\nu 2} \\ &= ig[(\partial_\mu W_\nu^+ - \partial_\nu W_\mu^+)W^{\mu -}W^{\nu 3} - (\partial_\mu W_\nu^- - \partial_\nu W_\mu^-)W^{\mu +}W^{\nu 3} \\ &+ \frac{1}{2}(\partial_\mu W_\nu^3 - \partial_\nu W_\mu^3)(W^{\mu +}W^{\nu -} - W^{\mu -}W^{\nu +})], \end{aligned} \quad (3.18)$$

and then substituting $W_\mu^3 = c_w Z_\mu + s_w A_\mu$ and $g = e/s_w$. Similarly, one can write-out $B_{\mu\nu} B^{\mu\nu}$ substituting $B_\mu = c_w A_\mu - s_w Z_\mu$ and $g' = e/c_w$. From the result one can derive the Feynman rules collected in Appendix A.

3.1.3. Fermions

The interactions between the fermions and the gauge field are given by the first part of the Lagrangian given in (3.1),

$$\mathcal{L}_{ferm} = i\bar{\Psi}_L \not{D} \Psi_L + i\bar{\psi}_R^e \not{D} \psi_R^e + i\bar{\Psi}_L^Q \not{D} \Psi_L^Q + i\bar{\psi}_R^u \not{D} \psi_R^u + i\bar{\psi}_R^d \not{D} \psi_R^d. \quad (3.19)$$

In $SU(2)_w$, the fermions occur as left-handed doublets Ψ_L , with weak isospin $I_w^i = \sigma^i/2$ and right-handed singlets ψ_R with $I_w^i = 0$. Writing out the covariant derivatives explicitly shows the fermion-gauge boson interactions, from which its Feynman rules can be derived, which are given in Appendix A. The *Gell-Mann-Nishijima relation* gives an expression for the electric charge Q in terms of the weak hypercharge Y_w through

$$Q = I_w^3 + Y_w/2. \quad (3.20)$$

An overview of the fermions in the Standard Model is given in table 3.1.

		1 st generation	2 nd generation	3 rd generation	I	I_w^3	Y_w	Q
quarks	Ψ_L^Q	$\begin{pmatrix} u \\ d \end{pmatrix}_L$	$\begin{pmatrix} c \\ s \end{pmatrix}_L$	$\begin{pmatrix} t \\ b \end{pmatrix}_L$	$\frac{1}{2}$	$\frac{1}{2}$	$\frac{1}{3}$	$\frac{2}{3}$
	ψ_R^u	u_R	c_R	t_R	0	0	$\frac{4}{3}$	$\frac{2}{3}$
	ψ_R^d	d_R	s_R	b_R	0	0	$-\frac{2}{3}$	$-\frac{1}{3}$
leptons	Ψ_L^ℓ	$\begin{pmatrix} \nu_e \\ e \end{pmatrix}_L$	$\begin{pmatrix} \nu_\mu \\ \mu \end{pmatrix}_L$	$\begin{pmatrix} \nu_\tau \\ \tau \end{pmatrix}_L$	$\frac{1}{2}$	$\frac{1}{2}$	-1	0
	ψ_R^e	e_R	μ_R	τ_R	0	0	-2	-1

Table 3.1.: The fermions in the Standard Model. In $SU(2)_w$, the fermions occur as left-handed doublets and right-handed singlets. There are three generations of fermions. The last four columns give the weak isospin I , its third component I_w^3 , the weak hypercharge Y_w and the electromagnetic charge Q . The latter is given by equation (3.20).

3.1.4. Yukawa couplings and fermion masses

The fourth part of the SM Lagrangian (3.1) in its most generic form is

$$\mathcal{L}_{Yuk} = -\bar{\Psi}_L G_\ell \psi_R^\ell \Phi - \bar{\Psi}_Q G_u \psi_R^u i\sigma^2 \Phi^* - \bar{\Psi}_Q G_d \psi_R^d \Phi + \text{h.c.}, \quad (3.21)$$

where h.c. abbreviates Hermitian conjugate. ℓ , u and d are meant to represent leptons and up- and down-type quarks respectively. Because there are three generations, G_f with $f = \ell, u, d$

are complex 3×3 matrices. The off-diagonal elements of these matrices mix left- and right-handed fermions from different generations. This oscillation of flavor is removed by switching from a flavor basis into a mass basis ($\hat{\psi}_{\tau i}$, with the generations $i = 1, 2, 3$),

$$\hat{\psi}_i^{f\tau} = U_{ij}^{f\tau} \psi_j^f, \quad \tau = L, R, \quad (3.22)$$

which diagonalizes the matrices G_f ,

$$U^{fL} G_f (U^{fR})^\dagger = \frac{\sqrt{2}}{v} \begin{pmatrix} m_{f1} & 0 & 0 \\ 0 & m_{f2} & 0 \\ 0 & 0 & m_{f3} \end{pmatrix}. \quad (3.23)$$

Changing into the mass basis causes the *Cabibbo-Kobayashi-Maskawa* (CKM) matrix, defined as

$$V = U^{uL} (U^{dL})^\dagger, \quad (3.24)$$

to appear in the interaction between fermions and the charged gauge bosons in (3.19). We will assume to always be in the mass basis and remove the hat from the fermionic fields from here on. In the unitary gauge the Yukawa Lagrangian simplifies to

$$\mathcal{L}_{Yuk} = - \sum_f m_f (\bar{\psi}_{fL} \psi_{fR} + \bar{\psi}_{fR} \psi_{fL}) \left(1 + \frac{H}{v} \right), \quad (3.25)$$

from which another set of Feynman rules collected in Appendix A can be derived. Notice that the Higgs mechanism not only introduced mass terms in the Lagrangian, but also predicts an interaction of the Higgs field with the fermions with a coupling proportional to their masses.

3.2. Quantum chromodynamics

The Lagrangian of quantum chromodynamics (QCD) consists of three parts. The classical part, the gauge fixing part and the ghost Lagrangian,

$$\mathcal{L}_{QCD} = \mathcal{L}_{cl} + \mathcal{L}_{gf} + \mathcal{L}_{gh}. \quad (3.26)$$

The covariant derivative is defined as

$$\begin{aligned} (D_\mu)_{ab} &= \partial^\mu \delta_{ab} + ig_s A_\mu^C t_{ab}^C && \text{fundamental representation,} \\ (D_\mu)_{AB} &= \partial^\mu \delta_{AB} + ig_s A_\mu^C T_{AB}^C && \text{adjoint representation,} \end{aligned} \quad (3.27)$$

where t_{ab}^C and T_{AB}^C the generator of the fundamental and adjoint representation of the gauge group respectively,

$$[t^A, t^B] = if^{ABC} t^C, \quad [T^A, T^B] = if^{ABC} T^C, \quad (T^A)_{BC} = -if^{ABC}. \quad (3.28)$$

Using the conventional normalization choice,

$$\text{Tr } t^A t^B = T_R \delta^{AB}, \quad T_R = \frac{1}{2}, \quad (3.29)$$

the color matrices have the following properties

$$\sum_A t_{ab}^A t_{bc}^A = C_F \delta_{ac}, \quad \text{Tr } T^A T^B = C_A \delta^{AB}. \quad (3.30)$$

In QCD, the Casimir operators are given by

$$C_F = \frac{4}{3}, \quad C_A = 3. \quad (3.31)$$

The classical part, which is extracted from several terms of (3.1), is given by

$$\mathcal{L}_{cl} = -\frac{1}{4} F_{\mu\nu}^A F_A^{\mu\nu} + \sum_f \bar{q}_a (i \not{D}_{ab} - m_q \delta_{ab}) q_b, \quad (3.32)$$

where the sum goes over the flavors f of the quarks (d, u, s, c, b and t) and with $F_{\mu\nu}^A$ being the field strength tensor for the gluon field A_μ^A

$$F_{\mu\nu}^A = \partial_\mu A_\nu^A - \partial_\nu A_\mu^A - g_s f^{ABC} A_\mu^B A_\nu^C. \quad (3.33)$$

g_s is the strong coupling constant, which is related to the symbol

$$\alpha_s = \frac{g_s^2}{4\pi}. \quad (3.34)$$

There are several choices available for the gauge fixing terms. One that is used most often is the covariant gauge fixing term,

$$\mathcal{L}_{gf} = -\frac{1}{2\lambda} (\partial^\mu A_\mu^A)^2, \quad (3.35)$$

with the gauge fixing parameter λ , which is usually set to unity (the Feynman gauge). This does require the introduction of a ghost field via the ghost Lagrangian, to cancel the unphysical degrees of freedom present in covariant gauges,

$$\mathcal{L}_{gh} = (\partial_\mu \eta^A) (D_{AB}^\mu \eta^B). \quad (3.36)$$

The ghost fields are scalar fields, but they obey fermionic anti-commutation relations. The Lagrangian in equation (3.26) leads to the Feynman rules in QCD, given in Appendix A.

3.2.1. Asymptotic freedom

When calculating higher order terms in α_s , often ultraviolet (UV) divergences will appear. In renormalizable theories these divergences can be absorbed by redefining the fields and parameters in the Lagrangian. The most important free parameter is the bare coupling g_s . Dimensional regularization introduces a mass scale μ_R , which is an unphysical scale. This means that for a general observable R , which depends on the energy scale Q and the renormalization scale, the renormalization group equation applies,

$$\mu_R^2 \frac{d}{d\mu_R^2} R(Q^2/\mu_R^2, \alpha_s) = \left[\mu_R^2 \frac{d}{d\mu_R^2} + \mu_R^2 \frac{\partial \alpha_s}{\partial \mu_R^2} \frac{\partial}{\partial \alpha_s} \right] R(Q^2/\mu_R^2, \alpha_s) = 0. \quad (3.37)$$

The coefficient of the second term is called the beta-function,

$$\beta(\alpha_s) \equiv \mu_R^2 \frac{\partial \alpha_s(\mu_R^2)}{\partial \mu_R^2}. \quad (3.38)$$

This equation shows that the coupling constant α_s depends on the energy scale, hence it is referred to as a running coupling constant $\alpha_s(Q^2)$. $\beta(\alpha_s)$ can be expanded in terms of α_s ,

$$\beta(\alpha_s) = -b\alpha_s(Q^2) \left[1 + b'\alpha_s(Q^2) + \mathcal{O}(\alpha_s^2(Q^2)) \right]. \quad (3.39)$$

Defining n_f as the number of flavors of massless quarks, the coefficients b and b' are given by

$$b = \frac{33 - 2n_f}{12\pi}, \quad b' = \frac{153 - 19n_f}{24\pi^2 b} = \frac{153 - 19n_f}{2\pi(33 - 2n_f)}. \quad (3.40)$$

Neglecting b' and all higher order terms, equation (3.38) is solved for α_s as

$$\alpha_s(Q^2) = \frac{\alpha_s(\mu_R^2)}{1 + \alpha_s(\mu_R^2)b \ln(Q^2/\mu_R^2)}. \quad (3.41)$$

Notice that b is positive as long as the number of massless flavors is smaller than $\frac{33}{2}$, which it quite comfortably is in the Standard Model. Equation (3.41) is divergent for values of the scale below the so called Landau pole $Q^2 = \Lambda_{QCD}$,

$$\Lambda_{QCD} = \mu_R^2 \exp \left[\frac{-1}{b\alpha_s(\mu_R^2)} \right]. \quad (3.42)$$

This gives an estimate of the scale below which the approximation breaks down. When decreasing the energy, the coupling constant becomes large and the perturbative expansion is no longer a valid approximation. This increase in coupling strength leads to *confinement* and prevents colored particles to appear as free particles. For large energies, on the other hand, the coupling constant asymptotically goes to zero, which is known as *asymptotic freedom*.

3.2.2. Scale dependence at NLO

For an N -point process, NLO observables should be independent of the renormalization scale up to order $\alpha_s^{N+1}(\mu_R^2)$, which can be written explicitly as

$$\mu_R^2 \frac{d\sigma_{\text{NLO}}}{d\mu_R^2} = 0 + \mathcal{O} \left(\alpha_s^{N+2}(\mu_R^2) \right). \quad (3.43)$$

The only μ_R^2 -dependence is contained in the coupling constants and the virtual contribution. It is therefore illustrative to rewrite equation (2.13) with explicit μ_R^2 -dependence,

$$\frac{d\sigma_{\text{NLO}}^N}{d\Phi} = \alpha_s^N(\mu_R^2)B + \alpha_s^{N+1} \left[V(\mu_R^2) + R \right], \quad (3.44)$$

where we used the differential cross section to not be distracted by the phase space integrals and used the abbreviations B , V and R for the Born, Virtual and Real contributions at the

respective orders in α_s . Using the QCD β -function, we can now write out the left-hand side of equation (3.43) as

$$\begin{aligned}
\mu_R^2 \frac{d\sigma_{\text{NLO}}}{d\mu_R^2} &= \mu_R^2 \frac{d(\alpha_s^N(\mu_R^2))}{d\mu_R^2} B + \mu_R^2 \frac{d(\alpha_s^{N+1}(\mu_R^2))}{d\mu_R^2} (V(\mu_R^2) + R) + \mu_R^2 \frac{dV(\mu_R^2)}{d\mu_R^2} \alpha_s^{N+1}(\mu_R^2) \\
&= N\alpha_s^{N-1}(\mu_R^2) \mu_R^2 \frac{d(\alpha_s(\mu_R^2))}{d\mu_R^2} B + \mu_R^2 \frac{dV(\mu_R^2)}{d\mu_R^2} \alpha_s^{N+1}(\mu_R^2) + \mathcal{O}\left(\alpha_s^{N+2}(\mu_R^2)\right) \\
&= -Nb\alpha_s^{N+1}(\mu_R^2) B + \mu_R^2 \frac{dV(\mu_R^2)}{d\mu_R^2} \alpha_s^{N+1}(\mu_R^2) + \mathcal{O}\left(\alpha_s^{N+2}(\mu_R^2)\right).
\end{aligned} \tag{3.45}$$

The full expression of the condition in (3.43) can now be rewritten, neglecting the higher order terms, to the differential equation

$$\mu_R^2 \frac{dV(\mu_R^2)}{d\mu_R^2} \alpha_s^{N+1}(\mu_R^2) = NbB, \tag{3.46}$$

which can be solved to give the difference between V at the renormalization scale and the characteristic energy scale Q^2 ,

$$V(\mu_R^2) - V(Q^2) = NbB \ln\left(\frac{\mu_R^2}{Q^2}\right). \tag{3.47}$$

This means one can split the virtual contribution into a sum of a μ_R^2 -independent term at a scale Q^2 and a logarithmic term. In the notation of equation (3.44),

$$\frac{d\sigma_{\text{NLO}}^N}{d\Phi} = \alpha_s^N(\mu_R^2) B + \alpha_s^{N+1}(\mu_R^2) \left[V(Q^2) + Nb \ln\left(\frac{\mu_R^2}{Q^2}\right) B \right] + \alpha_s^{N+1}(\mu_R^2) R. \tag{3.48}$$

4 ■ One-loop calculations in Quantum Field Theory

One-loop calculations have long been a bottleneck to the advancement of NLO calculations. Over the years several techniques have been designed to calculate them most effectively. In this chapter we will first discuss the regularization of one-loop integrals using the dimensional regularization method. We will then discuss Passarino-Veltman reduction and integrand reduction.

4.1. Regularization

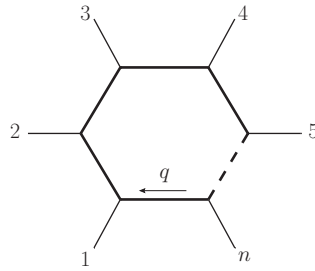


Figure 4.1.: A generic n -point loop-diagram

The most generic way to write a one-loop amplitude with n legs, as depicted in Figure 4.1 is

$$\mathcal{A}_n = \int d^4q \frac{N(q)}{D_0 D_1 \cdots D_{n-1}}, \quad (4.1)$$

where $N(q)$ is a numerator that depends on the loop momentum q and the propagators D_i are given by

$$D_i = (q + p_i)^2 - m_i^2, \quad (p_0 \neq 0). \quad (4.2)$$

Naive dimensional analysis, writing $d^4q = q^3 dq d\Omega_3$, immediately shows that this will give rise to divergences for $q \rightarrow \infty$, known as ultraviolet divergences. Denoting the rank in q of the numerator as r and noting that every denominator is of the order q^2 , we have

$$\lim_{q \rightarrow \infty} \int \frac{q^{3+r} dq}{q^{2n}} \propto \lim_{q \rightarrow \infty} q^{r+4-2n}, \quad (4.3)$$

which shows that integrals with a numerator of rank $r \geq 2n - 4$ are UV divergent. In particular, from the integrals with $N(q) = 1$, known as *scalar integrals*, the tadpole and bubble integrals are UV divergent. The most common way to regularize these infinities is *dimensional regularization*, in which the four-dimensional integral is replaced by a d -dimensional one, with the common choice $d = 4 - 2\epsilon$.

$$\int d^4 q f(q) \rightarrow \int d^d \bar{q} f(\bar{q}). \quad (4.4)$$

Objects with dimension $d = 4 - 2\epsilon$ are denoted with a bar. We will denote the -2ϵ -dimensional part of \bar{q} as μ ,

$$\bar{q} = \not{q} + \not{\mu}, \quad \text{with} \quad \bar{q}^2 = q^2 - \mu^2. \quad (4.5)$$

In d dimensions, the Clifford algebra generalizes to

$$\bar{g}^{\mu\nu} \bar{g}_{\mu\nu} = d, \quad \bar{\gamma}_\alpha \bar{\gamma}_\mu \bar{\gamma}^\alpha = (2 - d) \bar{\gamma}_\mu, \quad \text{Tr}(\bar{I}) = 2^{d/2}. \quad (4.6)$$

We will use for explicit calculations

$$\bar{g}^{\mu\nu} = g^{\mu\nu} + \tilde{g}^{\mu\nu}, \quad \bar{\gamma}^\mu = \gamma^\mu + \tilde{\gamma}^\mu, \quad (4.7)$$

which in particular means that

$$\tilde{g}^{\mu\nu} \bar{g}^{\mu\nu} = -2\epsilon, \quad \tilde{g}_{\mu\nu} \bar{q}^\mu \bar{q}^\nu = -\mu^2, \quad \tilde{g}_{\mu\nu} k^\mu = 0, \quad (4.8)$$

for any four-dimensional vector k^μ . The expression for the one-loop integral generalizes to

$$\begin{aligned} \mathcal{A}_n &= \int d^d \bar{q} A(\bar{q}, \epsilon), \\ A(\bar{q}, \epsilon) &= \frac{\mathcal{N}(\bar{q}, \epsilon)}{\bar{D}_0 \bar{D}_1 \cdots \bar{D}_{n-1}}. \end{aligned} \quad (4.9)$$

where the propagators \bar{D}_i are given by

$$\bar{D}_i = (\bar{q} + p_i)^2 - m_i^2 = (q + p_i)^2 - m_i^2 - \mu^2, \quad (p_0 \neq 0). \quad (4.10)$$

\mathcal{N} in its most general form is composed of three terms, as an expansion in ϵ ,

$$\mathcal{N}(\bar{q}) = N_1(q, \mu^2) + \epsilon N_2(q, \mu^2) + \epsilon^2 N_3(q, \mu^2). \quad (4.11)$$

In the remainder of this chapter \mathcal{N} will be written, with an implicit understanding that one should read any of $\{N_1, N_2, N_3\}$.

4.2. Tensor reduction

To avoid notation with obscuring indices on indices, we will use $(ijk..) \equiv (i_1 i_2 i_3 ..)$ as much as possible. This will of course not be possible in recurrence relations, but will help to clear

up the notation of the integrals. In renormalizable theories, the rank of the numerator cannot exceed the number of denominators,

$$r \leq n. \quad (4.12)$$

This means that in one-loop calculations one will encounter integrals of the form

$$I_i = \frac{1}{i\pi^{d/2}} \int d^d \bar{q} \frac{1}{\bar{D}_i} \quad (4.13)$$

$$I_{ij}; I_{ij}^\mu; I_{ij}^{\mu\nu} = \frac{1}{i\pi^{d/2}} \int d^d \bar{q} \frac{1; \bar{q}^\mu; \bar{q}^\mu \bar{q}^\nu}{\bar{D}_i \bar{D}_j} \quad (4.14)$$

$$I_{ijk}; I_{ijk}^\mu; I_{ijk}^{\mu\nu}; I_{ijk}^{\mu\nu\rho} = \frac{1}{i\pi^{d/2}} \int d^d \bar{q} \frac{1; \bar{q}^\mu; \bar{q}^\mu \bar{q}^\nu; \bar{q}^\mu \bar{q}^\nu \bar{q}^\rho}{\bar{D}_i \bar{D}_j \bar{D}_k} \quad (4.15)$$

$$I_{ijkl}; I_{ijkl}^\mu; I_{ijkl}^{\mu\nu}; I_{ijkl}^{\mu\nu\rho}; I_{ijkl}^{\mu\nu\rho\sigma} = \frac{1}{i\pi^{d/2}} \int d^d \bar{q} \frac{1; \bar{q}^\mu; \bar{q}^\mu \bar{q}^\nu; \bar{q}^\mu \bar{q}^\nu \bar{q}^\rho; \bar{q}^\mu \bar{q}^\nu \bar{q}^\rho \bar{q}^\sigma}{\bar{D}_i \bar{D}_j \bar{D}_k \bar{D}_\ell}. \quad (4.16)$$

Using the fact that there are only four independent vectors in four-dimensional space-time, in [75, 76], it was shown that integrals with more than four denominators can always be expressed as a linear combination of lower point integrals.

4.2.1. Passarino-Veltman reduction

The integrals listed above are tensors that transform under the Lorentz group transformations. Therefore, for example the bubble integral of rank one, I_{ij}^μ , has to transform like a vector. The vector space in this case is very limited, since there is just one independent vector available. This means that one can write the integral expanded in this very simple basis as

$$I_{ij}^\mu = B_1(ij) k_1^\mu. \quad (4.17)$$

Coefficient like $B_1(ij)$ are called *form factors*. Its argument is meant to keep track of the denominators of the expanded integral. Specifically, the argument (ij) shows that the masses m_i and m_j are present.

In the determination of form factors, often one encounters the product of the internal momentum q^μ with an external momentum k_n^μ . If k_n is defined as the effective incoming momentum between denominators $D_{i_{n-1}}$ and D_{i_n} , *i.e.* $k_n = p_j - p_i$, then it is possible to write

$$2k_n \cdot \bar{q} = \bar{D}_{i_n} - \bar{D}_{i_{n-1}} + f_{i_n}, \quad (4.18)$$

where f_{i_n} is defined to be

$$f_{i_n} \equiv m_{i_{n+1}}^2 - m_{i_n}^2 - k_n^2 - 2k_n \cdot \sum_{\alpha=1}^{n-1} k_\alpha. \quad (4.19)$$

Specifically relevant for this section which will only feature bubbles and triangles, we have

$$f_i = m_j^2 - m_i^2 - k_1^2, \quad (4.20)$$

$$f_j = m_k^2 - m_j^2 - k_2^2 - 2k_1 \cdot k_2. \quad (4.21)$$

We can now contract the expression in equation (4.17) with k_1 ,

$$\begin{aligned} k_1^2 B_1(ij) &= \frac{1}{i\pi^{d/2}} \int d^d \bar{q} \frac{\bar{q} \cdot k}{\bar{D}_i \bar{D}_j} = \frac{1}{2i\pi^{d/2}} \int d^d \bar{q} \frac{\bar{D}_j - \bar{D}_i + f_i}{\bar{D}_i \bar{D}_j} \\ &= \frac{1}{2i\pi^{d/2}} \left(\int d^d \bar{q} \frac{1}{\bar{D}_i} - \int d^d \bar{q} \frac{1}{\bar{D}_j} + \int d^d \bar{q} \frac{f_j}{\bar{D}_i \bar{D}_j} \right), \end{aligned} \quad (4.22)$$

which can be solved to give an expression of the form factor in terms of scalar integrals.

$$B_1(ij) = \frac{1}{2k_1^2} (I_i - I_j + f_i I_{ij}). \quad (4.23)$$

When considering triangles of rank one, I_{ijk}^μ , there are two independent vectors available, therefore an expansion featuring two form factors is required,

$$I_{ijk}^\mu = C_1(ijk)k_1^\mu + C_2(ijk)k_2^\mu. \quad (4.24)$$

We will use the short-hand notation with the numerator of the integrand as argument in square brackets,

$$I_{ijk}[\mathcal{N}(q)] = \frac{1}{i\pi^{d/2}} \int d^d \bar{q} \frac{\mathcal{N}(q)}{\bar{D}_i \bar{D}_j \bar{D}_k}. \quad (4.25)$$

Contracting with all possible combinations of k_1 and k_2 gives a system of equations

$$G_2 \begin{pmatrix} C_1(ijk) \\ C_2(ijk) \end{pmatrix} = \begin{pmatrix} I_{ijk}[\bar{q} \cdot k_1] \\ I_{ijk}[\bar{q} \cdot k_2] \end{pmatrix}, \quad (4.26)$$

where G_2 is the 2×2 Gram matrix

$$G_2 = \begin{pmatrix} k_1^2 & k_1 \cdot k_2 \\ k_1 \cdot k_2 & k_2^2 \end{pmatrix}, \quad (4.27)$$

and we can write

$$I_{ijk}[\bar{q} \cdot k_1] = \frac{1}{i\pi^{d/2}} \int d^d \bar{q} \frac{\bar{q} \cdot k_1}{\bar{D}_i \bar{D}_j \bar{D}_k} = \frac{1}{2i\pi^{d/2}} \int d^d \bar{q} \frac{\bar{D}_j - \bar{D}_i + f_j}{\bar{D}_i \bar{D}_j \bar{D}_k}, \quad (4.28)$$

which can be rewritten as a sum of scalar integrals,

$$I_{ijk}[\bar{q} \cdot k_1] = \frac{1}{2} (I_{ik} - I_{jk} + f_i I_{ijk}). \quad (4.29)$$

Similarly,

$$I_{ijk}[\bar{q} \cdot k_2] = \frac{1}{2} (I_{ij} - I_{ik} + f_j I_{ijk}). \quad (4.30)$$

The coefficients can now be obtained by simply inverting the system in (4.26),

$$\begin{pmatrix} C_1(ijk) \\ C_2(ijk) \end{pmatrix} = G_2^{-1} \begin{pmatrix} I_{ijk}[\bar{q} \cdot k_1] \\ I_{ijk}[\bar{q} \cdot k_2] \end{pmatrix}. \quad (4.31)$$

Tensor integrals with a higher rank can be treated in the same way to reduce them to lower rank and lower point integrals. For example, the bubble of rank two can be written as

$$I_{ij}^{\mu\nu} = B_{00} g^{\mu\nu} + B_{11} k_1^\mu k_1^\nu. \quad (4.32)$$

Contracting with $g_{\mu\nu}$ gives

$$g_{\mu\nu}I_{ij}^{\mu\nu} = 4B_{00} + k_1^2 B_{11}. \quad (4.33)$$

Contracting the d dimensional numerator $N(\bar{q}) = \bar{q}^\mu \bar{q}^\nu$ with the four-dimensional $g_{\mu\nu}$ projects out the four-dimensional part of the numerator, which can then be rewritten,

$$g_{\mu\nu}I_{ij}^{\mu\nu} = \frac{1}{i\pi^{d/2}} \int d^d \bar{q} \frac{q^2}{\bar{D}_i \bar{D}_j} = \frac{1}{i\pi^{d/2}} \int d^d \bar{q} \frac{\bar{D}_i + m_0^2 + \mu^2}{\bar{D}_i \bar{D}_j} = I_j + m_0^2 I_{ij} + I_{ij}[\mu^2]. \quad (4.34)$$

Contracting with $k_{1\nu}$ gives

$$k_{1\nu}I_{ij}^{\mu\nu} = k_1^2 B_{00} + k_1^4 B_{11}, \quad (4.35)$$

and

$$\begin{aligned} k_{1\nu}I_{ij}^{\mu\nu} &= \frac{1}{i\pi^{d/2}} \int d^d \bar{q} \frac{\bar{q}^\mu (\bar{q} \cdot k_1)}{\bar{D}_i \bar{D}_j} = \frac{1}{i\pi^{d/2}} \int d^d \bar{q} \frac{1}{2} \frac{\bar{q}^\mu (\bar{D}_j - \bar{D}_i + f_i)}{\bar{D}_i \bar{D}_j} \\ &= \frac{1}{2} \left(I_i^\mu - I_j^\mu + f_i I_{ij}^\mu \right). \end{aligned} \quad (4.36)$$

Notice that the rank one tadpole integral I_i^μ is zero because it is anti-symmetrical in \bar{q} . For the other tadpole we have to manipulate the expression by adding and subtracting k^μ ,

$$I_j^\mu = \frac{1}{i\pi^{d/2}} \int d^d \bar{q} \frac{(\bar{q}^\mu + k^\mu) - k^\mu}{(\bar{q} + k)^2 - m_j^2} = -k^\mu I_j. \quad (4.37)$$

where the first term now does vanish because of anti-symmetry. Also, we have already discussed how to reduce the rank one bubble I_{ij}^μ , whose result is given in (4.23). After contracting the last equation again with $k_{1\mu}$, we have the two equations,

$$\begin{aligned} 4B_{00} + k_1^2 B_{11} &= I_j + m_0^2 I_{ij} + I_{ij}[\mu^2], \\ k_1^2 B_{00} + k_1^4 B_{11} &= +k_{1\mu} \left(\frac{1}{2} f_i B_1(ij) + I_j \right) k_1^\mu = \frac{1}{4} f_i (I_i - I_j + f_i I_{ij}) + \frac{1}{2} k^2 I_j. \end{aligned} \quad (4.38)$$

which can be solved for B_{00} and B_{11} ,

$$\begin{aligned} B_{00} &= \frac{1}{12k^2} \left\{ (m_i^2 - m_j^2 + k^2) I_i + (m_j^2 - m_i^2 + k^2) I_j \right. \\ &\quad \left. + ((k^2 + m_j^2 - m_i^2) - 4k^2 m_i^2) I_{ij} + I_{ij}[\mu^2] \right\} \\ B_{11} &= \frac{1}{3k^4} \left\{ (m_i^2 - m_j^2 + k^2) I_i + (m_i^2 - m_j^2 + 2k^2) I_j \right. \\ &\quad \left. + (k^4 + k^2(m_i^2 - 2m_j^2) + (m_i^2 - m_j^2)^2) + I_{ij}[\mu^2] \right\}. \end{aligned} \quad (4.39)$$

The d -dimensional integral appearing in this expression is a remnant of the shift to d dimensions. It can be calculated explicitly (see Appendix B.1),

$$I_{ij}[\mu^2] = \frac{1}{i\pi^{d/2}} \int d^d \bar{q} \frac{\mu^2}{\bar{D}_i \bar{D}_j} = -\frac{1}{2} \left[m_i^2 + m_j^2 - \frac{1}{3} k^2 \right] + \mathcal{O}(\epsilon). \quad (4.40)$$

Terms like these are called *rational terms*, because the numerator and the denominator are polynomials, which is the definition of a rational expression. Using this, the expressions can be worked out, *mutatis mutandis*, to the expressions given *e.g* in Appendix C of [77].

The integral of a triangle of rank two can be written as

$$I_{ijk}^{\mu\nu} = C_{00}g^{\mu\nu} + C_{11}k_1^\mu k_1^\nu + C_{12}k_1^\mu k_2^\nu + C_{21}k_2^\mu k_1^\nu + C_{22}k_2^\mu k_2^\nu, \quad (4.41)$$

where the arguments, which are (ijk) for all form factors, are temporarily suppressed for increased readability. Contracting one time with k_1^μ and k_2^μ gives

$$\begin{aligned} k_{1\mu}I_{ijk}^{\mu\nu} &= k_1^\nu(k_1^2 C_{11} + k_1 \cdot k_2 C_{12} + C_{00}) + k_2^\nu(k_1^2 C_{12} + k_1 \cdot k_2 C_{22}), \\ k_{2\mu}I_{ijk}^{\mu\nu} &= k_1^\nu(k_1 \cdot k_2 C_{11} + k_2^2 C_{12}) + k_2^\nu(k_1 \cdot k_2 C_{12} + k_2^2 C_{22} + C_{00}). \end{aligned} \quad (4.42)$$

The left-hand side of the first equation can be expanded as

$$k_{1\mu}I_{ijk}^{\mu\nu} = \frac{1}{i\pi^{d/2}} \int d^d \bar{q} \frac{\bar{q}^\nu (\bar{q} \cdot k)}{\bar{D}_i \bar{D}_j \bar{D}_k} = \frac{1}{2} (I_{ik}^\nu - I_{jk}^\nu + f_i I_{ijk}^\nu), \quad (4.43)$$

which is a sum of bubbles and a triangle of rank one. The reduction of both of those classes was covered above, but one has to be careful to put the bubbles in the right format. For I_{ik}^ν , the independent momentum to construct the basis is $k_1 + k_2$,

$$I_{ik}^\nu = B_1(ik)(k_1^\nu + k_2^\nu). \quad (4.44)$$

For I_{jk}^μ , a shift of the integration variable $\bar{q} \rightarrow \bar{q} - k_1$ is needed,

$$\begin{aligned} I_{jk}^\nu &= \frac{1}{i\pi^{d/2}} \int \frac{\bar{q}^\nu}{((\bar{q} + k_1 + k_2)^2 - m_j^2)(\bar{q} + k_1 + k_2)^2 - m_k^2} \\ &= \frac{1}{i\pi^{d/2}} \int \frac{\bar{q}^\nu - k_1^\nu}{((\bar{q} + k_2)^2 - m_j^2)(\bar{q} + k_2)^2 - m_k^2} \\ &= B_1(jk)k_2^\nu - I_{jk}k_1^\nu. \end{aligned} \quad (4.45)$$

The reduction of the triangle of rank one is already given in (4.24). Similarly, for the left-hand side of the second equation we have

$$k_{2\mu}I_{ijk}^{\mu\nu} = \frac{1}{2} (I_{ij}^\nu - I_{ik}^\nu + f_j I_{ijk}^\nu). \quad (4.46)$$

The reductions of these three are all given above.

Collecting all the terms proportional to either k_1^ν or k_2^ν to get the two expressions in the format of equation (4.42), shows that we can write

$$G_2 \begin{pmatrix} C_{11}(ijk) \\ C_{12}(ijk) \end{pmatrix} = \begin{pmatrix} R_1^{c1} \\ R_2^{c1} \end{pmatrix}, \quad G_2 \begin{pmatrix} C_{21}(ijk) \\ C_{22}(ijk) \end{pmatrix} = \begin{pmatrix} R_1^{c2} \\ R_2^{c2} \end{pmatrix}, \quad (4.47)$$

where we defined

$$\begin{aligned} R_1^{c1} &= \frac{1}{2} (f_1 C_1(ijk) + B_1(ik) + I_{jk} - 2C_{00}(ijk)) \\ R_2^{c1} &= \frac{1}{2} (f_2 C_1(ijk) + B_1(ij) - B_1(ik)) \\ R_1^{c2} &= \frac{1}{2} (f_1 C_2(ijk) + B_1(ik) - B_1(jk)) \\ R_2^{c2} &= \frac{1}{2} (f_2 C_2(ijk) - B_1(ik) - 2C_{00}(ijk)). \end{aligned} \quad (4.48)$$

The last form factor can be found by contracting $I_{ijk}^{\mu\nu}$ with $g^{\mu\nu}$,

$$g_{\mu\nu}I_{ijk}^{\mu\nu} = \frac{1}{i\pi^{d/2}} \int \frac{q^2}{\bar{D}_i\bar{D}_j\bar{D}_k} = \frac{1}{i\pi^{d/2}} \int \frac{\bar{D}_i + m_i^2 + \mu^2}{\bar{D}_i\bar{D}_j\bar{D}_k} = I_{jk} + m_i^2 I_{ijk} + I_{ijk}[\mu^2]. \quad (4.49)$$

Contracting the expansion in equation (4.42) with $g_{\mu\nu}$ gives

$$g_{\mu\nu}I_{ijk}^{\mu\nu} = 4C_{00} + R_1^{c1} + R_2^{c2} \quad (4.50)$$

, which means one ends up with

$$C_{00}(ijk) = \frac{1}{4} \left(2m_i^2 I_{ijk} + 2I_{ijk}[\mu^2] - f_j C_2(ijk) - f_i C_1(ijk) + I_{jk} \right). \quad (4.51)$$

The d -dimensional integral can again be calculated explicitly (see Appendix B.1),

$$I_{ijk}[\mu^2] = \frac{1}{i\pi^{d/2}} \int d^d \bar{q} \frac{\mu^2}{\bar{D}_i\bar{D}_j\bar{D}_k} = \frac{1}{2} + \mathcal{O}(\epsilon). \quad (4.52)$$

It is illustrative to summarize the reduction steps discussed here schematically,

$$\begin{aligned} C_{ij} &\rightarrow C_{00}, C_i, B_i, I_{jk} \\ C_{00} &\rightarrow C_i, I_{jk}, I_{ijk}, R \\ C_i &\rightarrow I_{ij}, I_{ik}, I_{jk}, I_{ijk} \\ B_{11} &\rightarrow I_{ij}, I_i, I_j, R \\ B_{00} &\rightarrow I_{ij}, I_i, I_j, R \\ B_i &\rightarrow I_i, I_j, I_{ij}. \end{aligned} \quad (4.53)$$

This pattern generalizes for all integrals with rank $r \leq n$ and is given for example in Table 2.1 of [78]. Any one-loop integral can be reduced until it is decomposed into a basis of scalar integrals. This basis consists of the scalar tadpole, bubble, triangle and box integral. In d -dimensions, this is not a complete basis because of the appearance of rational terms. Hence one can write

$$\int d^d q \frac{\bar{N}(q)}{\bar{D}_1 \dots \bar{D}_n} = \sum_{(ijkl)} c_{4,0}^{(ijkl)} I_{ijkl} + \sum_{(ijk)} c_{3,0}^{(ijk)} I_{ijk} + \sum_{(ij)} c_{2,0}^{(ij)} I_{ij} + \sum_i c_{1,0}^i I_i + R. \quad (4.54)$$

The procedure is known as *Passarino-Veltman reduction* and was introduced in [31].

4.2.2. Singular kinematic regions

The calculation of the form factors requires to invert the Gram matrix. These inverse Gram matrices can cause numerical instabilities when applying Passarino-Veltman reduction. As a simple example, we will consider the inverse Gram matrix in the 2×2 case, given by

$$G_2^{-1} = \frac{1}{\Delta_G(k_1, k_2)} \begin{pmatrix} k_2^2 & -k_1 \cdot k_2 \\ -k_1 \cdot k_2 & k_1^2 \end{pmatrix}, \quad (4.55)$$

where

$$\Delta_G(k_1, k_2) = \det(G_2) = k_1^2 k_2^2 - (k_1 \cdot k_2)^2. \quad (4.56)$$

In the limit in which k_1 and k_2 are collinear, this determinant vanishes and the inverse Gram matrix becomes singular. However, this singularity only occurs because in this limit the expansion in (4.24) of I_{ijk}^μ is incorrect, since k_1 and k_2 are no longer independent. Therefore, the algebraic solution to this particular problem is to introduce a new basis with independent vectors. For this purpose, we can write k_2 as a linear combination of k_1 and a unit vector n^μ perpendicular to k_1 ,

$$k_2^\mu = \kappa k_1^\mu + \delta n^\mu, \quad n^2 = 1, \quad k_1 \cdot n = 0. \quad (4.57)$$

The collinear region is now parametrized by $\delta \ll 1$. Introducing a new vector,

$$k_2^{\mu'} = \delta n^\mu, \quad (4.58)$$

we can write the decomposition as

$$I_{ijk}^\mu = C_1 k_1^\mu + C_2' k_2^{\mu'}, \quad (4.59)$$

which gives a Gram determinant

$$\Delta_G(k_1, k_2') = \delta^2 k_1^2. \quad (4.60)$$

Contracting with k_1 and k_2' and solving for C_1 and C_2' gives

$$C_1 = \frac{I_{ijk}[\bar{q} \cdot k_1]}{k_1^2}, \quad C_2' = \frac{k_1^2 I_{ijk}[\bar{q} \cdot k_2']}{\Delta_G(k_1, k_2')}. \quad (4.61)$$

$C_1 k_1^\mu$ is of course finite, and because $k_2' = \mathcal{O}(\delta)$ and $C_2' = \mathcal{O}(\delta^{-1})$, also $C_2' k_2^{\mu'}$ is finite, making the whole expansion for I_{ijk}^μ finite. Expanding I_{ijk}^μ , and with it C_2' , in the Master Integrals basis obscures this cancellation, because contributions to it come from various parts in the expansion. This is one of the main problems of a plain application of Passarino-Veltman reduction, because these so-called *exceptional points* lead to numerical instabilities, even though there is no divergence of the original integral.

4.3. Rational terms

The treatment of the rational terms, which originate from calculating the integrals in d dimensions, is an important part of the calculation, for which several strategies have been developed. There are two sources of rational terms, denoted R_1 and R_2 , whose sum is the full rational term,

$$R = R_1 + R_2. \quad (4.62)$$

In essence, R_2 comes from the d dimensionality of the numerators, whereas R_1 comes from the d dimensionality of the denominators. The latter is illustrated by the calculation that was being performed when we introduced the rational term: For the four-dimensional q^2 to cancel against one of the denominators, it was needed to add a term with $N(\bar{q}) = \mu^2$, which integrates to a rational expression. The R_1 rational terms therefore originate in the mismatch between the four-dimensional numerator and the d -dimensional denominators.

4.3.1. Structure of rational terms

The structure of the rational terms becomes especially clear using the notation of the integrand reduction. We will save the detailed discussion for the next section, in which we will discuss the full d -dimensional integrand reduction, but for now we will use the fact that the numerator can be written as a product of polynomials in q and μ^2 times a collection of denominators (the full expression will be given in equation (4.133)),

$$\bar{N}(\bar{q}) = \sum_i \bar{\Delta}_{(i)}(q, \mu^2) \prod_{j \notin (i)} \bar{D}_j \equiv \bar{\Delta} \otimes \bar{D}. \quad (4.63)$$

Here a short-hand notation is introduced with the symbol \otimes to indicate the sum of products with the proper number of denominators for the respective terms. We can separate the terms multiplying at least one power of μ^2 from the rest in an explicit polynomial description,

$$\bar{\Delta}_{(i)}(q, \mu^2) = \sum_{k=0} (\mu^2)^k \Delta_{(i)k} = \Delta(q) + \mu^2 \sum_{k=1} (\mu^2)^{k-1} \Delta_{(i)k} = \Delta_{(i)} + \tilde{\Delta}_{(i)}. \quad (4.64)$$

We can use a similar notation for the numerator,

$$\bar{N}(q, \mu^2) = \sum_{k=0} (\mu^2)^k N_k = N_0(q) + \mu^2 \sum_{k=1} (\mu^2)^{k-1} N_k = N_0(q) + \tilde{N}(q, \mu^2). \quad (4.65)$$

Dropping the indices (i) and arguments to improve readability, this means we can write for the numerator

$$\bar{N} = N_0 + \tilde{N} = \bar{\Delta} \otimes \bar{D} = (\Delta + \tilde{\Delta}) \otimes \bar{D} = \Delta \otimes \bar{D} + \tilde{\Delta} \otimes \bar{D}. \quad (4.66)$$

The product of denominators in the first term will cancel against the corresponding ones in the denominator and the integral will reduce to a sum of scalar integrals. Note that all terms contained in $\tilde{\Delta}$ multiply at least one power of μ^2 . The full rational term is therefore acquired by the integration over the second term,

$$I[\tilde{\Delta} \otimes \bar{D}] = R. \quad (4.67)$$

where the definition in equation (4.25) was reused. We will now show the separation of R into R_1 and R_2 . We define R_2 as the integral over the d -dimensional part of the numerator,

$$R_2 = I[\tilde{N}]. \quad (4.68)$$

The remaining part N_0 can be written again as a sum over products between polynomials and denominators,

$$N_0 = \bar{\Delta}_0 \otimes \bar{D}. \quad (4.69)$$

Notice however that the denominators have a μ^2 dependence and the final result of the expression, $N_0(q)$, does not. This means that the polynomial itself must contain some μ^2 dependence, to ensure a cancellation. We can separate again the μ^2 dependent and independent parts,

$$\bar{\Delta}_0 \equiv \bar{\Delta}_0(q, \mu^2) = \Delta_0 + \tilde{\Delta}_0. \quad (4.70)$$

The remaining part of the numerator can therefore be written as

$$N_0 = (\Delta_0 + \tilde{\Delta}_0) \otimes \bar{D} = \Delta_0 \otimes \bar{D} + \tilde{\Delta}_0 \otimes \bar{D}. \quad (4.71)$$

We define the integration over the second part as R_1

$$I[\tilde{\Delta}_0 \otimes \bar{D}] = R_1. \quad (4.72)$$

Comparing the two approaches shows that indeed the full rational term is the sum of R_1 and R_2 ,

$$\left. \begin{aligned} I[\bar{N}] &= I[\Delta_0 \otimes \bar{D}] + R_1 + R_2 \\ I[\tilde{N}] &= I[\Delta_0 \otimes \bar{D}] + R \end{aligned} \right\} R = R_1 + R_2. \quad (4.73)$$

In the traditional approach, all quantities appearing (the numerators, denominators and the polynomials) are considered four-dimensional,

$$N_0 = \Delta_0 \otimes D. \quad (4.74)$$

To separate the rational term, the replacement $D = \bar{D} + \mu^2$ needs to be made,

$$N_0 = \Delta_0 \otimes D = \Delta_0 \otimes (\bar{D} + \mu^2) = \Delta_0 \otimes \bar{D} + F(\Delta_0, \mu^2, \bar{D}), \quad (4.75)$$

where a function F was introduced to indicate the remaining nontrivial sum of products between Δ_0 , powers of μ^2 and collections of denominators. Comparing with equation (4.71), it is clear that the integral over this function is in fact R_1 ,

$$I[F(\Delta_0, \mu^2, \bar{D})] = I[\tilde{\Delta}_0 \otimes \bar{D}] = R_1, \quad (4.76)$$

which leads to the conclusion that $\tilde{\Delta}_0$ can be constructed from products of Δ_0 with denominators and powers of μ^2 ,

$$\tilde{\Delta}_0 \equiv \tilde{\Delta}_0(\Delta_0, \mu^2, \bar{D}). \quad (4.77)$$

This means it is feasible to treat the integrand as being four-dimensional and then calculate the R_1 term from the four-dimensional polynomials $\Delta_{(i)0}$.

4.3.2. R_2 rational terms from effective rules

The R_2 contribution is defined by the integral over the -2ϵ -dimensional part of the numerator. Writing

$$\bar{N}(\bar{q}) = N(q) + \tilde{N}(q, \mu^2, \epsilon), \quad (4.78)$$

we have

$$R_2 = \frac{1}{i\pi^{d/2}} \int d^d \bar{q} \frac{\tilde{N}(q, \mu^2, \epsilon)}{\bar{D}_0 \dots \bar{D}_n}. \quad (4.79)$$

As an example, we will consider the one-loop vertex correction in QED (see Figure 4.2), which can be written as

$$\bar{N}(\bar{q}) = e^3 \left\{ \bar{\gamma}_\beta(\mathcal{Q}_1 + m_e) \gamma_\mu(\mathcal{Q}_2 + m_e) \bar{\gamma}^\beta \right\} = N(q) + \tilde{N}(q, \mu^2, \epsilon), \quad (4.80)$$

with

$$\begin{aligned} N(q) &= e^3 \left\{ \gamma_\beta(\mathcal{Q}_1 + m_e) \gamma_\mu(\mathcal{Q}_2 + m_e) \gamma^\beta \right\} \\ \tilde{N}(q, \mu^2, \epsilon) &= e^3 \left\{ 2\epsilon(\mathcal{Q}_1 + m_e) \gamma_\mu(\mathcal{Q}_2 + m_e) - \epsilon \mu^2 \gamma_\mu + \mu^2 \gamma_\beta \gamma_\mu \gamma^\beta \right\}. \end{aligned} \quad (4.81)$$

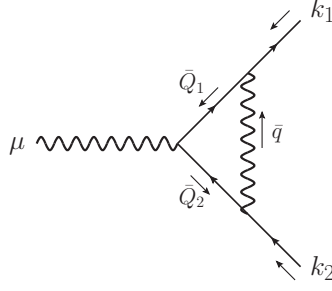


Figure 4.2.: One-loop correction to the QED vertex.

Using the integrals

$$\int d^d \bar{q} \frac{\mu^2}{\bar{D}_i \bar{D}_j \bar{D}_k} = \frac{i\pi^2}{2} + \mathcal{O}(\epsilon), \quad (4.82)$$

$$\int d^d \bar{q} \frac{q^\mu q^\nu}{\bar{D}_i \bar{D}_j \bar{D}_k} = \frac{i\pi^2}{2\epsilon} + \mathcal{O}(1), \quad (4.83)$$

the contributions to R_2 can be obtained. Because of the ϵ in front, the first term only gives finite contributions for the combination $\not{q}\gamma_\mu\not{q}$

$$-\epsilon\gamma_\alpha\gamma_\mu\gamma_\beta \frac{1}{(2\pi)^4} \int \frac{q^\alpha q^\beta}{D_0 D_1 D_2} = -\frac{i}{16\pi^2} \gamma_\mu + \mathcal{O}(\epsilon). \quad (4.84)$$

The second term will give results of order $\mathcal{O}(\epsilon)$. The third term gives

$$\gamma_\beta\gamma_\mu\gamma^\beta \frac{1}{(2\pi)^4} \int \frac{\mu^2}{D_0 D_1 D_2} = -\frac{i}{16\pi^2} \gamma_\mu + \mathcal{O}(\epsilon). \quad (4.85)$$

The full R_2 contribution therefore is

$$R_2 = -\frac{ie^3}{8\pi^2} \gamma_\mu + \mathcal{O}(\epsilon), \quad (4.86)$$

which shows that R_2 can be computed by adding an effective Feynman rule. This procedure was outlined in [79].

4.4. Construction of a massless basis

Throughout the rest of this chapter, it will prove to be convenient to work in a basis of four massless vectors. This means we will write q , the four-dimensional part of \bar{q} , as

$$q = -p_0 + x_1 e_1 + x_2 e_2 + x_3 e_3 + x_4 e_4. \quad (4.87)$$

In particular, for the basis, we want that

$$e_i^2 = 0, \quad e_1 \cdot e_3 = e_1 \cdot e_4 = 0, \quad e_2 \cdot e_3 = e_2 \cdot e_4 = 0, \quad e_1 \cdot e_2 = -e_3 \cdot e_4. \quad (4.88)$$

We will first show that it is always possible to construct two massless vectors from two massive ones. One can then take, in the notation of the *spinor helicity mechanism* presented in Appendix C,

$$e_3^\mu = \frac{\langle e_1 | \gamma^\mu | e_2 \rangle}{2}, \quad e_4^\mu = \frac{\langle e_2 | \gamma^\mu | e_1 \rangle}{2}, \quad (4.89)$$

to get a four-dimensional massless basis [33, 80, 81]. For the two massive vectors used to construct this basis, at the four- and three-point level, one can take two of the external momenta. At the two-point level, there is only one independent external momentum and at the one-point level there are none, so there one needs one respectively both massive vectors to be chosen arbitrarily.

Given two massive vectors K_1 and K_2 , we need to construct two massless ones ($e_1^2 = e_2^2 = 0$) that serve as a basis for the massive ones,

$$\begin{pmatrix} K_1 \\ K_2 \end{pmatrix} = \begin{pmatrix} a & b \\ c & d \end{pmatrix} \begin{pmatrix} e_1 \\ e_2 \end{pmatrix}. \quad (4.90)$$

We first need to get the inverse of this matrix, which is the adjoint divided by the determinant,

$$\begin{pmatrix} e_1 \\ e_2 \end{pmatrix} = \frac{1}{ad - bc} \begin{pmatrix} d & -b \\ -c & a \end{pmatrix} \begin{pmatrix} K_1 \\ K_2 \end{pmatrix}. \quad (4.91)$$

We have the two equations that state that the e 's are massless to reduce the number of coefficients by two,

$$e_1^2 = \left(\frac{dK_1 - bK_2}{ad - bc} \right)^2 = 0 \Rightarrow d^2 K_1^2 + b^2 K_2^2 - 2bd K_1 \cdot K_2 = 0. \quad (4.92)$$

This is a quadratic equation that we can solve for d ,

$$\begin{aligned} d &= \frac{2bK_1 \cdot K_2 \pm \sqrt{4b^2(K_1 \cdot K_2)^2 - 4b^2 K_1^2 K_2^2}}{2K_1^2} \\ &= b \left[\frac{K_1 \cdot K_2 \pm \sqrt{(K_1 \cdot K_2)^2 - K_1^2 K_2^2}}{K_1^2} \right] = \frac{b\gamma_\pm}{K_1^2}, \end{aligned} \quad (4.93)$$

where we introduced the shorthand notation γ_\pm for the numerator with a plus or minus sign in front of the square root,

$$\gamma_\pm = K_1 \cdot K_2 \pm \sqrt{(K_1 \cdot K_2)^2 - K_1^2 K_2^2}. \quad (4.94)$$

We can do the same with the equation $e_2^2 = 0$ to get a similar relation between a and c ,

$$c = \frac{a\gamma_\pm}{K_1^2}. \quad (4.95)$$

The denominator in the expressions for e_1 and e_2 become singular if the same sign is chosen for the γ 's of c and d . We therefore choose

$$d = \frac{b\gamma_+}{K_1^2} \quad (4.96)$$

$$c = \frac{a\gamma_-}{K_1^2}. \quad (4.97)$$

Notice that the sum of the two is

$$\gamma_+ + \gamma_- = 2K_1 \cdot K_2, \quad (4.98)$$

and the product of the two γ 's is simply

$$\gamma_+ \gamma_- = K_1^2 K_2^2, \quad (4.99)$$

which can be used to rewrite the denominator as

$$ad - bc = ad \left(1 - \frac{bc}{ad}\right) = ad \left(1 - \frac{\gamma_-}{\gamma_+}\right) = ad \left(1 - \frac{K_1^2 K_2^2}{\gamma_+^2}\right). \quad (4.100)$$

Calling the expression between brackets β ,

$$\beta = 1 - \frac{K_1^2 K_2^2}{\gamma_+^2}, \quad (4.101)$$

we get for e_1

$$e_1 = \frac{1}{ad\beta} (dK_1 - bK_2) = \frac{1}{a\beta} \left(K_1 - \frac{K_1^2}{\gamma_+} K_2\right). \quad (4.102)$$

For e_2 we get

$$e_2 = \frac{1}{ad\beta} (-cK_1 + aK_2) = \frac{1}{d\beta} \left(-\frac{\gamma_-}{K_1^2} K_1 + K_2\right) = \frac{1}{d\beta} \left(K_2 - \frac{K_2^2}{\gamma_+} K_1\right). \quad (4.103)$$

a and d can be chosen freely, so we conveniently set them to one, which gives our final result,

$$e_1 = \frac{1}{\beta} \left(K_1 - \frac{K_1^2}{\gamma_+} K_2\right), \quad e_2 = \frac{1}{\beta} \left(K_2 - \frac{K_2^2}{\gamma_+} K_1\right). \quad (4.104)$$

There are two fractions that occur often, so it is useful to rewrite this expression,

$$r_1 = \frac{K_1^2}{\gamma_+}, \quad r_2 = \frac{K_2^2}{\gamma_+}, \quad (4.105)$$

which gives for their product

$$r_1 r_2 = \frac{\gamma_-}{\gamma_+}. \quad (4.106)$$

We then have for β

$$\beta = 1 - r_1 r_2, \quad (4.107)$$

and for the two basis vectors

$$e_1 = \frac{1}{\beta} (K_1 - r_1 K_2), \quad e_2 = \frac{1}{\beta} (K_2 - r_2 K_1). \quad (4.108)$$

This can be used to simplify the product between the two,

$$\begin{aligned} e_1 \cdot e_2 &= \frac{1}{\beta^2} \left(K_1 \cdot K_2 - r_1 K_2^2 - r_2 K_1^2 + r_1 r_2 K_1 \cdot K_2\right) \\ &= \frac{1}{\beta^2} \left(\frac{\gamma_+ + \gamma_-}{2} - 2\gamma_- + \frac{\gamma_-}{\gamma_+} \left(\frac{\gamma_+ + \gamma_-}{2}\right)\right) \\ &= \frac{\gamma_+}{2\beta^2} \left(1 - 2\frac{\gamma_-}{\gamma_+} + \frac{\gamma_-^2}{\gamma_+^2}\right) = \frac{\gamma_+}{2\beta^2} (1 - r_1 r_2)^2 \\ &= \frac{\gamma_+}{2}. \end{aligned} \quad (4.109)$$

4.5. d -dimensional integrand decomposition

In Section 4.2 has been shown that a generic n -point integral can be decomposed in a set of Master Integrals (MIs) times coefficients, but that in d dimensions rational terms appear because of the integration over terms proportional to μ^2 . A different approach was developed in [35, 36], that treats the integrals $I_{i_1 \dots i_k}[(\mu^2)^\alpha]$ appearing as being part of the MI basis. In the remainder of this chapter, we will drop the bar-notation for d -dimensional denominators, as no four-dimensional ones will appear anymore. The full expression for a generic n -point integral is then

$$\begin{aligned} \mathcal{A}_n &= \int d^d \bar{q} A(\bar{q}) = \sum_{(ijklm)} \int d^d \bar{q} \frac{c_{5,0}^{(ijklm)} \mu^2}{D_i D_j D_k D_l D_m} \\ &+ \sum_{(ijkl)} \int d^d \bar{q} \frac{c_{4,0}^{(ijkl)} + c_{4,4}^{(ijkl)} \mu^4}{D_i D_j D_k D_l} + \sum_{(ijk)} \int d^d \bar{q} \frac{c_{3,0}^{(ijk)} + c_{3,7}^{(ijk)} \mu^2}{D_i D_j D_k} \\ &+ \sum_{(ij)} \int d^d \bar{q} \frac{c_{2,0}^{(ij)} + c_{2,9}^{(ij)} \mu^2}{D_i D_j} + \sum_{(i)} \int d^d \bar{q} \frac{c_{1,0}^{(i)}}{D_i}. \end{aligned} \quad (4.110)$$

The notation $(ijk..)$ is meant to signify that the summation goes over all combinations of $\{ijk..\}$. Denoting the MIs in their usual way,

$$I_{i_1 \dots i_k}[\alpha] \equiv \int d^d \bar{q} \frac{\alpha}{D_{i_1} \dots D_{i_k}}, \quad I_{i_1 \dots i_k} \equiv I_{i_1 \dots i_k}[1], \quad (4.111)$$

one can rewrite this as

$$\begin{aligned} \mathcal{A}_n &= \sum_{(ijkl)}^{n-1} \left\{ c_{4,0}^{(ijkl)} I_{ijkl} + c_{4,4}^{(ijkl)} I_{ijkl}[\mu^4] \right\} + \sum_{(ijk)}^{n-1} \left\{ c_{3,0}^{(ijk)} I_{ijk} + c_{3,7}^{(ijk)} I_{ijk}[\mu^2] \right\} + \\ &\sum_{(ij)}^{n-1} \left\{ c_{2,0}^{(ij)} I_{ij} + c_{2,1}^{(ij)} I_{ij}[(q + p_i) \cdot e_2] + c_{2,2}^{(ij)} I_{ij}[(q + p_i) \cdot e_2]^2 + c_{2,9}^{(ij)} I_{ij}[\mu^2] \right\} + \sum_i^{n-1} c_{1,0}^{(i)} I_i. \end{aligned} \quad (4.112)$$

The two additional bubbles are included to remedy the possible vanishing of Gram-determinants [34]. Integrals with μ^2 in the numerator can be traded for higher dimensional ones using (see Appendix B.1),

$$I_{i_1 \dots i_k}[(\mu^2)^r f(q, \mu^2)] = \frac{1}{\pi^r} \prod_{\kappa=1}^r \left(\kappa - 3 + \frac{d}{2} \right) \int d^{d+2r} \bar{q} \frac{f(q, \mu^2)}{D_{i_1} \dots D_{i_k}}. \quad (4.113)$$

Equation (4.110) holds at the integral level. In order to get a similar expression at the integrand level, it is not allowed to simply remove the integral signs, because this would ignore the overall integration constants of all the individual integrals. Rather, one needs to add so called *spurious functions*, functions that vanish upon integration. Using the notation:

$$\int d^d \bar{q} \frac{f_{ijk..}^s(\bar{q})}{D_i D_j D_{k..}} = 0 \quad (4.114)$$

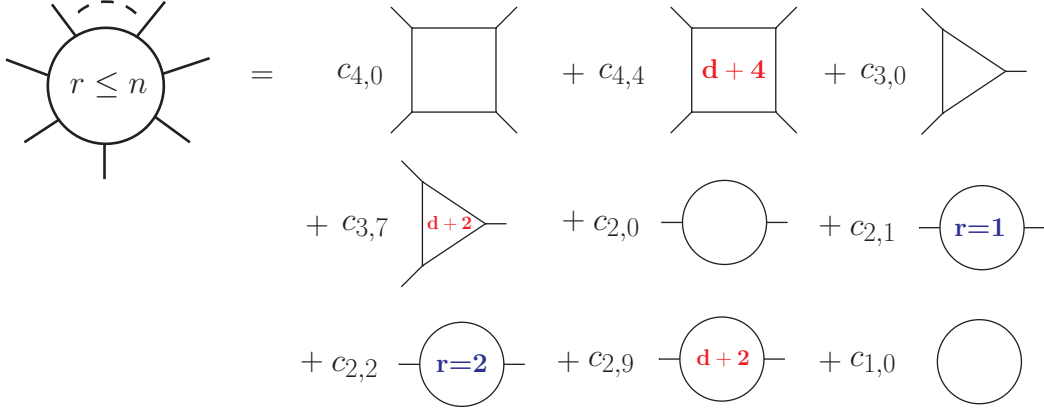


Figure 4.3.: Depiction of the decomposition of a generic integral in a set of master integrals.

we can write the corresponding equation at the integrand level:

$$\begin{aligned}
 A(\bar{q}) &= \sum_{(ijklm)} \frac{c_{5,0}\mu^2 + f_{ijklm}^s(\bar{q})}{D_i D_j D_k D_l D_m} \\
 &+ \sum_{(ijkl)} \frac{c_{4,0} + c_{4,4}\mu^4 + f_{ijkl}^s(\bar{q})}{D_i D_j D_k D_l} + \sum_{(ijk)} \frac{c_{3,0} + c_{3,7}\mu^2 + f_{ijk}^s(\bar{q})}{D_i D_j D_k} \\
 &+ \sum_{(ij)} \frac{c_{2,0} + c_{2,1}w + c_{2,2}w^2 + c_{2,9}\mu^2 + f_{ij}^s(\bar{q})}{D_i D_j} + \sum_{(i)} \frac{c_{1,0} + f_i^s(\bar{q})}{D_i},
 \end{aligned} \tag{4.115}$$

with $w = (q + p_i) \cdot e_2$. Collecting all terms in one symbol, we can write the numerators in a generic form,

$$\begin{aligned}
 A(\bar{q}) &= \sum_{(ijklm)} \frac{\Delta_{ijklm}(\bar{q})}{D_i D_j D_k D_l D_m} + \sum_{(ijkl)} \frac{\Delta_{ijkl}(\bar{q})}{D_i D_j D_k D_l} \\
 &+ \sum_{(ijk)} \frac{\Delta_{ijk}(\bar{q})}{D_i D_j D_k} + \sum_{(ij)} \frac{\Delta_{ij}(\bar{q})}{D_i D_j} + \sum_{(i)} \frac{\Delta_i(\bar{q})}{D_i}.
 \end{aligned} \tag{4.116}$$

We now have the task to find the parametric form for the $\Delta_{ij\dots}$. If a part of the numerator can be expressed in terms of propagators that appear in the denominator, this would reduce this part to a lower level term in the summation. Therefore, these nominators can only be multivariate polynomials in the *Irreducible Scalar Products* (ISPs) involving q . For example, a term proportional to q^2 cannot appear in the numerator, because it can be reduced to a term proportional to one of the denominators and another scalar product involving q ,

$$q^2 = D_i - 2q \cdot p_i - p_i^2 + m_i^2. \tag{4.117}$$

In order to find the most generic form of any polynomial, one needs to know its rank. As stated before, in a renormalizable theory, the rank of the numerator cannot exceed the number

of of propagators,

$$r \leq n, \quad (4.118)$$

so for now we will use this limitation. When we will consider effective vertices later on, it will turn out to alter this rule.

4.6. Parametric form of the numerators

All considering, the strategy will consists of the same steps for every level. Firstly, all the ISPs need to be determined. Then, the most generic multivariate polynomial in these ISPs up to the rank allowed by equation (4.118) is to be constructed. Finally, if this yields products of ISPs which in combination are again reducible, they ought to be excluded.

4.6.1. Five-point contributions

At the five point contribution, due to momentum conservation, there are four independent momenta. Therefore, one can construct a four-dimensional basis using these vectors. There are in this basis then five independent scalar products, q^2 and $q \cdot K_i$. We already know that q^2 is reducible. Furthermore, one can write

$$q \cdot K_i = q \cdot (p_i - p_{i-1}) \propto D_i - D_{i-1} + \text{const}. \quad (4.119)$$

Therefore, there are no ISPs at the five-point level and we would have only the coefficients of unity, μ^2 and μ^4 left. However, in [82], it was shown that those can be written as linear combinations of one another and that it is most convenient to keep the one of μ^2 . One can write

$$\begin{aligned} (\mu^2)^\alpha &= \left[D_i + m_i^2 - p_i^2 - 2(q \cdot p_i) - q^2 \right]^\alpha \\ &= \left[D_i + m_i^2 - p_i^2 - 2(q \cdot p_i) - 2(q \cdot e_1)(q \cdot e_2) + 2(q \cdot e_3)(q \cdot e_4) \right]^\alpha \\ &= \text{constant terms} + \text{RSPs}, \end{aligned} \quad (4.120)$$

where RSP is meant to indicate Reducible Scalar Products. This means one can express all powers of μ^2 in terms of one particular one $(\mu^2)^{\alpha_0}$. Choosing $\alpha_0 = 1$, we have

$$\Delta_{ijklm}(q, \mu^2) = c_{5,0}^{(ijklm)} \mu^2. \quad (4.121)$$

4.6.2. Four-point contributions

At the four-point contribution, there are three independent vectors. Now, in order to find the ISPs, we replace e_3 and e_4 with the new vectors,

$$\begin{aligned} v &\equiv (K_3 \cdot e_4)e_3 + (K_3 \cdot e_3)e_4 \\ v_\perp &\equiv (K_3 \cdot e_4)e_3 - (K_3 \cdot e_3)e_4. \end{aligned} \quad (4.122)$$

v is now a linear combination of K_1 , K_2 and K_3 . v_\perp is orthogonal to all the external momenta. In this basis we can find five independent scalar products,

$$q^2, \quad (q \cdot e_1), \quad (q \cdot e_2), \quad (q \cdot v), \quad (q \cdot v_\perp). \quad (4.123)$$

q^2 is reducible and the next three are linear combinations of K_i . Therefore $(q \cdot v_\perp)$ is the only ISP at this level. The metric of this basis can be written as

$$g^{\mu\nu} = \frac{e_1^\mu e_2^\nu + e_2^\mu e_1^\nu}{e_1 \cdot e_2} + \frac{v^\mu v^\nu}{v^2} + \frac{v_\perp^\mu v_\perp^\nu}{v_\perp^2}. \quad (4.124)$$

This can be used to write q^2 as

$$q^2 = q_\mu q_\nu g^{\mu\nu} \Rightarrow (q \cdot v_\perp)^2 = v_\perp^2 \left(q^2 + \frac{(q \cdot e_1)(q \cdot e_2)}{e_1 \cdot e_2} + \frac{(q \cdot v)^2}{v^2} \right). \quad (4.125)$$

All terms between brackets are reducible, therefore also $(q \cdot v_\perp)^2$ is reducible. Any higher powers of $(q \cdot v_\perp)$ can be rewritten with $(q \cdot v_\perp)^2$ split out. Hence, although in principle we should consider polynomial terms up to rank four, only one power of this ISP is enough,

$$\Delta_{ijkl}(q, \mu^2) = \Delta_{ijkl}^R(q, \mu^2) + c_{4,0}^{(ijkl)} + c_{4,2}^{(ijkl)} \mu^2 + c_{4,4}^{(ijkl)} \mu^4, \quad (4.126)$$

with

$$\Delta_{ijkl}^R(q, \mu^2) = \left(c_{4,1}^{(ijkl)} + c_{4,3}^{(ijkl)} \mu^2 \right) (q + p_i) \cdot v_\perp. \quad (4.127)$$

4.6.3. Three-point contributions

At the three-point contribution, there are only two independent external vectors. This means that only e_1 and e_2 are linear combinations of the external momenta and therefore $(q \cdot e_3)$ and $(q \cdot e_4)$ are ISPs. The metric in this case is

$$g^{\mu\nu} = \frac{e_1^\mu e_2^\nu + e_2^\mu e_1^\nu}{e_1 \cdot e_2} - \frac{e_3^\mu e_4^\nu + e_4^\mu e_3^\nu}{e_3 \cdot e_4}. \quad (4.128)$$

As in the previous section, starting with the reducibility of q^2 , it is easy to show that $(q \cdot e_3)(q \cdot e_4)$ can be written as

$$(q \cdot e_3)(q \cdot e_4) = \frac{e_3 \cdot e_4}{2} \left(\frac{(q \cdot e_1)(q \cdot e_2)}{e_1 \cdot e_2} - q^2 \right), \quad (4.129)$$

which again has between brackets expressions that are reducible and makes the cross product as a whole reducible, as are its higher powers. The ISPs are therefore limited to just powers of $(q \cdot e_3)$ and $(q \cdot e_4)$ and cross products with μ^2 , up to a total rank of three,

$$\Delta_{ijk}(q, \mu^2) = \Delta_{ijk}^R(q, \mu^2) + c_{3,0}^{(ijk)} + c_{3,7}^{(ijk)} \mu^2, \quad (4.130)$$

with

$$\begin{aligned} \Delta_{ijk}^R(q, \mu^2) = & \left(c_{3,1}^{(ijk)} + c_{3,8}^{(ijk)} \mu^2 \right) (q + p_i) \cdot e_3 \\ & + \left(c_{3,4}^{(ijk)} + c_{3,9}^{(ijk)} \mu^2 \right) (q + p_i) \cdot e_4 \\ & + c_{3,2}^{(ijk)} ((q + p_i) \cdot e_3)^2 + c_{3,5}^{(ijk)} ((q + p_i) \cdot e_4)^2 \\ & + c_{3,3}^{(ijk)} ((q + p_i) \cdot e_3)^3 + c_{3,6}^{(ijk)} ((q + p_i) \cdot e_4)^3. \end{aligned}$$

4.6.4. Two-point contributions

At the two-point contribution, there is only one independent external momentum vector. The other massive vector needed to construct the massless basis can be chosen randomly, but this means that only one of $(q \cdot e_1)$ and $(q \cdot e_2)$ is reducible, where we will choose the former. $(q \cdot e_2)$, $(q \cdot e_3)$ and $(q \cdot e_4)$ are then irreducible. The metric from the previous section is still valid, and therefore also the argumentation not to have cross product of the type $(q \cdot e_3)(q \cdot e_4)$ still holds. Cross products with $(q \cdot e_2)$ are irreducible though, and we get up to rank two

$$\Delta_{ij}(q, \mu^2) = \Delta_{ij}^R(q, \mu^2) + c_{2,0}^{(ij)} + c_{2,9}^{(ij)} \mu^2, \quad (4.131)$$

with

$$\begin{aligned} \Delta_{ij}^R(q, \mu^2) = & c_{2,1}^{(ij)}(q + p_i) \cdot e_2 + c_{2,2}^{(ij)}((q + p_i) \cdot e_2)^2 \\ & + c_{2,3}^{(ij)}(q + p_i) \cdot e_3 + c_{2,4}^{(ij)}((q + p_i) \cdot e_3)^2 \\ & + c_{2,5}^{(ij)}(q + p_i) \cdot e_4 + c_{2,6}^{(ij)}((q + p_i) \cdot e_4)^2 \\ & + c_{2,7}^{(ij)}((q + p_i) \cdot e_2)((q + p_i) \cdot e_3) \\ & + c_{2,8}^{(ij)}((q + p_i) \cdot e_2)((q + p_i) \cdot e_4). \end{aligned}$$

4.6.5. One-point contributions

Since we have no independent momentum vector available at the one-point contribution, we have to construct our basis with two random massive vectors and we have the full set of four ISPs: $(q \cdot e_1)$, $(q \cdot e_2)$, $(q \cdot e_3)$ and $(q \cdot e_4)$. The expression up to rank one gives trivially

$$\begin{aligned} \Delta_i(q, \mu^2) = & c_{1,0}^{(i)} + c_{1,1}^{(i)}((q + p_i) \cdot e_1) + c_{1,2}^{(i)}((q + p_i) \cdot e_2) \\ & + c_{1,3}^{(i)}((q + p_i) \cdot e_3) + c_{1,4}^{(i)}((q + p_i) \cdot e_4). \end{aligned} \quad (4.132)$$

4.7. Integrand reduction algorithm

The expressions that have been established for the numerators of equation (4.116) are independent of the specific process under consideration. The actual numerical values of all the coefficients, on the other hand, do depend on the specific process. An efficient way to obtain these values of the coefficients is by using the method invented by Ossola, Papadopoulos and Pittau [33, 34], and later extended in [35, 36], which is therefore often referred to as the *OPP method*. Multiplying equation (4.116) on both sides with all the propagators of the diagram, an explicit expression for the numerator is obtained,

$$\begin{aligned} N(\bar{q}) = & \sum_{(ijklm)}^{n-1} \Delta_{ijklm}(\bar{q}) \prod_{h \neq i,j,k,\ell,m}^{n-1} D_h + \sum_{(ijkl)}^{n-1} \Delta_{ijkl}(\bar{q}) \prod_{h \neq i,j,k,\ell}^{n-1} D_h + \\ & + \sum_{(ijk)}^{n-1} \Delta_{ijk}(\bar{q}) \prod_{h \neq i,j,k}^{n-1} D_h + \sum_{(ij)}^{n-1} \Delta_{ij}(\bar{q}) \prod_{h \neq i,j}^{n-1} D_h + \sum_i^{n-1} \Delta_i(\bar{q}) \prod_{h \neq i}^{n-1} D_h, \end{aligned} \quad (4.133)$$

which allows one to see instantly that the $\Delta_{ij..}$ are just the residues of the diagram with the corresponding propagators put on shell after subtraction of the higher order levels.

$$\begin{aligned}
\Delta_{ijklm}(\bar{q}) &= \text{Res}_{ijklm} \left\{ \frac{N(\bar{q})}{D_0 \cdots D_{n-1}} \right\} \\
\Delta_{ijk\ell}(\bar{q}) &= \text{Res}_{ijk\ell} \left\{ \frac{N(\bar{q})}{D_0 \cdots D_{n-1}} - \sum_{(ijklm)}^{n-1} \frac{\Delta_{ijklm}(\bar{q})}{D_i D_j D_k D_\ell D_m} \right\} \\
\Delta_{ijk}(\bar{q}) &= \text{Res}_{ijk} \left\{ \frac{N(\bar{q})}{D_0 \cdots D_{n-1}} - \sum_{(ijklm)}^{n-1} \frac{\Delta_{ijklm}(\bar{q})}{D_i D_j D_k D_\ell D_m} - \sum_{(ijk\ell)}^{n-1} \frac{\Delta_{ijk\ell}(\bar{q})}{D_i D_j D_k D_\ell} \right\} \\
\Delta_{ij}(\bar{q}) &= \text{Res}_{ij} \left\{ \frac{N(\bar{q})}{D_0 \cdots D_{n-1}} - \sum_{(ijklm)}^{n-1} \frac{\Delta_{ijklm}(\bar{q})}{D_i D_j D_k D_\ell D_m} \right. \\
&\quad \left. - \sum_{(ijk\ell)}^{n-1} \frac{\Delta_{ijk\ell}(\bar{q})}{D_i D_j D_k D_\ell} - \sum_{(ijk)}^{n-1} \frac{\Delta_{ijk}(\bar{q})}{D_i D_j D_k} \right\}, \\
\Delta_i(\bar{q}) &= \text{Res}_i \left\{ \frac{N(\bar{q})}{D_0 \cdots D_{n-1}} - \sum_{(ijklm)}^{n-1} \frac{\Delta_{ijklm}(\bar{q})}{D_i D_j D_k D_\ell D_m} + \right. \\
&\quad \left. - \sum_{(ijk\ell)}^{n-1} \frac{\Delta_{ijk\ell}(\bar{q})}{D_i D_j D_k D_\ell} - \sum_{(ijk)}^{n-1} \frac{\Delta_{ijk}(\bar{q})}{D_i D_j D_k} - \sum_{(ij)}^{n-1} \frac{\Delta_{ij}(\bar{q})}{D_i D_j} \right\}. \tag{4.134}
\end{aligned}$$

Since $N(\bar{q})$ is generally known for each diagram, we now have all the ingredients to write down the algorithm:

- Start at the highest level available. For pentagons and larger diagrams, the highest level is the quintuple cut.
- Subtract the previous levels from the integrand.
- For all combinations, cut all the corresponding propagators to calculate the residue. These cuts impose conditions on the components of \bar{q} .
- Sample, *i.e.* evaluate at a convenient \bar{q} that is allowed by the cut conditions, the residue as many times as there are coefficients to be determined.
- Determine the coefficients by solving this system of equations.
- Go down one level.

Figure 4.4.: The integrand reduction algorithm.

This algorithm was implemented in the program SAMURAI [37] and its extension XSAMURAI [12], which will be the subject of the next chapter.

5 ■ Extended d -dimensional integrand reduction

With the d -dimensional integrand reduction algorithm defined, in this chapter we will look at its implementation, where we will go through all the levels of the integrand decomposition algorithm systematically. In Section 5.1 we will consider the normal rank situation, followed by the higher-rank extension in Section 5.2. We will follow closely the implementation in the program SAMURAI [37] and its extension XSAMURAI [12].

5.1. Samurai: d -dimensional integrand reduction

We will make frequent use of the Discrete Fourier Transformation (DFT) to project out the coefficients. Therefore, first we will look at how the DFT works for simple polynomials.

5.1.1. Discrete Fourier Transformation (DFT)

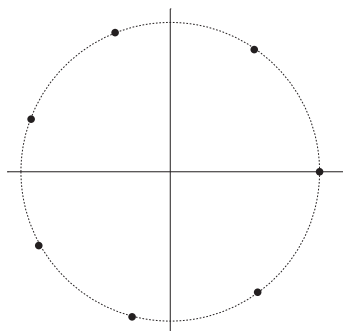


Figure 5.1.: Illustration of the idea of sampling symmetrically in the complex plane, in this case for $n = 7$.

There are no restrictions other than the cut imposed conditions to the values of \bar{q} used in the sampling, apart from avoiding to make the system of equations degenerate. However, if the size of the system becomes large, the solutions may become such large expressions that they lose accuracy when evaluated numerically. We therefore need a systematic approach. As an illustrative example, we will first look at how to determine the coefficients of a simple univariate polynomial up to rank n ,

$$P(x) = c_0 + c_1x + c_2x^2 + \dots + c_nx^n. \quad (5.1)$$

An efficient way to determine these coefficients is to sample symmetrically in a circle in the complex plane (an illustration is given in Figure 5.1),

$$x_k = \rho \exp \left[-2\pi i \frac{k}{n+1} \right], \quad (5.2)$$

thereby obtaining the values

$$P_k = P(x_k) = \sum_{l=0}^n c_l \rho^l \exp \left[-2\pi i \frac{k}{(n+1)} l \right], \quad (5.3)$$

and then use the orthogonality relation,

$$\sum_{n=0}^{N-1} \exp \left[2\pi i \frac{k}{N} n \right] \exp \left[-2\pi i \frac{k'}{N} n \right] = N \delta_{kk'}, \quad (5.4)$$

to project out the coefficients,

$$c_l = \frac{\rho^{-l}}{n+1} \sum_{k=0}^n P_k \exp \left[2\pi i \frac{k}{n+1} l \right]. \quad (5.5)$$

This procedure is of course the simple discrete Fourier transformation (DFT). In [83], this method was first explored in the context of projecting out the coefficients of the residues in integrand decomposition. In the actual calculations, ρ depends on the external kinematics, and in certain cases it can become small. Notice that the above formula for the coefficients becomes numerically unstable in this case. Therefore, to employ the idea of DFT, in the multivariate polynomials we have to deal with, we will manipulate the DFT sampling procedure to achieve expressions for coefficients which are stable also when radius of the DFT sampling is small, as long as the cut is non-degenerate. A cut is degenerate when the solution of a given cut at level m , makes $m+1$ denominators vanish. This situation occurs in correspondence with vanishing Gram determinants. In this cases the integrand reduction must be modified, since the form of the residue changes as well. The recent study in [84] allows for the determination of the residues also in such bad kinematic configurations, but in the current implementation of the integrand reduction algorithm, hereby discussed, we will focus on non-degenerate cuts.

5.1.2. Quintuple cut

At the quintuple cut, we want to determine the coefficient in the expression for the residue

$$\Delta_{ijklm}(q, \mu^2) = c_{5,0}^{(ijklm)} \mu^2. \quad (5.6)$$

The five cuts,

$$D_i = D_j = D_k = D_\ell = D_m = 0, \quad (5.7)$$

impose five conditions on the components of \bar{q} .

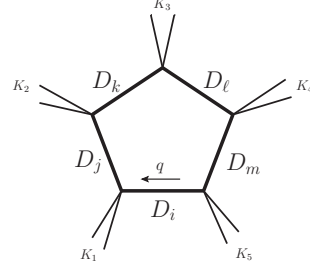


Figure 5.2.: A quintuple cut.

Determining the sampling value

The first cut we consider is

$$D_i = q^2 - m_i^2 - \mu^2 = 0 \Rightarrow q^2 = m_i^2 + \mu^2. \quad (5.8)$$

This can be used subsequently to write

$$D_j = (q + K_1)^2 - m_j^2 - \mu^2 = 0 \Rightarrow 2(q \cdot K_1) = m_j^2 - m_i^2 - K_1^2, \quad (5.9)$$

and

$$D_m = (q - K_5)^2 - m_m^2 - \mu^2 = 0 \Rightarrow 2(q \cdot K_5) = m_i^2 - m_m^2 + K_5^2. \quad (5.10)$$

Writing $q = \sum x_i e_i$ and using the notation of Section 4.4, with K_1 and K_5 as massive vectors for the basis, we can write

$$\begin{aligned} q \cdot K_1 &= (bx_1 + ax_2)e_1 \cdot e_2 = (r_1x_1 + x_2)e_1 \cdot e_2, \\ q \cdot K_5 &= (dx_1 + cx_2)e_1 \cdot e_2 = (x_1 + r_2x_2)e_1 \cdot e_2. \end{aligned} \quad (5.11)$$

Equating the two expressions for both scalar products, we end up with two equations for the two variables x_1 and x_2 ,

$$\begin{aligned} r_1x_1 + x_2 &= \frac{m_j^2 - m_i^2 - K_1^2}{2e_1 \cdot e_2}, \\ x_1 + r_2x_2 &= \frac{m_i^2 - m_m^2 + K_5^2}{2e_1 \cdot e_2}, \end{aligned} \quad (5.12)$$

which we can solve,

$$\begin{aligned} x_1 &= \frac{m_m^2 - m_i^2 - K_5^2 + r_2(m_j^2 - m_i^2 - K_1^2)}{2e_1 \cdot e_2(-1 + r_1r_2)}, \\ x_2 &= \frac{m_i^2 - m_j^2 + K_1^2 + r_1(m_i^2 - m_m^2 + K_5^2)}{2e_1 \cdot e_2(-1 + r_1r_2)}. \end{aligned} \quad (5.13)$$

Using expression (4.109) we can rewrite this as

$$\begin{aligned} x_1 &= \frac{m_m^2 - r_2m_j^2 - (1 + r_2)m_i^2 - 2e_1 \cdot e_2r_2(1 + r_1)}{2e_1 \cdot e_2(-1 + r_1r_2)}, \\ x_2 &= \frac{-m_j^2 - r_1m_m^2 + (1 + r_1)m_i^2 + 2e_1 \cdot e_2r_1(1 + r_2)}{2e_1 \cdot e_2(-1 + r_1r_2)}, \end{aligned} \quad (5.14)$$

which is the form implemented in SAMURAI. To determine x_3 and x_4 we consider the remaining two cuts. Using the expression for q^2 that was derived before and defining, mainly for visibility, the effective second and third vector $v_2 = K_1 + K_2$ and $v_3 = K_1 + K_2 + K_3$, we can write

$$\begin{aligned} D_k &= (q + v_2)^2 - m_k^2 - \mu^2 = 0 \Rightarrow 2(q \cdot v_2) = m_k^2 - m_i^2 - v_2^2, \\ D_\ell &= (q + v_3)^2 - m_\ell^2 - \mu^2 = 0 \Rightarrow 2(q \cdot v_3) = m_\ell^2 - m_i^2 - v_3^2. \end{aligned} \quad (5.15)$$

Unlike K_1 and K_2 , these two vectors do have contributions in the e_3 and e_4 direction. Note that our basis is not a standard orthonormal one, so the elements $v^{(i)}$ are not simply $(v \cdot e_i)$, but rather

$$v^{(1)} = \frac{v \cdot e_2}{e_1 \cdot e_2}, \quad v^{(2)} = \frac{v \cdot e_1}{e_1 \cdot e_2}, \quad v^{(3)} = -\frac{v \cdot e_4}{e_1 \cdot e_2}, \quad v^{(4)} = -\frac{v \cdot e_3}{e_1 \cdot e_2}. \quad (5.16)$$

Given the definition of q and the properties of the basis, this means one can write

$$\begin{aligned} 2(q \cdot v) &= 2(e_1 \cdot e_2) \left[x_1 v^{(2)} + x_2 v^{(1)} - x_3 v^{(4)} - x_4 v^{(3)} \right] \\ &= 2 \left[x_1 (v \cdot e_1) + x_2 (v \cdot e_2) + x_3 (v \cdot e_3) + x_4 (v \cdot e_4) \right]. \end{aligned} \quad (5.17)$$

So in the end, scalar products between two vectors in this basis still work normally. Therefore, combining with equation (5.15), one is left with the following system of equations:

$$\begin{aligned} 2 \left[x_1 (v_2 \cdot e_1) + x_2 (v_2 \cdot e_2) + x_3 (v_2 \cdot e_3) + x_4 (v_2 \cdot e_4) \right] &= m_k^2 - m_i^2 - v_2^2, \\ 2 \left[x_1 (v_3 \cdot e_1) + x_2 (v_3 \cdot e_2) + x_3 (v_3 \cdot e_3) + x_4 (v_3 \cdot e_4) \right] &= m_\ell^2 - m_i^2 - v_3^2, \end{aligned} \quad (5.18)$$

which can be solved for x_3 and x_4 . Defining for increased readability

$$f_i = v_i^2 + 2x_1 (v_i \cdot e_1) + 2x_2 (v_i \cdot e_2), \quad (5.19)$$

the solutions are

$$\begin{aligned} x_3 &= \frac{(v_2 \cdot e_4)(f_3 + m_i^2 - m_\ell^2) - (v_3 \cdot e_4)(f_2 + m_i^2 - m_k^2)}{2(v_2 \cdot e_3)(v_3 \cdot e_4) - 2(v_3 \cdot e_3)(v_2 \cdot e_4)}, \\ x_4 &= \frac{(v_3 \cdot e_3)(f_2 + m_i^2 - m_k^2) - (v_2 \cdot e_3)(f_3 + m_i^2 - m_\ell^2)}{2(v_2 \cdot e_3)(v_3 \cdot e_4) - 2(v_3 \cdot e_3)(v_2 \cdot e_4)}. \end{aligned} \quad (5.20)$$

We have determined four variables using five equations, so there still is one variable that we can fix, which is μ^2 . This can be easily done through rewriting equation (5.8) to

$$\mu^2 = q^2 - m_i^2 = 2e_1 \cdot e_2 (x_1 x_2 - x_3 x_4) - m_i^2. \quad (5.21)$$

Determining the coefficient

With $\bar{q} = (\mu^2, x_1, x_2, x_3, x_4)$ fully fixed, it is now trivial to extract the one coefficient at this level,

$$c_{5,0}^{(ijklm)} = \frac{\Delta_{ijklm}(q, \mu^2)}{\mu^2}. \quad (5.22)$$

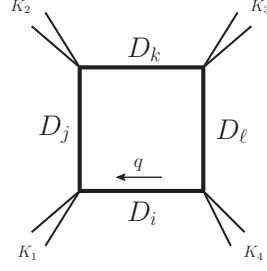


Figure 5.3.: A quadruple cut.

5.1.3. Quadruple cut

At the quadruple cut, we want to determine the coefficient in the expression

$$\Delta_{ijkl}(q, \mu^2) = c_{4,0}^{(ijkl)} + c_{4,2}^{(ijkl)} \mu^2 + c_{4,4}^{(ijkl)} \mu^4 + \left(c_{4,1}^{(ijkl)} + c_{4,3}^{(ijkl)} \mu^2 \right) (q + p_i) \cdot v_\perp. \quad (5.23)$$

The four cuts,

$$D_i = D_j = D_k = D_\ell = 0, \quad (5.24)$$

impose four conditions on the components of \bar{q} .

Determining the sampling values

The first steps involving the cuts of D_i , D_j and D_ℓ are identical to the quintuple cut case. After the appropriate substitution of vectors and indices, the result for x_1 and x_2 is therefore the same,

$$\begin{aligned} x_1 &= \frac{m_\ell^2 - m_i^2 - K_4^2 + r_2(m_j^2 - m_i^2 - K_1^2)}{2e_1 \cdot e_2(-1 + r_1 r_2)}, \\ x_2 &= \frac{m_i^2 - m_j^2 + K_1^2 + r_1(m_i^2 - m_\ell^2 + K_4^2)}{2e_1 \cdot e_2(-1 + r_1 r_2)}, \end{aligned} \quad (5.25)$$

where now K_1 and K_4 are used to construct the basis. To get x_3 and x_4 , we need to consider the first cut again and write out q^2 ,

$$\begin{aligned} q^2 &= 2e_1 \cdot e_2(x_1 x_2 - x_3 x_4) = m_i^2 + \mu^2 \Rightarrow \\ x_3 x_4 &= x_1 x_2 - \frac{m_i^2 + \mu^2}{2e_1 \cdot e_2} \equiv C_1(\mu^2). \end{aligned} \quad (5.26)$$

Note that we will not be able to fix μ^2 anymore with only four equations, so the product of x_3 and x_4 is a constant that still depends on what one chooses for the value of μ^2 . Now consider the last equation, again defining $v_2 = K_1 + K_2$. Following the same steps as in the quintuple cut, we still get

$$2[x_1(v_2 \cdot e_1) + x_2(v_2 \cdot e_2) + x_3(v_2 \cdot e_3) + x_4(v_2 \cdot e_4)] = m_k^2 - m_i^2 - v_2^2, \quad (5.27)$$

which can be rewritten as

$$x_3(v_2 \cdot e_3) + x_4(v_2 \cdot e_4) = -x_1(v_2 \cdot e_1) - x_2(v_2 \cdot e_2) + \frac{1}{2} \left(m_k^2 - m_i^2 - v_2^2 \right) \equiv C_2, \quad (5.28)$$

to get again an expression which involves x_3 and x_4 that is equal to a constant. In combination, we can substitute x_3 to get a quadratic expression in x_4 ,

$$C_1(v_2 \cdot e_3) - C_2 x_4 + (v_2 \cdot e_4) x_4^2 = 0. \quad (5.29)$$

Solving it gives two possible values for x_4 ,

$$x_4 = \frac{C_2 \pm \sqrt{C_2^2 - 4C_1(v_2 \cdot e_3)(v_2 \cdot e_4)}}{2(v_2 \cdot e_4)}. \quad (5.30)$$

The value of x_3 can then be obtained by substituting back in either equation (5.26) or equation (5.28).

Determining the coefficients

Equation (5.23) is simple enough to choose convenient values for μ^2 without much further consideration. Choosing $\mu^2 = 0$ and $\mu^2 = +\mu_s^2$ both two times, with the plus- and minus-solutions q_{\pm} from equation (5.30), and $-\mu_s^2$ one further time gives a non-degenerate system of equations,

$$\begin{aligned} \Delta_{ijkl}(0, q_{\pm}) &= c_{4,0}^{(ijkl)} + c_{4,1}^{(ijkl)}(q_{\pm} + p_i) \cdot v_{\perp} \\ \Delta_{ijkl}(+\mu_s^2, q_{\pm}) &= c_{4,0}^{(ijkl)} + c_{4,2}^{(ijkl)} \mu_s^2 + c_{4,4}^{(ijkl)} \mu_s^4 + \left(c_{4,1}^{(ijkl)} + c_{4,3}^{(ijkl)} \mu_s^2 \right) (q_{\pm} + p_i) \cdot v_{\perp} \\ \Delta_{ijkl}(-\mu_s^2, q_{+}) &= c_{4,0}^{(ijkl)} - c_{4,2}^{(ijkl)} \mu_s^2 + c_{4,4}^{(ijkl)} \mu_s^4 + \left(c_{4,1}^{(ijkl)} - c_{4,3}^{(ijkl)} \mu_s^2 \right) (q_{+} + p_i) \cdot v_{\perp}, \end{aligned} \quad (5.31)$$

where μ_s^2 can be any non-zero value, in particular $\mu_s^2 = 1$ further simplifies the system. The solutions for the coefficients can now be obtained by solving this system of equations. They are too involved to show here, but can be found in the source code of SAMURAI. The sampling for the quadruple cut is summarized in Table 5.1.

Quadruple cut	number of samplings
$\Lambda(0, q)$	2
$\Lambda(+\mu_s^2, q)$	2
$\Lambda(-\mu_s^2, q)$	1

Table 5.1.: The number of samplings per polynomial at the quadruple cut at normal rank.

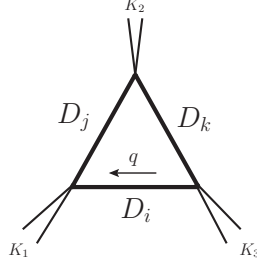


Figure 5.4.: A triple cut.

5.1.4. Triple cut

At the triple cut, we want to determine the coefficients in the expression given in equation (4.130). It will be more useful if we expand q in its basis right away,

$$\begin{aligned}
 \Delta_{ijk}(\mu^2, x_3, x_4) &= c_{3,0}^{(ijk)} + c_{3,7}^{(ijk)} \mu^2 \\
 &+ \left(c_{3,1}^{(ijk)} + c_{3,8}^{(ijk)} \mu^2 \right) (e_1 \cdot e_2) x_4 \\
 &+ \left(c_{3,4}^{(ijk)} + c_{3,9}^{(ijk)} \mu^2 \right) (e_1 \cdot e_2) x_3 \\
 &+ c_{3,2}^{(ijk)} (e_1 \cdot e_2)^2 x_4^2 + c_{3,5}^{(ijk)} (e_1 \cdot e_2)^2 x_3^2 \\
 &+ c_{3,3}^{(ijk)} (e_1 \cdot e_2)^3 x_4^3 + c_{3,6}^{(ijk)} (e_1 \cdot e_2)^3 x_3^3.
 \end{aligned} \tag{5.32}$$

The three cuts,

$$D_i = D_j = D_k = 0, \tag{5.33}$$

impose three conditions on the components of \bar{q} .

Determining the sampling values

Again, as in the previous two cuts, we use two of these conditions to fix x_1 and x_2 ,

$$\begin{aligned}
 x_1 &= \frac{m_k^2 - m_i^2 - K_3^2 + r_2(m_j^2 - m_i^2 - K_1^2)}{2e_1 \cdot e_2(-1 + r_1 r_2)}, \\
 x_2 &= \frac{m_i^2 - m_j^2 + K_1^2 + r_1(m_i^2 - m_k^2 + K_3^2)}{2e_1 \cdot e_2(-1 + r_1 r_2)}.
 \end{aligned} \tag{5.34}$$

The last remaining cut and its consequential condition remains of the same shape as before as well,

$$x_3 x_4 = x_1 x_2 - \frac{m_i^2 + \mu^2}{2e_1 \cdot e_2} \equiv C(\mu^2). \tag{5.35}$$

This fixes the relation between the three variables x_3 , x_4 and μ^2 .

Determining the coefficients

Let us start with choosing $\mu^2 = 0$, since this will reduce the number of terms in equation (4.130) from ten to seven: Three multiplying x_3 , three multiplying x_4 and one overall constant. Defining $C_0 \equiv C(0)$, one can now either replace $x_4 \rightarrow C_0/x_3$ and sample seven times over x_3 using the DFT or instead replace $x_3 \rightarrow C_0/x_4$ and sample seven times over x_4 . This will give identical results, since it only changes the direction one goes symmetrically around the complex plane. This gives expressions for the coefficients that are inversely proportional to C_0 and this will cause problems if C_0 is close to zero. An alternative way is to sample four times with x_3 and three times with x_4 , which will give rise to coefficients proportional to $1 - C_0^n$ with a certain power n , which is numerically unsafe around $C_0 = 1$. In fact, the system of equations is degenerate for $C_0 = 1$, since the first point one samples on in the first batch is $(x_3, x_4) = (1, C_0)$ and the first point in the second batch is $(x_3, x_4) = (C_0, 1)$. One should therefore implement both sampling strategies and branch in the code according to the value of C_0 . For the remaining coefficients, one can choose a sampling value $\mu^2 = \mu_s^2$ with the only restriction that $C(\mu_s^2)$ is nonzero and sample three times with either x_3 or x_4 , replacing one with $C(\mu_s^2)$ divided by the other. The sampling strategy for the triple cut is summarized in Table 5.2.

Triple cut	$C = 0$	$C \neq 0$
$\Lambda(0, x_3, C_0/x_3)$	4	7
$\Lambda(0, C_0/x_4, x_4)$	3	0
$\Lambda(\mu_s^2, x_3, C(\mu_s^2)/x_3)$	-	3

Table 5.2.: The number of samplings per polynomial at the triple cut at normal rank.

5.1.5. Double cut

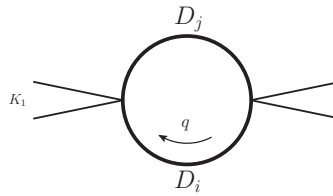


Figure 5.5.: A double cut.

At the double cut, we want to determine the coefficients in the expression

$$\begin{aligned}
 \Delta_{ij}(\mu^2, x_1, x_3, x_4) &= c_{2,0}^{(ij)} + c_{2,9}^{(ij)}\mu^2 + c_{2,1}^{(ij)}(e_1 \cdot e_2)x_1 + c_{2,2}^{(ij)}(e_1 \cdot e_2)^2x_1^2 \\
 &\quad - c_{2,3}^{(ij)}(e_1 \cdot e_2)x_4 + c_{2,4}^{(ij)}(e_1 \cdot e_2)^2x_4^2 \\
 &\quad - c_{2,5}^{(ij)}(e_1 \cdot e_2)x_3 + c_{2,6}^{(ij)}(e_1 \cdot e_2)^2x_3^2 \\
 &\quad - c_{2,7}^{(ij)}(e_1 \cdot e_2)^2x_1x_4 - c_{2,8}^{(ij)}(e_1 \cdot e_2)^2x_1x_3.
 \end{aligned}$$

The two cuts,

$$D_i = D_j = 0, \quad (5.36)$$

impose two conditions on the components of \bar{q} .

Determining the sampling values

Notice that at this level we have only one independent external vector to build our basis with. A convenient choice for the second vector is

$$K_2 = \left(c \frac{K_1^0}{|K_1^0|}, \frac{-c}{\sqrt{3}} \frac{K_1^i}{|K_1^i|} \right), \quad (5.37)$$

where c can be any positive constant. Notice that $K_2^2 = 0$ and that

$$K_1 \cdot K_2 = c|K_1^0| + \sum_i \frac{c}{\sqrt{3}} |K_1^i| > 0. \quad (5.38)$$

This means that $\gamma_+ = 2K_1 \cdot K_2$, $r_2 = 0$ and $\beta = 1$, which in turn means that $e_1 \cdot e_2 = K_1 \cdot K_2$ and therefore

$$r_1 = \frac{K_1^2}{2e_1 \cdot e_2}. \quad (5.39)$$

The second cut, which gives a similar relation between x_1 and x_2 as before,

$$r_1 x_1 + x_2 = \frac{m_j^2 - m_i^2 - K_1^2}{2e_1 \cdot e_2}, \quad (5.40)$$

can therefore now be rewritten as an explicit dependence of x_2 on the now free variable x_1 ,

$$x_2(x_1) = \frac{m_j^2 - m_i^2 - K_1^2(1 + x_1)}{2e_1 \cdot e_2}. \quad (5.41)$$

The other cut imposes a constraint on the relation between μ^2 , x_1 , x_3 and x_4 ,

$$x_3 x_4 = x_1 x_2(x_1) - \frac{m_i^2 + \mu^2}{2e_1 \cdot e_2} \equiv F(\mu^2, x_1). \quad (5.42)$$

Determining the coefficients

Let us start with choosing $x_1 = \mu^2 = 0$, which reduces our polynomial from ten to five terms. Notice that

$$F_{00} \equiv F(0, 0) = \frac{-m_i^2}{2e_1 \cdot e_2}, \quad (5.43)$$

which can very easily be zero (every time a massless particle appears in the loop). In all other cases, because in equation (5.38) we noticed that $e_1 \cdot e_2 = K_1 \cdot K_2$ is always positive, F_{00} is a negative number. This means that we cannot simply sample five times with $(x_3, x_4) = (x_3, F_{00}/x_3)$, which will give coefficients inversely proportional to F_{00} again. Instead, we have to split again, sampling two times with x_3 and three times with x_4 or vice versa.

In the next step we have to choose x_1 nonzero. One possibility is to sample three times with $x_1 = 1$, but in order to discriminate between the coefficients of x_1 and x_1^2 , at least one additional time should be sampled with $x_1 = -1$. The three times should again be split in two times with x_4 and one time with x_3 . For the final coefficient one should have μ^2 nonzero, but now x_1 can be set to zero to reduce the complexity of the equation.

The whole procedure for the double cut is summarized in Table 5.3.

$\Delta(\mu^2, x_1)$	x_3	x_4
$\Delta(0, 0)$	3	2
$\Delta(0, 1)$	2	1
$\Delta(0, -1)$	1	0
$\Delta(\mu_s^2, 0)$	1	0

Table 5.3.: The number of samplings per polynomial at the normal rank double cut.

5.1.6. Single cut

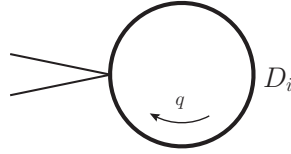


Figure 5.6.: A single cut.

At the single cut, we want to determine the coefficients in the expression of equation (4.132). Expanded in its basis this simply reads

$$\begin{aligned} \Delta_i(q, \mu^2) = & c_{1,0}^{(i)} + c_{1,1}^{(i)}(e_1 \cdot e_2)x_2 + c_{1,2}^{(i)}((e_1 \cdot e_2)x_1 \\ & - c_{1,3}^{(i)}(e_1 \cdot e_2)x_4 - c_{1,4}^{(i)}(e_1 \cdot e_2)x_3. \end{aligned} \quad (5.44)$$

The only cut,

$$D_i = 0, \quad (5.45)$$

imposes one condition on the components of \bar{q} .

Determining the sampling values

At this level there is just one overall relation between the five variables,

$$x_1x_2 - x_3x_4 = \frac{m_i^2 + \mu^2}{2e_1 \cdot e_2} \equiv G(\mu^2), \quad (5.46)$$

Determining the coefficients

Note that μ^2 is not present in the polynomial anymore at this level (and this rank). There are so few coefficients at this level that one can choose convenient values by hand, because a DFT-based sampling would not add anything. There are several ways to sample correctly, one possibility is listed in Table 5.4.

$\Delta(x_1, x_2, x_3, x_4)$
$\Delta(G, 1, 0, 0)$
$\Delta(-G, -1, 0, 0)$
$\Delta(G, 1, 1, 0)$
$\Delta(0, 1, -1, G)$
$\Delta(0, 1, 1, -G)$

Table 5.4.: One of the possible choices at the normal rank single cut.

5.2. Xsamurai: Higher rank integrand reduction

In renormalizable theories, the rank in q and μ^2 of the numerator of each residue cannot exceed the number of propagators. However, when one considers effective field theories, additional powers can appear. There are several more exotic models that cause higher-rank numerators to appear, such as models which feature a graviton. Particularly important for the following chapters will be the effective field theory which employs the large top mass limit in the Higgs boson production via gluon fusion (GF). In the plain Standard Model, only the fermionic propagator and the three-gluon vertex contribute one power of the loop momentum to the numerator of the integrand. All the other propagators and vertices have no momentum dependence in the numerator, as can be easily verified by looking at the Feynman rules collected in Appendix A. In the large top mass limit, however, the loop of the loop-induced Higgs boson production in GF is effectively shrunk to a new vertex. The Feynman rules that follow show that this effective vertex contributes two powers of the momentum to the rank of the numerator. This means that in this theory, the rank of the numerators, at every level, can exceed the number of propagators by exactly one,

$$r \leq n + 1. \quad (5.47)$$

This alters the decomposition of equation (4.112) which acquires additional terms,

$$\begin{aligned} \delta\mathcal{A}_n &= \sum_{(ijk)}^{n-1} c_{3,14}^{(ijk)} I_{ijk}[\mu^4] + \sum_{(ij)}^{n-1} \left\{ c_{2,13}^{(ij)} I_{ij}[\mu^2((q+p_i) \cdot e_2)^3] + c_{2,10}^{(ij)} I_{ij}[\mu^2((q+p_i) \cdot e_2)] \right\} \\ &+ \sum_i^{n-1} \left\{ c_{1,14}^{(i)} I_i[\mu^2] + c_{1,15}^{(i)} I_i[\mu^2((q+p_i) \cdot e_3)((q+p_i) \cdot e_4)] \right\}. \end{aligned} \quad (5.48)$$

These additional master integrals are given in Appendix B.1.1. The form of the residues in equation (4.116) has to be extended as well [85].

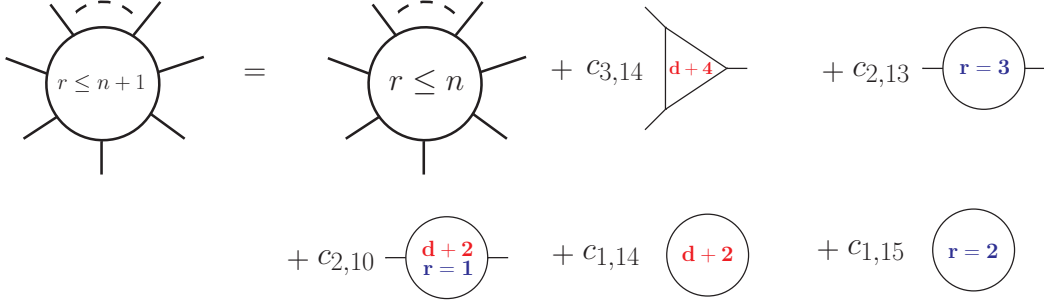


Figure 5.7.: Depiction of the decomposition of a generic integral with higher rank in a set of master integrals.

5.2.1. Parametric form of the higher-rank residues

To clearly distinguish between normal and higher-rank residues, we will use $\Delta_{ijk..}$ for the former and $\Lambda_{ijk..}$ for the latter. The final results are collected in Appendix D. Note that especially the additional lower-point contributions are numerous, which will warrant a more systematic sampling strategy at those levels.

Five-point contributions

At the five-point level, the numerator could now contain terms with μ^6 . However, for the same reason as before with 1 and μ^4 , these can be rewritten as a linear combination of the already existing μ^2 , which means nothing changes at higher rank,

$$\Lambda_{ijklm}(q, \mu^2) = \Delta_{ijklm}(q, \mu^2). \quad (5.49)$$

Four-point contributions

At the four-point level, terms up to rank five can appear. However, terms of higher power of $(q \cdot v_\perp)$ are still reducible, so there is only one new term in the higher-rank polynomial,

$$\Lambda_{ijkl}(q, \mu^2) = \Delta_{ijkl}(q, \mu^2) + c_{4,5}^{(ijkl)} \mu^4 (q + p_i) \cdot v_\perp. \quad (5.50)$$

Three-point contributions

At the three-point level, there are five new terms to the higher-rank residues,

$$\begin{aligned} \Lambda_{ijk}(q, \mu^2) = & \Delta_{ijk}(q, \mu^2) + c_{3,14}^{(ijk)} \mu^4 \\ & + c_{3,10}^{(ijk)} \mu^2 ((q + p_i) \cdot e_3)^2 \\ & + c_{3,11}^{(ijk)} \mu^2 ((q + p_i) \cdot e_4)^2 \\ & + c_{3,12}^{(ijk)} ((q + p_i) \cdot e_3)^4 \\ & + c_{3,13}^{(ijk)} ((q + p_i) \cdot e_4)^4. \end{aligned} \quad (5.51)$$

Two-point contributions

At the two-point level, because of all the cross product that are of rank three, the amount of terms increases massively from ten to twenty,

$$\begin{aligned}
 \Lambda_{ij}(q, \mu^2) &= \Delta_{ij}(q, \mu^2) \\
 &+ \mu^2 \left(c_{2,10}^{(ij)} (q + p_i) \cdot e_2 + c_{2,11}^{(ij)} (q + p_i) \cdot e_3 + c_{2,12}^{(ij)} (q + p_i) \cdot e_4 \right) \\
 &+ c_{2,13}^{(ij)} ((q + p_i) \cdot e_2)^3 + c_{2,14}^{(ij)} ((q + p_i) \cdot e_3)^3 + c_{2,15}^{(ij)} ((q + p_i) \cdot e_4)^3 \\
 &+ c_{2,16}^{(ij)} ((q + p_i) \cdot e_2)^2 ((q + p_i) \cdot e_3) \\
 &+ c_{2,17}^{(ij)} ((q + p_i) \cdot e_2)^2 ((q + p_i) \cdot e_4) \\
 &+ c_{2,18}^{(ij)} ((q + p_i) \cdot e_2) ((q + p_i) \cdot e_3)^2 \\
 &+ c_{2,19}^{(ij)} ((q + p_i) \cdot e_2) ((q + p_i) \cdot e_4)^2.
 \end{aligned} \tag{5.52}$$

One-point contributions

Finally, also at the one-point level the increase of terms in the higher-rank residues is enormous, with ten new coefficients to a total of fifteen. Note that for historical reasons, there is no $c_{1,9}^{(i)}$,

$$\begin{aligned}
 \Lambda_i(q, \mu^2) &= \Delta_i(q, \mu^2) + \\
 &+ c_{1,5}^{(i)} ((q + p_i) \cdot e_1)^2 + c_{1,6}^{(i)} ((q + p_i) \cdot e_2)^2 \\
 &+ c_{1,7}^{(i)} ((q + p_i) \cdot e_3)^2 + c_{1,8}^{(i)} ((q + p_i) \cdot e_4)^2 \\
 &+ c_{1,10}^{(i)} ((q + p_i) \cdot e_1) ((q + p_i) \cdot e_3) + c_{1,11}^{(i)} ((q + p_i) \cdot e_1) ((q + p_i) \cdot e_4) \\
 &+ c_{1,12}^{(i)} ((q + p_i) \cdot e_2) ((q + p_i) \cdot e_3) + c_{1,13}^{(i)} ((q + p_i) \cdot e_2) ((q + p_i) \cdot e_4) \\
 &+ c_{1,14}^{(i)} \mu^2 + c_{1,15}^{(i)} ((q + p_i) \cdot e_3) ((q + p_i) \cdot e_4).
 \end{aligned} \tag{5.53}$$

5.2.2. Quintuple and quadruple cut at higher rank

Since there are no new coefficients at higher rank for the quintuple cut, the way to acquire the one coefficient at this level remains unchanged.

At the quadruple cut, there is one new coefficient, which means we will have to sample one additional time. The obvious extension, sampling now also two times with $-\mu_s^2$, with both solutions q_{\pm} , gives an efficient way to obtain all six coefficients.

5.2.3. Triple cut at higher rank

Although the number of coefficients has increased considerable for the triple cut going to higher rank, the strategy to determine them remains essentially the same. According to the value of $C_0 \equiv C(\mu^2 = 0)$, one can use a DFT on the nine coefficients that do not multiply a power of μ^2 or has to split it in $5 + 4$ sampling with x_3 and x_4 . The remaining six coefficients

Quadruple cut	number of samplings
$\Lambda(0, q)$	2
$\Lambda(+\mu_s^2, q)$	2
$\Lambda(-\mu_s^2, q)$	2

Table 5.5.: The number of samplings per polynomial at the quadruple cut at higher rank.

cannot be determined in one DFT, since, for a fixed value $\mu^2 = \mu_s^2$, this would not be able to discriminate between the coefficients of μ^2 and μ^4 . Therefore, one final sampling at $\mu^2 = -\mu_s^2$ is necessary. The restriction that $C(\mu_s^2) \neq 0$ still applies.

Triple cut	$C = 0$	$C \neq 0$
$\Lambda(0, x_3, C/x_3)$	5	9
$\Lambda(0, C/x_4, x_4)$	4	0
$\Lambda(+\mu_s^2, x_3, C/x_3)$	-	5
$\Lambda(-\mu_s^2, 1, C)$	-	1

Table 5.6.: The number of samplings per polynomial at the triple cut at higher rank.

5.2.4. Double cut at higher rank

The extension to higher rank at the quintuple, quadruple and triple cut has been relatively straightforward. Although there were slightly more terms in the polynomial, the strategy to determine the coefficients did not change significantly. This is different at the lower two levels. The sheer number of coefficients at these levels demand that we search more stringently for options to reduce the number of coefficients to be determined simultaneously. Let us look more closely at equation (5.42), and write out the explicit x_1 dependence,

$$x_3x_4 = Ax_1^2 + Bx_1 + C(\mu^2) \equiv F(\mu^2, x_1), \quad (5.54)$$

which is a simple univariate quadratic function in x_1 with

$$A = \frac{-K_1^2}{2e_1 \cdot e_2} \quad (5.55)$$

$$B = \frac{m_j^2 - m_i^2 - K_1^2}{2e_1 \cdot e_2} \quad (5.56)$$

$$C(\mu^2) = -\frac{m_i^2 + \mu^2}{2e_1 \cdot e_2}. \quad (5.57)$$

Notice that these three semi-constants (it is probably preferable to avoid calling them coefficients) can in principle all be zero. Every combination of one, two or all three of them being zero simplifies the system considerably. It is therefore really beneficial for us to consider all of them, in a way similar to the treatment of C_0 at the triple cut, implementing all possibilities and building a branching structure around them. It is worth noting that rather than avoiding

$F = 0$, we are better off actually aiming at $F = 0$, since this will yield expressions for the coefficients that are smaller and numerically much more stable. We will therefore try to use solutions to (5.54) as sampling values. In order to compactify the description, from here on the phrase ‘sample $(n + m)$ ’ times will be an abbreviation of ‘Sample n times with x_3 and m times with x_4 using the DFT’.

First seven coefficients

Let us start again by putting $\mu^2 = x_1 = 0$, which reduces number of coefficients to be determined to seven. The value of A and B are now irrelevant and this puts us back in the situation we also had in the normal rank, which means our strategy will be the same. $F_{00} \equiv F(0, 0)$ can be zero or nonzero depending on the value of m_i^2 , and based on this we either sample $(7 + 0)$ times with x_3 or $(4 + 3)$ times with x_3 and x_4 .

Coefficients at $\mu^2 = 0$

Depending on A , B and C being zero or nonzero, and on the value of the discriminant $D = \sqrt{B^2 - 4AC}$ there could be zero, one, two or infinite nonzero solutions to equation (5.54). An overview is given in Table 5.7.

	number of nonzero solutions
$A = B = C = 0$	∞
$A = B = 0$	0
$A = C = 0$	0
$B = C = 0$	0
$A = 0$	1
$B = 0$	2
$C = 0$	1
all nonzero, $D > 0$	2
all nonzero, $D = 0$	1
all nonzero, $D < 0$	0

Table 5.7.: Number of nonzero solutions to equation (5.54) for all combinations of A , B and C being zero or nonzero.

If present, let us define the first (second) nonzero solution to $F(0, x_1) = 0$ as x_{1a} (x_{1b}). Here, and for later on, we also need to define random nonzero values y_1 , y_2 and y_3 . We cannot simply use one value for x_1 at this stage, because it would be impossible to distinguish all coefficients. Also, we need at least one sampling for which $F \neq 0$. Since there are nine new coefficients at this stage, we have to be careful that these first eight samplings should not be split into $(4 + 4)$, because this could lead to overlapping samplings when $F(0, x_1) = 1$, similar to the situation at the triple cut. The strategy at this point therefore is as follows: Sample x_1 at the first solution $(3 + 2)$ times, or if there is no nonzero solution $(5 + 0)$ times at a random value. Then sample x_1 at the second solution $(2 + 1)$ times or $(3 + 0)$ at a second random value if there is no second solution. Finally sample x_1 one time at a third random value, that is nonzero and not a solution of equation (5.54), with $(x_3, x_4) = (1, F)$.

This leads to the pseudo-code in Figure 5.8 to maximally use solutions to $F(0, x_1) = 0$.

```

if (A==B==C==0)
  x1s1 = y1
  Sample x1=x1s1 (3+2)
else if ( (A==B==0) or (A==C==0) or (B==C==0) or D<0 )
  Sample x1=y1 (5+0)
else
  if (A==0)
    x1s1 = -C/B
  else if (C==0)
    x1s1 = -B/A
  else
    x1s1 = (-B-sqrt(D))/(2A)
  Sample x1=x1s1 (3+2)

if (A==B==C==0)
  x1s2 = y2
  Sample x1=x1s2 (2+1)
else if ( (A==0) or (C==0) or (D<0) )
  Sample x1=y2 (3+0)
else
  x1s2 = (-B+sqrt(D))/(2A)
  Sample x1=x1s2 (2+1)

Sample x1=y3 (1+0)

```

Figure 5.8.: Pseudo-code for maximal use of the solutions to $F(0, x_1) = 0$. $x1s1$ ($x1s2$) is the first (second) solution of this equation, equivalent to x_a (x_b) in the text. $y1$, $y2$ and $y3$ are random nonzero values that are not solutions, corresponding to y_1 , y_2 and y_3 in the text. $(n+m)$ is an abbreviation for: Using the DFT, sample n times with x_3 and m times with x_4 .

Coefficients at nonzero μ^2

To get the remaining four coefficients, which are all multiplying terms containing μ^2 , there is one further simplification to reduce the size of the system of equations that need to be solved simultaneously. This is to give μ^2 a value μ_s^2 , but let one other variable be zero. Since setting either one of x_3 or x_4 to zero will make the value of the other irrelevant, and therefore less useful to sample with, the obvious choice is to set $x_1 = 0$ and sample three times. Naturally, we split again in $(2 + 1)$ if $F(\mu_s^2, 0) = 0$ and sample simply $(3 + 0)$ if $F(\mu_s^2, 0) \neq 0$. For the final disentanglement of all coefficient, the last sampling should be with all variables, *e.g.* $(\mu^2, x_1, x_3, x_4) = (\mu_s^2, 1, 1, F)$.

The whole procedure is summarized in Table 5.8.

	$F = 0$	$F \neq 0$
$\Lambda(0, 0, x_3, F/x_3)$	4	7
$\Lambda(0, 0, F/x_4, x_4)$	3	0
$\Lambda(0, x_{1a}, x_3, F/x_3)$	3	5
$\Lambda(0, x_{1a}, F/x_4, x_4)$	2	0
$\Lambda(0, x_{1b}, x_3, F/x_3)$	2	3
$\Lambda(0, x_{1b}, F/x_4, x_4)$	1	0
$\Lambda(0, x_{1c}, 1, F)$	1	1
$\Lambda(\mu_s^2, 0, x_3, F/x_3)$	2	3
$\Lambda(\mu_s^2, 0, F/x_4, x_4)$	1	0
$\Lambda(\mu_s^2, 1, 1, F)$	1	1

Table 5.8.: The number of samplings per polynomial at the double cut at higher rank. x_{1a} (x_{1b}) is the first (second) nonzero solution to $F(0, x_1) = 0$ if such a solution exists, and a random number otherwise. x_{1c} is always a random number.

5.2.5. Single cut at higher rank

At the single cut we can optimize in a similar fashion as at the double cut. $G(0)$ will be zero most of the time, but can also be nonzero when dealing with massive particles in the loop. Therefore, also here we have to implement both possibilities and branch in the code. If $G(0) = 0$, this has the nice advantage that we can set a whole range of variables to zero, which will dramatically reduce the complexity of the system we are trying to solve. If $G(0) \neq 0$, only a pair of variables can be set to zero, but then one can still apply a simple DFT. Hence, to acquire the first ten coefficients, we first set $x_3 = x_4 = 0$ and sample on x_1 and x_2 ($3 + 2$) times if $G = 0$ and ($5 + 0$) times otherwise. Then, symmetrically, we set $x_1 = x_2 = 0$ and sample with x_3 and x_4 either ($3 + 2$) or ($5 + 0$) times, again dependent on the value of G . For the next four coefficients, the ‘cross terms’ that multiply x_1 or x_2 with x_3 or x_4 , we first set $(x_3, x_4) = (1, 0)$ and sample with x_1 and x_2 either ($1 + 1$) or ($2 + 0$) times, then do the same with $(x_3, x_4) = (0, 1)$. Finally, we need a way to determine the coefficient multiplying μ^2 , so we set $\mu^2 = \mu_s^2$, and set $(x_1, x_2, x_3, x_4) = (0, 0, 0, 0)$ if $G(\mu_s^2) = 0$ or $(x_1, x_2, x_3, x_4) = (1, G, 0, 0)$ otherwise. The procedure for the single cut is summarized in Table 5.9.

5.2.6. Numerical considerations

Although this procedure works well algebraically, there is one caveat when one wants to implement it in a code, which is the selection on C , F and G at their respective levels being zero or nonzero. Numerically, this means that one needs to set a threshold, *e.g.* 10^{-10} , below which a number is considered a zero. The arbitrariness of the actual value of the threshold is of course an unwanted feature. Moreover, even if variables pass the threshold, the result can diverge if manipulated enough. For example, at the triple cut in the final expressions for the coefficients, a factor of $1/C^{20}$ is not uncommon. If C were 10^{-9} to begin with, it would have passed the threshold, but $1/C^{20}$ would be of the order 10^{-29} , which is far below the

	$G = 0$	$G \neq 0$
$\Lambda(0, x_1, G/x_1, 0, 0)$	3	5
$\Lambda(0, G/x_2, x_2, 0, 0)$	2	0
$\Lambda(0, 0, 0, x_3, G/x_3)$	3	5
$\Lambda(0, 0, 0, G/x_4, x_4)$	2	0
$\Lambda(0, x_1, -G/x_1, 1, 0)$	1	2
$\Lambda(0, -G/x_2, x_2, 1, 0)$	1	0
$\Lambda(0, x_1, -G/x_1, 0, 1)$	1	2
$\Lambda(0, -G/x_2, x_2, 0, 1)$	1	0
$\Lambda(\mu_s^2, 0, 0, 0, 0)$	1	0
$\Lambda(\mu_s^2, 1, G, 0, 0)$	0	1

Table 5.9.: The number of samplings per polynomial at the single cut at higher rank.

double precision (10^{-16}) most codes use for their variables. Fortunately, our treatment of the triple and double cut has been constructed to work as well as possible around these problems. In the single cut case, however, it has proven to be necessary to introduce an intermediate branch. Apart from the branches for $G = 0$ and $G \neq 0$, a new branch was implemented for $G \sim 0$, where $G \sim 0$ is defined as the absolute value of G being in the range $[10^{-10}, 10^{-1}]$. The sampling is done with G present as a variable, but it is executed as if G were zero, *i.e.* split into $(3 + 2)$ in the first step instead of $(5 + 0)$ etc.

5.2.7. XSAMURAI

The changes described above were implemented in SAMURAI. This extended version was therefore named XSAMURAI [12]. MATHEMATICA was used to perform the DFTs and solve the large system of equations. The expressions for the coefficients were written out to FORTRAN and put in SAMURAI. Also the selection of sampling values for \bar{q} and the combination with the master integrals had to be rewritten. Some additional master integrals were implemented using the expressions given in [86]. Several tests were performed to check the validity of XSAMURAI. A number of processes that are provided in SAMURAI as example processes were calculated with the same settings in SAMURAI and XSAMURAI. These processes included for example QED corrections to $\gamma\gamma \rightarrow \gamma\gamma$, with a fermion loop and massive and massless photons, and a hexagon with a tensor of arbitrary rank as numerator. The first comparison was to confirm that at normal rank all coefficients matched between the two codes, and that the higher-rank coefficients in XSAMURAI were reconstructed as numerically zero. Also all so called $\mathcal{N} = \mathcal{N}$ tests were performed. These tests, presented in [37, 87], exploit the fact that there are two representations of the numerator present in the code, namely the input numerator and the reconstructed numerator in terms of algebraic expressions involving the calculated coefficients. These test can be performed both at the level of a residue of every individual cut (the local $\mathcal{N} = \mathcal{N}$ -test) or at the level of the entire diagram (the global $\mathcal{N} = \mathcal{N}$ -test). Comparing the results of the $\mathcal{N} = \mathcal{N}$ -tests for normal rank processes between both codes also gave a good indication of the loss of precision due to the larger size of the systems of equations that

are needed to be solved simultaneously at higher rank. At higher rank, comparisons with SAMURAI were not possible, but the $\mathcal{N} = \mathcal{N}$ -tests could still be performed.

6 ■ Automation of one-loop calculations

In this chapter we will describe the automation of one-loop calculations, as implemented in the framework GOSAM. An overview of the code is given in Section 6.1 and a discussion on its stability and rescue system in Section 6.2. In Section 6.3, we will describe the interface of one-loop providers like GOSAM to Monte Carlo programs, which is necessary for full NLO calculations.

6.1. The GoSAM framework

The algorithm outlined in the previous chapter was constructed with the idea of automation in mind. The OPP method has been at the basis of various codes, for example CUTTOOLS [87]. The specific reduction method described in detail in Section 5.1 has been implemented in the code SAMURAI [37] and the extension to higher-rank presented in Section 5.2 in its extension XSAMURAI [12]. A different approach to one-loop calculations, via Passarino-Veltman reduction, was implemented in the code GOLEM95C [40–43]. Both codes required a framework around them to translate the physical processes to the integrands that are input to both reduction programs. Collaborating on this framework resulted in the PYTHON-based software package GOSAM [39], which is an open source package and uses open source third-party dependencies only. Furthermore, it has been constructed to work with all versions of the *Binoth-Les-Houches Accord* (BLHA) [8, 46], which allows interfacing to a large number of Monte Carlo Programs (MCs), and can therefore be used fairly easily to do full NLO calculations. This will be covered in Section 6.3. We will first assume one runs GOSAM as a standalone code.

6.1.1. Overview

A schematic workflow of GOSAM is depicted in Figure 6.1. After installing the code and all of its dependencies, the user can write a process card that defines the process in terms of incoming and outgoing particles and the perturbative order of the calculation. Additional options, such as filtering out certain diagrams or activating certain optimizations to be used, can be specified in the card as well. If the input card is called `process.in`, the generation of the code is invoked by typing

```
$ gosam.py process.in
```

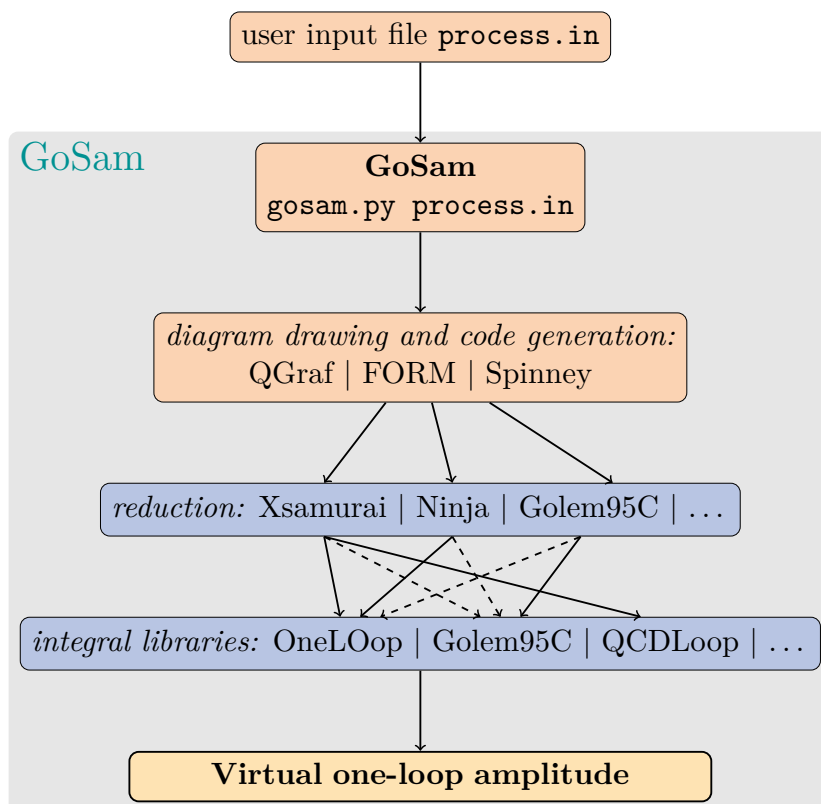


Figure 6.1.: The basic workflow of GoSAM. The user writes an input card `process.in`, on which the executable `gosam.py` is invoked. GoSAM will then start drawing the diagrams using QGRAF. FORM and/or HAGGIES are then used to generate and optimize the code. During run-time, any of the reduction programs XSAMURAI, NINJA or GOLEM95C can be used to reduce the integrands. Combined with the expressions for the integrals, using any of the integral libraries ONELOOP, QCDDLOOP or the ones present in GOLEM95C, this yields the result for the virtual one-loop amplitude. The modular setup of the code means it is relatively easy to include new reduction programs or integral libraries.

This will call QGRAF [88] to generate the diagrams of the process. After the files are created, typing

```
$ make source
```

will make FORM [89,90] generate the algebraic expressions for the amplitudes. In this step, SPINNEY [91] is used for the spinor algebra in FORM. In older versions of GoSAM, HAGGIES [92] was used for the code generation as well, but recently this has been replaced with features from FORM4 [90].

Finally, typing

```
$ make compile
```

will compile all the FORTRAN90 files. A simple example to illustrate this is given in Appendix E.

Diagram generation

Diagrams in GOSAM are generated by QGRAF. QGRAF has its own syntax of excluding diagrams that are unwanted. This includes options to specify or exclude the use of certain propagators or vertices and options to impose constraints on the allowed topologies, like excluding tadpole configurations. In GOSAM, these possibilities have been extended by an additional PYTHON-filter. A comprehensive list of all possibilities of diagram selection can be found in the manual.

Code generation

In preparation of the numerical evaluation of the numerators, first factors of μ^2 , as defined in (4.5), or dot-products involving the loop momentum q are separated from other factors. The remaining expressions are substituted by abbreviation symbols. These abbreviations are calculated only once for each phase space point.

Integral libraries

The evaluation of the Master Integrals that appear in expressions (4.112) can be delegated to external integral libraries. The integrand reduction programs of GOSAM can use the integral libraries ONELOOP [93] or QCDCLOOP [94]. Tensorial reconstruction using the libraries for the integrals already present in GOLEM95C is an alternative possibility. The higher-rank extension as given in expression (5.48) can also be used with these three programs. Because of the modular structure of the code, interfaces with other integral libraries, such as *e.g.* LOOPTOOLS [95,96], PJFRY [97] or COLLIER [98] should be relatively easy to implement.

6.1.2. Amplitudes convention

For this section we will assume that the user wants to calculate the QCD corrections to a process. The tree-level matrix element squared in GOSAM is given by

$$|\mathcal{M}|_{\text{tree}}^2 = \mathcal{A}_0^\dagger \mathcal{A}_0 = (g_s)^{2b} \cdot a_0, \quad (6.1)$$

with b being the number of QCD couplings at tree-level. The fully renormalized one-loop matrix element is then

$$\begin{aligned} |M|_{1\text{-loop}}^2 &= \mathcal{A}_1^\dagger \mathcal{A}_0 + \mathcal{A}_0^\dagger \mathcal{A}_1 = 2\Re[\mathcal{A}_0^\dagger \mathcal{A}_1] = |M|_{\text{bare}}^2 + |M|_{\text{ct},\delta m_Q}^2 + |M|_{\text{ct},\alpha_s}^2 + |M|_{\text{wf,g}}^2 + |M|_{\text{wf,Q}}^2 \\ &= \frac{\alpha_s(\mu^2)}{2\pi} \frac{(4\pi)^\epsilon}{\Gamma(1-\epsilon)} (g_s)^{2b} \cdot \left[c_0 + \frac{c_{-1}}{\epsilon} + \frac{c_{-2}}{\epsilon^2} + \mathcal{O}(\epsilon) \right], \end{aligned} \quad (6.2)$$

where the five terms are respectively the bare matrix element squared, the counterterms for the masses of the quarks and for the coupling, and the renormalization terms of the wave functions of the gluons and quarks. Calling the subroutine `samplitude` returns an array with $(a_0, c_0, c_{-1}, c_{-2})$. Averaging over initial state helicities and colors is part of the default setup. Calling the subroutine `ir_subtractions` returns an array with the IR poles, calculated from their universal behavior. This provides a way to check the accuracy of the result (see Section 6.2.1).

UV renormalization in QCD

GOSAM uses the $\overline{\text{MS}}$ -scheme for the massless quarks and gluons. For massive quarks, instead, subtraction at zero momentum is employed. QCD renormalization is performed automatically, EW renormalization at present still needs to be implemented by hand. The QCD mass counterterm is given by

$$\frac{\delta m}{m} = \frac{\alpha_s}{2\pi} \frac{(4\pi)^\epsilon}{\Gamma(1-\epsilon)} \frac{C_F}{2} \left(\frac{\mu^2}{m^2}\right)^\epsilon \left[\frac{3}{\epsilon} + 5 - 1_{\text{tHV}} \right], \quad (6.3)$$

where 1_{tHV} equals one in the 't Hooft-Veltman scheme (tHV) and zero in the dimensional reduction scheme (DRED). The renormalization of α_s is given by

$$|\mathcal{M}|_{\text{ct},\alpha_s}^2 = b \cdot \frac{\alpha_s}{2\pi} \frac{(4\pi)^\epsilon}{\Gamma(1-\epsilon)} |\mathcal{M}|_{\text{tree}}^2 \cdot \left[-\frac{\beta_0}{\epsilon} + \frac{2T_R}{3\epsilon} \sum_{q=n_f+1}^{n_f+n_{f,h}} \left(\frac{\mu^2}{m_q^2}\right)^\epsilon + \frac{C_A}{6}(1 - 1_{\text{tHV}}) \right], \quad (6.4)$$

with $\beta_0 = (11C_A - 4T_R n_f)/6$ (corresponding to $2\pi b$ as defined in equation (3.40)) and n_f and $n_{f,h}$ the number of light and heavy quarks respectively. The wave function renormalization of massive quark external lines is given by

$$|\mathcal{M}|_{\text{wf},Q}^2 = -\frac{\alpha_s}{2\pi} \frac{(4\pi)^\epsilon}{\Gamma(1-\epsilon)} \frac{C_F}{2} \sum_{Q(m) \in Q_h} \left(\frac{\mu^2}{m^2}\right)^\epsilon \left[\frac{3}{\epsilon} + 5 - 1_{\text{tHV}} \right] \cdot |\mathcal{M}|_{\text{tree}}^2, \quad (6.5)$$

where Q_h is the set of external massive quark lines. The wave function of the gluons is affected by the availability of closed fermion loops of heavy quarks. Denoting the number of external gluon lines by N_g , we can write this contribution as

$$|\mathcal{M}|_{\text{wf},g}^2 = -\frac{\alpha_s}{2\pi} \frac{(4\pi)^\epsilon}{\Gamma(1-\epsilon)} N_g \frac{2T_R}{3\epsilon} \sum_{q=n_f+1}^{n_f+n_{f,h}} \left(\frac{\mu^2}{m_q^2}\right) \cdot |\mathcal{M}|_{\text{tree}}^2. \quad (6.6)$$

The user can switch on or off parts of the renormalization with several keywords defined in the configuration module file. These keywords can also be specified in the card used to generate the process. The keyword `renormalisation` can be set to 0, 1 or 2. `renormalisation=0` switches off the renormalization and none of the counterterms are present. `renormalisation=2` only includes $|\mathcal{M}|_{\text{ct},\delta m,Q}^2$, which is the counterterm coming from the terms in the form of (6.3). `renormalisation=1` allows for more detailed control of the renormalization, in which every term can be switched on or off independently, using the following keywords:

`renorm_logs` set to `false` disables the generation of logarithms in all counterterms.

`renorm_beta` set to `false` sets the term $|\mathcal{M}|_{\text{ct},\alpha_s}^2$ to zero.

`renorm_mqwf` set to `false` sets the term $|\mathcal{M}|_{\text{wf},Q}^2$ to zero.

`renorm_mqse` set to `false` sets the term $|\mathcal{M}|_{\text{ct},\delta m_Q}^2$ to zero.

`renorm_decoupling` set to `false` sets the term $|\mathcal{M}|_{\text{wf},g}^2$ to zero.

By default, `renormalisation` is set to 1 and all keywords listed above are set to `true`.

6.1.3. Integrand reduction programs

In GOSAM there is a choice of three integrand reduction programs. Since the release of GOSAM2.0, all of them support higher rank as well.

XSAMURAI

The original release of SAMURAI [37] was the implementation of the integrand reduction algorithm as described in Section 5.1. XSAMURAI [12] is an implementation of the extension of SAMURAI to higher rank as described in Section 5.2. In the latest release of the package, the code has at every cut-level n an implementation for a numerator of a rank in the range $0 < r \leq (n + 1)$, and switches automatically to the right branch according to the value of the rank of the current numerator being processed. This makes sure no coefficients are calculated which are known to be algebraically zero, thereby leading to a considerable increase in speed and accuracy of the code.

GOLEM95

GOLEM95C [40–43] employs tensorial reconstruction in the traditional Passarino-Veltman reduction approach. Tensorial reconstruction is a relative time-consuming process, but is in general numerically more stable than the other reduction programs. Hence GOLEM95C is used in GOSAM primarily as a rescue program, meaning it will recalculate results for phase space points for which there is reason to doubt their stability. The rescue system is explained in more detail in Section 6.2.

NINJA

In [84, 99], the method presented in Chapter 5 has been refined. It was realized that one can obtain the residues more efficiently through the use of multivariate polynomial division and algebraic geometry. The idea of these novel methods, originally presented in [80, 100] and elaborated in [85], is to extract the coefficients in the d -dimensional integrand-reduction by performing a *Laurent expansion* of the integrand. When the multiple-cut conditions are not fully constraining the loop momentum, the solutions are functions of free parameters. They can, for example, depend on the components of momentum. In the method Chapter 5, the general strategy is to sample with the parameters and solve system of equations. However, one first always needs to subtract the contributions from higher-point residues. Instead, in [85], it

is proposed to perform a Laurent expansion in one of the free parameters. Since the integrand and subtraction terms have the same polynomial behavior of the residue in the asymptotic limit, the contributions of subtraction terms are corrections at the coefficient level rather than integrand level. This causes the system of equations to become diagonal rather than triangular, which means a massive reduction in number of coefficients present in every subtracted term. In particular, boxes and pentagons are separated from the other levels entirely.

This method of integrand-reduction via Laurent expansion has been implemented in a semi-numerical way in the C++ library NINJA [44,45], and interfaced to the GOSAM framework [2] for the evaluation of virtual one-loop scattering amplitudes. Tests show a large improvement in numerical accuracy and computing speed. Also NINJA uses external integral libraries to calculate the Master Integrals which are multiplied with the calculated coefficients to get the integrated result. It can switch between different libraries at run-time and there are interfaces available with ONELoop [93,101], which is the default, and LOOPTOOLS [95,96]. NINJA is also capable of computing integrals with higher rank, *i.e.* with $r \leq n + 1$ in the terminology of Section 5.2. In the interface between GOSAM and NINJA, GOSAM provides the analytic expressions for the integrands of one-loop diagrams, which are required to adapt the algebraic manipulation of the integrands.

6.1.4. GoSAM-2.0

In the first years after its release, GOSAM has been used to calculate a wide variety of processes [3–5,102–111]. Many of these processes pushed the limits in terms of final state multiplicity or number of NLO diagrams to be calculated. This triggered the need for improvement of the code on several fronts. Version 2.0 of GOSAM [1] collected all these improvements. The resulting code shows considerable improvement in speed, both in the generation of the code and in the evaluation of the amplitudes. The generated code is written in a more compact way and has proven to give a more stable numerical evaluation. The code can now deal with effective theories and BSM physics. Several more improvements will be discussed below.

Code generation improvements

In the original version of GOSAM, HAGGIES was used to write the FORTRAN code for the amplitudes. In GOSAM2.0, this functionality has been replaced for a substantial part with the features provided by FORM4 [90], which produces more compact code. This speeds up the evaluation of the amplitudes by roughly a factor ten.

Numerical polarization vectors

By default, for massless gauge bosons (photons and gluons), numerical polarization vectors are used. This means that the helicity configurations for these particles are evaluated numerically, using a code with generic polarization vectors, instead of writing separate code for each helicity configuration. Writing `polvec=explicit` in the input card switches off this feature, which can be useful to manually choose the reference vectors for each helicity configuration or to check Ward identities.

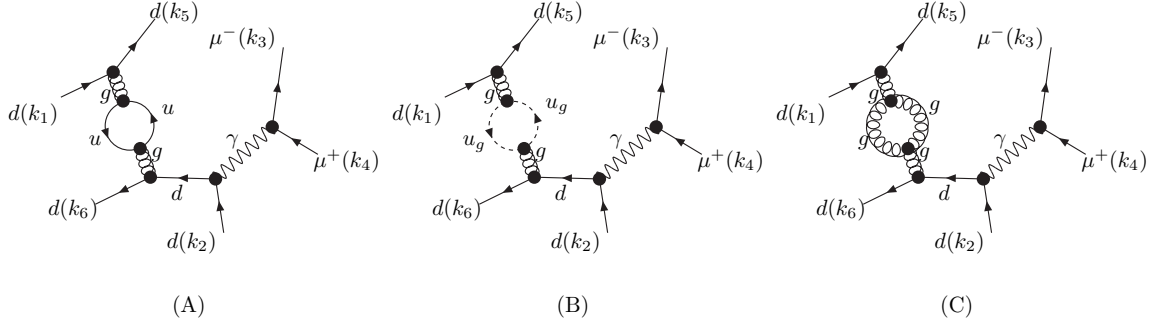


Figure 6.3.: These three diagrams are summed when the `diagsum` option is set to `diagsum=true`, because they share a common loop propagator with a different particle inside the loop.

Electroweak scheme choice

For the regularization and renormalization in the Standard Model, there are several electroweak parameters of which only three are independent. This leads to different possible electroweak scheme choices, which choose which three of those parameters are input and which two are calculated. There is not a unique scheme highly favored by the community, and this means that GOSAM should be able to switch easily between the EW schemes, to compare with other calculations or to interface to Monte Carlo programs. By default GOSAM uses the mass of the W and the Z bosons (M_W and M_Z) and the elementary charge e or the fine-structure constant $\alpha = e^2/4\pi$ as input parameters, but there are eight other possibilities implemented, which can be activated in the input card through the variable `ewchoice`. They are given in Table 6.1. The relations between the parameters can be found in Section 3.1.

<code>ewchoice</code>	input parameters	derived parameters
1	G_F, M_W, M_Z	e, sw
2	α, M_W, M_Z	e, sw
3	α, sw, M_Z	e, M_W
4	α, sw, G_F	e, M_W
5	α, G_F, M_Z	e, M_W, sw
6	e, M_W, M_Z	sw
7	e, sw, M_Z	M_W
8	e, sw, G_F	M_W, M_Z

Table 6.1.: Possible choices to select the electroweak scheme. `sw` is an abbreviation for the sine of the weak mixing angle. Of course, when one sets `e` to one in the card, the last three options are not possible.

Complex masses

Unstable fermions and gauge bosons can be treated by introducing a corresponding decay width. The complex mass scheme described in [112] is a consistent way to treat the resulting

complex W and Z -boson masses. In this scheme, the boson masses are shifted in the complex plane,

$$m_V^2 \rightarrow \mu_V^2 = m_V^2 - im_V \Gamma_V, \quad V = W, Z. \quad (6.7)$$

The definition of the weak mixing angle has to be modified as well to obey gauge invariance,

$$\cos^2 \theta_W = \frac{\mu_W^2}{\mu_Z^2}. \quad (6.8)$$

Both GOSAM and the integral libraries it uses are capable of using complex masses. Two new model files were introduced for this, named `sm_complex` for a model with a full CKM matrix and `smdiag_complex` for a model with a diagonal CKM matrix.

6.2. Stability test and rescue system

It is important to have reliable techniques to assess the accuracy of the final results of GOSAM. In particular, we want to determine in a regularized way, for every phase space point (PSP), the precision of the finite part and the IR poles. The general approach in GOSAM is to check the accuracy of every PSP and if this is below a certain threshold, either discard the point or repeat the evaluation with a different reduction program. This procedure is known as a *rescue system*.

6.2.1. Precision tests

There are several ways to detect low precision on a PSP that are implemented in various automated tools for the calculation of one-loop diagrams.

pole test

A commonly used method to quickly assess the precision of a PSP is to compare the computed infrared pole coefficients with their known analytic values, which are given by the universal behavior of infrared singularities [113]. The calculation of the analytic values takes negligible additional time, so this evaluation of the precision basically comes for free. It will, however, in general give an overestimation of the precision, because not all diagrams that take part in the calculation actually contribute to the poles. The actual accuracy of the finite part will therefore in general be lower than the ones of the poles.

scaling test

The scaling properties of the scattering amplitude under a transformation of multiplying all physical scales (the momenta, the masses and the renormalization scale) with the same factor can be used to test the precision. Using dimensional analysis on equation (2.4) shows the

scaling property of the matrix element. For an n -point amplitude, multiplying all physical scales with a factor x gives

$$|\mathcal{M}(xk_i, x\mu_i, xm_i)|^2 = x^{2(4-n)} |\mathcal{M}(k_i, \mu_i, m_i)|^2. \quad (6.9)$$

In [114] it was shown that comparing the results of the evaluation with the original scales and with the rescaled ones gives an estimation of the precision which shows a very good correlation with the actual precision of the finite parts.

rotation test

Scattering amplitudes are invariant under azimuthal rotation of the final state around the beam axis, the direction of the incoming particles. Comparing the evaluation with the original vectors and the evaluation with the rotated vectors gives another estimate of the precision in integrand reduction methods. Notice that this kind of a rotation leaves the initial states invariant, as well as the relative positions of the final state particles. It does however lead to different bases of the parametrization of the residues and different coefficients that multiply the master integrals. The numerical values of the computed master integrals will also differ. This technique was validated in [2] and discussed in more detail in Section 6.2.2.

$\mathcal{N} = \mathcal{N}$ tests

Within integrand-reduction based codes, an additional type of tests, performed on the numerator before integration, known as $\mathcal{N} = \mathcal{N}$ tests, has been presented in [37, 87], see Section 5.2.7 for more details. This technique, however, works at the level of an individual diagram instead of on the full result. Using this method as rescue system is therefore not practical.

While the *scaling* and the *rotation test* provide a more reliable estimate of the precision of the finite parts that enter in the phase space integration, their downside is that they require two evaluations of the same matrix element, therefore leading to a doubling in the computation time.

6.2.2. Rescue system in GoSAM

As argued before, performing the pole test does not increase the computation measurably, but the test will overestimate the precision. The scaling and rotation tests provide a more reliable estimate of the accuracy of the finite part, but they effectively double the computation time. In GoSAM, therefore, a hybrid method is implemented which features three thresholds: P_{low} , P_{high} and P_{fin} . After the computation of the matrix elements, GoSAM checks the precision δ_{pole} , defined as

$$\delta_{pole} = \left| \frac{\mathcal{S}_{IR} - \mathcal{S}}{\mathcal{S}_{IR}} \right|, \quad (6.10)$$

where \mathcal{S} is the single pole provided by GoSAM and \mathcal{S}_{IR} is the single pole known from the universal behavior of infrared singularities. From this the precision of the single pole is calculated through

$$P_{pole} = -\log_{10}(\delta_{pole}), \quad (6.11)$$

which is a representation of the precision that corresponds to the intuitive way of counting agreeing digits. GOSAM then compares this number with two of the thresholds. If $P_{pole} \geq P_{high}$ the point is accepted without further tests. The threshold P_{high} needs to be set to such a high number that passing this selection indeed means that it is very unlikely that the finite part is bad. If $P_{pole} \leq P_{low}$ the point is discarded or sent to the rescue system if present. The idea behind this is that if the pole already shows a low precision, it is very likely the finite part is equally bad or worse. In the intermediate region $P_{low} < P_{pole} < P_{high}$, the estimated precision on the pole coefficients is not enough to confidently declare a point good or bad. Only on this class of points a recalculation of the point using the rotation test is performed. Defining the finite part evaluated before and after the rotation as A^{fin} and A_{rot}^{fin} respectively, the error δ_{rot} estimated with the rotation is defined as

$$\delta_{rot} = 2 \left| \frac{A_{rot}^{\text{fin}} - A^{\text{fin}}}{A_{rot}^{\text{fin}} + A^{\text{fin}}} \right|. \quad (6.12)$$

Notice that we now do not have an absolute reference of the correct result, like before with S_{IR} for the poles. The best we can do now is compare the difference of the two finite parts with their average. In a similar fashion as before, the precision of the rotation test is defined as

$$P_{rot} = -\log_{10}(\delta_{rot}). \quad (6.13)$$

In [2] and here in Section 6.2.3 it is shown that P_{rot} gives a reliable estimate of the precision of the finite part. The point is then accepted if $P_{rot} > P_{fin}$ and discarded otherwise. The values of the three thresholds P_{high} , P_{low} and P_{fin} can be set by the user, either in the input card or even after the code has generated. In the input card, P_{high} , P_{low} and P_{fin} correspond to PSP_chk_th1, PSP_chk_th2 and PSP_chk_th3 respectively. Note that the rotation test can be bypassed altogether by equating the two initial thresholds $P_{low} = P_{high}$, which will cause the code to only use the pole test for the evaluation of the precision and the selection of points.

6.2.3. Precision tests on massive high-multiplicity processes

To assess the precision of the GOSAM2.0 framework, in [2], several five-, six- and seven-point processes were tested. Here the rotation test as discussed before was employed to estimate the precision on the finite part. In order to know if the rotation test indeed gives a reasonable estimate of the precision, the process $u\bar{d} \rightarrow Wb\bar{b}g$ with massive bottom quarks, a non-trivial process, was generated twice: one copy in the standard double precision and one copy in quadruple precision. Then 10^4 points for this process were generated and evaluated with both codes, which will be denoted here as A and A_{quad} respectively. The process was also evaluated in double precision after rotating the phase space point, whose result we will denote here as A_{rot} . The exact error was defined δ_{ex} as

$$\delta_{ex} = \left| \frac{A_{quad} - A}{A_{quad}} \right|, \quad (6.14)$$

and the estimated error δ_{rot} as

$$\delta_{rot} = 2 \left| \frac{A_{rot} - A}{A_{rot} + A} \right|. \quad (6.15)$$

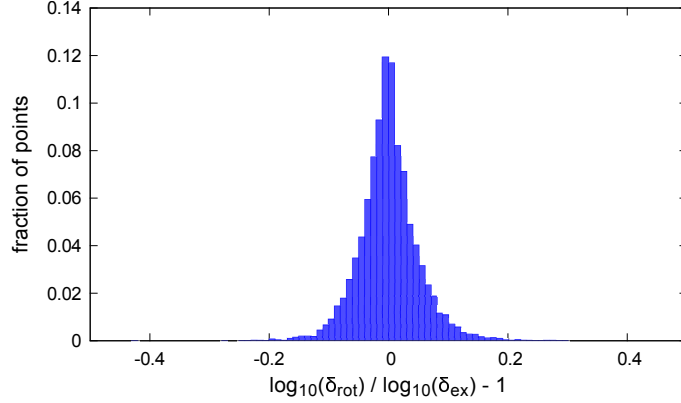


Figure 6.4.: Correlation plot based on 10^4 points for the process $u\bar{d} \rightarrow Wb\bar{b}g$ with massive bottom quarks.

These two can be used to construct an expression for the correlation,

$$\mathcal{C} = \frac{\log_{10}(\delta_{rot})}{\log_{10}(\delta_{ex})} - 1. \quad (6.16)$$

The distribution of this quantity is plotted in Figure 6.4. There are two features of this plot that are worth noting. Firstly, if the rotation test would be a perfect way of estimating the precision, the value of \mathcal{C} would be zero every time. Notice that by taking the logarithm in equation (6.16), the plot shows roughly the number of agreeing digits. The fact that there are hardly any points outside the range $[-0.2, 0.2]$, means that the rotation in general estimates the number of agreeing digits correctly within an error of far less than one digit. Secondly, the plot is very symmetrical around zero. This means that the rotation test is equally overestimating and underestimating the precision of the results.

Let us define the precision of the finite part as $P_0 = \log_{10}(\delta_0)$, with δ_0 defined by equation (6.12). Using equation (6.10) for the single and double poles and with the known expressions for the IR poles instead of the results in quadruple precision, we can similarly define $P_{-1} = \log_{10}(\delta_{-1})$ and $P_{-2} = \log_{10}(\delta_{-2})$ as the precisions of the single and double pole.

In Figures 6.5, the distributions of P_0 , P_{-1} and P_{-2} are plotted for two challenging processes, $u\bar{u} \rightarrow Hu\bar{u}gg$ ($Hjjjj$) in VBF (see Section 7.1) and $gg \rightarrow t\bar{t}Hg$ ($t\bar{t}Hj$, see Section 7.3) respectively. These two plots were produced using $1 \cdot 10^5$ and $5 \cdot 10^4$ phase space points respectively, without cuts in the selection of the points. The points were generated using RAMBO, which is an algorithm that provides points randomly distributed over the entire available phase space of the final state particles. Now a threshold like in Section 6.2 can be set to have a rejection criterion above which a point is considered bad. This threshold is of course very process dependent and one should consider the actual phenomenological analysis when setting it. Table 6.2 specifies the percentage of points with a precision that fails this rejection criterion, for different values of this threshold and for the two processes shown.

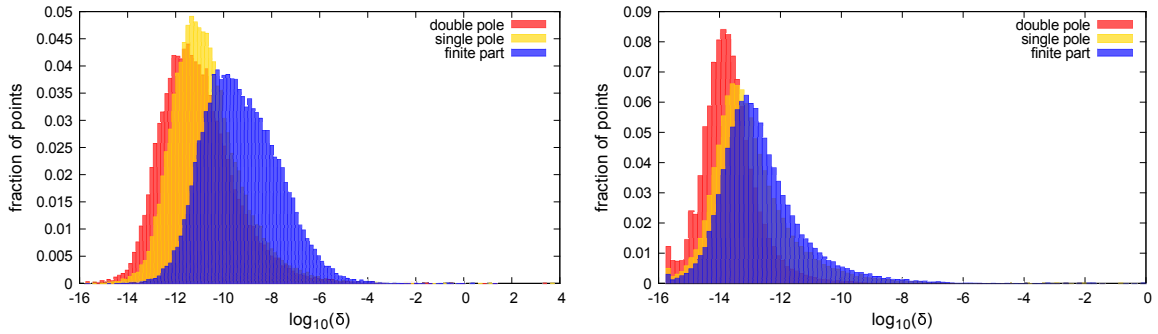


Figure 6.5.: Precision plots for $gg \rightarrow t\bar{t}Hg$ (left) and for $u\bar{u} \rightarrow Hu\bar{u}gg$ in VBF (right) the distributions are obtained using respectively $5 \cdot 10^4$ and 10^5 randomly distributed phase space points.

P_0	$u\bar{u} \rightarrow Hu\bar{u}gg$	$gg \rightarrow t\bar{t}Hg$
-3	0.02%	0.06%
-4	0.04%	0.16%
-5	0.08%	0.56%

Table 6.2.: Percentage of bad points as a function of the rejection threshold P_0 for the two subprocesses mentioned in the text.

Example processes

The GOSAM+NINJA interface was used to compute a large number of non-trivial processes, with six, seven or even eight external particles. The processes to test were selected to have massive particles running in the loop or as final state particles. Among these processes there were four for which the virtual NLO QCD contributions had not been calculated before. These were the processes $pp \rightarrow Wb\bar{b} + n$ jets ($n = 1, 2$), $pp \rightarrow Zb\bar{b}j$, $pp \rightarrow Zt\bar{t}j$, $pp \rightarrow VVVj$ (with $V = W, Z$), $pp \rightarrow ZZZZ$, and $pp \rightarrow H + n$ jets ($n = 4, 5$) in VBF. If the bottom quark was present in the final state, it was considered massive. The details of all these processes can be found in the appendices of [2]. In Appendix F.3, the processes $pp \rightarrow t\bar{t}e^+e^-$ and $pp \rightarrow t\bar{t}e^+e^-j$ are presented in more detail as an example.

6.3. Binoth Les Houches Accord

GOSAM, as introduced in the previous section, is one of many programs dedicated to the calculation of one-loop diagrams. Other programs might choose a less automated generic approach and instead focus on the optimization of a specific process. For example, the program NJET [115] is a library for the evaluation of one-loop virtual corrections to the production of multi-jet final states in massless QCD. Also on the side of the Monte Carlo programs (MCs), there are numerous options. In recent years one could witness a lot of activity in calculations using SHERPA [26], the MADGRAPH framework [116] and AMC@NLO [117] (recently merged in MADGRAPH5_AMC@NLO [47], see Chapter 8), POWHEG [118], HERWIG [119] and PYTHIA8

[120]. With increasingly difficult processes to compute, the need for the ability of combining MCs with so-called One-Loop-Providers (OLPs) like GOSAM quickly rose as well. In [46] a standardized interface between MCs and OLPs was proposed under the name *Binoth-Les-Houches Accord* (BLHA). This first version of the BLHA is still used for some processes. It is often referred to as BLHA1 and will be discussed in Section 6.3.1. Recently, an update of the interface has been presented in [8]. The changes in this new version (BLHA2) with respect to the first one will be discussed in Section 6.3.2.

6.3.1. BLHA1

The original version of the BLHA proposed a standardized way for the OLPs and the MCs to interact. It noted that the interface should not limit the OLP in any way, but at the same time it should try to shield the internal working of the OLP for the MCs as much as possible. It divided the interface in two steps: The initialization phase and the run-time phase. The purpose of the initialization phase was to communicate the basic information to the OLP. Minimal requirements at this step are to specify the partonic subprocesses, certain input parameters and to fix some basic options. In the run-time phase then, the OLP would be called to provide phase space point dependent values. This includes the one-loop contribution plus additional information.

Initialization phase

In the initialization phase the MC starts by writing out a file named *order file*. This contains information about the subprocesses and is processed by the OLP, which then writes a *contract file* in response.

order file

The order file can contain a number of flags. We will go through the most important ones here.

- `MatrixElementSquaredType` specifies whether the returned matrix elements are color (C) or helicity (H) (or both or neither) summed or averaged through keywords like `CHsummed`, `Csummed` `Hsummed`, `NOTsummed` or `CHaveraged` etc.
- The flag `CorrectionType` specifies what type of NLO calculation is being performed; options are QCD, EW or QED.
- The flags `AlphasPower` and `AlphaPower` specify the powers of α_s and α of the process.
- The flag `IRregularisation` specifies which regularization scheme is used for the treatment of IR divergences. Often used keywords here are CDR, DRED and tHV. Notice that it is assumed that the OLP produces output that is UV renormalized. Also, the BLHA suggest to use natural numbers $\hbar = c = 1$ and to use as standard the unit *GeV*.

- Not all OLPs evaluate the couplings, because it can be useful to provide only the kinematic information. The flag `OperationMode` specifies whether this is the case through the keyword `CouplingsStrippedOff`. The MC then has to take care of the multiplication with the correct powers of α_s and α .
- Comments are written with a #.
- At the end of the file the requested subprocesses are listed, using the format

```
[PDGcode1] [PDGcode2] -> [PDGcode3] ... [PDGcodeN]
```

for a $2 \rightarrow N - 2$ process, where `PDGcode` uses the standard numbering from the Particle Data Group. The most frequently used numbers are given in Table 6.3. Anti-particles are given by corresponding negative number, *i.e.* -1 is a \bar{d} , -11 is a e^+ , -24 is a W^- etc. The full list is much longer than the summary given in Table 6.3, because it also encodes several other theories beyond the Standard Model, and also includes all composite particles (mesons and baryons etc.), that are used in hadronization codes.

quarks	leptons	bosons	other
d 1	e^- 11	g 21	p (proton) 2212
u 2	ν_e 12	γ 22	n (neutron) 2112
s 3	μ^- 13	Z 23	j (jet) 93
c 4	ν_μ 14	W^+ 24	
b 5	τ^- 15	H 25	
t 6	ν_τ 16		

Table 6.3.: The most often used Particle Data Group codes (PDG codes). Anti-particles are given by the corresponding negative number. Note that particle 25 is the Standard Model Higgs boson, several other numbers exist to code Beyond the Standard Model particles, including supersymmetric Higgs particles. Numbers 81 – 100 are reserved for internal MC use, so 93 for a jet, as in SHERPA, might not be true everywhere.

contract file

In the contract file the OLP writes basically a copy of the order file, with its response attached at the end of each line. The response is separated from the flag and keywords by a |. If there are no problems, the OLP responds simply with `OK`. Otherwise, it writes `Error`, followed by an explanation of the error, for example: `Error: file not found`. The response for the list of subprocesses is an integer label.

run-time phase

At run-time, some OLPs need to be reminded of the contract file. This is done through a function `OLP_Start(string, integer)`, which takes as arguments the filename of the contract file and returns an integer that indicates success with the value 1. After this, the evaluation of the subprocesses is called through the function `OLP_EvalSubProcess(...)` which takes the following arguments:

- The integer label of the subprocess.
- A one-dimensional array of the momenta of the external particles, with the format $(E_i, p_i^x, p_i^y, p_i^z, m_i)$ for all particles i .
- The renormalization scale μ_R .
- The value of $\alpha_s(\mu_R)$ or an array `parameters` with $\alpha_s(\mu_R)$ as its first entry this value. The latter was chosen for GOSAM.
- An array to be filled with the results, with the format $(c_{-2}, c_{-1}, c_0, a_0)$.

where c_{-2}, c_{-1}, c_0 and a_0 are the double pole, single pole, finite part and Born amplitude squared, as defined in (6.2) and (6.1), respectively.

6.3.2. BLHA2

The update of the BLHA known as BLHA2 [8] is not backwards compatible. Since there are still numerous interfaces that work with BLHA1, the first new flag introduced in BLHA2 is `InterfaceVersion` which can be either BLHA1 or BLHA2. The function `OLP_Start` already present in BLHA1 is still there, but the initialization phase has been extended with a new function, `OLP_Info(olp_name, olp_version, message)`, that takes as argument the name of the OLP and its version and returns a message that enumerates the publications that need to be cited when using this OLP.

An important new function is `OLP_SetParameter(para, re, im, ierr)`, which can be used both to define static parameters at the start once and for all, or to define dynamic parameters at run-time. It takes a string for the name of the parameter to be set, followed by two doubles to allow for complex parameters. The return value `ierr` is defined to indicate success when it equals one and failure when it equals zero. If it is equal to two this means that the parameter is unknown or the setting is ignored, but that the code will proceed anyway. The function `OLP_PrintParameter(filename)` prints out the current parameter settings to a file specified in the argument. The output format is `parameter_name value state`, where `value` can be a complex number in the (a, b) notation for a complex number $a + ib$. `state` is optional to distinguish whether the parameter was set by `OLP_SetParameter` or defined internally.

The function calling for the evaluation of the subprocesses has changed significantly. To avoid confusion with the function `OLP_EvalSubProcess` in BLHA1, its updated version in BLHA2 has had its name extended to `OLP_EvalSubProcess2`. The function takes five arguments: `OLP_EvalSubProcess2(i, pp, mu, rval, acc)`. The first three arguments are unchanged with respect to the previous version: an integer label to indicate the subprocess, a one-dimensional array for the momenta and masses of all particles involved, and the renormalization scale. The coupling constants, however, are left out because those can now be set using `OLP_SetParameter`. The fourth argument are the return values in the same format as before. The last argument states the accuracy as estimated by the OLP. This can be either a fractional accuracy in double precision or a binary check result, where zero means simply it passed the check and a large number means it failed. An overview of the BLHA2 is given in Figure 6.3.2.

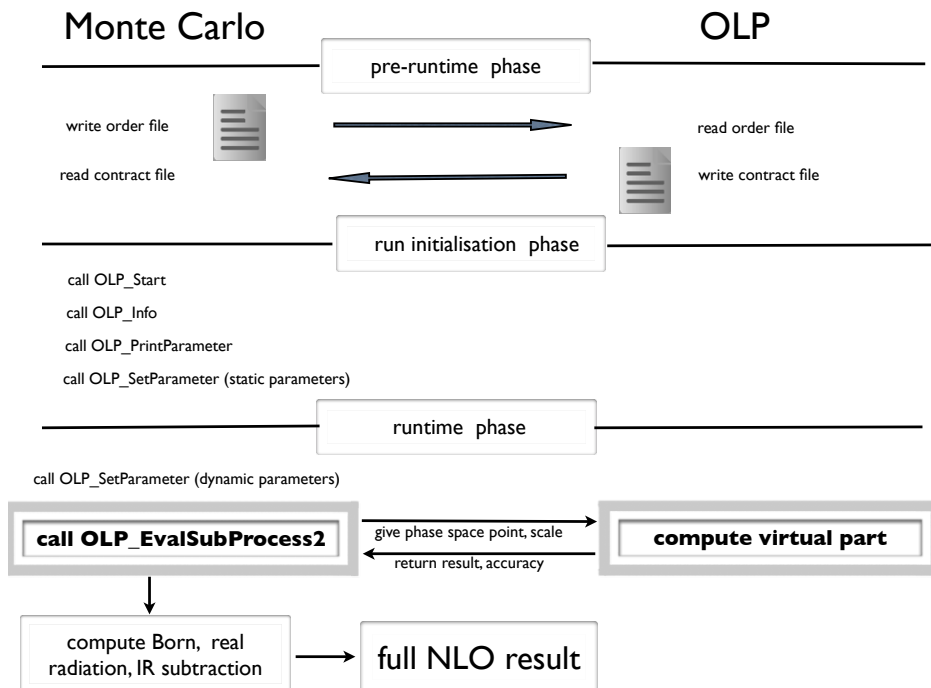


Figure 6.6.: The flowchart of BLHA2. The MC first writes an order file with the calculation requirements that is read and processed by the OLP. The OLP then writes a contract file as a confirmation. The MC then goes through an initialization phase in which the static parameters are fixed. During run-time the MC can still set dynamic parameters. The MC provides the OLP with a phase space point and a scale for a certain subprocess, for which the OLP returns the result and accuracy. The Born can be calculated by either the MC or the OLP. The MC takes care of the real radiation contributions and the IR subtraction.

7 ■ Higgs boson phenomenology

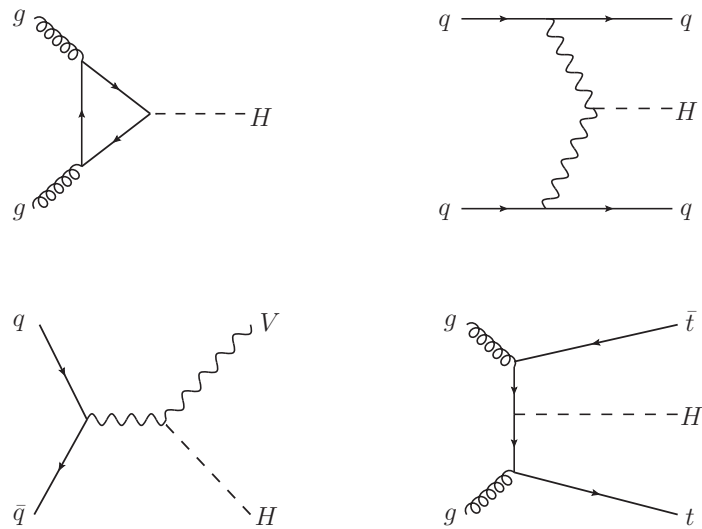


Figure 7.1.: The four most important Higgs boson channels. At the top gluon fusion (left) and vector boson fusion (right). At the bottom HV production (left) and $t\bar{t}H$ production (right).

There are four important channels to produce a Higgs boson at the LHC. The most important one is Higgs boson production in *gluon fusion* (GF), in which two gluons produce a Higgs boson via a top loop. Important for measuring the couplings to the other electroweak gauge bosons are the production in *vector boson fusion* (VBF), to which Higgs boson production in association with jets in GF is an obvious background, and Higgs boson production in association with a vector boson (*HV production*), also known as *Higgsstrahlung*. An important channel to directly measure the Yukawa couplings is Higgs boson production in association with a top anti-top pair ($t\bar{t}H$). These four channels are depicted in Figure 7.1. Their cross sections at highest known order as a function of the center-of-mass energy are given on the left of Figure 7.2.

The Higgs particle is of course very short-lived and decays well before direct detection would be possible. It decays predominantly into the heaviest pair of particles that is kinematically available. On the right of Figure 7.2, the branching ratios are given for a range of values for the Higgs boson mass around 125 GeV. From this figure, it is clear that most of the time a Higgs particle will decay into a $b\bar{b}$ pair, but other decay channels might be easier to detect.

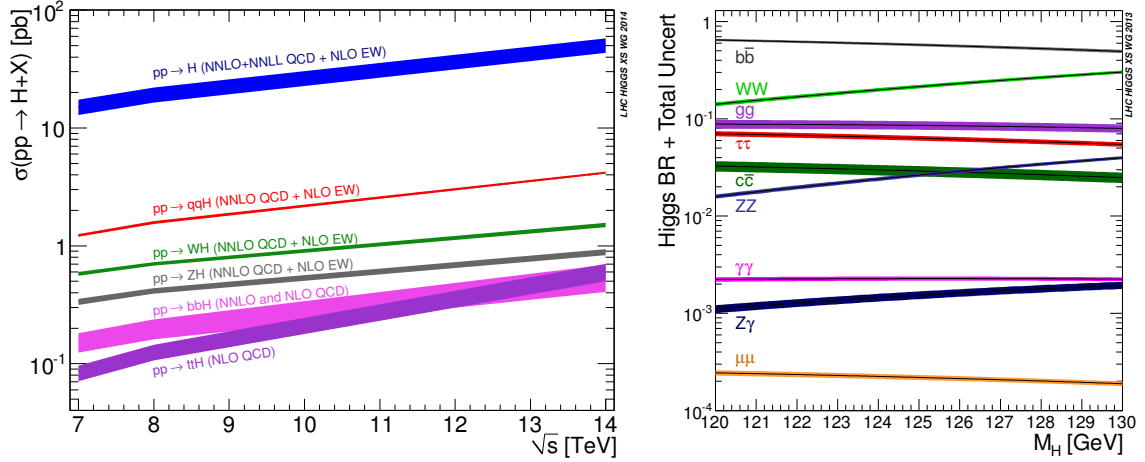


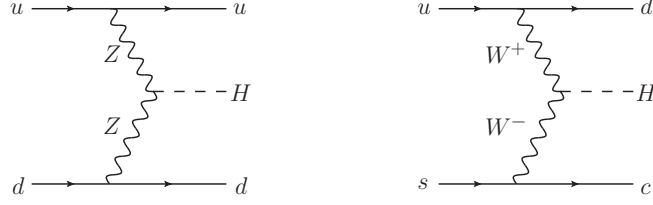
Figure 7.2.: On the left the cross sections of Higgs boson production channels are given at highest known order as a function of the center-of-mass energy \sqrt{s} [7]. $pp \rightarrow H$ is Higgs boson production in Gluon Fusion (GF), which has a cross section which is consistently about an order of magnitude larger than the other channels. $pp \rightarrow qqH$ is Higgs boson production in Vector Boson Fusion (VBF), other important channels are Higgs boson production in association with a vector boson (Z or W^\pm) and in association with a heavy quark anti-quark pair ($b\bar{b}$ and $t\bar{t}$). On the right, the branching ratios for possible Higgs boson decays are given for a Higgs boson mass around 125 GeV [7]. Although the decay into a $b\bar{b}$ pair has the highest decay width, it is notoriously difficult to separate from the QCD background. Therefore other channels, such as $H \rightarrow \gamma\gamma$ and $H \rightarrow \mu^+\mu^-$, although occurring less frequent, are often considered more useful for Higgs boson detection.

7.1. Higgs boson plus jets production in Vector Boson Fusion

The production of a Higgs boson through *vector boson fusion* (VBF) is considered one of the most important Higgs boson production channels. It can assist in determining the CP -properties of the Higgs boson and in constraining the couplings of the Higgs boson to the heavy gauge bosons. The dominant background to the production of a Higgs boson in association with jets in VBF is the *gluon fusion* (GF) channel, which will be covered in Section 7.2. Since the main decay channels of the Higgs boson are $H \rightarrow b\bar{b}$ and $H \rightarrow W^+W^-$ (see Figure 7.2), other important backgrounds are those in which these decay products are produced directly, such as in the process $pp \rightarrow W^+W^-jj$. t -channel exchanges of quarks and gluons have a tendency to produce harder and more central radiation than the t -channel exchange of vector bosons present in VBF. This is because the color singlet exchange in VBF suppresses central region jet activity, resulting in a typical VBF signature of two forward-backward pointing hard jets with a large rapidity gap. Therefore, applying what is known as *VBF cuts*, requiring a large rapidity separation of the two jets and applying stringent cuts on the decay products of the Higgs boson, offers a way to suppress all mentioned background processes considerably.

$pp \rightarrow H + 3j$ in VBF is an interesting process to calculate with GOSAM because of the possibility of the vector bosons appearing in the loop, which illustrates the need for the complex mass scheme implemented in GOSAM2.0.

7.1.1. Diagram selection

Figure 7.3.: Two examples of subprocesses occurring in $pp \rightarrow H + 2j$ in VBF.

There are seven independent subprocesses for this process, assuming a diagonal CKM matrix. Other subprocesses can be mapped onto these six through crossing and relabeling. These subprocesses are for $pp \rightarrow H + 2j$:

$$\begin{aligned}
 uu &\rightarrow Huu, & dd &\rightarrow Hdd, \\
 ud &\rightarrow Hud, & us &\rightarrow Hus, \\
 uc &\rightarrow Huc, & ds &\rightarrow Hds, \\
 us &\rightarrow Hdc. & &
 \end{aligned} \tag{7.1}$$

The list of subprocesses for $pp \rightarrow H + 3j$ is a trivial modification of this one, adding an additional gluon to the final state. Only starting at $pp \rightarrow H + 4j$ the list becomes more involved, because of possible splittings of gluons into quarks. Since electroweak couplings to fermions are proportional to the electric charge of the fermion, the charge of the quark matters when determining this list. For example, even with a diagonal CKM matrix, $uc \rightarrow uc$ is not identical to $us \rightarrow us$. Also, because of the diagonal CKM matrix, subprocesses cannot be remapped if the quarks are from different generations; for example, $us \rightarrow Hus$ cannot be calculated from $ud \rightarrow Hud$, because the latter can have W boson exchanges. Notice that topologically, crossing also yields Higgsstrahlung diagrams with the vector boson decaying hadronically (see Figure 7.4).

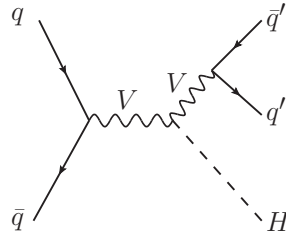


Figure 7.4.: Crossing VBF subprocesses can lead to topologies that are classified as Higgsstrahlung with the vector boson subsequently decaying hadronically.

Since they are of the correct order, α^3 at LO and $\alpha^3\alpha_S$ at NLO QCD, these Higgsstrahlung diagrams need to be added to the calculation of $pp \rightarrow H + 2j$. However, the typical forward-

backward pointing jet signature of VBF is absent in their contribution. Therefore, imposing a cut on the rapidity separation should make this contribution negligible.

In GOSAM, the diagrams are drawn automatically from an input of initial and final state particles and the order of the diagram. In that case, one needs to be careful not to include loop induced Higgs boson production diagrams that use the gluon as a bridge, such as the one shown in Figure 7.5. These kind of diagrams are of the same order as the loop-diagrams that are NLO QCD corrections to the subprocesses of $pp \rightarrow H + 2j$ in VBF, however, there are no Born diagrams to which they are a QCD correction. They are in fact Born diagrams themselves, but at a higher order than what we are considering. Together with the selection not to have the Higgs boson being emitted from a quark line, the correct selection of diagrams in GOSAM can be achieved by adding the following lines to the input card

```
filter.lo=lambda d: (not d.vertices(QUARKS,QUARKS,H) > 0)
filter.nlo=lambda d: ( (not d.vertices(QUARKS,QUARKS,H) > 0) and (d.chord(g) > 0) )
```

The filter $d.chord(g) > 0$ requires the diagrams to be generated to have at least one gluon in the loop.

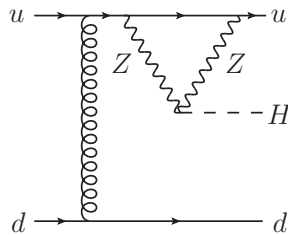


Figure 7.5.: Loop induced Higgs boson production. Although this diagram is of the same order ($g_W^3 g_s^2$) as loop-corrections to the subprocesses of $pp \rightarrow H + 2j$ in VBF, there is actually no Born diagram to which this one can be a QCD correction. It is therefore a Born diagram at an order higher than the one we are considering. Hence, attention should be paid to removing it from the regular calculation.

7.1.2. Higgs boson plus two jets in VBF

$pp \rightarrow H + 2j$ in VBF is known at NNLO QCD accuracy [121]. The NLO QCD corrections have been calculated in [122,123]. Although in principle pentagons could appear in this calculation, they do not contribute to this process. This is because of color algebra in the squared matrix element.

Because the vector bosons are colorless, the color algebra structure of a pentagon has two fermion loops connected by a gluon propagator, see Figure 7.6.

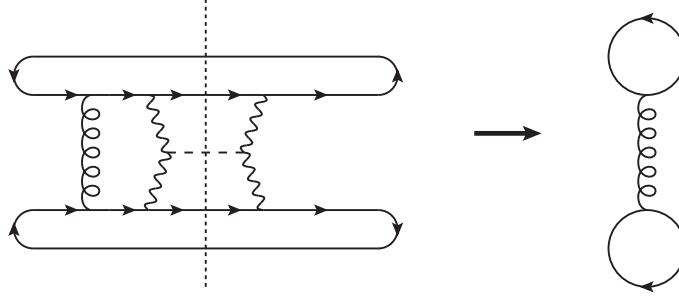


Figure 7.6.: The color algebra of the squared matrix element, $|\mathcal{M}_V|^2 \propto 2\Re(\mathcal{M}_{1\text{-loop}}\mathcal{M}_{\text{Born}}^*)$, involves two traces of the $SU(3)$ generator t_{ij}^a .

Any of those two connected loops is essentially the trace of the generator of $SU(3)$, which is zero:

$$\text{Tr}(t^a) = 0$$

This makes $pp \rightarrow H + 2j$ in VBF a relatively easy process to calculate, because although it is a five-point process, the loops are maximally three-point.

Comparison fixed order cross sections

The process $pp \rightarrow H + 2j$ in VBF was calculated using MCFM, VBFNLO, SHERPA+GOSAM and AMC@NLO+GOSAM. For the latter, a preliminary version of the interface described in Chapter 8 was used. In AMC@NLO the possibility exists to remove the diagrams in which the vector bosons appear in the s -channel. The parameters used are given in Table 7.1.

Parameter	value
\sqrt{s}	8 TeV
M_H	125 GeV
M_Z	91.1876 GeV
M_W	80.398 GeV
Γ_Z	2.50842 GeV
Γ_W	2.097673 GeV
G_F	$1.6637 \cdot 10^{-5} \text{ GeV}^{-2}$

Table 7.1.: The parameters used in the comparison between various programs of the process $pp \rightarrow H + 2j$ in VBF.

Given in this table are the input parameters for the electroweak scheme used by MCFM, VBFNLO and SHERPA+GOSAM, where the input parameters are M_Z , M_W and G_F . Instead, in AMC@NLO, the input parameters are M_Z , G_F and α , which were calculated from the given

values by hand. For the jets, the k_t algorithm was used, requiring jets with

$$p_{tj} > 20, \quad |\eta_j| < 4.5, \quad \Delta R_{jj} > 0.8. \quad (7.2)$$

In the calculations using SHERPA and AMC@NLO, FASTJET [73, 124, 125] was used. The PDF set used was CTEQ6mE [126]. The NLO QCD calculation was performed with VBF cuts, the LO calculation both with and without VBF cuts. In this case, because the Higgs boson is not decayed, the VBF cuts only consists of a requirement on the rapidity separation of the two jets,

$$|\eta_{jj}| > 4.0. \quad (7.3)$$

	LO without vbf cuts	LO with vbf cuts	NLO with vbf cuts
MCFM	1204.8 ± 0.2	601.0 ± 0.7	615.5 ± 1.7
VBFNLO	1204.6 ± 0.9	601.7 ± 0.7	612.5 ± 1.5
SHERPA+GoSAM	1627.1 ± 1.9	601.5 ± 0.5	618.3 ± 1.0
AMC@NLO+GoSAM	1627.0 ± 1.6	599.2 ± 0.2	
AMC@NLO+GoSAM (excl. s-channel)	1202.0 ± 1.0	598.8 ± 0.4	614.7 ± 2.1

Table 7.2.: The LO and NLO total cross sections with various programs, using the setup of parameters and cuts described in the text. The LO result is given with and without VBF cuts. AMC@NLO has the explicit option of removing vector bosons from the s -channel. Comparing the first two columns it is clearly visible that the VBF cuts effectively remove the s -channel contributions.

In the first two columns of Table 7.2, the LO total cross sections are given with and without applying the VBF cuts given in (7.3). Without the cuts, there is a distinct difference between the programs that include the diagrams with s -channel vector bosons and those which exclude them. Among the members of either of those categories, the results agree very well. When applying the VBF cuts, the differences between all programs disappear. This shows that VBF cuts are indeed very efficient in removing the effect of the Higgsstrahlung diagrams. The NLO total cross sections with the VBF cuts in place all agree very well.

7.1.3. Higgs boson plus three jets in VBF

The simplification of the calculation of $pp \rightarrow H + 2j$ in VBF caused by the color algebra does not hold anymore when adding an extra jet. Hence, in the calculation with an additional jet, boxes, pentagons and hexagons can appear. The number of loop diagrams for $pp \rightarrow H + 2j$ and $pp \rightarrow H + 3j$ in VBF are given for comparison in Table 7.3 and one can see that there are actually nine times as many diagrams to calculate for the latter. Apart from the added complexity through the increase in possible loop sizes, also now the vector bosons can appear in the loop, which requires the use of the complex mass scheme. The full calculation of $pp \rightarrow H + 3j$ in VBF at NLO QCD appeared only very recently [127]. Up until then, the only calculations that were available omitted the pentagons and hexagons, because their contribution is small [128].

Results

The virtual corrections to $pp \rightarrow H + 3j$ in VBF were calculated using GOSAM with the complex mass scheme activated. The CKM matrix was taken to be diagonal, leading to the

$pp \rightarrow H + 2j$	240	$pp \rightarrow H + 3j$	2160
$us \rightarrow Hdc$	24	$us \rightarrow Hdcg$	216
$uc \rightarrow Huc$	24	$uc \rightarrow Hucg$	216
$us \rightarrow Hus$	24	$us \rightarrow Husg$	216
$ds \rightarrow Hds$	24	$ds \rightarrow Hds g$	216
$ud \rightarrow Hud$	48	$ud \rightarrow Hudg$	432
$uu \rightarrow Huu$	48	$uu \rightarrow Huug$	432
$dd \rightarrow Hdd$	48	$dd \rightarrow Hddg$	432

Table 7.3.: The number of loop diagrams for $pp \rightarrow H + 3j$ in VBF.

Parameter	value
α^{-1}	137.036
\sqrt{s}	500 GeV
M_H	125 GeV
M_Z	91.1876 GeV
M_W	80.376 GeV
Γ_Z	2.4952 GeV
Γ_W	2.124 GeV

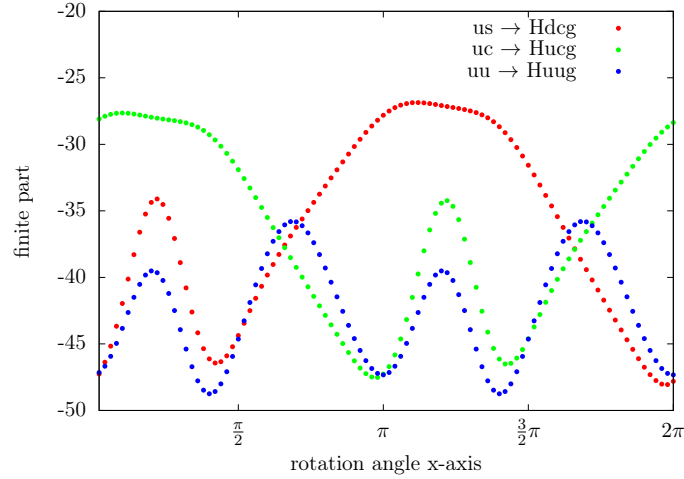
Table 7.4.: The parameters used in the evaluation phase space points for $pp \rightarrow H + 3j$ in VBF.

Figure 7.7.: Using the setup as given in the text with the parameters set to the values in Table 7.4, the subprocesses $us \rightarrow Hdcg$, $uc \rightarrow Hucg$ and $uu \rightarrow Huug$ were evaluated for one phase space point. The final state of this phase space point was rotated around the x -axis, perpendicular to the beam axis in the z -direction, and the subprocesses reevaluated at a hundred different values of the angle of this rotation. The finite part of the calculation is plotted here against this angle.

seven independent subprocesses listed in Table 7.3. The setup given in Table 7.4 was used to calculate the results for a non-exceptional phase space point provided by RAMBO. For each of

the subprocesses, this result is listed in Appendix F.1.

For three of the subprocesses, $uu \rightarrow Huug$, $uc \rightarrow Hucg$, and $us \rightarrow Hdcg$, an analysis of the stability of the result was performed. Starting from the phase space point given in the appendix, the subprocesses were evaluated at the phase space point with the final state rotated around an axis perpendicular to the beam axis. In Figure 7.7, the finite part of the calculation is plotted against this rotation angle. The figure shows that no instabilities are encountered.

GOSAM is also capable of including even more jets to Higgs boson production in VBF, as was shown for example by the subprocesses of $pp \rightarrow H + 4j$ in VBF used for the stability tests of GOSAM in Section 6.2.

7.2. Higgs boson plus jets production in Gluon Fusion

From Figure 7.2 it is clear that the most frequent production channel of the Higgs boson at LHC is through *gluon fusion* (GF). In the Standard Model, the production of a Higgs boson in GF is a loop induced process, where the interaction is mediated through a heavy quark loop. This is predominantly a top loop, because of its high mass and the resulting strong Yukawa coupling.

The computation of $gg \rightarrow H$ at LO [129] and at NLO, both in the heavy top-mass limit [130, 131] and with the full top- and bottom mass dependence maintained [132, 133], have been known for a long time now. $gg \rightarrow H$ has been calculated at NNLO and very recent even at NNNLO, only in the heavy top-mass limit, in [134–136] and [137] respectively.

Including a jet in the final state opens up the possibility of quarks in the initial state. $pp \rightarrow H + 1j$ at LO and NLO have been calculated as part of the calculations of $gg \rightarrow H$ at NLO and NNLO respectively. Recently, it was calculated at NNLO [27, 138]. $pp \rightarrow H + 2j$ was calculated at LO with full top-mass dependence in [139]. The calculation at NLO in the heavy top-mass limit followed in [140]. $pp \rightarrow H + 3j$ was calculated at LO in the heavy top-mass limit in [141] and more recently with full top-mass dependence in [142].

7.2.1. Effective Field Theory

It has been shown [143] that one can replace the heavy fermion loop by an effective local interaction, known as the infinite top mass limit ($m_t \rightarrow \infty$). In this limit the loop effectively shrinks to a point and this vertex is then described by the following Lagrangian,

$$\mathcal{L} = -\frac{g_{\text{eff}}}{4} H \text{tr} (G_{\mu\nu} G^{\mu\nu}) . \quad (7.4)$$

In the $\overline{\text{MS}}$ scheme, the coefficient g_{eff} is given by [130, 131]

$$g_{\text{eff}} = -\frac{\alpha_s}{3\pi v} \left(1 + \frac{11}{4\pi} \alpha_s \right) + \mathcal{O}(\alpha_s^3), \quad (7.5)$$

where v is the Higgs boson vacuum expectation value. Expanding the terms in the Lagrangian leads to the Feynman rules given in Appendix A.3. An illustration is given in Figure 7.2.1.

Notice that if the gluons are in the loop, the first vertex in Figure 7.2.1 contributes two powers of the loop momentum q to integrand. This can lead to the higher-rank numerators as described in Section 5.2. The other two effective vertices do not lead to higher-rank polynomials: The coupling of a Higgs boson and three gluons and the coupling of a Higgs boson and four gluons contribute no powers of q at all. The appearance of higher-rank numerators in the loop caused by the effective vertices made the production of a Higgs boson in association with up to three jets in GF at NLO an excellent first application of XSAMURAI.

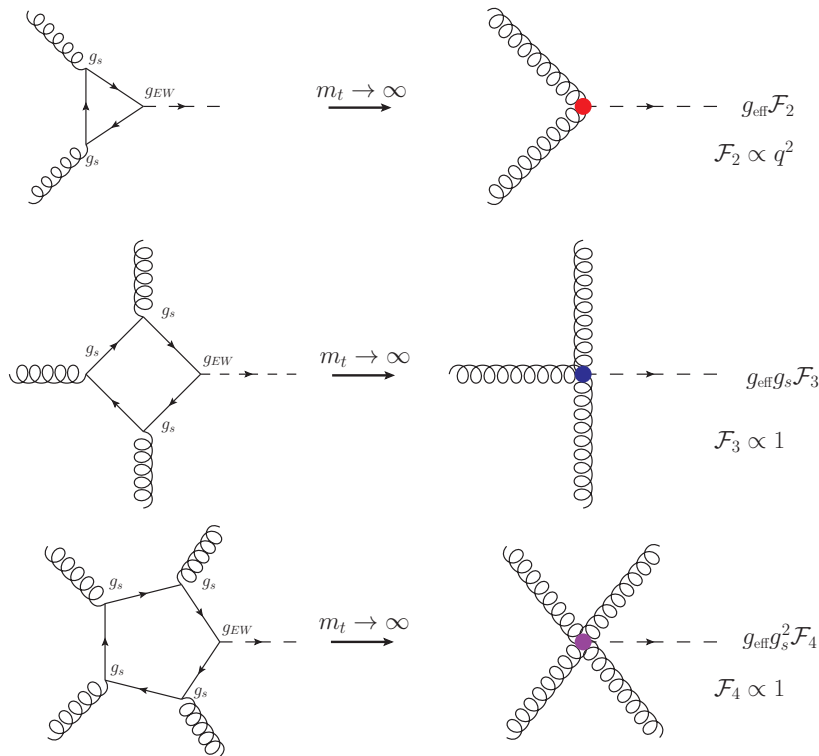


Figure 7.8.: Illustration of the heavy top-mass limit, in which the top loop shrinks to an effective vertex. The exact expressions are given in Appendix A.3. Important to note is the momentum dependence of the kinematic factors, parametrized here by F_i . The numerators in the expressions for F_3 and F_4 do not depend on the momenta of the particles involved. However, the numerator of F_2 is proportional to the square of the loop momentum q , if the gluons are in the loop.

In [144, 145] the validity of this approximation was analyzed in the NNLO calculation of $gg \rightarrow H$. It was shown that the large m_t approximation works very well, with the effect of the top quark mass suppressed terms being less than one percent, far below the uncertainty due to scale variations.

7.2.2. Higgs boson plus two jets in GF

In [5] the full calculation of $pp \rightarrow H + 2j$ at NLO was presented, using GOSAM for the virtual corrections. The full process $pp \rightarrow H + 2j$ has the following partonic processes in its contract

file:

$$\begin{aligned}
qq &\rightarrow Hqq, & q\bar{q} &\rightarrow Hq\bar{q}, \\
q\bar{q} &\rightarrow Hgg, & q\bar{q} &\rightarrow Hq'q', \\
qq' &\rightarrow Hqq', & qg &\rightarrow Hgq, \\
\bar{q}q &\rightarrow Hq\bar{q}, & \bar{q}q' &\rightarrow Hq'\bar{q}, \\
gq &\rightarrow Hgq, & gg &\rightarrow Hq\bar{q}, \\
gg &\rightarrow Hgg. & &
\end{aligned} \tag{7.6}$$

Of course, these processes are not independent, because they can be mapped to each other using crossing and/or relabeling. The minimal set of these subprocesses that GOSAM identifies and generates are

$$\begin{aligned}
gg &\rightarrow Hgg, & gg &\rightarrow Hq\bar{q}, \\
q\bar{q} &\rightarrow Hq\bar{q}, & q\bar{q} &\rightarrow Hq'q'.
\end{aligned} \tag{7.7}$$

The code for these subprocesses was tested in a non-exceptional phase space point. The results are given in Appendix F.4. The poles showed very good agreement with the ones obtained from the universal IR behavior. Additionally, the benchmark point presented in [146] was tested and excellent agreement was found.

Interface

The calculation was performed using GOSAM for the virtual amplitudes and the Monte Carlo program SHERPA [26] for the LO diagrams and the real radiation matrix elements. SHERPA also regularized the soft and collinear singularities via the Catani-Seymour dipole formalism for the subtraction terms, and performed the integration over phase space. The employed interface between SHERPA and GOSAM was using the BLHA1 standards.

Setup and parameters

The singularities (ultraviolet, IR and collinear) were regularized through dimensional reduction (DRED). The $\overline{\text{MS}}$ scheme was used to renormalize the UV divergences. The parameters used for the calculation are listed in Table 7.5.

Parameter	value
\sqrt{s}	8 TeV
m_H	125 GeV
G_F	$1.6639 \cdot 10^{-5} \text{ GeV}^{-2}$
$\alpha_s^{\text{LO}}(M_Z)$	0.129783
$\alpha_s^{\text{NLO}}(M_Z)$	0.117981
v^2	$(\sqrt{2}G_F)^{-1}$

Table 7.5.: The parameters used in the calculation of $pp \rightarrow H + 2j$ in GF.

The variable `ewchoice` from Table 6.1 was set to 1, with $M_W = 80.385$ GeV and $M_Z = 91.188$ GeV.

For the parton distribution functions (PDFs), `CTEQ6L1` and `CTEQ6mE` [126] were used for the LO and NLO calculations respectively. The publicly available library `LHAPDF` [147] was employed to interface with the PDF sets in a calculation in a standardized way. The jets were clustered using the anti- k_T algorithm, as given by the `FASTJET` package [73, 124, 125]. The cuts on the jets were set to:

$$p_{t,j} \geq 20\text{GeV}, \quad |\eta_j| \leq 4.0, \quad R = 0.5. \quad (7.8)$$

There was no decay mode included for the Higgs boson, which was therefore treated as a stable on-shell particle. The factorization and renormalization scale at its central value were defined at

$$\mu = \mu_R = \mu_F = \hat{H}_T, \quad (7.9)$$

where the following definition was used

$$\hat{H}_T = \sqrt{M_H^2 + p_{t,H}^2} + \sum_j p_{t,j}, \quad (7.10)$$

with $p_{t,H}$ and $p_{t,j}$ as the transverse momenta of the Higgs boson and the final state partons. The strong coupling at this scale, $\alpha_s(\mu)$, is calculated by the PDF set from the initial value of $\alpha_s(M_Z)$ in Table 7.5. To assess the theoretical uncertainties, μ was varied in the range

$$\frac{1}{2}\hat{H}_T < \mu < 2\hat{H}_T. \quad (7.11)$$

By taking the envelope of the distributions at these different scales, the error could be estimated.

Reduction to normal rank

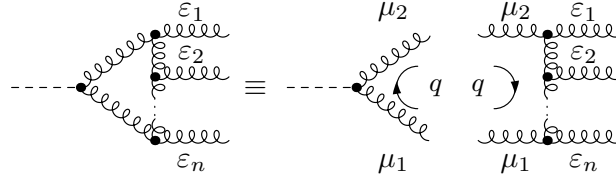
Comparing the results using `SAMURAI` and its extension `XSAMURAI`, it was realized that although higher-rank numerators appear in the calculation, they can always be reduced to normal rank in an integrand reduction approach. For this process, higher-rank integrands only appear in diagrams with a purely gluonic loop involving only three-gluon vertices and one effective Higgs coupling. The generic numerator $\Gamma^{\varepsilon_1 \dots \varepsilon_n}$ of a one-loop diagram including an effective ggH coupling with $(n+1)$ denominators can be written as

$$\Gamma^{\varepsilon_1 \dots \varepsilon_n} \equiv \mathcal{F}_{\mu_1 \mu_2} \mathcal{G}^{\mu_1 \mu_2 \varepsilon_1 \dots \varepsilon_n}, \quad (7.12)$$

where q is the loop momentum and $\mathcal{F}_{\mu_1 \mu_2}$ is the effective gluon Higgs vertex defined as

$$\mathcal{F}_{\mu_1 \mu_2} = \delta_{ab} (q_1^\nu q_2^\mu - q_1 \cdot q_2 g^{\mu\nu})$$

and $\mathcal{G}^{\mu_1 \mu_2 \varepsilon_1 \dots \varepsilon_n}$ is the numerator of a tree-level diagram with $(n+2)$ denominators. The latter can be represented by



Neglecting all external momenta and all the terms that are proportional to q^2 , equation (7.12) can be written as

$$\mathcal{F}_{\mu_1\mu_2} = q_{\mu_1} q_{\mu_2} + \mathcal{O}(q^2), \quad (7.13)$$

The generic tensor structure of $\mathcal{G}^{\mu_1\mu_2\epsilon_1\cdots\epsilon_n}$ can be written as

$$\begin{aligned} \mathcal{G}^{\mu_1\mu_2\epsilon_1\cdots\epsilon_n} &= q^{\mu_1} \mathcal{T}_1^{\mu_2\epsilon_1\cdots\epsilon_n} + q^{\mu_2} \mathcal{T}_2^{\mu_1\epsilon_1\cdots\epsilon_n} + \\ &+ g^{\mu_1\mu_2} \mathcal{T}_g^{\epsilon_1\cdots\epsilon_n} + \mathcal{O}(q^2), \end{aligned} \quad (7.14)$$

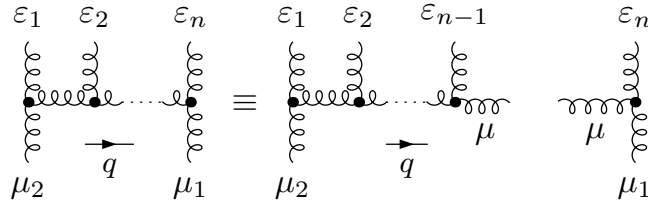
with $\mathcal{T}_1, \mathcal{T}_2$, and \mathcal{T}_g being tensors which could also depend on q . Equation (7.14) is given for $n = 0$ and $n = 1$ as

$$\begin{aligned} \mathcal{G}^{\mu_1\mu_2} &= g^{\mu_1\mu_2} \\ \mathcal{G}^{\mu_1\mu_2\epsilon_1} &= g^{\mu_1\epsilon_1} q^{\mu_2} + g^{\mu_2\epsilon_1} q^{\mu_1} - 2g^{\mu_2\mu_1} q^{\epsilon_1}, \end{aligned} \quad (7.15)$$

For $n > 1$ equation (7.14) can be proven to hold by induction over n , using

$$\mathcal{G}^{\mu_1\mu_2\epsilon_1\cdots\epsilon_n} = \mathcal{G}_\mu^{\mu_2\epsilon_1\cdots\epsilon_{n-1}} \mathcal{G}^{\mu_1\mu\epsilon_n}, \quad (7.16)$$

which can be represented as



The combination of equation (7.13) and equation (7.14) then shows that every rank- $(n + 2)$ term of a diagram with $n + 1$ denominators $\Gamma^{\epsilon_1\cdots\epsilon_n}$ is proportional to q^2 . In essence a factor q^2 can be removed together with one denominator, which leads to an integrand of n denominators which has a numerator of rank n . This meant the numerically faster original version of SAMURAI could be used.

Results

With the setup as described above, the following cross sections were obtained,

$$\sigma_{\text{LO}}[\text{pb}] = 1.90^{+0.58}_{-0.41}, \quad \sigma_{\text{NLO}}[\text{pb}] = 2.90^{+0.05}_{-0.20}. \quad (7.17)$$

Converting the results from DRED to the tHV scheme, there was excellent agreement for the subprocesses with MCFM (version 6.4). For the computation of the LO distribution 2.5×10^7 phase space points were used. For the NLO distributions, 4.0×10^6 phase space points were used for the Born and the virtual correction and 5.0×10^8 points for the computation of the real radiation. In Figure 7.9 the distributions of the transverse momentum p_T and the pseudorapidity η of the Higgs boson are given. The K-factor, defined for each bin as the NLO result divided by the LO result, is consistently at a value of about 1.5 – 1.6 over a large kinematic range.

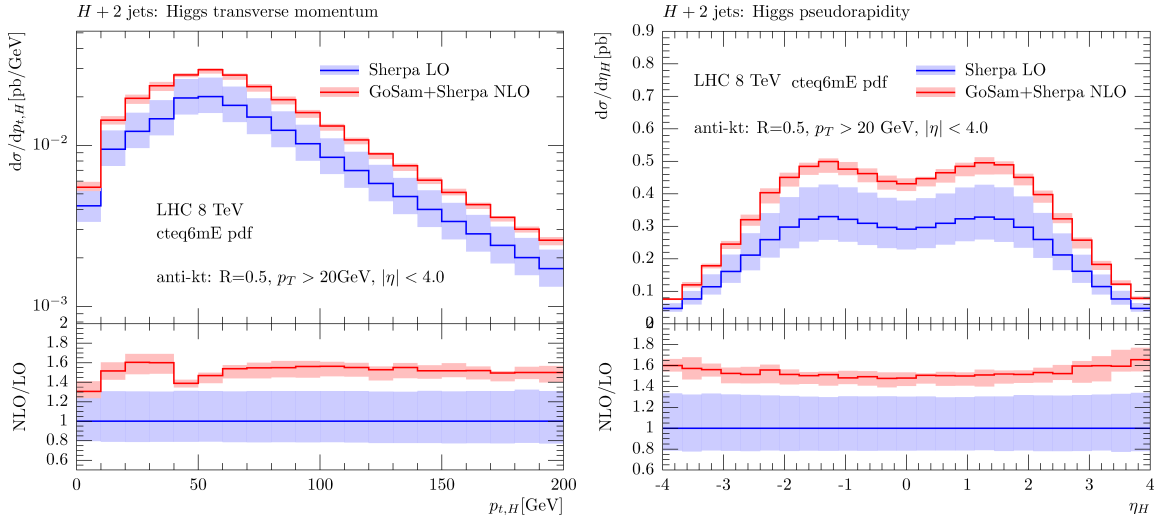


Figure 7.9.: Distributions of the transverse momentum p_T and pseudorapidity η of the Higgs boson in the process $pp \rightarrow H + 2j$ in GF.

The NLO calculation is clearly less dependent on the unphysical scale μ , as the estimated error through scale variation is reduced by about 50%. In Figure 7.10 and 7.11 the distributions of the transverse momentum and pseudorapidity of the first and second jet respectively are shown. Also for the pseudorapidity distributions of the jets, the K-factor is very flat at about 1.5 – 1.6. For the transverse momentum distributions, however, the shapes change slightly. For the leading jet, the K-factor decrease from 1.6 to 1.4 with increasing p_T , whereas for the second jet, it increase from 1.4 to 1.6.

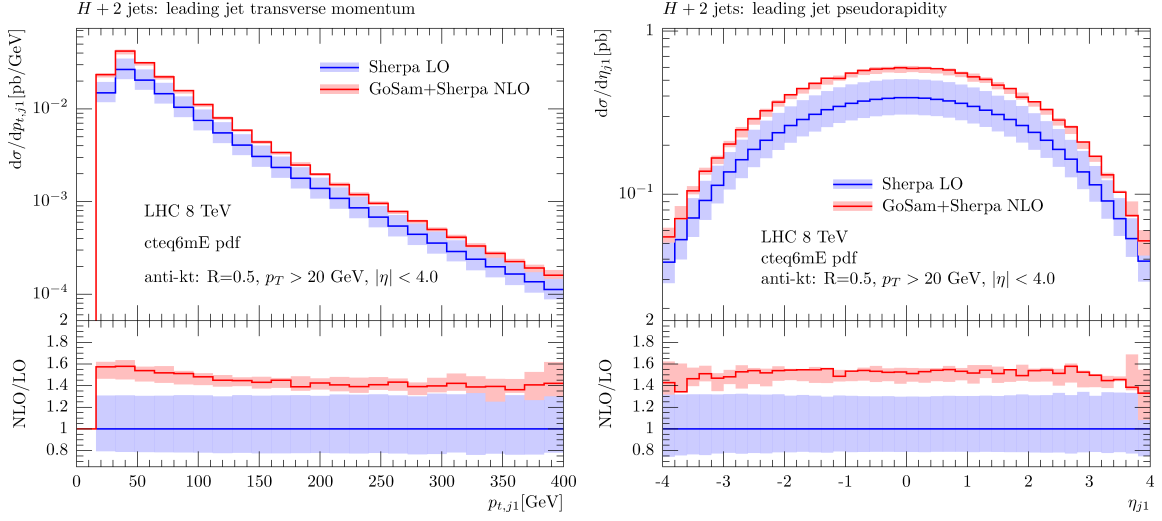


Figure 7.10.: Distributions of the transverse momentum p_T and pseudorapidity η of the first jet in the process $pp \rightarrow H + 2j$ in GF.

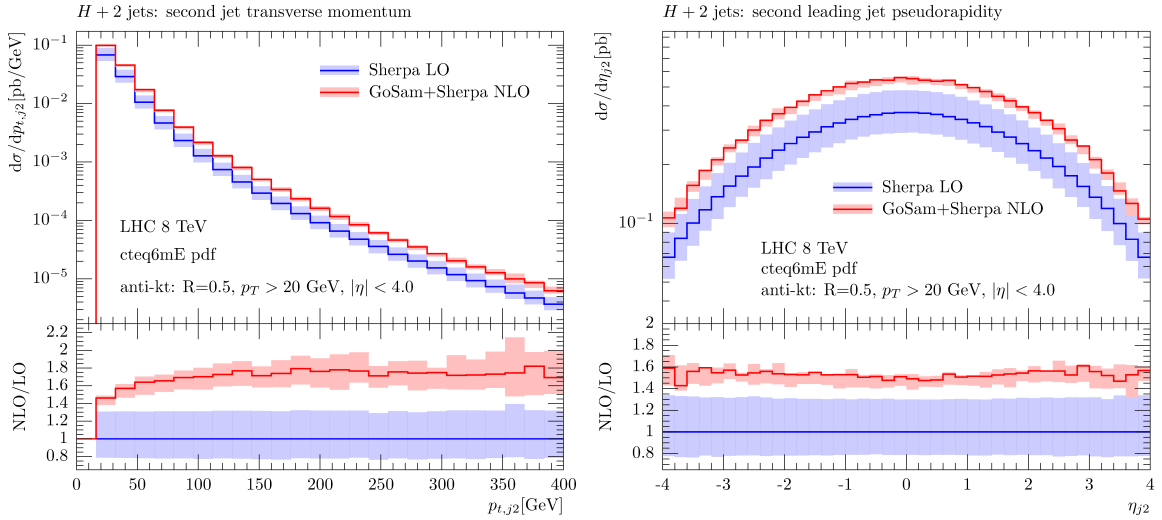


Figure 7.11.: Distributions of the transverse momentum p_T and pseudorapidity η of the second jet in the process $pp \rightarrow H + 2j$ in GF.

7.2.3. Higgs boson plus three jets in GF

For $pp \rightarrow H + 3j$ [4], there are numerous channels that can all be mapped by crossing and relabeling to four independent subprocesses

$$\begin{aligned}
 gg &\rightarrow H g g g, & gg &\rightarrow H q \bar{q} g, \\
 q\bar{q} &\rightarrow H q q \bar{q}, & q\bar{q} &\rightarrow H q' \bar{q}' g.
 \end{aligned}
 \tag{7.18}$$

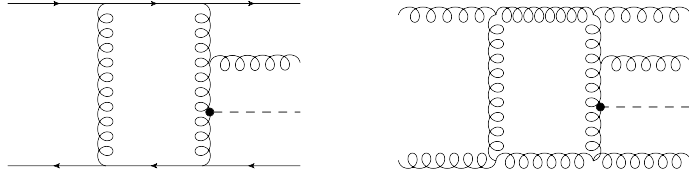


Figure 7.12.: Examples of hexagon diagrams which enter in the six-parton one-loop amplitudes for $q\bar{q} \rightarrow Hq\bar{q}g$ and $gg \rightarrow Hggg$. The dot represents the effective ggH vertex.

The number of NLO diagrams increases massively for each additional jet, see Table 7.6. There are well over thirteen thousand diagrams to be computed; many of which have higher-rank terms, including sixty rank-seven hexagons. We checked for gauge invariance by generating the code with analytical polarization vectors and checking their Ward identities by replacing the polarization vectors one at the time with their momenta. Similarly as in the previous section, the results for a non-exceptional phase space point are provided for the four subprocesses in Appendix F.5.

$pp \rightarrow H + 0j$	2 NLO
$gg \rightarrow H$	2 NLO
$pp \rightarrow H + 1j$	62 NLO
$qq \rightarrow Hg$	14 NLO
$gg \rightarrow Hg$	48 NLO
$pp \rightarrow H + 2j$	926 NLO
$qq' \rightarrow Hqq'$	32 NLO
$qq \rightarrow Hqq$	64 NLO
$qg \rightarrow Hqg$	179 NLO
$gg \rightarrow Hgg$	651 NLO
$pp \rightarrow H + 3j$	13179 NLO
$qq' \rightarrow Hqq'g$	467 NLO
$qq \rightarrow Hqqg$	868 NLO
$qg \rightarrow Hqgg$	2519 NLO
$gg \rightarrow Hggg$	9325 NLO

Table 7.6.: The number of NLO diagrams for the production of Higgs boson plus jets in gluon fusion, split out for the different subprocesses, as generated by GoSAM.

To check the stability of the result, we evaluated the phase space point of the appendix with the final state rotated around an axis perpendicular to the beam axis. In Figure 7.13, it can be seen that no instabilities occur.

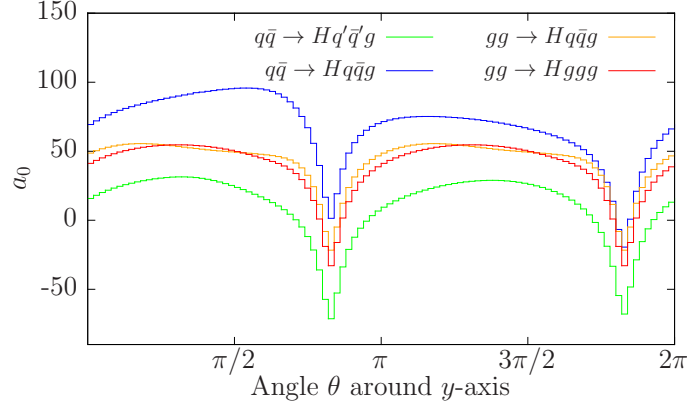


Figure 7.13.: Finite-term a_0 of the virtual matrix-elements for $q\bar{q} \rightarrow Hq'\bar{q}'g$ (green), $q\bar{q} \rightarrow Hq\bar{q}g$ (blue), $gg \rightarrow Hq\bar{q}g$ (orange) and $gg \rightarrow Hggg$ (red) for the phase space point given in Table F.9 with the final state particles rotated around the y axis, perpendicular to the beam axis. The processes were reevaluated at a hundred different values of the angle of this rotation.

Interface

Since at the time there was no Monte Carlo program available that could provide all the ingredients for a full NLO calculation, a hybrid setup was constructed. GOSAM and SHERPA were used for the Born and virtual contributions and an *ad hoc* framework consisting of MADGRAPH [148, 149], MADDIPOLE [150, 151] and MADEVENT [152] was constructed for the real contributions, the subtraction terms and the integrated dipoles. Several tests were performed to check the consistency of this interface. Firstly, the calculation of $pp \rightarrow H + 2j$ was redone with this hybrid setup and found agreement with the results using only SHERPA with GOSAM. Then, it was checked that the LO diagrams for $pp \rightarrow H + 3j$ matched between MADGRAPH and SHERPA. Finally, the independence of the α -parameter (see Section 2.2) was confirmed.

Setup and parameters

The setup of this calculation was almost identical to the one of the calculation of $pp \rightarrow H + 2j$. The only difference was that for the central renormalization and factorization scale, now we used $\mu = m_H$ in the effective vertices, so the overall scale dependence of the strong coupling was

$$\alpha_s^5 \rightarrow \alpha_s^2(m_H)\alpha_s^3(\hat{H}_T/2). \quad (7.19)$$

If the Born term is evaluated at different scales $\{\mu_i\}$, equation (3.48) generalizes to a sum of logarithms for each individual coupling constant,

$$\frac{d\sigma_{\text{NLO}}^N}{d\Phi} = \prod_{i=1}^N \alpha_s(\mu_i^2)B + \alpha_s^{N+1}(\mu_R^2) \left[V(Q^2) + b \sum_{i=1}^N \ln\left(\frac{\mu_i^2}{Q^2}\right) B \right] + \alpha_s^{N+1}(\mu_R^2)R. \quad (7.20)$$

This scale compensation at NLO is ensured independently for each μ_i that is varied. For the scale compensation the actual values of $\mu_R^{2'}$ and $\mu_R^{2''}$ are irrelevant because $\alpha_s(\mu_R^2) - \alpha_s(\mu_R^{2'}) = \mathcal{O}(\alpha_s^2)$. Since in NLO calculations often just one renormalization scale is used, a useful reformulation of this formula is to use for the renormalization scale of the virtual term the geometric mean of the $\{\mu_i^2\}$,

$$\mu_R^2 = \left(\prod_{i=1}^N \mu_i^2 \right)^{1/N}. \quad (7.21)$$

This is equivalent to evaluating the virtual contribution at a random scale μ_0^2 and compensating by adding logarithms for each scale, *i.e.* adding to the full expression a term

$$\alpha_s^{N+1}(\mu_R^{2'}) bB \sum_{i=1}^N \ln \left(\frac{\mu_i^2}{\mu_0^2} \right). \quad (7.22)$$

This procedure was recently derived in [153].

Results

With this setup we acquired the following total cross sections:

$$\sigma_{\text{LO}}[\text{pb}] = 0.962_{-0.31}^{+0.51}, \quad \sigma_{\text{NLO}}[\text{pb}] = 1.18_{-0.22}^{+0.01}. \quad (7.23)$$

We varied the renormalization and factorization scale simultaneously around the central value, by a factor 2 and $\frac{1}{2}$. The result is given in Figure 7.14. It can be seen that including the NLO corrections strongly reduces the scale dependence of the total cross section.

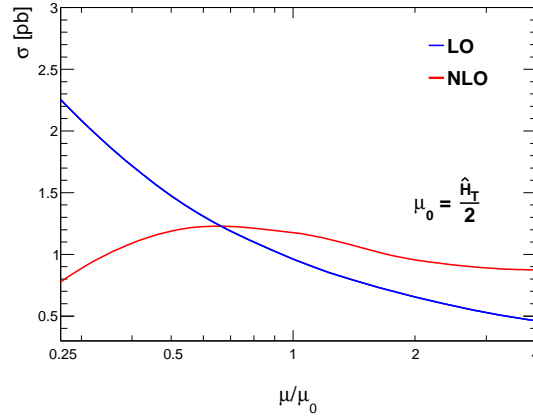


Figure 7.14.: Scale dependence of the total cross section of $pp \rightarrow H + 3j$ in GF at LO and NLO. The scale μ was varied around the central scale $\mu_0 = \hat{H}_T/2$, by evaluating the process for five values in the range $\mu_0/4 < \mu < 4\mu_0$.

In Figure 7.15, the p_T distributions of the Higgs boson and the three jets are shown. An interesting feature of all four distributions is that the K-factor seems to go down linearly from

low to high transverse momentum: For values below about 150 – 200 the NLO corrections enhance the distributions, for higher values they decrease them. The K-factor is explicitly shown for the p_T of the Higgs boson.

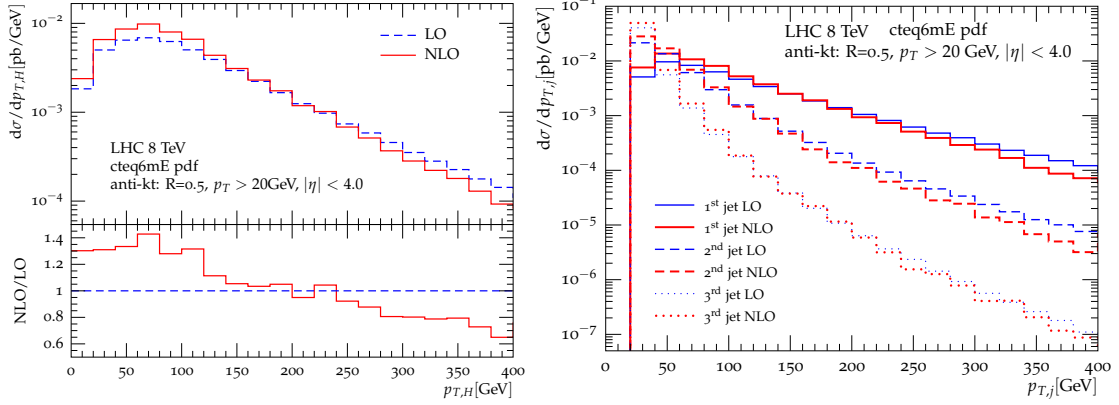


Figure 7.15.: Transverse momentum (p_T) distributions of the Higgs boson (left), including the K-factor, and the first, second, and third leading jet (right) in the process $pp \rightarrow H + 3j$ in GF.

7.2.4. H+2j and H+3j with ATLAS setup

A follow-up study of Higgs boson plus two and three jets production in gluon fusion was presented in [7]. Here, specific ATLAS cuts on the jets were used,

$$R = 0.4, \quad p_T > 30\text{GeV}, \quad |\eta| < 4.4. \quad (7.24)$$

and NINJA was used instead of XSAMURAI as integrand reduction library. Furthermore, the Higgs boson mass was changed to $m_H = 126$ GeV and the central scale set to $\mu = \hat{H}_T/2$ for both processes this time. This setup produced the following full LO and NLO cross sections. For $pp \rightarrow H + 2j$:

$$\sigma_{LO}[\text{pb}] = 1.23^{+37\%}_{-24\%} \quad \sigma_{NLO}[\text{pb}] = 1.590^{+4\%}_{-7\%}$$

and for $pp \rightarrow H + 3j$:

$$\sigma_{LO}[\text{pb}] = 0.381^{+53\%}_{-31\%} \quad \sigma_{NLO}[\text{pb}] = 0.485^{+3\%}_{-13\%}$$

Several preliminary distributions are presented in [7]. In Figure 7.16 the distributions of the transverse momentum and rapidity of the Higgs boson using this setup are given. Figures 7.17, 7.18 and 7.19 show these distributions for the leading, second leading and third leading jet respectively.

7.3. Higgs boson production in association with a $t\bar{t}$ pair and a jet

The production of a Higgs boson in association with a $t\bar{t}$ pair is a very important process, because it allows for a direct measurement of the Standard Model Yukawa coupling. Although

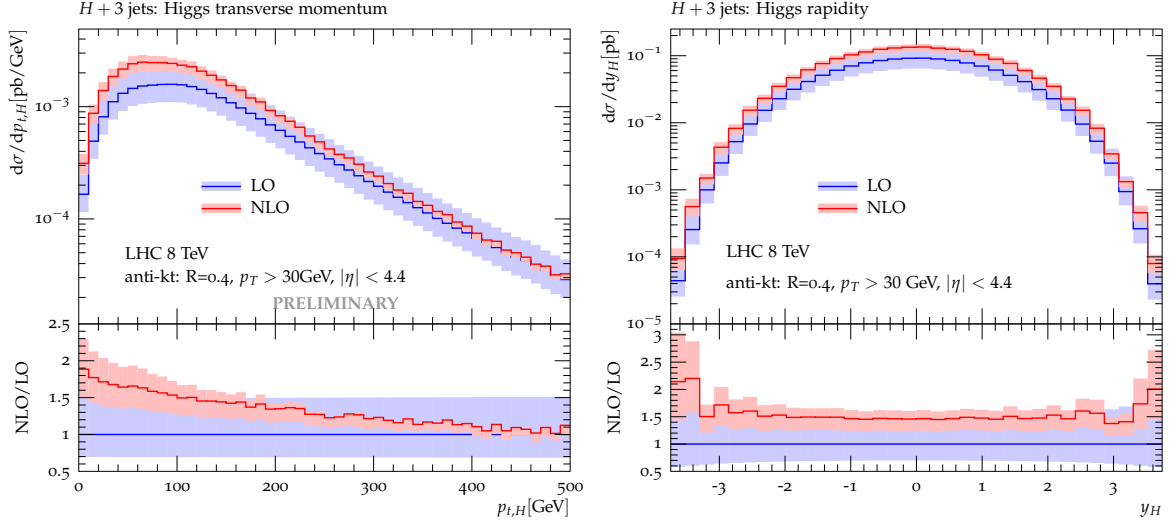


Figure 7.16.: Transverse momentum (p_T) and rapidity (y) distributions for the Higgs boson in the process $pp \rightarrow H + 3j$ in GF, using the ATLAS setup.

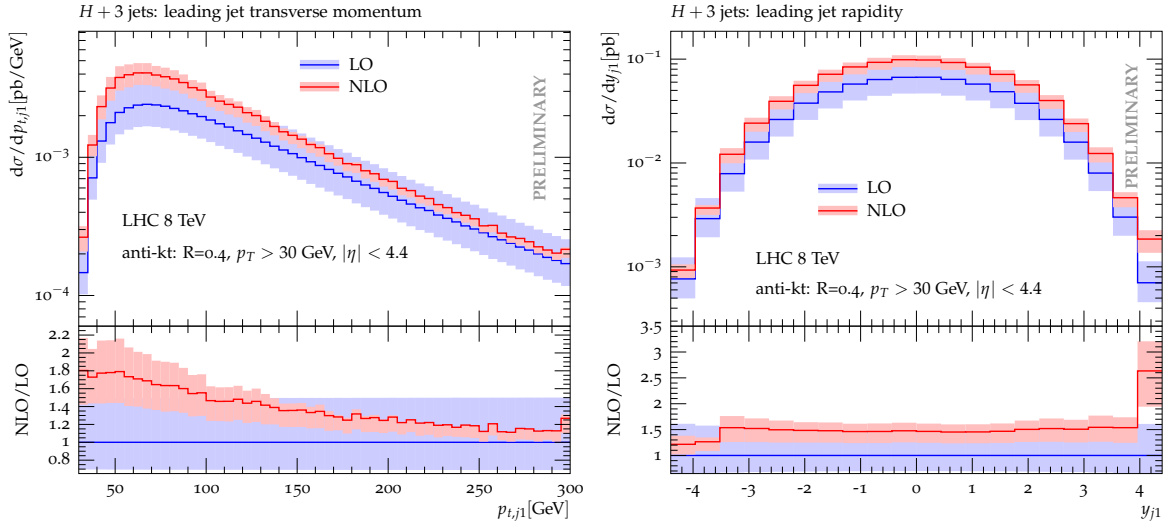


Figure 7.17.: Transverse momentum (p_T) and rapidity (y) distributions for the leading jet in the process $pp \rightarrow H + 3j$ in GF, using the ATLAS setup.

in theory this could be measured with Higgs boson production in association with any massive quark anti-quark pair, since the Yukawa coupling is proportional to the quarks mass, the one with the $t\bar{t}$ pair is by far the most relevant. Furthermore, differential observables and distributions of this process help in determining the coupling structure and parity properties of the Higgs boson [117, 154]. However, this process is difficult to measure with high statistics. Not only does it require a large center of mass energy for the creation of three heavy particles, which is suppressed by the PDFs, but also separating the signal and the background is far from trivial [155].

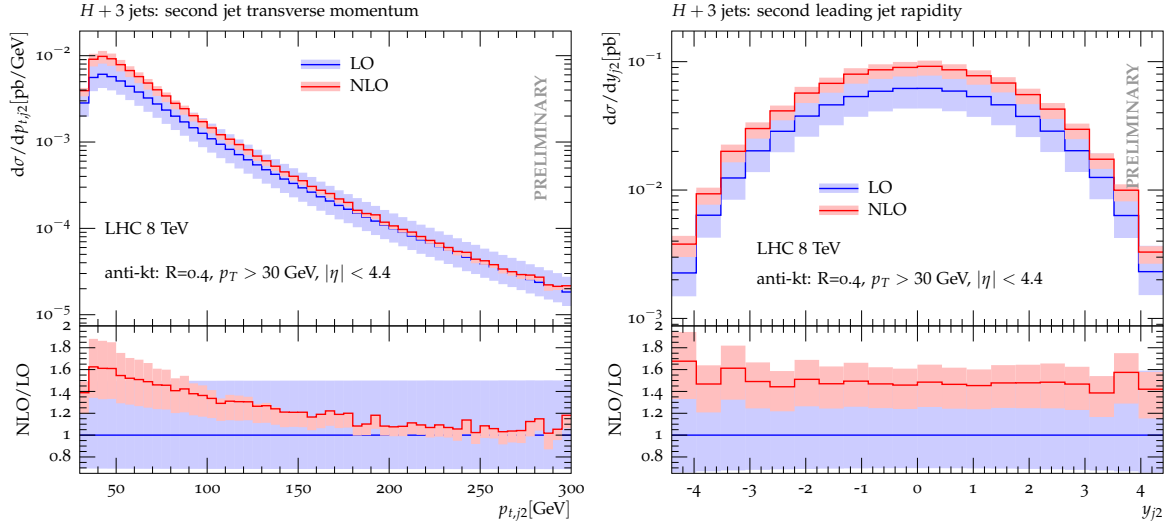


Figure 7.18.: Transverse momentum (p_T) and rapidity (y) distributions for the second leading jet in the process $pp \rightarrow H + 3j$ in GF, using the ATLAS setup.

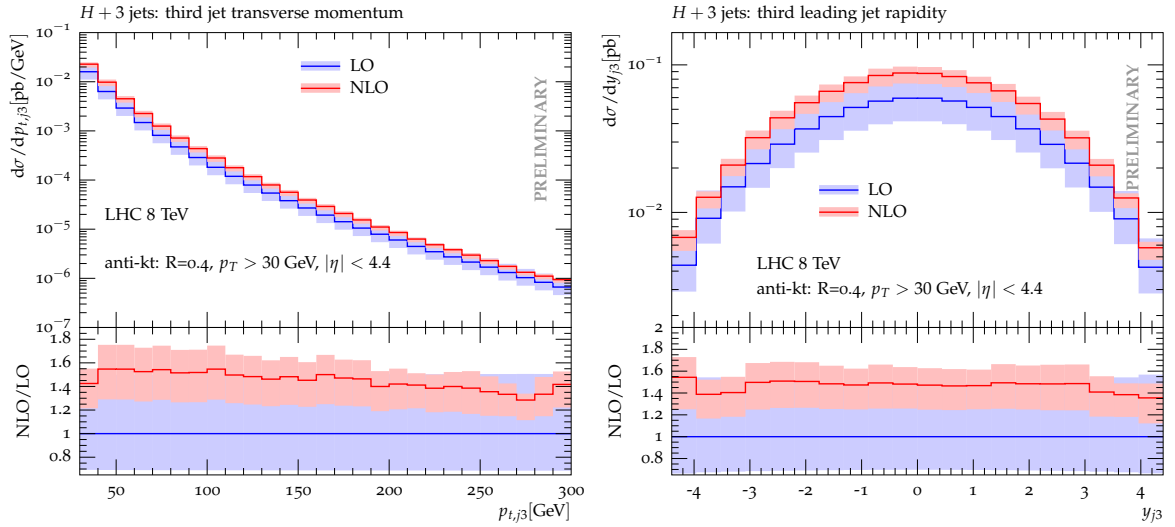


Figure 7.19.: Transverse momentum (p_T) and rapidity (y) distributions for the third leading jet in the process $pp \rightarrow H + 3j$ in GF, using the ATLAS setup.

7.3.1. $pp \rightarrow Ht\bar{t}j$

The production of $pp \rightarrow Ht\bar{t}$ at NLO in QCD has been calculated a while back [156–160]. In recent years, with the LHC going to higher center of mass energies, the process has been getting renewed attention [117, 154, 155, 161]. In [3], the calculation with an additional jet in the final state was presented: $pp \rightarrow Ht\bar{t}j$. Phenomenological analysis of this process is warranted, since the extra jet has an important impact on the kinematic region with high transverse momentum. In Figure 7.20, two example one-loop diagrams for this process are

shown.

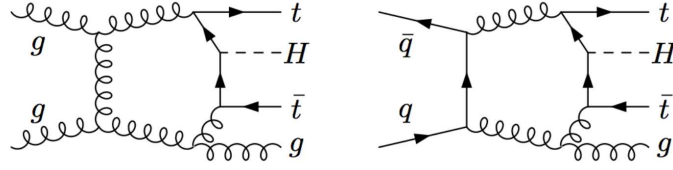


Figure 7.20.: Example of one-loop diagrams contributing to the NLO QCD corrections of $gg \rightarrow t\bar{t}Hg$ and $q\bar{q} \rightarrow t\bar{t}Hg$.

7.3.2. Renormalization of the Yukawa coupling

GOSAM automatically takes care of UV renormalization in QCD, but not of EW quantities. The renormalization of the Yukawa coupling of the $Ht\bar{t}$ -vertex appearing in this calculation therefore needs to be considered separately. The Yukawa coupling is proportional to the top-mass, for which we know the renormalization,

$$g_{Htt}^0 = -i \frac{m_t^0}{v} = -i \frac{(m_t + \delta m_t)}{v}, \quad (7.25)$$

where $v = 2M_W/g_W$ is the Higgs vacuum expectation value. The squared matrix element is proportional to the square of the expression, $2\Re[\mathcal{A}_0^\dagger \mathcal{A}_1] \propto (g_{Htt}^0)^2$, but since we know that $\delta m_t \propto \alpha_s$ (see (6.3)), we can ignore terms $(\delta m)^2 \propto \alpha_s^2$, because they are of a higher order than the one we are considering. Therefore the Yukawa counterterm is given by

$$\begin{aligned} |\mathcal{M}|_{\text{ct,Yuk}}^2 &= - \left(\frac{2\delta m_t}{m_t} \right) \cdot |\mathcal{M}|_{\text{tree}}^2 = - \frac{\alpha_s}{2\pi} \frac{(4\pi)^\epsilon}{\Gamma(1-\epsilon)} C_F \left(\frac{\mu^2}{m_t^2} \right)^\epsilon \left[\frac{3}{\epsilon} + 5 - 1_{\text{tHV}} \right] \cdot |\mathcal{M}|_{\text{tree}}^2 \\ &= - \frac{\alpha_s}{2\pi} \frac{(4\pi)^\epsilon}{\Gamma(1-\epsilon)} C_F \left[\frac{3}{\epsilon} + 3 \ln \left(\frac{\mu^2}{m_t^2} \right) + 5 \right] \cdot |\mathcal{M}|_{\text{tree}}^2 + \mathcal{O}(\epsilon), \end{aligned} \quad (7.26)$$

where in the last line the expression was truncated in the dimensional reduction scheme (DRED) at order $\mathcal{O}(\epsilon)$. From this one can read that the single pole acquires an additional piece,

$$\delta c_{-1} = -3C_F \cdot |\mathcal{M}|_{\text{tree}}^2, \quad (7.27)$$

and for the finite part this additional piece is

$$\delta c_0 = - \left[5C_F + 3C_F \ln \left(\frac{\mu^2}{m_t^2} \right) \right] |\mathcal{M}|_{\text{tree}}^2. \quad (7.28)$$

This is also the renormalization procedure followed in [157] and [159].

7.3.3. Setup and parameters

For the Born and real radiation contributions, the Monte Carlo program SHERPA [26] and the library AMEGIC [162] were used. SHERPA uses the Catani-Seymour dipole formalism [61,

62] and also performs the integration over the phase space and the analysis. The virtual contributions were provided by GOSAM, using ONELOOP [93] to provide the master integrals. This process was the first application where the integrand reduction program NINJA was used. The interface between SHERPA and GOSAM was realized using the BLHA1 standards. There are two independent subprocesses for this calculation,

$$q\bar{q} \rightarrow t\bar{t}Hg, \quad gg \rightarrow t\bar{t}Hg, \quad (7.29)$$

while the other subprocesses can be calculated by using crossings and/or relabeling. The ultraviolet, infrared and collinear singularities were regularized using DRED. Furthermore, following [157, 159], we used the $\overline{\text{MS}}$ scheme with the wave functions of the partons renormalized on-shell, causing the corresponding renormalization constants to exactly cancel the external self-energy corrections. The functioning of NINJA was checked against SAMURAI with ten thousand phase space points. We checked the cancellation of the poles from NINJA against their known values and verified the gauge invariance by replacing the external polarization vectors with their momentum to check the Ward identities. Just a few per mill of the points were unstable and all of them were recovered using GOLEM95C as rescue system. A non-exceptional phase space point for this process is given in Appendix F.6.

The EW scheme was set to the default in GOSAM, *i.e.* `ewchoice` equal to 1. The parameters for this calculation are given in Table 7.7.

Parameter	value
\sqrt{s}	8 TeV
m_H	126 GeV
m_t	172.5 GeV
m_W	80.419 GeV
m_Z	91.1876 GeV
α_{EW}^{-1}	132.50698

Table 7.7.: The parameters used in the calculation of $pp \rightarrow Ht\bar{t}j$.

The PDF sets used were CTEQ11 for the LO calculation and CT10 for the NLO one. We used the `anti-kt` algorithm implemented in FASTJET with the following cuts

$$p_{t,j} \geq 15\text{GeV}, \quad |\eta_j| \leq 4.0, \quad R = 0.5. \quad (7.30)$$

The calculations were performed using two different choices for the central renormalization and factorization scales $\mu_R = \mu_F = \mu_0$, namely $\mu_0 = \hat{H}_T$ and $\mu_0 = 2 \times \text{GA}_T$ with

$$\hat{H}_T = \sum_{\substack{\text{final} \\ \text{states } f}} |p_{T,f}|, \quad (7.31)$$

$$\text{GA}_T = \sqrt[3]{m_{T,H} m_{T,t} m_{T,\bar{t}}} + \sum_j |p_{T,j}|, \quad (7.32)$$

where the sum goes over the light partons j and GA_T abbreviates transverse geometric average.

7.3.4. Results

To validate our setup we first calculated the process without the additional jet, $pp \rightarrow Ht\bar{t}$. We compared it with the results in [117, 163] and found excellent agreement.

Proceeding to $pp \rightarrow Ht\bar{t}j$, with this setup, for the two scale choices, we obtain the total LO and NLO cross sections reported in Table 7.8.

Central Scale	σ_{LO} [fb]	σ_{NLO} [fb]
$2 \times GA_T$	$80.03^{+35.64}_{-23.02}$	$100.6^{+0.00}_{-9.43}$
\hat{H}_T	$88.93^{+41.41}_{-26.13}$	$102.3^{+0.00}_{-15.82}$

Table 7.8.: Total cross section for $pp \rightarrow t\bar{t}Hj$ for different choices of the central scale at LO and NLO.

We varied the renormalization and factorization scale simultaneously around the two central values and the result shows that the scale dependence is strongly reduced, see Figure 7.21. Both central scales appear to be close to the local extremum and are therefore close to the physical scale.

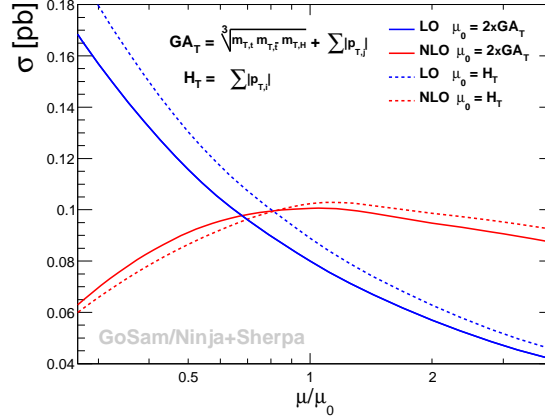


Figure 7.21.: Scale dependence of the total cross section for $pp \rightarrow Ht\bar{t}j$ at LO and NLO of.

In Figure 7.22 the invariant mass distributions of the $t\bar{t}$ pair at NLO are shown for the processes with and without the additional jet, relative to the LO of $pp \rightarrow Ht\bar{t}j$. These plots have $\mu = 2 \times GA_T$ as renormalization and factorization scale. For the process including the jet, the NLO distribution shows an increase with respect to the LO of about 20-35 percent, but a decrease with respect to the NLO of $pp \rightarrow Ht\bar{t}$. This is because the jet takes away energy from $t\bar{t}$ pair, which is in particular visible around the threshold. For higher values, the curves get closer.

In Figures 7.23 the distributions of the transverse momentum and pseudo-rapidity of the Higgs boson are given. The renormalization and factorization scale used for these plots was $\mu = \hat{H}_T$. NLO corrections become especially important in the kinematical regions of high transverse

momentum and low pseudo-rapidity. These are indeed the kinematical regions for boosted analyses [161, 164].

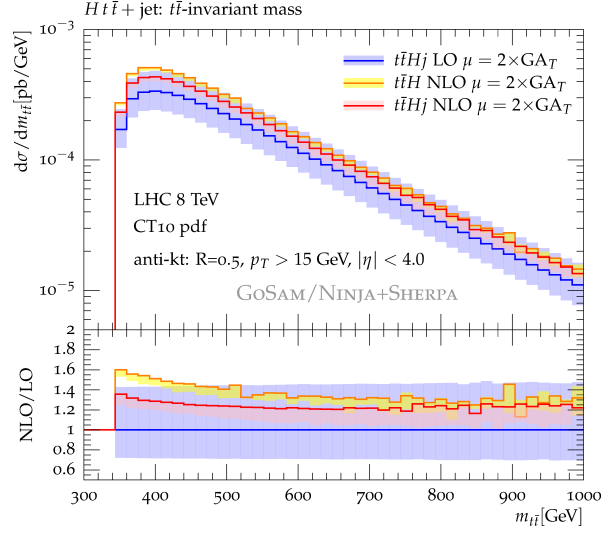


Figure 7.22.: Invariant mass distributions of the $t\bar{t}$ -pairs for $pp \rightarrow t\bar{t}H$ and $pp \rightarrow t\bar{t}Hj$ at NLO relative to the $pp \rightarrow t\bar{t}Hj$ at LO for $\mu = 2 \times GA_T$.

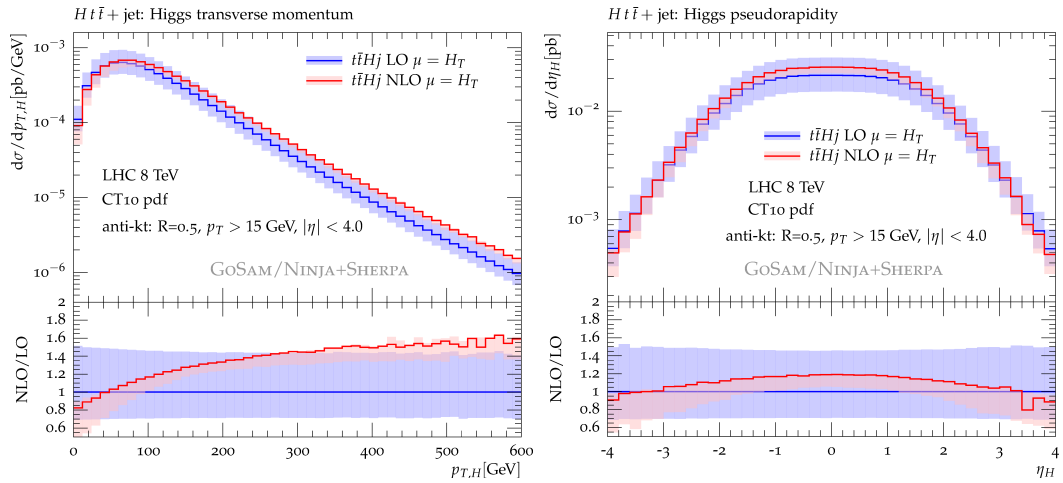


Figure 7.23.: Transverse momentum p_T and pseudo-rapidity η distribution of the Higgs boson at LO and NLO for $\mu = \hat{H}_T$.

8 ■ Framework for fully automatic NLO calculations

MADGRAPH5_AMC@NLO [47] is a publically available and fully automated framework for the computation of LO and NLO cross sections, also matched to parton showers, for any process. It merged its predecessors MADGRAPH5 [116] and AMC@NLO [117] into one code, with additional functionality. MADGRAPH5_AMC@NLO has a built-in OLP module called MADLOOP [163], that employs both an integrand decomposition procedure based on the OPP method and a tensor integral reduction procedure.

8.1. Overview MadGraph5_aMCatNLO

MADGRAPH5_AMC@NLO can be run through an interactive session, both for the generation of the code for a specific process and its actual calculation. Alternatively, one can use input cards specifying the details of the process. When generating a process, one needs to indicate if the process is to be calculated at LO or NLO. It will then proceed to write the code for the process in a directory specified by the user. When the generation is done, one can choose to launch the calculation, specifying either a fixed order calculation or including a parton shower. Decaying the particles using the MADSPIN module [165] is also a possibility. In the code there is the possibility to write an `analysis_card` to generate histograms, where the user implements his own analysis.

8.2. Description of the interface

The interface between GOSAM and MADGRAPH5_AMC@NLO is based on the BLHA1 standards [46]. MADGRAPH5_AMC@NLO can write a BLHA order file, which is then processed by GOSAM. The BLHA1 defines an array to pass the numerical value of parameters that are dynamical variables. The definition of the parameters passed through this array is set in the order file using the keyword `Parameters`. Although in principle extendable to up to ten parameters, at present only the first entry is used, to communicate the value of α_s . The order and contract files for the process computed in Section 8.4 are shown in Figures 8.2 and 8.2.

In order to run MADGRAPH5_AMC@NLO with GOSAM, a recent version of MADGRAPH5_AMC@NLO and GOSAM should be installed and the path to GOSAM included in the `$PATH` environment variable. When running the interactive session of MADGRAPH5_AMC@NLO, the command `set OLP GoSam` (case sensitive) changes the employed OLP from its default MadLoop to GOSAM. Alternatively, the file `/input/mg5_configuration.txt` can be directly

```

#OLE_order written by MadGraph5_aMC@NLO

MatrixElementSquareType CHaveraged
CorrectionType          QCD
IRregularisation       CDR
AlphasPower            2
AlphaPower             2
NJetSymmetrizeFinal    Yes
ModelFile              ./param_card.dat
Parameters             alpha_s

# process
21 21 -> 22 22 6 -6
2 -2 -> 22 22 6 -6
1 -1 -> 22 22 6 -6
-2 2 -> 22 22 6 -6
-1 1 -> 22 22 6 -6

```

Figure 8.1.: Example of an order file used in the interface between `MADGRAPH5_AMC@NLO` and `GoSam`.

edited to include the line `OLP = GoSam`.

After this is set, an NLO process can be generated in the usual way. The final step in the generation of a process, generating a directory for the output using the `output <dirname>` command, will now also generate a directory `<dirname>/OLP_virtuals` which contains the order and contract files along with a log file of the `GoSam` generation script `gosam.py` and a directory `/Virtuals` which contains the actual `GoSam` code.

8.3. Benchmark processes

In [47] a large number of example processes were calculated at LO and NLO, in the latter case using `MADLOOP`. Using the interface, a couple of these processes with up to five external particles were recalculated. Firstly, the LO and NLO results were confirmed using `MADGRAPH5_AMC@NLO` with `MADLOOP`, then the NLO result was recalculated using the interface with `GoSam`.

The list of parameters and cuts used for this reproduction of [47] is given in Table 8.3. The PDF set used was `MSTW2008nlo` with error at 68% confidence level (both for LO and NLO). The central scale was chosen to be

$$\mu_0 = \sum_i \hat{H}_T/2, \quad \text{with} \quad \hat{H}_T = \sqrt{p_{T,i}^2 + m_i^2}, \quad (8.1)$$

with the sum over the final state particles, and the renormalization and factorization scales were varied between $\frac{\mu_0}{2} < \mu_F, \mu_R < 2\mu_0$. The jet algorithm used was the anti- k_t algorithm, and photons were isolated using Frixione isolation with $\epsilon_\gamma = n = 1$ (see Section 2.4). The CKM matrix was chosen to be diagonal and all widths were set to zero.

The statistics per process were increased until the error was reduced to the same order of magnitude as the one quoted for that process in [47]. For some processes, this increase in

```

# vim: syntax=olp
#@OLP GoSam 2.0.0
#@IgnoreUnknown True
#@IgnoreCase False
#@SyntaxExtensions
MatrixElementSquareType CHaveraged | OK
CorrectionType QCD | OK
IRregularisation CDR | OK
AlphasPower 2 | OK
AlphaPower 2 | OK
NJetSymmetrizeFinal Yes | OK # Ignored by OLP
ModelFile ./param_card.dat | OK
Parameters alpha_s | OK
21 21 -> 22 22 6 -6 | 1 2
2 -2 -> 22 22 6 -6 | 1 0
1 -1 -> 22 22 6 -6 | 1 3
-2 2 -> 22 22 6 -6 | 1 1
-1 1 -> 22 22 6 -6 | 1 4

```

Figure 8.2.: Example of a contract file used in the interface between MADGRAPH5_AMC@NLO and GoSAM.

masses	
m_H	125 GeV
m_t	173.2 GeV
n_f	5
jets	
$R = 0.5, \quad p_{Tj} < 30, \quad \eta_j < 4.0$	
photons	
$R_\gamma = 0.7, \quad p_{T\gamma} < 20, \quad \eta_\gamma < 2.0$	
$\epsilon = n = 1.0$	

Table 8.1.: The parameters and cuts used for the reproduction of several processes in [47].

statistics was done through combining multiple runs of lower statistics through a weighted mean. For n measurements x_i with statistical error σ_i , this weighted mean is given by

$$\langle x \rangle = \left(\sum_{i=1}^n \frac{x_i}{\sigma_i^2} \right) \left(\sum_{i=1}^n \frac{1}{\sigma_i^2} \right)^{-1}, \quad (8.2)$$

and its standard deviation by

$$\sigma = \left(\sum_{i=1}^n \frac{1}{\sigma_i^2} \right)^{-\frac{1}{2}}. \quad (8.3)$$

In Table 8.3 these results are collected. It shows in the last column the agreement between the two results as the fraction of the standard deviation,

$$\frac{|x_G - x_M|}{\sqrt{\sigma_G^2 + \sigma_M^2}}, \quad (8.4)$$

		MADGRAPH5_AMC@NLO + MADLOOP	MADGRAPH5_AMC@NLO + GoSAM	st.dev.
$pp \rightarrow Z$	LO	$(4.248 \pm 0.005) \cdot 10^4$		
	NLO	$(5.410 \pm 0.022) \cdot 10^4$	$(5.414 \pm 0.013) \cdot 10^4$	0.088
$pp \rightarrow Zj$	LO	$(7.209 \pm 0.005) \cdot 10^3$		
	NLO	$(9.742 \pm 0.035) \cdot 10^3$	$(9.712 \pm 0.040) \cdot 10^3$	0.564
$pp \rightarrow Zjj$	LO	$(2.348 \pm 0.006) \cdot 10^3$		
	NLO	$(2.665 \pm 0.010) \cdot 10^3$	$(2.672 \pm 0.029) \cdot 10^3$	0.228
$pp \rightarrow W^\pm$	LO	$(1.375 \pm 0.002) \cdot 10^5$		
	NLO	$(1.773 \pm 0.007) \cdot 10^5$	$(1.779 \pm 0.013) \cdot 10^5$	0.406
$pp \rightarrow W^\pm j$	LO	$(2.045 \pm 0.001) \cdot 10^4$		
	NLO	$(2.843 \pm 0.010) \cdot 10^4$	$(2.832 \pm 0.024) \cdot 10^4$	0.423
$pp \rightarrow W^\pm jj$	LO	$(6.805 \pm 0.015) \cdot 10^3$		
	NLO	$(7.786 \pm 0.030) \cdot 10^3$	$(7.851 \pm 0.098) \cdot 10^3$	0.634
$pp \rightarrow t\bar{t}$	LO	$(4.584 \pm 0.003) \cdot 10^2$		
	NLO	$(6.741 \pm 0.023) \cdot 10^2$	$(6.746 \pm 0.025) \cdot 10^2$	0.147
$pp \rightarrow t\bar{t}\gamma$	LO	$(1.204 \pm 0.001) \cdot 10^0$		
	NLO	$(1.744 \pm 0.005) \cdot 10^0$	$(1.745 \pm 0.001) \cdot 10^0$	0.157
$pp \rightarrow t\bar{t}Z$	LO	$(5.273 \pm 0.004) \cdot 10^{-1}$		
	NLO	$(7.598 \pm 0.026) \cdot 10^{-1}$	$(7.619 \pm 0.009) \cdot 10^{-1}$	0.756
$pp \rightarrow t\bar{t}H$	LO	$(3.579 \pm 0.003) \cdot 10^{-1}$		
	NLO	$(4.608 \pm 0.016) \cdot 10^{-1}$	$(4.608 \pm 0.006) \cdot 10^{-1}$	0.012
$pp \rightarrow t\bar{t}Hj$	LO	$(2.674 \pm 0.041) \cdot 10^{-1}$		
	NLO	$(3.244 \pm 0.025) \cdot 10^{-1}$	$(3.205 \pm 0.009) \cdot 10^{-1}$	1.455

Table 8.2.: Reproduction of fixed order NLO cross sections in pb for a number of processes from [47] with GoSAM. The last column shows the agreement between the two numbers using formula (8.4).

where $x_G \pm \sigma_G$ and $x_M \pm \sigma_M$ are the results using GoSAM and MADLOOP respectively. Results that are less than two standard deviations apart were classified as being in good enough agreement.

8.4. Production of a top anti-top pair in association with two photons

In addition to the comparison of the processes listed in Table 8.3, which were used to validate the interface, a more thorough analysis was performed for the production of a top anti-top pair in association with two photons, which will be presented in ???. This is an important background to the production of a Higgs boson with a top anti-top pair, $pp \rightarrow Ht\bar{t}$, with the Higgs boson subsequently decaying into two photons.

8.4.1. Setup

Two different cases for the center-of-mass energy were considered, 8 TeV and 13 TeV. The setup was very similar to the one in Section 8.3, but there are some important differences. The mass of the Higgs boson was set to $m_H = 125$ GeV, the mass of the top quark to $m_t = 173.2$. The process was calculated in the $n_f = 5$ model. As indicated in [166], the value of the electroweak coupling should be set to its low energy limit $\alpha_{EW}^{-1} = 137.0$. The mass of the Z boson was set to $m_Z = 91.1876$ GeV and the value of the Fermi constant to $G_F = 1.16639 \cdot 10^{-5}$, which fixes the electroweak scheme. For the jets that can occur in the real radiation, the anti- k_t algorithm was used, as implemented in the code FASTJET [73, 124, 125], with minimal transverse momentum $p_{jT\min} = 20$ GeV, jet-radius $R = 0.4$ and maximal absolute pseudo-rapidity $|\eta_j| < 4.4$. For the photons, Frixiene isolation (see Section 2.4) was used, with minimal transverse momentum $p_{\gamma T\min} = 20$, radius of isolation $R_\gamma < 0.4$ and Frixiene parameters $n = 1.0$ and $\epsilon_\gamma = 1.0$. Furthermore, an isolation radius between the two photons $R_{\gamma\gamma} = 0.4$ was implemented by hand. In leading order calculations, the PDF set CTEQ6L1 [126] was used, at next-to-leading order the PDF set CT10. The renormalization and factorization scale were set to $\mu_R = \mu_F = \mu_0$ with

$$\mu_0 = \hat{H}_T/2, \quad \text{with} \quad \hat{H}_T = \sum_{\text{final state } i} m_{T,i}, \quad (8.5)$$

where the sum goes over the final state particles.

8.4.2. Comparison with Sherpa and MadLoop

To confirm the interface was working properly, first the total integrated cross section was calculated at LO and NLO for three combinations: MADGRAPH5_AMC@NLO + GoSAM, SHERPA + GoSAM and MADGRAPH5_AMC@NLO + MADLOOP. The results are given in Tables 8.3 and 8.4. The LO is calculated by the MC alone, hence at LO there are only two numbers to compare. The LO cross sections agreed very well.

$\sqrt{s} = 8$ TeV	SHERPA+GoSAM	MADGRAPH5_AMC@NLO + MADLOOP	MADGRAPH5_AMC@NLO + GoSAM
LO	$1.0246 \pm 3.51 \cdot 10^{-4}$	$1.0241 \pm 5.50 \cdot 10^{-4}$	
NLO	$1.3593 \pm 1.80 \cdot 10^{-3}$	$1.3507 \pm 5.85 \cdot 10^{-3}$	$1.3537 \pm 1.21 \cdot 10^{-3}$

Table 8.3.: Total cross sections in fb at center-of-mass energy $\sqrt{s} = 8$ TeV for combinations of MCs and OLPs, at LO and NLO.

$\sqrt{s} = 13$ TeV	SHERPA + GoSAM	MADGRAPH5_AMC@NLO + MADLOOP	MADGRAPH5_AMC@NLO + GoSAM
LO	$3.1101 \pm 1.65 \cdot 10^{-3}$	$3.1131 \pm 1.72 \cdot 10^{-3}$	$3.1102 \pm 1.69 \cdot 10^{-3}$
NLO	$4.3875 \pm 6.83 \cdot 10^{-3}$	$4.3576 \pm 1.59 \cdot 10^{-2}$	$4.3194 \pm 1.89 \cdot 10^{-2}$

Table 8.4.: Total cross sections in fb at center-of-mass energy $\sqrt{s} = 13$ TeV for combinations of MCs and OLPs, at LO and NLO.

Proceeding to NLO, notice that MADGRAPH5_AMC@NLO + MADLOOP agrees excellently with MADGRAPH5_AMC@NLO + GoSAM, which also was the conclusion in the last section. Also, SHERPA+GoSAM agrees very well with MADGRAPH5_AMC@NLO + MADLOOP.

To fully test the remaining relation, between SHERPA+GoSAM and MADGRAPH5_AMC@NLO + GoSAM, the process with center-of-mass energy 8 TeV was rerun for both combinations with higher statistics and an analysis file in place to create differential distributions. These are shown in Figures 8.3, 8.4 and 8.5. The ratio of the two results is shown at the bottom of each plot. The width of the band of this ratio is calculated by using the relative errors in quadrature:

$$\sigma_{\text{ratio}} = \sqrt{\left(\frac{\sigma_S}{x_S}\right)^2 + \left(\frac{\sigma_{\text{MG}}}{x_{\text{MG}}}\right)^2} \quad (8.6)$$

where x and σ are the result and error for a bin for SHERPA (S) and MADGRAPH5_AMC@NLO (MG).

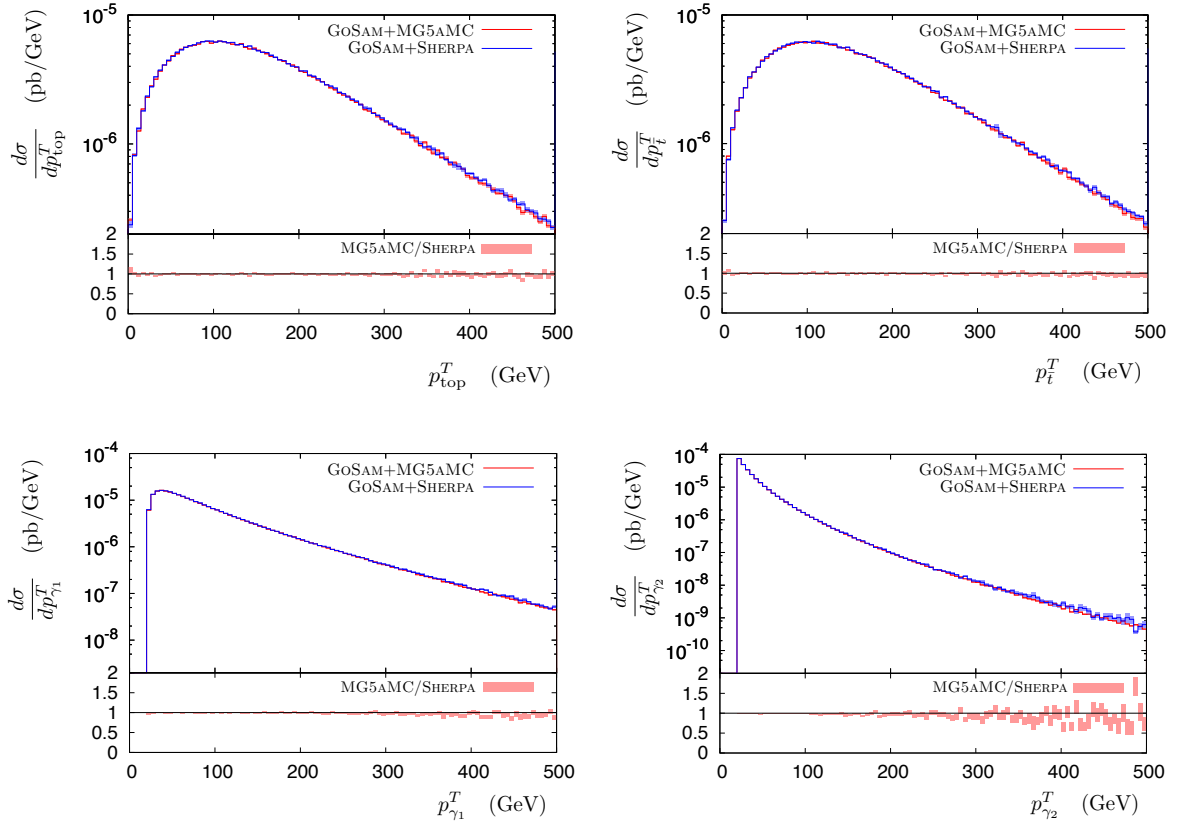


Figure 8.3.: The distributions of the transverse momenta of the four particles, using SHERPA + GoSAM (blue) and MADGRAPH5_AMC@NLO + GoSAM (red). The width of the band in the ratio plot at the bottom of each plot is calculated using equation (8.7).

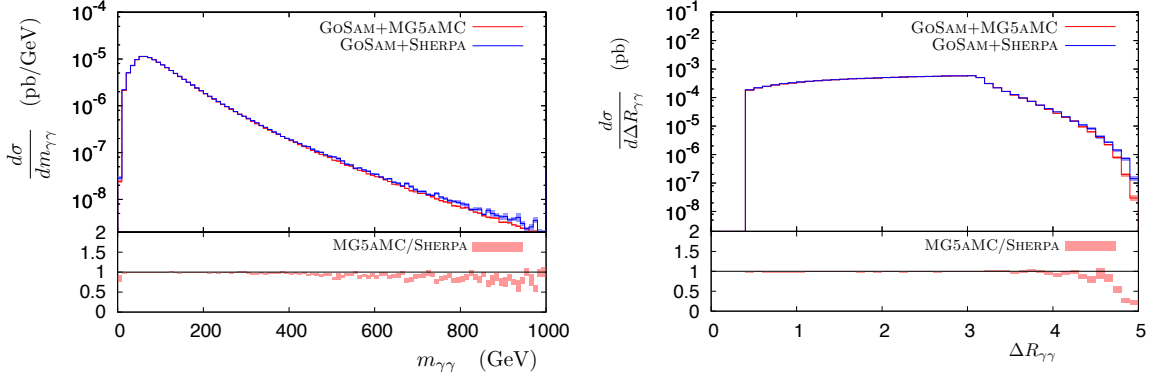


Figure 8.4.: The distributions of the invariant mass $m_{\gamma\gamma}$ (left) and separation $\Delta R_{\gamma\gamma}$ (right) of the two photons, using SHERPA + GoSAM (blue) and MADGRAPH5_AMC@NLO + GoSAM (red). The width of the band in the ratio plot at the bottom of each plot is calculated using equation (8.7).

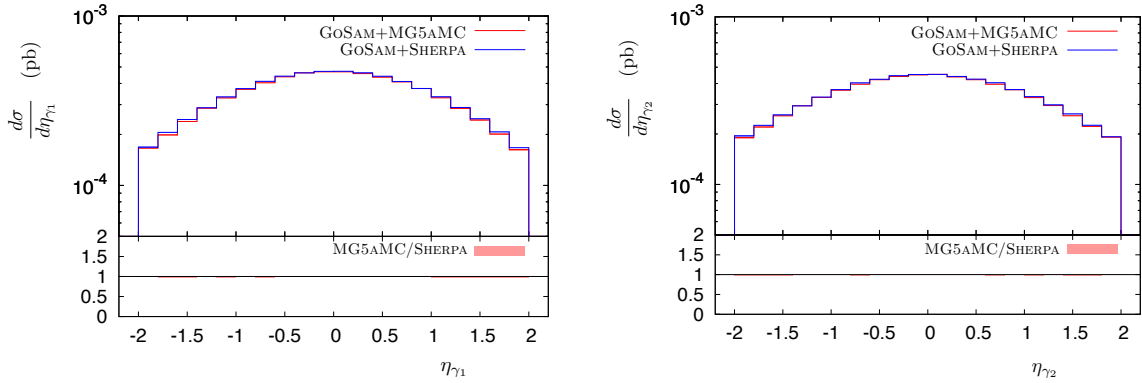


Figure 8.5.: The LO distributions of the rapidity of the hardest photon (left) and second hardest photon (right), using SHERPA + GoSAM (blue) and MADGRAPH5_AMC@NLO + GoSAM (red). The width of the band in the ratio plot at the bottom of each plot is calculated using equation (8.7).

8.4.3. Phenomenological results

In Figures 8.6, 8.7, 8.8 and 8.9 the differential distributions for the calculation using MADGRAPH5_AMC@NLO + GoSAM are shown again, but this time with respect to the same distributions at LO. It is interesting to note that the K-factor is really flat at about 30% for the entire range of transverse momentum distributions (figure 8.6), as well as for the rapidity distributions of the photons (figure 8.9). For the invariant mass $m_{\gamma\gamma}$ of the two photons and their separation $\Delta R_{\gamma\gamma}$ (figure 8.7), although less so in the high energy tail, this also seems to hold quite well. The rapidity distributions of the top and the anti-top (figure 8.8) show a more involved

K-factor. Similarly as before, the bandwidth of the K-factor is given by

$$\sigma_{\text{K-factor}} = \sqrt{\left(\frac{\sigma_{\text{NLO}}}{x_{\text{NLO}}}\right)^2 + \left(\frac{\sigma_{\text{LO}}}{x_{\text{LO}}}\right)^2}. \quad (8.7)$$

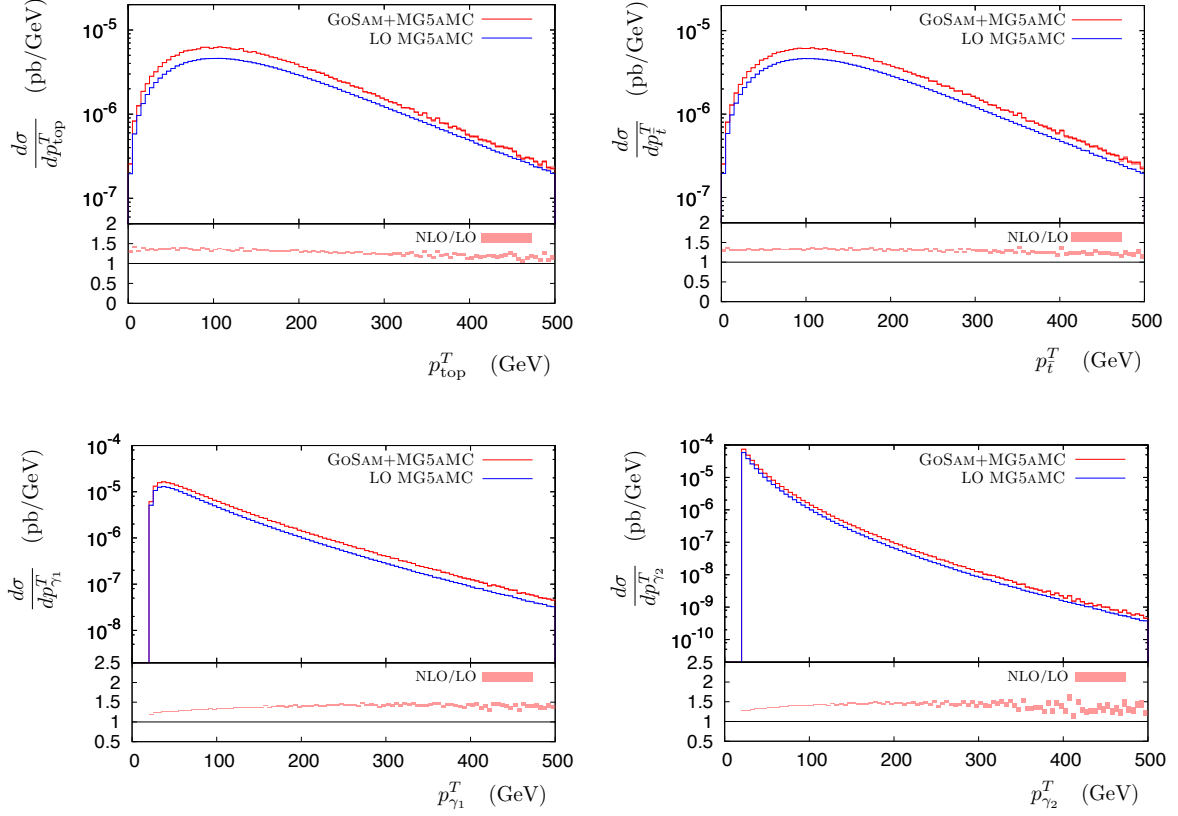


Figure 8.6.: The LO (blue) and NLO (red) distributions of the transverse momenta of the four particles. The width of the band in the K-factor at the bottom of each plot is calculated using equation (8.7).

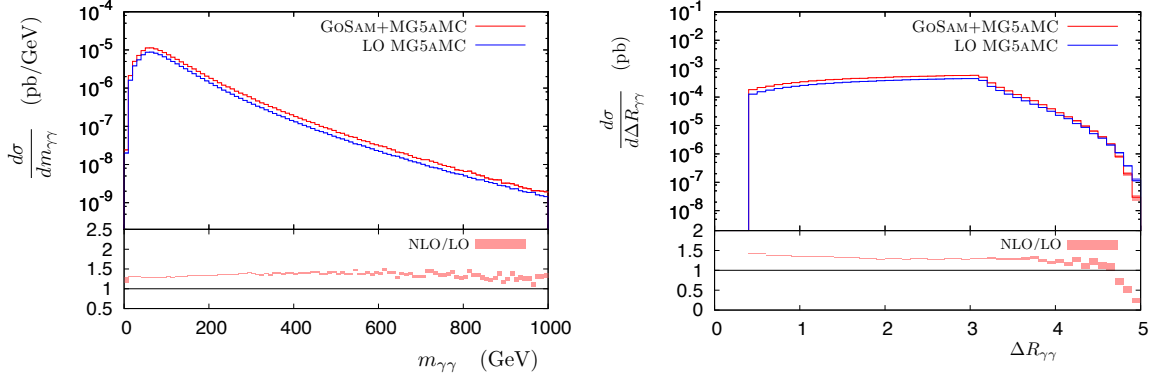


Figure 8.7.: The LO (blue) and NLO (red) distributions of the invariant mass $m_{\gamma\gamma}$ (left) and separation $\Delta R_{\gamma\gamma}$ (right) of the two photons. The width of the band in the K-factor at the bottom of each plot is calculated using equation (8.7).

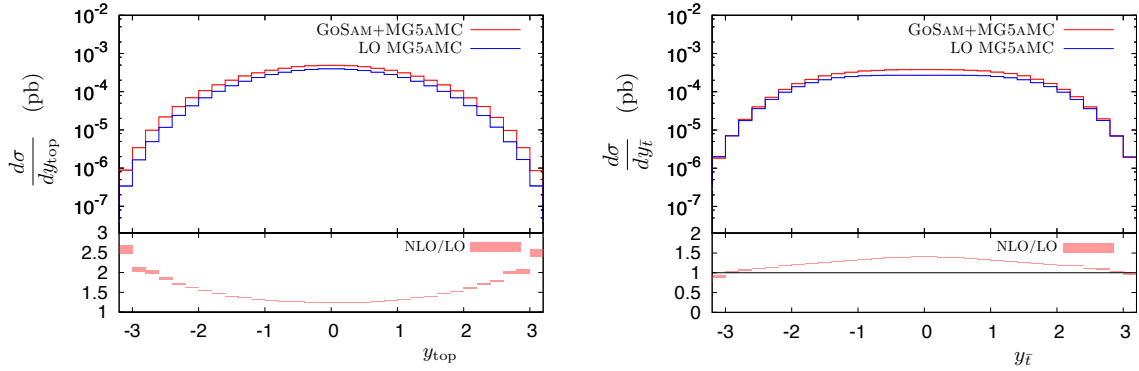


Figure 8.8.: The LO (blue) and NLO (red) distributions of the rapidity of the top (left) and anti-top (right). The width of the band in the K-factor at the bottom of each plot is calculated using equation (8.7).

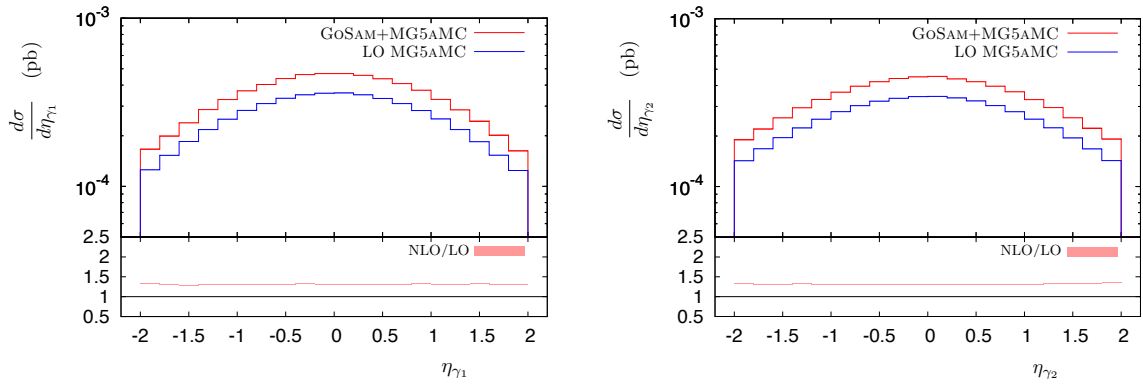


Figure 8.9.: The LO (blue) and NLO (red) distributions of the rapidity of the hardest photon (left) and second hardest photon (right). The width of the band in the K-factor at the bottom of each plot is calculated using equation (8.7).

9 ■ Conclusions

With the successful running of the LHC in recent years and the resulting increased precision of experimental measurements, efforts on increasing the precision on theoretical predictions have had to keep pace. This requirement manifested itself at two frontiers: Firstly, due to increased center-of-mass energy, there was an increased need for higher final state multiplicity processes, often including massive particles. Secondly, calculations at higher orders in perturbation theory were warranted, in particular the standard had to shift from leading order to *next-to-leading order* (NLO) in perturbation theory to obtain the desired accuracy. The combination of these two elements leads to calculations with thousands or even tens of thousands of one-loop diagrams. It was this challenge that pushed for more efficient ways to treat one-loop calculations, as well as for the automation of these kind of calculations.

With this in mind, several novel techniques for one-loop calculations were developed in recent years. We discussed the mechanics of *Passarino-Veltman reduction*, but we mainly focused on the *d-dimensional integrand reduction algorithm* as implemented in SAMURAI. This code is embedded in GOSAM, an automated framework for the generation and evaluation of one-loop diagrams, which was described with a particular focus on its recent upgrade to GOSAM2.0. As an example of the strength and range of capabilities of the framework, the virtual QCD corrections to the production of a Higgs boson with two and three associated jets in *vector boson fusion* ($pp \rightarrow H + \text{jets}$ in VBF) were computed. The tests performed on the precision and stability of GOSAM2.0 were described, as well as its application to a process very relevant to LHC, the production of a Higgs boson in association with a $t\bar{t}$ pair and an additional jet ($pp \rightarrow Ht\bar{t}j$). The Higgs boson production channel with the highest cross section, as well as the main background to VBF, is through *gluon fusion*. The effective vertex appearing in this calculation can cause the rank of the numerator of the integrand to exceed the number of denominators; one-loop diagrams with this property are hence known as higher-rank diagrams. The original integrand reduction algorithm was not equipped to handle these higher-rank numerators and therefore had to be extended. This extension was implemented in XSAMURAI, which was used for the calculation of the associated production of a Higgs boson with two and three additional jets in gluon fusion ($pp \rightarrow H + 3j$ in GF). The latter encompasses the calculation of well over thirteen thousand loop diagrams and can therefore without doubt be considered among the most challenging NLO calculations ever performed. Because of the higher-rank extension, GOSAM is to this date the only program capable of calculating this process. One-loop calculations are only one ingredient of a full NLO calculation; the other ones are provided by Monte Carlo programs (MCs). With the increase in number of available one-loop providers (OLPs) like GOSAM, as well as Monte Carlo tools, the need for a standardized interface between the two became apparent. This standard, known as the *Binoth-Les Houches Accord* (BLHA), was described, as well as its recent upgrade. Particular detail was given to the

implementation of the BLHA to the interface between GOSAM and MADGRAPH5_AMC@NLO, focussing on the production of a $t\bar{t}$ pair in association with two photons ($pp \rightarrow t\bar{t}\gamma\gamma$), an important background process to $pp \rightarrow Ht\bar{t}$.

It is worth to stress again the importance of automation in modern particle physics phenomenology. Many of the calculations performed in recent years, including some of the more challenging ones described in this work, were unthinkable only a decade ago. Yet, these calculations proved to be imperative by the parallel swift advancement on the experimental side. The framework presented in this work covers a wide range of ingredients, from the algebraic treatment of integrands all the way to distributions of observables in Monte Carlo event simulations. In essence, thanks to the full automation of all its ingredients and the realized interface between them, NLO calculations that used to require years of expertise and dedication have been reduced to figuratively ‘pressing a button’.

A ■ Feynman rules

In this appendix the Feynman rules derived in Chapter 3 and Section 7.2 are collected.

A.1. Electroweak sector

The Feynman rules collected in this section are derived in Section 3.1. They are given in the unitary gauge. GOSAM uses a different gauge, in which Goldstone bosons and ghosts can participate. However, these are only relevant when doing NLO EW calculations, which are not discussed in this work. Goldstone bosons can and do appear in the calculation of Higgs boson production in VBF, but since their couplings to fermions are proportional to the fermion mass, this contribution is zero. For clarity, the notation g_W is used as the coupling of $SU(2)_w$, corresponding to g in Section 3.1.

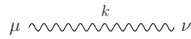
Vector boson propagator

photon

$$\frac{-ig^{\mu\nu}}{k^2 + i\epsilon}$$

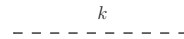
V=W,Z

$$\frac{-i}{k^2 - m_V^2 + i\epsilon} \left(g^{\mu\nu} - \frac{k^\mu k^\nu}{m_V^2} \right)$$

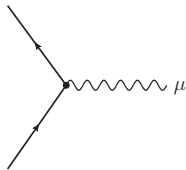


Higgs boson propagator

$$\frac{i}{k^2 - m_H + i\epsilon}$$



Fermion-vector boson vertex



Fermion-photon vertex

$$-iQ_f e \gamma^\mu$$

Lepton-W vertex

$$-i \frac{g_W}{2\sqrt{2}} \gamma^\mu (1 - \gamma^5)$$

Fermion-W vertex

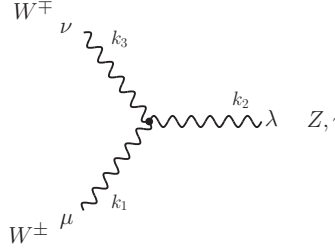
$$-i \frac{e_f}{2\sqrt{2} \sin \theta_W} \gamma^\mu (1 - \gamma^5) V_{ji}$$

Fermion-Z vertex

$$-i \frac{e_f}{2 \sin \theta_W \cos \theta_W} \gamma^\mu (V - A \gamma^5)$$

with $V = I_3^f - 2Q_f \sin \theta_W$ and $A = I_3^f$.

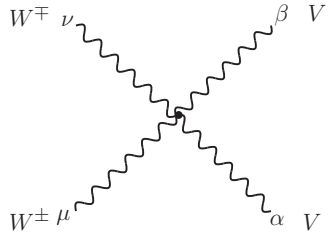
W-Photon,Z three-vertex



$$ig_V \left(g^{\mu\nu} (k_1 - k_2)^\lambda + g^{\nu\lambda} (k_2 - k_3)^\mu + g^{\lambda\mu} (k_3 - k_1)^\nu \right)$$

with $g_V = e, e \cot \theta_W$ for γ, Z .

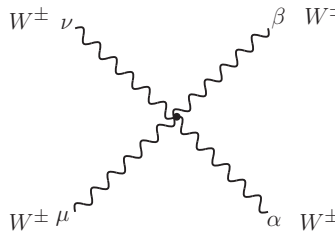
W-{Photon,Z} four-vertex



$$-ig_{V_1} g_{V_2} \left(2g^{\alpha\beta} g^{\mu\nu} - g^{\alpha\mu} g^{\beta\nu} - g^{\alpha\nu} g^{\beta\mu} \right)$$

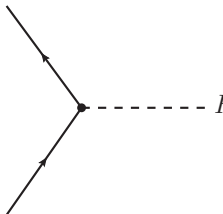
with $g_V = e, e \cot \theta_W$ for γ, Z .

W-boson four-vertex



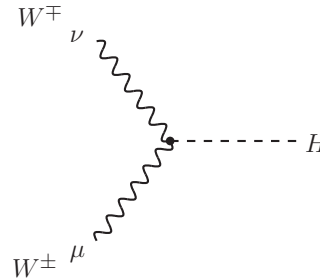
$$ig_W^2 \left(2g^{\alpha\beta} g^{\mu\nu} - g^{\alpha\mu} g^{\beta\nu} - g^{\alpha\nu} g^{\beta\mu} \right)$$

fermion-Higgs boson coupling



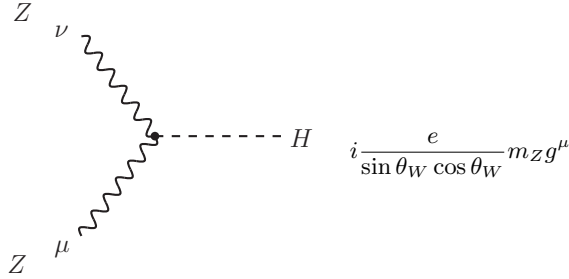
$$-i \frac{g_W}{2m_W} m_f$$

W-Higgs boson three-vertex

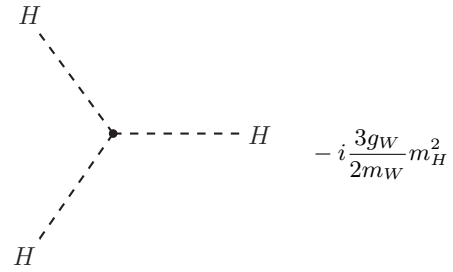


$$ig_W m_W g^{\mu\nu}$$

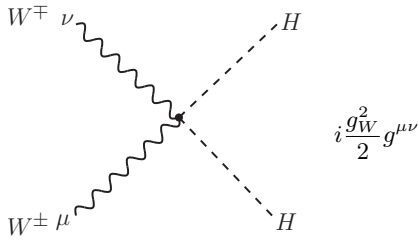
Z-Higgs boson three-vertex



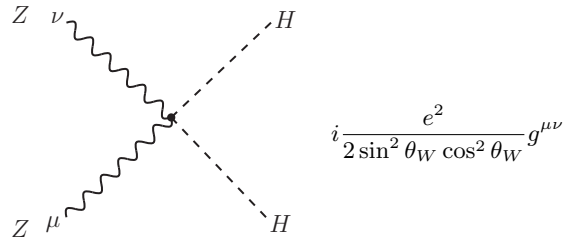
Higgs boson three-vertex



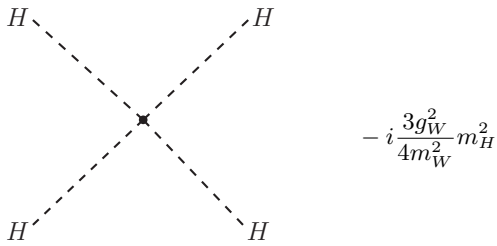
W-Higgs boson four-vertex



Z-Higgs boson four-vertex



Higgs boson four-vertex



A.2. Quantum Chromodynamics

The Feynman rules collected in this section are derived in Section 3.2. λ is the gauge fixing parameter as defined by expression (3.35).

Gluon propagator

$$\mu, a \overbrace{\text{oooooooooooooooooooo}}^k \nu, b \quad \frac{i\delta^{AB}}{k^2 + i\epsilon} \left(-g^{\mu\nu} + (1 - \lambda) \frac{k^{\mu\nu}}{k^2 + i\epsilon} \right)$$

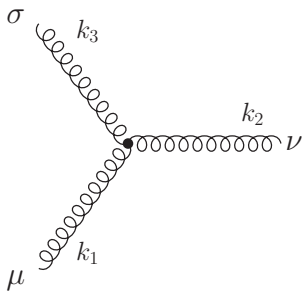
Ghost propagator

$$i \text{---} \xrightarrow{k} \text{---} j \quad \delta^{AB} \frac{i}{(k^2 + i\epsilon)}$$

Quark propagator

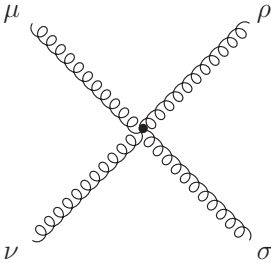
$$i \xrightarrow{k} j \quad \delta^{ab} \frac{i}{(\not{k} - m + i\epsilon)_{ji}}$$

Three-gluon vertex



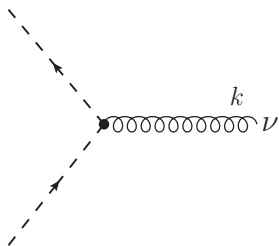
$$-g_s f^{ABC} \left(g^{\mu\nu} (k_1 - k_2)^\rho + g^{\nu\rho} (k_2 - k_3)^\mu + g^{\rho\mu} (k_3 - k_1)^\nu \right)$$

Four-gluon vertex



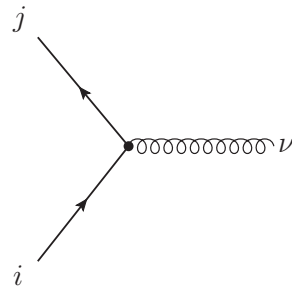
$$-ig_s^2 \left(f^{EAC} f^{EBD} (g^{\mu\nu} g^{\rho\sigma} - g^{\mu\sigma} g^{\nu\rho}) \right. \\ \left. f^{EAD} f^{EBC} (g^{\mu\nu} g^{\rho\sigma} - g^{\mu\rho} g^{\nu\sigma}) \right. \\ \left. f^{EAB} f^{ECD} (g^{\mu\sigma} g^{\nu\rho} - g^{\mu\rho} g^{\nu\sigma}) \right)$$

Ghost-gluon vertex



$$g_s f^{ABC} k^\mu$$

Quark-gluon vertex

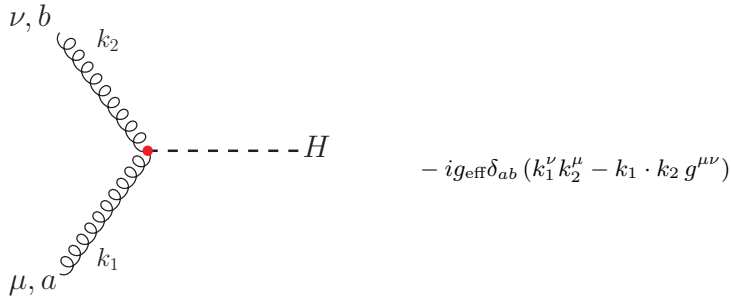


$$-ig_s (t^A)_{cb} (\gamma^\mu)_{ji}$$

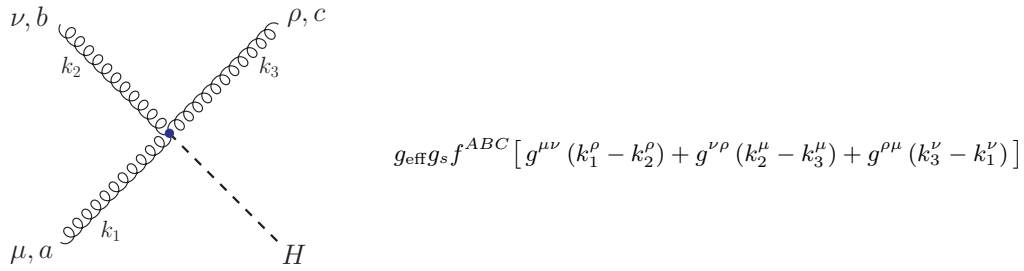
A.3. Effective Higgs boson vertices

In this section the Feynman rules for effective Higgs boson vertices are collected, using g_{eff} as given by equation (7.5).

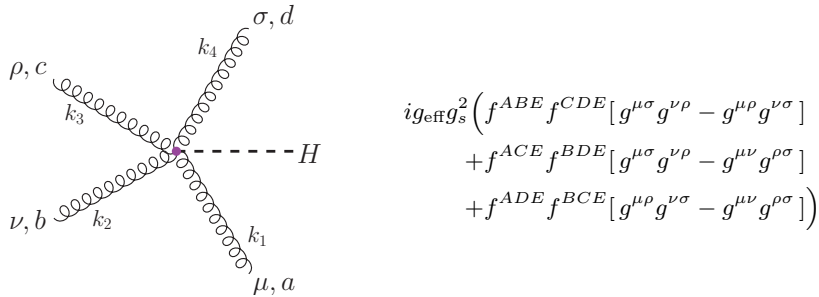
Higgs boson-gluon three-vertex



Higgs boson-gluon four-vertex



Higgs boson-gluon five-vertex



B ■ One-loop integrals

In this appendix explicit expressions for relevant one-loop integrals are derived. We will make frequent use of the Gamma function,

$$\Gamma(t) = \int_0^\infty dx x^{t-1} e^{-x}, \quad (\text{B.1})$$

which is the generalization of the factorial function from natural to real and complex numbers,

$$\Gamma(n) = (n-1)! \quad \forall n \in \mathbb{N}. \quad (\text{B.2})$$

It has the properties

$$\Gamma(1) = 1, \quad \Gamma(z+1) = z\Gamma(z), \quad z \in \mathbb{C}. \quad (\text{B.3})$$

The expressions for scalar integrals used in this section can be found in the literature, for example in Appendix A.1 of [167]. Important to note here is that

$$\lim_{\epsilon \rightarrow 0} (\epsilon I_i) = m_i^2, \quad \lim_{\epsilon \rightarrow 0} (\epsilon I_{ij}) = \frac{1}{2}, \quad \lim_{\epsilon \rightarrow 0} (\epsilon I_{ijk}) = 0. \quad (\text{B.4})$$

B.1. Higher dimensional integrals

Integrals with a power of μ^2 in the numerator of the integrand can always be rewritten to higher dimensional ones. Consider an integral

$$\int d^d \bar{q} (\mu^2)^r f(q^\alpha, \mu^2) = \int d^4 q \int d^{-2\epsilon} \mu (\mu^2)^r f(q^\alpha, \mu^2). \quad (\text{B.5})$$

In general for an integration over an n -dimensional space, one has

$$d^n x = x^{n-1} dx d\Omega_{n-1}, \quad \int d\Omega_n = \frac{2\pi^{(n+1)/2}}{\Gamma\left(\frac{n+1}{2}\right)}, \quad (\text{B.6})$$

so we can write, using the fact that $d\mu = \frac{1}{2}(\mu^2)^{-1} d\mu^2$,

$$\begin{aligned} \int d^{-2\epsilon} \mu (\mu^2)^r f(q^\alpha, \mu^2) &= \int d\Omega_{-1-2\epsilon} \int_0^\infty d\mu^2 (\mu^2)^{-1-\epsilon-r} f(q^\alpha, \mu^2) \\ &= \frac{\int d\Omega_{-1-2\epsilon}}{\int d\Omega_{2r-1-2\epsilon}} \int_0^\infty d^{2r-2\epsilon} \mu f(q^\alpha, \mu^2). \end{aligned} \quad (\text{B.7})$$

Since $r \in \mathbb{N}$, we can write for the factor in front,

$$\begin{aligned} \frac{\int d\Omega_{-1-2\epsilon}}{\int d\Omega_{2r-1-2\epsilon}} &= \frac{1}{\pi^r} \frac{\Gamma(r-\epsilon)}{\Gamma(-\epsilon)} = \frac{1}{\pi^r \Gamma(-\epsilon)} (r-\epsilon-1)\Gamma(r-\epsilon-1) = \dots \\ &= \frac{1}{\pi^r \Gamma(-\epsilon)} (r-\epsilon-1)(r-\epsilon-2)\dots(1-\epsilon)(-\epsilon)\Gamma(-\epsilon) \\ &= \frac{1}{\pi^r} \prod_{\kappa=1}^r (\kappa-1-\epsilon). \end{aligned} \quad (\text{B.8})$$

Together with the four dimensional part, we therefore have

$$\int d^d \bar{q} (\mu^2)^r f(q^\alpha, \mu^2) = \frac{1}{\pi^r} \prod_{\kappa=1}^r (\kappa-1-\epsilon) \int d^{d+2r} \bar{q} f(q^\alpha, \mu^2). \quad (\text{B.9})$$

B.1.1. $I_{ij}[\mu^2]$

Contracting expression (4.32) with $\tilde{g}^{\mu\nu}$ instead of the four-dimensional part, we have

$$I_{ij}[\mu^2] = 2\epsilon B_{00}. \quad (\text{B.10})$$

Filling in the known expression for B_{00} from equation (4.39), we end up with

$$I_{ij}[\mu^2] = \frac{1}{2} \left(m_i^2 + m_j^2 - \frac{k^2}{3} \right) + \mathcal{O}(\epsilon). \quad (\text{B.11})$$

B.1.2. $I_{ijk}[\mu^2]$

Contracting expression (4.41) with $\tilde{g}^{\mu\nu}$ removes all the four-dimensional terms multiplying $k_i^\mu k_j^\nu$ and we have

$$I_{ijk}[\mu^2] = 2\epsilon C_{00} = \frac{1}{2} \epsilon \left(2m_i^2 I_{ijk} + 2I_{ijk}[\mu^2] - f_j C_2(ijk) - f_i C_1(ijk) + I_{jk} \right). \quad (\text{B.12})$$

I_{ijk} is of order $\mathcal{O}(\epsilon)$. For C_1 and C_2 , which are linear combinations of the two integrals

$$I_{ijk}[\bar{q} \cdot k_1] = \frac{1}{2} (I_{ik} - I_{jk} + f_i I_{ijk}), \quad I_{ijk}[\bar{q} \cdot k_2] = \frac{1}{2} (I_{ij} - I_{ik} + f_j I_{ijk}), \quad (\text{B.13})$$

we see that the multiplication with ϵ exactly cancels out the first term against the second in both expressions, whereas the last terms are again $\mathcal{O}(\epsilon)$. Therefore, the only contribution is from the last term $I_{jk} = \frac{1}{2} + \mathcal{O}(\epsilon)$, which gives for the total integral simply

$$I_{ijk}[\mu^2] = \frac{1}{2} + \mathcal{O}(\epsilon). \quad (\text{B.14})$$

B.2. Higher rank integrals

The extension to higher rank introduces four new master integrals, that are given below. They were calculated in [85]. Using the notation $p_{ji} = (p_j - p_i)$, they are given by

$$\begin{aligned}
 I_i[\mu^2] &= \frac{i\pi^2 m_i^4}{2} + \mathcal{O}(\epsilon) \\
 I_i[(q + p_i) \cdot e_3][(q + p_i) \cdot e_4] &= -\frac{m_i^2 I_i + I_i[\mu^2]}{4} + \mathcal{O}(\epsilon) \\
 I[\mu^2((q + p_i) \cdot e_2)] &= \frac{i\pi^2}{12} (p_{ji} \cdot e_2)(p_{ji}^2 - 2m_i^2 - 4m_j^2) + \mathcal{O}(\epsilon) \\
 I_{ijk}[\mu^4] &= \frac{i\pi^6}{4} \left(\frac{p_{jk}^2 + p_{ji}^2 + p_{ki}^2}{4} - m_i^2 - m_j^2 - m_k^2 \right) + \mathcal{O}(\epsilon).
 \end{aligned} \tag{B.15}$$

C ■ Spinor helicity formalism

The *spinor helicity formalism* is used very often in the calculation of scattering amplitudes. Here the notation will be introduced and a few useful identities will be derived. More information can be found in several reviews, for example in [168, 169].

Massless fermions obey the Dirac equation,

$$\not{p}U(p) = 0. \quad (\text{C.1})$$

In the Weyl basis, the right- and left-handed spinors that are a solution to this equation are the spinors,

$$U_R = \begin{pmatrix} 0 \\ u_R(p) \end{pmatrix}, \quad U_L = \begin{pmatrix} u_L(p) \\ 0 \end{pmatrix}, \quad (\text{C.2})$$

where the two entries satisfy

$$p \cdot \sigma u_R = 0, \quad p \cdot \bar{\sigma} u_L = 0. \quad (\text{C.3})$$

In the massless case, the anti-particle solutions to the Dirac equation satisfy the same equation as $U(p)$. Considering everything outgoing, left- and right-handed fermions can be represented as \bar{U}_L and \bar{U}_R . Left- and right-handed anti-fermions are then represented by U_R and U_L . The spinors are written compactly as

$$\bar{U}_L(p) = \langle p, \quad \bar{U}_R = [p, \quad U_L(p) = p], \quad U_R(p) = p \rangle. \quad (\text{C.4})$$

This allows us to write common occurring expressions in a compact way. First of all, the Dirac equation now reads

$$\not{p}p \rangle = p \rangle = 0. \quad (\text{C.5})$$

The Lorentz-invariant spinor product becomes

$$\bar{U}_L(p)U_R(q) = \langle pq \rangle, \quad \bar{U}_R(p)U_L(q) = [pq]. \quad (\text{C.6})$$

The chiral projection becomes

$$p \rangle [p = U_R(p)\bar{U}_R(p) = \not{p} \left(\frac{1 - \gamma^5}{2} \right), \quad p \rangle \langle p = U_L(p)\bar{U}_L(p) = \not{p} \left(\frac{1 + \gamma^5}{2} \right). \quad (\text{C.7})$$

Note that this implies

$$\langle pq \rangle = [qp]^*. \quad (\text{C.8})$$

Taking the trace of two projection operators gives

$$\langle qp \rangle [pq] = \text{Tr} \left[p \rangle [pq] \langle q \right] = \text{Tr} \left[\not{p} \left(\frac{1 - \gamma^5}{2} \right) \not{q} \left(\frac{1 + \gamma^5}{2} \right) \right] = 2p \cdot q, \quad (\text{C.9})$$

which means that

$$|\langle pq \rangle|^2 = |[qp]|^2 = 2p \cdot q. \quad (\text{C.10})$$

Using the asymmetry of σ^2 one can furthermore show that

$$\langle pq \rangle = -\langle qp \rangle \quad [pq] = -[qp]. \quad (\text{C.11})$$

From this it trivially follows that

$$\langle pp \rangle = [pp] = 0. \quad (\text{C.12})$$

From equation (C.3) it follows that we can write

$$u_R(p) = i\sigma^2 u_L^*(p). \quad (\text{C.13})$$

This expression can be used to rewrite

$$\begin{aligned} u_L^\dagger(p) \bar{\sigma}^\mu u_L(q) &= u_L^\dagger(p) \bar{\sigma}^\mu (-i\sigma^2)^2 u_L(q) \\ &= u_L^\dagger(p) (-i\sigma^2) \sigma^{\mu T} (i\sigma^2) u_L(q) \\ &= u_R^T(p) \sigma^{\mu T} u_R^*(q) \\ &= u_R^\dagger(q) \sigma^\mu u_R(p), \end{aligned} \quad (\text{C.14})$$

which means that

$$\langle p\gamma^\mu q \rangle = [q\gamma^\mu p]. \quad (\text{C.15})$$

Similarly, using the Fierz identity of the sigma matrices one gets

$$\langle p\gamma^\mu q \rangle \langle k\gamma_\mu l \rangle = 2\langle pk \rangle [lq], \quad \langle p\gamma^\mu q \rangle [k\gamma_\mu l] = 2\langle pl \rangle [kq]. \quad (\text{C.16})$$

The Schouten identity reads

$$\begin{aligned} \langle ij \rangle \langle kl \rangle + \langle ik \rangle \langle lj \rangle + \langle il \rangle \langle jk \rangle &= 0 \\ [ij] [kl] + [ik] [lj] + [il] [jk] &= 0. \end{aligned} \quad (\text{C.17})$$

With these identities it is possible to construct a spinor representation of polarization vectors for massless gauge bosons of definite helicity ± 1 ,

$$\epsilon_+^{*\mu}(k) = \frac{1}{\sqrt{2}} \frac{\langle r\gamma^\mu k \rangle}{\langle rk \rangle}, \quad \epsilon_-^{*\mu}(k) = \frac{1}{\sqrt{2}} \frac{[r\gamma^\mu k]}{[rk]}, \quad (\text{C.18})$$

where r is an auxiliary light like four-vector known as a reference vector. This definition has all the necessary properties of a polarization vector. Since the Dirac equation tells us that $\not{k}|k\rangle = \not{k}|k] = 0$, this polarization vector is transverse to its momentum for any reference vector,

$$\epsilon^\pm(k, r) \cdot k = 0. \quad (\text{C.19})$$

Furthermore, it satisfies

$$\begin{aligned} \epsilon^+ \cdot (\epsilon^+)^* &= \epsilon^+ \cdot \epsilon^- = -\frac{1}{2} \frac{\langle r\gamma^\mu k \rangle [r\gamma_\mu k]}{\langle rk \rangle [rk]} = -1, \\ \epsilon^+ \cdot (\epsilon^-)^* &= \epsilon^+ \cdot \epsilon^+ = \frac{1}{2} \frac{\langle r\gamma^\mu k \rangle \langle r\gamma_\mu k \rangle}{\langle rk \rangle^2} = 0, \end{aligned} \quad (\text{C.20})$$

where the Fierz identities from equation (C.16) were used to make the numerator of the former cancel against its denominator and make the numerator of the latter become proportional to $\langle rr \rangle$ and hence vanish.

D ■ Residues

In this appendix the explicit expressions for the residues appearing in the d -dimensional integrand reduction algorithm are collected, which were derived in Chapters 5.1 and 5.2. They are given both in normal and higher rank.

D.1. Five-point contributions

D.1.1. Normal rank

$$\Delta_{ijklm}(q, \mu^2) = c_{5,0}^{(ijklm)} \mu^2 \quad (\text{D.1})$$

D.1.2. Higher rank

$$\Lambda_{ijklm}(q, \mu^2) = \Delta_{ijklm}(q, \mu^2) \quad (\text{D.2})$$

D.2. Four-point contributions

D.2.1. Normal rank

$$\Delta_{ijk\ell}(q, \mu^2) = \Delta_{ijk\ell}^R(q, \mu^2) + c_{4,0}^{(ijk\ell)} + c_{4,2}^{(ijk\ell)} \mu^2 + c_{4,4}^{(ijk\ell)} \mu^4 \quad (\text{D.3})$$

with

$$\Delta_{ijk\ell}^R(q, \mu^2) = \left(c_{4,1}^{(ijk\ell)} + c_{4,3}^{(ijk\ell)} \mu^2 \right) (q + p_i) \cdot v_{\perp} \quad (\text{D.4})$$

D.2.2. Higher rank

$$\Lambda_{ijk\ell}(q, \mu^2) = \Delta_{ijk\ell}(q, \mu^2) + c_{4,5}^{(ijk\ell)} \mu^4 (q + p_i) \cdot v_{\perp} \quad (\text{D.5})$$

D.3. Three-point contributions

D.3.1. Normal rank

$$\Delta_{ijk}(q, \mu^2) = \Delta_{ijk}^R(q, \mu^2) + c_{3,0}^{(ijk)} + c_{3,7}^{(ijk)} \mu^2 \quad (\text{D.6})$$

with

$$\begin{aligned} \Delta_{ijk}^R(q, \mu^2) &= \left(c_{3,1}^{(ijk)} + c_{3,8}^{(ijk)} \mu^2 \right) (q + p_i) \cdot e_3 \\ &+ \left(c_{3,4}^{(ijk)} + c_{3,9}^{(ijk)} \mu^2 \right) (q + p_i) \cdot e_4 \\ &+ c_{3,2}^{(ijk)} ((q + p_i) \cdot e_3)^2 + c_{3,5}^{(ijk)} ((q + p_i) \cdot e_4)^2 \\ &+ c_{3,3}^{(ijk)} ((q + p_i) \cdot e_3)^3 + c_{3,6}^{(ijk)} ((q + p_i) \cdot e_4)^3 \end{aligned}$$

D.3.2. Higher rank

$$\begin{aligned} \Lambda_{ijk}(q, \mu^2) &= \Delta_{ijk}(q, \mu^2) + c_{3,14}^{(ijk)} \mu^4 \\ &+ c_{3,10}^{(ijk)} \mu^2 ((q + p_i) \cdot e_3)^2 \\ &+ c_{3,11}^{(ijk)} \mu^2 ((q + p_i) \cdot e_4)^2 \\ &+ c_{3,12}^{(ijk)} ((q + p_i) \cdot e_3)^4 \\ &+ c_{3,13}^{(ijk)} ((q + p_i) \cdot e_4)^4 \end{aligned} \quad (\text{D.7})$$

D.4. Two-point contributions

D.4.1. Normal rank

$$\Delta_{ij}(q, \mu^2) = \Delta_{ij}^R(q, \mu^2) + c_{2,0}^{(ij)} + c_{2,9}^{(ij)} \mu^2 \quad (\text{D.8})$$

with

$$\begin{aligned} \Delta_{ij}^R(q, \mu^2) &= c_{2,1}^{(ij)} (q + p_i) \cdot e_2 + c_{2,2}^{(ij)} ((q + p_i) \cdot e_2)^2 \\ &+ c_{2,3}^{(ij)} (q + p_i) \cdot e_3 + c_{2,4}^{(ij)} ((q + p_i) \cdot e_3)^2 \\ &+ c_{2,5}^{(ij)} (q + p_i) \cdot e_4 + c_{2,6}^{(ij)} ((q + p_i) \cdot e_4)^2 \\ &+ c_{2,7}^{(ij)} ((q + p_i) \cdot e_2)((q + p_i) \cdot e_3) \\ &+ c_{2,8}^{(ij)} ((q + p_i) \cdot e_2)((q + p_i) \cdot e_4). \end{aligned}$$

D.4.2. Higher rank

$$\begin{aligned}
\Lambda_{ij}(q, \mu^2) &= \Delta_{ij}(q, \mu^2) \\
&+ \mu^2 \left(c_{2,10}^{(ij)} (q + p_i) \cdot e_2 + c_{2,11}^{(ij)} (q + p_i) \cdot e_3 + c_{2,12}^{(ij)} (q + p_i) \cdot e_4 \right) \\
&+ c_{2,13}^{(ij)} ((q + p_i) \cdot e_2)^3 + c_{2,14}^{(ij)} ((q + p_i) \cdot e_3)^3 + c_{2,15}^{(ij)} ((q + p_i) \cdot e_4)^3 \\
&+ c_{2,16}^{(ij)} ((q + p_i) \cdot e_2)^2 ((q + p_i) \cdot e_3) \\
&+ c_{2,17}^{(ij)} ((q + p_i) \cdot e_2)^2 ((q + p_i) \cdot e_4) \\
&+ c_{2,18}^{(ij)} ((q + p_i) \cdot e_2) ((q + p_i) \cdot e_3)^2 \\
&+ c_{2,19}^{(ij)} ((q + p_i) \cdot e_2) ((q + p_i) \cdot e_4)^2
\end{aligned} \tag{D.9}$$

D.5. One-point contributions

D.5.1. Normal rank

$$\begin{aligned}
\Delta_i(q, \mu^2) &= c_{1,0}^{(i)} + c_{1,1}^{(i)} ((q + p_i) \cdot e_1) + c_{1,2}^{(i)} ((q + p_i) \cdot e_2) \\
&+ c_{1,3}^{(i)} ((q + p_i) \cdot e_3) + c_{1,4}^{(i)} ((q + p_i) \cdot e_4)
\end{aligned} \tag{D.10}$$

D.5.2. Higher rank

Note that for historical reasons, there is no $c_{1,9}^{(i)}$.

$$\begin{aligned}
\Lambda_i(q, \mu^2) &= \Delta_i(q, \mu^2) \\
&+ c_{1,5}^{(i)} ((q + p_i) \cdot e_1)^2 + c_{1,6}^{(i)} ((q + p_i) \cdot e_2)^2 \\
&+ c_{1,7}^{(i)} ((q + p_i) \cdot e_3)^2 + c_{1,8}^{(i)} ((q + p_i) \cdot e_4)^2 \\
&+ c_{1,10}^{(i)} ((q + p_i) \cdot e_1) ((q + p_i) \cdot e_3) + c_{1,11}^{(i)} ((q + p_i) \cdot e_1) ((q + p_i) \cdot e_4) \\
&+ c_{1,12}^{(i)} ((q + p_i) \cdot e_2) ((q + p_i) \cdot e_3) + c_{1,13}^{(i)} ((q + p_i) \cdot e_2) ((q + p_i) \cdot e_4) \\
&+ c_{1,14}^{(i)} \mu^2 + c_{1,15}^{(i)} ((q + p_i) \cdot e_3) ((q + p_i) \cdot e_4)
\end{aligned} \tag{D.11}$$

E ■ GOSAM example

As a simple example to illustrate the basic functioning of GOSAM, let us assume we want to calculate to order $O(\alpha\alpha_s)$ the process $e^+e^- \rightarrow t\bar{t}$, which are QCD corrections to the electroweak LO process. The minimal input card named `eett.in` would look like Figure E.1.

```
process_path=eett
in = e+, e-
out = t, t~
order = gs, 0, 2
```

Figure E.1.: The minimal input card for the process $e^+e^- \rightarrow t\bar{t}$. The process is written in a directory ‘./eett’ relative to the current working directory. The corrections are QCD, which means that the LO diagrams have no factors of g_s , whereas the NLO diagrams have two powers of g_s .

A complete description of all possible options in the input card is given in the manual. The code generation can be invoked by calling the `gosam.py` executable on this card. After generating and compiling the source code, going in the directory ‘./eett/matrix’ and typing

```
$ make test.exe
```

will create a useful testing executable that generates a number of phase space points and returns the Born contribution, the finite part and the single and double pole of the calculation. Also the IR poles to check against and an estimation of the timing per phase space point are printed.

In this example the first phase space point generated (which may vary from one installation to another) is given in Table E.1. Running the executable prints out (along with the banners of the programs involved) the setup used and the results as shown in Figure E.2.

particle	E	p_x	p_y	p_z
p_1	250.00000000000000	0.0000000000000000	0.0000000000000000	249.99999999947775
p_2	250.00000000000000	0.0000000000000000	0.0000000000000000	-249.99999999947775
p_3	249.99999999999994	159.08877886329807	-21.562578473620317	86.118381599711881
p_4	250.00000000000006	-159.08877886329827	21.562578473620317	-86.118381599711938

Table E.1.: Benchmark phase-space point for $e^+e^- \rightarrow t\bar{t}$.

```

# ----- SETUP -----
# renormalisation = 1
# scheme = DRED
# reduction with NINJA
# rescue with GOLEM95
# --- PARAMETER VALUES ---
# Boson masses
# mZ = 91.18760000000000
# mW = 80.37600000000000
# mH = 125.00000000000000
# wZ = 2.495200000000000
# wW = 2.124000000000000
# wH = 0.000000000000000
# Active light quarks:
# Nf = 5.000000000000000
# Nfgen = -1.000000000000000
# Fermion masses
# mc = 1.270000000000000
# mb = 4.200000000000000
# mbMS = 4.200000000000000
# wb = 0.000000000000000
# mt = 171.2000000000000
# wt = 0.000000000000000
# mtau = 1.776840000000000
# wtau = 0.000000000000000
# -----
# Renormalisation scale:
# mu = 499.9999999994778
# -----

#          LO: 0.3096926486067998E-01
# NLO, finite part: 22.22515377498502
# NLO, single pole: 2.521442058297684
# NLO, double pole: 0.000000000000000
# IR, single pole: 2.521442057085296
# IR, double pole: 0.000000000000000
# Time/Event [ms]: 2.000

```

Figure E.2.: The output of the executable created from the input card in E.1 using the phase space point given in E.1.

All of the settings in this output can be set both in the original input card or after generation and compilation in the file `test.f90`, after importing them from the configuration module.

F ■ Benchmark phase space points

In this appendix all the phase space points referred to in the main text are collected. They can be used as benchmarks to check results against. The finite part, single pole and double pole are given as c_0 , c_{-1} and c_{-2} , defined by

$$\frac{2 \Re \left\{ \mathcal{M}^{\text{tree-level}^*} \mathcal{M}^{\text{one-loop}} \right\}}{(\alpha_s/2\pi) |\mathcal{M}^{\text{tree-level}}|^2} \equiv \frac{c_{-2}}{\epsilon^2} + \frac{c_{-1}}{\epsilon} + c_0. \quad (\text{F.1})$$

Note that the results are normalized to the tree-level matrix element squared. For some processes it may be useful to also list this tree-level matrix element squared, denoted as a_0 and given (unless otherwise specified) by

$$a_0 = \frac{|\mathcal{M}^{\text{tree-level}}|^2}{(4\pi\alpha_s)^b}, \quad (\text{F.2})$$

with its tree-level QCD coupling stripped off, as defined in equation (6.1). The reconstruction of the renormalized pole can be checked against the value of c_{-1} and c_{-2} obtained by the universal singular behavior of the dimensionally regularized one-loop amplitudes [113], while the precision of the finite parts is estimated by re-evaluating the amplitudes for a set of momenta rotated by an arbitrary angle about the axis of collision (see Section 6.2.1). The accuracy of the results in this appendix is indicated by the digits in boldface.

F.1. SAMURAI and Ninja $pp \rightarrow H + 3j$ in VBF

In this appendix we collect numerical results for the renormalized virtual contributions to the subprocesses of $pp \rightarrow H + 3j$ in VBF as described in Section 7.1, in correspondence to the phase-space point in Table F.1. The results are collected in the tables in Figure F.2 and are computed using dimensional reduction.

particle	E	p_x	p_y	p_z
p_1	250.00000000000000	0.0000000000000000	0.0000000000000000	250.00000000000000
p_2	250.00000000000000	0.0000000000000000	0.0000000000000000	-250.00000000000000
p_3	131.06896655823209	27.707264814722667	-13.235482900394146	24.722529472591685
p_4	164.74420140597425	-129.37584098675183	-79.219260486951597	-64.240582451932028
p_5	117.02953632773803	54.480516624273569	97.990504664150677	-33.550658370629378
p_6	87.157295708055642	47.188059547755266	-5.5357612768047906	73.068711349969661

Table F.1.: Benchmark phase-space point for $pp \rightarrow H + 3j$ in VBF.

$dd \rightarrow Hddg$	SAMURAI	NINJA
a_0	1.519753605442887	
c_0	-49.62885275361386	-49.62885275380776
c_{-1}	-28.21416578385935	-28.21416578391514
c_{-2}	-8.333333333333529	-8.33333333333366

$ds \rightarrow Hdsg$	SAMURAI	NINJA
a_0	0.2511067733973208	
c_0	-27.91604024256694	-27.91604024290788
c_{-1}	-23.04838629098442	-23.04838629110849
c_{-2}	-8.333333333333222	-8.33333333333332

$uc \rightarrow Hucg$	SAMURAI	NINJA
a_0	0.1220793683951386	
c_0	-28.00158510004069	-28.00158510046460
c_{-1}	-23.05619736939017	-23.05619736954724
c_{-2}	-8.333333333333233	-8.33333333333336

$ud \rightarrow Hudg$	SAMURAI	NINJA
a_0	7.296212701461837	
c_0	-43.40744002959294	-43.40744002965619
c_{-1}	-28.66853328380996	-28.66853328382680
c_{-2}	-8.333333333333263	-8.33333333333337

$us \rightarrow Husg$	SAMURAI	NINJA
a_0	0.1732508159673296	
c_0	-27.94376246701186	-27.94376246744694
c_{-1}	-23.05249781250525	-23.05249781264788
c_{-2}	-8.333333333333231	-8.33333333333334

$us \rightarrow Hcdg$	SAMURAI	NINJA
a_0	6.905052324462774	
c_0	-47.02344237420569	-47.02344237420878
c_{-1}	-28.99396496272290	-28.99396496272331
c_{-2}	-8.33333333333343	-8.33333333333362

$uu \rightarrow Huug$	SAMURAI	NINJA
a_0	0.8025232323452055	
c_0	-48.90884551361260	-48.90884551379160
c_{-1}	-28.26517439546503	-28.26517439551836
c_{-2}	-8.333333333333519	-8.33333333333366

Table F.2.: Numerical results for the subprocesses of $pp \rightarrow H + 3j$ in VBF as described in Section 7.1, evaluated at the phase-space point given in Table F.1, with both SAMURAI and NINJA. at a scale $\mu = 2p_1 \cdot p_2 = 500$ GeV.

F.2. Ninja $Zt\bar{t}$

In this section the results are collected for the process $pp \rightarrow Zt\bar{t}$, with the Z subsequently decaying into a e^+e^- pair, as described in Section 6.2.

F.2.1. $u\bar{u} \rightarrow t\bar{t}e^+e^-$

particle	E	p_x	p_y	p_z
p_1	250.0000000000000000	0.0000000000000000	0.0000000000000000	250.0000000000000000
p_2	250.0000000000000000	0.0000000000000000	0.0000000000000000	-250.0000000000000000
p_3	198.2750073412062761	-4.9121008822519290	15.8302462223025771	98.6347459347833393
p_4	173.6629710756763814	16.3353989288707595	-23.9314331386695365	-3.1350873345500285
p_5	46.8935971645872911	-36.1432949461904798	-18.9709760240555774	-23.0818923436094785
p_6	81.1684244185300656	24.7199968995716510	27.0721629404225368	-72.4177662566238212

PARAMETER	VALUE
m_H	125.0
m_W	80.376
m_Z	91.1876
m_t	171.2
m_b	0.0
n_f	5
$n_{f,\text{gen}}$	2
μ^2	250000.0

$u\bar{u} \rightarrow t\bar{t}e^+e^-$	
c_0	12.5823450965837065
c_{-1}	-7.9257868784365293
c_{-2}	-2.6666666666673140

Table F.3.: Benchmark point for the subprocess $u(p_1)\bar{u}(p_2) \rightarrow t(p_3)\bar{t}(p_4)e^+(p_5)e^-(p_6)$.

F.2.2. $g\bar{g} \rightarrow t\bar{t}e^+e^-$

particle	E	p_x	p_y	p_z
p_1	250.0000000000000000	0.0000000000000000	0.0000000000000000	250.0000000000000000
p_2	250.0000000000000000	0.0000000000000000	0.0000000000000000	-250.0000000000000000
p_3	182.1516563163594071	24.8252511898625059	15.4219345397897296	-54.9149955586248879
p_4	183.3554226695324587	-42.7895170685190607	43.4712527757529159	24.2709380426964820
p_5	62.5564264059783639	24.4748131480545723	-42.3016153533453831	-39.0494986466153833
p_6	71.9364946081297632	-6.5105472693980087	-16.5915719621972677	69.6935561625437856

PARAMETER	VALUE
m_H	125.0
m_W	80.376
m_Z	91.1876
m_t	171.2
m_b	0.0
n_f	5
$n_{f,\text{gen}}$	2
μ^2	250000.0

$g\bar{g} \rightarrow t\bar{t}e^+e^-$	
c_0	17.2203140681080065
c_{-1}	-11.3322887135133410
c_{-2}	-5.9999999999999787

Table F.4.: Benchmark point for the subprocess $g(p_1)\bar{g}(p_2) \rightarrow t(p_3)\bar{t}(p_4)e^+(p_5)e^-(p_6)$.

F.3. Ninja $Zt\bar{t}j$

In this section the results are collected for the process $pp \rightarrow Zt\bar{t}j$, with the Z subsequently decaying into a e^+e^- pair, as described in Section 6.2.

F.3.1. $u\bar{u} \rightarrow t\bar{t}e^+e^-g$

particle	E	p_x	p_y	p_z
p_1	250.0000000000000000	0.0000000000000000	0.0000000000000000	250.0000000000000000
p_2	250.0000000000000000	0.0000000000000000	0.0000000000000000	-250.0000000000000000
p_3	183.2414081421947287	-30.2337217736484156	32.1314578860740667	48.1815850690226029
p_4	199.0327070603159996	74.5268539046026035	-40.9270527537185629	-55.4554134393922311
p_5	70.1181125436057044	-63.0760999348447697	21.5315800178266556	21.7794946135846281
p_6	20.7607087314536756	-7.2430664321972609	-7.1983324871256098	-18.0756472939650585
p_7	26.8470635224299627	26.0260342360878454	-5.5376526630565506	3.5699810507501222

PARAMETER	VALUE
m_H	125.0
m_W	80.376
m_Z	91.1876
m_t	171.2
m_b	0.0
f	5
$n_{f,\text{gen}}$	2
μ^2	250000.0

$u\bar{u} \rightarrow t\bar{t}e^+e^-g$	
c_0	-20.4367763710913373
c_{-1}	-25.9078542815554513
c_{-2}	-5.6666666665792098

Table F.5.: Benchmark point for the subprocess $u(p_1)\bar{u}(p_2) \rightarrow t(p_3)\bar{t}(p_4)e^+(p_5)e^-(p_6)g(p_7)$.

F.3.2. $gg \rightarrow t\bar{t}e^+e^-g$

particle	E	p_x	p_y	p_z
p_1	250.0000000000000000	0.0000000000000000	0.0000000000000000	250.0000000000000000
p_2	250.0000000000000000	0.0000000000000000	0.0000000000000000	-250.0000000000000000
p_3	174.2203895522303014	-25.0977827305029138	-19.5610151031829993	5.5472629175473589
p_4	186.7123996976260685	-14.0800163072181022	56.3619207264196902	-46.6601246640355427
p_5	60.3016377245591073	38.1795332240129639	22.1553968884492853	41.0822241824339116
p_6	18.6184873501163182	5.2347824612577458	-1.6661313271933778	-17.7895792583830961
p_7	60.1470856754682259	-4.2365166475497116	-57.2901711844925998	17.8202168224373914

PARAMETER	VALUE
m_H	125.0
m_W	80.376
m_Z	91.1876
m_t	171.2
m_b	0.0
n_f	5
$n_{f,\text{gen}}$	2
μ^2	250000.0

$gg \rightarrow t\bar{t}e^+e^-g$	
c_0	9.2826425323344441
c_{-1}	-26.2816094048822784
c_{-2}	-9.0000000000005702

Table F.6.: Benchmark point for the subprocess $g(p_1)g(p_2) \rightarrow t(p_3)\bar{t}(p_4)e^+(p_5)e^-(p_6)g(p_7)$.

F.4. SAMURAI $pp \rightarrow H + 2j$ in GF

In this appendix the results for the renormalized virtual contributions of the process $pp \rightarrow H + 2j$ in GF are given for a non-exceptional phase space point. The setup is the one as given in Section 7.2.2, except that here we use for the renormalization and factorization scales the value of the Higgs boson mass. Assigning the momenta as

$$\begin{aligned}
 g(p_1) g(p_2) &\rightarrow H(p_3) g(p_4) g(p_5), \\
 g(p_1) g(p_2) &\rightarrow H(p_3) q(p_4) \bar{q}(p_5), \\
 q(p_1) \bar{q}(p_2) &\rightarrow H(p_3) q(p_4) \bar{q}(p_5), \\
 q(p_1) \bar{q}(p_2) &\rightarrow H(p_3) q'(p_4) \bar{q}'(p_5),
 \end{aligned} \tag{F.3}$$

for the phase space point given in Table F.7, the results are given in Table F.8. They are computed in the dimensional reduction scheme. For this process, the tree-level matrix element squared is given by

$$a_0 \equiv \frac{|\mathcal{M}^{\text{tree-level}}|^2}{(4\pi\alpha_s)^2 g_{eff}^2}. \tag{F.4}$$

To check the precision of the renormalized poles, their values are compared with the value that are given by the universal singular behavior of dimensionally regularized one-loop amplitudes [113]. The agreeing digits are given in boldface.

particle	E	p_x	p_y	p_z
p_1	250.00000000000000	0.0000000000000000	0.0000000000000000	250.00000000000000
p_2	250.00000000000000	0.0000000000000000	0.0000000000000000	-250.00000000000000
p_3	143.67785106160801	51.663364918413812	-22.547134012261804	42.905108772983255
p_4	190.20318863787611	-153.36110830475005	-108.23578590696623	-30.702411577195452
p_5	166.11896030051594	101.69774338633616	130.78291991922802	-12.202697195787838

Table F.7.: Benchmark phase space point for Higgs boson plus two jets production in GF.

$gg \rightarrow Hgg$		$gg \rightarrow Hq\bar{q}$	
a_0	$0.1507218951429643 \cdot 10^{-3}$	a_0	$0.5677813961826772 \cdot 10^{-6}$
c_0	59.8657965614009	c_0	66.6635142370683
c_{-1}	- 26.4694115468536	c_{-1}	- 16.5816633315627
c_{-2}	- 12.0000000000001	c_{-2}	- 8.6666666666669
$q\bar{q} \rightarrow Hq\bar{q}$		$q\bar{q} \rightarrow Hq'\bar{q}'$	
a_0	$0.1099527895267439 \cdot 10^{-5}$	a_0	$0.1011096724203529 \cdot 10^{-6}$
c_0	88.2959834057198	c_0	33.9521626734153
c_{-1}	- 10.9673755313443	c_{-1}	- 13.864929283413
c_{-2}	- 5.3333333333332	c_{-2}	- 5.3333333333334

Table F.8.: Numerical results for the processes listed in equation (F.3).

F.5. SAMURAI $pp \rightarrow H + 3j$ in GF

In this appendix the results for the renormalized virtual contributions of the process $pp \rightarrow H + 3j$ in GF are given for a non-exceptional phase space point. The setup is the one as given in Section 7.2.3, except that here we use for the renormalization and factorization scales the value of the Higgs boson mass. Assigning the momenta as

$$\begin{aligned}
 g(p_1) g(p_2) &\rightarrow H(p_3) g(p_4) g(p_5) g(p_6), \\
 g(p_1) g(p_2) &\rightarrow H(p_3) q(p_4) \bar{q}(p_5) g(p_6), \\
 q(p_1) \bar{q}(p_2) &\rightarrow H(p_3) q(p_4) \bar{q}(p_5) g(p_6), \\
 q(p_1) \bar{q}(p_2) &\rightarrow H(p_3) q'(p_4) \bar{q}'(p_5) g(p_6),
 \end{aligned}
 \tag{F.5}$$

for the phase space point given in Table F.9, the results are given in Table F.10. They are computed in the dimensional reduction scheme. For this process, the tree-level matrix element squared is given by

$$a_0 \equiv \frac{|\mathcal{M}^{\text{tree-level}}|^2}{(4\pi\alpha_s)^3 g_{eff}^2}.
 \tag{F.6}$$

particle	E	p_x	p_y	p_z
p_1	250.00000000000000	0.0000000000000000	0.0000000000000000	250.00000000000000
p_2	250.00000000000000	0.0000000000000000	0.0000000000000000	-250.00000000000000
p_3	131.06896655823209	27.707264814722667	-13.235482900394146	24.722529472591685
p_4	164.74420140597425	-129.37584098675183	-79.219260486951597	-64.240582451932028
p_5	117.02953632773803	54.480516624273569	97.990504664150677	-33.550658370629378
p_6	87.157295708055642	47.188059547755266	-5.5357612768047906	73.068711349969661

Table F.9.: Benchmark phase-space point for $pp \rightarrow H + 3j$ in GF.

	$gg \rightarrow Hggg$	$gg \rightarrow Hq\bar{q}g$	$q\bar{q} \rightarrow Hq\bar{q}g$	$q\bar{q} \rightarrow Hq'\bar{q}'g$
c_0	41.22878766741685	48.68424134989478	69.32351140474695	15.79262767177915
c_{-1}	-47.16715419132659	-36.08277728077228	-29.98862932963659	-32.35320587073968
c_{-2}	-14.99999999999991	-11.66666666666683	-8.333333333333339	-8.333333333333398

Table F.10.: Numerical results for the processes listed in equation (F.5).

F.6. Ninja $pp \rightarrow Ht\bar{t}j$

In this appendix we collect numerical results for the renormalized virtual contributions to the processes (7.29), in correspondence to the phase-space point in Table F.11. The results are collected in Table F.12 and are computed using dimensional reduction.

particle	E	p_x	p_y	p_z
p_1	250.00000000000000	0.0000000000000000	0.0000000000000000	250.00000000000000
p_2	250.00000000000000	0.0000000000000000	0.0000000000000000	-250.00000000000000
p_3	177.22342332868467	-31.917865771774753	-19.543909461587205	-15.848571666570733
p_4	174.89951284907735	13.440699620020803	24.174898117950033	-8.2771667589629576
p_5	126.37478917634435	6.8355633672742222	-3.2652801590882752	6.0992096455298030
p_6	21.502274645893632	11.641602784479652	-1.3657084972745175	18.026528780003872

Table F.11.: Benchmark phase-space point for $t\bar{t}Hj$ production.

	$q\bar{q} \rightarrow t\bar{t}Hg$	$gg \rightarrow t\bar{t}Hg$
c_0	-71.8886458274311	-37.18424603354295
c_{-1}	-32.6902910180535	-35.92174974376358
c_{-2}	-5.66666666663801	-9.00000000056112

Table F.12.: Numerical results for the two subprocesses listed in equation (7.29) evaluated at the phase-space point of Table F.11 for a scale $\mu = 2p_1 \cdot p_2 = 500$ GeV.

Bibliography

- [1] G. Cullen, H. van Deurzen, N. Greiner, G. Heinrich, G. Luisoni, et al. *GOSAM-2.0: a tool for automated one-loop calculations within the Standard Model and beyond*. Eur.Phys.J., C74(8):3001, 2014.
- [2] H. van Deurzen, G. Luisoni, P. Mastrolia, E. Mirabella, G. Ossola, et al. *Multi-leg One-loop Massive Amplitudes from Integrand Reduction via Laurent Expansion*. JHEP, 1403:115, 2014.
- [3] H. van Deurzen, G. Luisoni, P. Mastrolia, E. Mirabella, G. Ossola, et al. *Next-to-Leading-Order QCD Corrections to Higgs Boson Production in Association with a Top Quark Pair and a Jet*. Phys.Rev.Lett., 111(17):171801, 2013.
- [4] G. Cullen, H. van Deurzen, N. Greiner, G. Luisoni, P. Mastrolia, et al. *NLO QCD corrections to Higgs boson production plus three jets in gluon fusion*. Phys.Rev.Lett., 111:131801, 2013.
- [5] H. van Deurzen, N. Greiner, G. Luisoni, P. Mastrolia, E. Mirabella, et al. *NLO QCD corrections to the production of Higgs plus two jets at the LHC*. Phys.Lett., B721:74–81, 2013.
- [6] H. van Deurzen, R. Frederix, V. Hirschi, G. Luisoni, P. Mastrolia, and G. Ossola. *Mad-Graph5_aMC@NLO + GoSam, a complete NLO event generator, in preparation*. 2015.
- [7] J. Butterworth, G. Dissertori, S. Dittmaier, D. de Florian, N. Glover, et al. *Les Houches 2013: Physics at TeV Colliders: Standard Model Working Group Report*. 2014.
- [8] S. Alioli, S. Badger, J. Bellm, B. Biedermann, F. Boudjema, et al. *Update of the Binoth Les Houches Accord for a standard interface between Monte Carlo tools and one-loop programs*. Comput.Phys.Commun., 185:560–571, 2014.
- [9] S. Heinemeyer et al. *Handbook of LHC Higgs Cross Sections: 3. Higgs Properties*. 2013.
- [10] H. van Deurzen, N. Greiner, J. Huston, G. Luisoni, P. Mastrolia, et al. *Recent progress in higher order computations for the physics of the Higgs boson*. PoS, LL2014:038, 2014.
- [11] H. van Deurzen, N. Greiner, G. Heinrich, G. Luisoni, E. Mirabella, et al. *Automated one-loop calculations with GoSam 2.0*. PoS, LL2014:021, 2014.
- [12] H. van Deurzen. *Associated Higgs Production at NLO with GoSam*. Acta Phys.Polon., B44(11):2223–2230, 2013.

- [13] G. Cullen, H. van Deurzen, N. Greiner, G. Heinrich, G. Luisoni, et al. *GoSam @ LHC: algorithms and applications to Higgs production*. PoS, RADCOR2013:029, 2013.
- [14] H. van Deurzen, G. Luisoni, P. Mastrolia, E. Mirabella, G. Ossola, et al. *Multi-loop Integrand Reduction via Multivariate Polynomial Division*. PoS, RADCOR2013:012, 2013.
- [15] G. Cullen, H. van Deurzen, N. Greiner, G. Heinrich, G. Luisoni, et al. *NLO QCD Production of Higgs plus jets with GoSam*. PoS, EPS-HEP2013:446, 2013.
- [16] G. Cullen, H. van Deurzen, N. Greiner, G. Heinrich, G. Luisoni, et al. *GoSam applications for automated NLO calculations*. J.Phys.Conf.Ser., 523:012056, 2014.
- [17] P. Mastrolia, E. Mirabella, G. Ossola, T. Peraro, and H. van Deurzen. *The Integrand Reduction of One- and Two-Loop Scattering Amplitudes*. PoS, LL2012:028, 2012.
- [18] G. Aad et al. *Observation of a new particle in the search for the Standard Model Higgs boson with the ATLAS detector at the LHC*. Phys.Lett., B716:1–29, 2012.
- [19] S. Chatrchyan et al. *Observation of a new boson at a mass of 125 GeV with the CMS experiment at the LHC*. Phys.Lett., B716:30–61, 2012.
- [20] F. Englert and R. Brout. *Broken Symmetry and the Mass of Gauge Vector Mesons*. Phys.Rev.Lett., 13:321–323, 1964.
- [21] P. W. Higgs. *Broken symmetries, massless particles and gauge fields*. Phys.Lett., 12:132–133, 1964.
- [22] P. W. Higgs. *Broken Symmetries and the Masses of Gauge Bosons*. Phys.Rev.Lett., 13:508–509, 1964.
- [23] G. Guralnik, C. Hagen, and T. Kibble. *Global Conservation Laws and Massless Particles*. Phys.Rev.Lett., 13:585–587, 1964.
- [24] P. W. Higgs. *Spontaneous Symmetry Breakdown without Massless Bosons*. Phys.Rev., 145:1156–1163, 1966.
- [25] T. Kibble. *Symmetry breaking in nonAbelian gauge theories*. Phys.Rev., 155:1554–1561, 1967.
- [26] T. Gleisberg, S. Hoeche, F. Krauss, M. Schonherr, S. Schumann, et al. *Event generation with SHERPA 1.1*. JHEP, 0902:007, 2009.
- [27] R. Boughezal, F. Caola, K. Melnikov, F. Petriello, and M. Schulze. *Higgs boson production in association with a jet at next-to-next-to-leading order in perturbative QCD*. JHEP, 1306:072, 2013.
- [28] M. Czakon, P. Fiedler, A. Mitov, and J. Rojo. *Further exploration of top pair hadroproduction at NNLO*. 2013.
- [29] Z. Bern, L. J. Dixon, D. C. Dunbar, and D. A. Kosower. *Fusing gauge theory tree amplitudes into loop amplitudes*. Nucl.Phys., B435:59–101, 1995.
- [30] R. Britto, F. Cachazo, and B. Feng. *Generalized unitarity and one-loop amplitudes in $N=4$ super-Yang-Mills*. Nucl.Phys., B725:275–305, 2005.

-
- [31] G. Passarino and M. Veltman. *One Loop Corrections for $e^+ e^-$ Annihilation Into $\mu^+ \mu^-$ in the Weinberg Model*. Nucl.Phys., B160:151, 1979.
- [32] A. Denner and S. Dittmaier. *Reduction schemes for one-loop tensor integrals*. Nucl.Phys., B734:62–115, 2006.
- [33] G. Ossola, C. G. Papadopoulos, and R. Pittau. *Reducing full one-loop amplitudes to scalar integrals at the integrand level*. Nucl.Phys., B763:147–169, 2007.
- [34] G. Ossola, C. G. Papadopoulos, and R. Pittau. *Numerical evaluation of six-photon amplitudes*. JHEP, 0707:085, 2007.
- [35] W. T. Giele, Z. Kunszt, and K. Melnikov. *Full one-loop amplitudes from tree amplitudes*. JHEP, 0804:049, 2008.
- [36] R. K. Ellis, W. T. Giele, Z. Kunszt, and K. Melnikov. *Masses, fermions and generalized D -dimensional unitarity*. Nucl.Phys., B822:270–282, 2009.
- [37] P. Mastrolia, G. Ossola, T. Reiter, and F. Tramontano. *Scattering AMplitudes from Unitarity-based Reduction Algorithm at the Integrand-level*. JHEP, 1008:080, 2010.
- [38] Z. Bern, L. Dixon, F. Febres Cordero, S. Höche, H. Ita, et al. *Next-to-Leading Order $W + 5$ -Jet Production at the LHC*. Phys.Rev., D88(1):014025, 2013.
- [39] G. Cullen, N. Greiner, G. Heinrich, G. Luisoni, P. Mastrolia, et al. *Automated One-Loop Calculations with GoSam*. Eur.Phys.J., C72:1889, 2012.
- [40] T. Binoth, J. Guillet, and G. Heinrich. *Reduction formalism for dimensionally regulated one loop N point integrals*. Nucl.Phys., B572:361–386, 2000.
- [41] T. Binoth, J. P. Guillet, G. Heinrich, E. Pilon, and C. Schubert. *An Algebraic/numerical formalism for one-loop multi-leg amplitudes*. JHEP, 0510:015, 2005.
- [42] T. Reiter. *Automated Evaluation of One-Loop Six-Point Processes for the LHC*. 2009.
- [43] G. Cullen, J. P. Guillet, G. Heinrich, T. Kleinschmidt, E. Pilon, et al. *Golem95C: A library for one-loop integrals with complex masses*. Comput.Phys.Commun., 182:2276–2284, 2011.
- [44] T. Peraro. *Integrand-level Reduction at One and Higher Loops*. Acta Phys.Polon., B44:2215–2221, 2013.
- [45] T. Peraro. *Ninja: Automated Integrand Reduction via Laurent Expansion for One-Loop Amplitudes*. Comput.Phys.Commun., 185:2771–2797, 2014.
- [46] T. Binoth, F. Boudjema, G. Dissertori, A. Lazopoulos, A. Denner, et al. *A Proposal for a standard interface between Monte Carlo tools and one-loop programs*. Comput.Phys.Commun., 181:1612–1622, 2010.
- [47] J. Alwall, R. Frederix, S. Frixione, V. Hirschi, F. Maltoni, et al. *The automated computation of tree-level and next-to-leading order differential cross sections, and their matching to parton shower simulations*. JHEP, 1407:079, 2014.
- [48] V. Gribov and L. Lipatov. *$e^+ e^-$ pair annihilation and deep inelastic $e p$ scattering in perturbation theory*. Sov.J.Nucl.Phys., 15:675–684, 1972.

- [49] V. Gribov and L. Lipatov. *Deep inelastic $e p$ scattering in perturbation theory.* Sov.J.Nucl.Phys., 15:438–450, 1972.
- [50] G. Altarelli and G. Parisi. *Asymptotic Freedom in Parton Language.* Nucl.Phys., B126:298, 1977.
- [51] Y. L. Dokshitzer. *Calculation of the Structure Functions for Deep Inelastic Scattering and $e+ e-$ Annihilation by Perturbation Theory in Quantum Chromodynamics.* Sov.Phys.JETP, 46:641–653, 1977.
- [52] A. Martin, W. Stirling, R. Thorne, and G. Watt. *Parton distributions for the LHC.* Eur.Phys.J., C63:189–285, 2009.
- [53] G. 't Hooft and M. Veltman. *Regularization and Renormalization of Gauge Fields.* Nucl.Phys., B44:189–213, 1972.
- [54] W. Siegel. *Supersymmetric Dimensional Regularization via Dimensional Reduction.* Phys.Lett., B84:193, 1979.
- [55] S. Catani, M. Seymour, and Z. Trocsanyi. *Regularization scheme independence and unitarity in QCD cross-sections.* Phys.Rev., D55:6819–6829, 1997.
- [56] J. Smith and W. van Neerven. *The Difference between n -dimensional regularization and n -dimensional reduction in QCD.* Eur.Phys.J., C40:199–203, 2005.
- [57] A. Signer and D. Stockinger. *Using Dimensional Reduction for Hadronic Collisions.* Nucl.Phys., B808:88–120, 2009.
- [58] F. Bloch and A. Nordsieck. *Note on the Radiation Field of the electron.* Phys.Rev., 52:54–59, 1937.
- [59] T. Kinoshita. *Mass singularities of Feynman amplitudes.* J.Math.Phys., 3:650–677, 1962.
- [60] T. Lee and M. Nauenberg. *Degenerate Systems and Mass Singularities.* Phys.Rev., 133:B1549–B1562, 1964.
- [61] S. Catani, S. Dittmaier, M. H. Seymour, and Z. Trocsanyi. *The Dipole formalism for next-to-leading order QCD calculations with massive partons.* Nucl.Phys., B627:189–265, 2002.
- [62] T. Gleisberg and F. Krauss. *Automating dipole subtraction for QCD NLO calculations.* Eur.Phys.J., C53:501–523, 2008.
- [63] D. A. Kosower. *Antenna factorization of gauge theory amplitudes.* Phys.Rev., D57:5410–5416, 1998.
- [64] A. Daleo, T. Gehrmann, and D. Maitre. *Antenna subtraction with hadronic initial states.* JHEP, 0704:016, 2007.
- [65] S. Frixione, Z. Kunszt, and A. Signer. *Three jet cross-sections to next-to-leading order.* Nucl.Phys., B467:399–442, 1996.
- [66] Z. Nagy and Z. Trocsanyi. *Next-to-leading order calculation of four jet observables in electron positron annihilation.* Phys.Rev., D59:014020, 1999.

-
- [67] Z. Nagy. *Next-to-leading order calculation of three jet observables in hadron hadron collision*. Phys.Rev., D68:094002, 2003.
- [68] G. F. Sterman and S. Weinberg. *Jets from Quantum Chromodynamics*. Phys.Rev.Lett., 39:1436, 1977.
- [69] S. Catani, Y. L. Dokshitzer, M. Olsson, G. Turnock, and B. Webber. *New clustering algorithm for multi - jet cross-sections in $e^+ e^-$ annihilation*. Phys.Lett., B269:432–438, 1991.
- [70] S. Catani, Y. L. Dokshitzer, M. Seymour, and B. Webber. *Longitudinally invariant K_t clustering algorithms for hadron hadron collisions*. Nucl.Phys., B406:187–224, 1993.
- [71] S. D. Ellis and D. E. Soper. *Successive combination jet algorithm for hadron collisions*. Phys.Rev., D48:3160–3166, 1993.
- [72] Y. L. Dokshitzer, G. Leder, S. Moretti, and B. Webber. *Better jet clustering algorithms*. JHEP, 9708:001, 1997.
- [73] M. Cacciari, G. P. Salam, and G. Soyez. *The Anti- $k(t)$ jet clustering algorithm*. JHEP, 0804:063, 2008.
- [74] S. Frixione. *Isolated photons in perturbative QCD*. Phys.Lett., B429:369–374, 1998.
- [75] D. Melrose. *Reduction of Feynman diagrams*. Nuovo Cim., 40:181–213, 1965.
- [76] W. van Neerven and J. Vermaseren. *LARGE LOOP INTEGRALS*. Phys.Lett., B137:241, 1984.
- [77] M. Veltman. *Diagrammatica: The Path to Feynman rules*. Cambridge Lect.Notes Phys., 4:1–284, 1994.
- [78] R. K. Ellis, Z. Kunszt, K. Melnikov, and G. Zanderighi. *One-loop calculations in quantum field theory: from Feynman diagrams to unitarity cuts*. Phys.Rept., 518:141–250, 2012.
- [79] G. Ossola, C. G. Papadopoulos, and R. Pittau. *On the Rational Terms of the one-loop amplitudes*. JHEP, 0805:004, 2008.
- [80] D. Forde. *Direct extraction of one-loop integral coefficients*. Phys.Rev., D75:125019, 2007.
- [81] F. del Aguila and R. Pittau. *Recursive numerical calculus of one-loop tensor integrals*. JHEP, 0407:017, 2004.
- [82] K. Melnikov and M. Schulze. *NLO QCD corrections to top quark pair production in association with one hard jet at hadron colliders*. Nucl.Phys., B840:129–159, 2010.
- [83] P. Mastrolia, G. Ossola, C. Papadopoulos, and R. Pittau. *Optimizing the Reduction of One-Loop Amplitudes*. JHEP, 0806:030, 2008.
- [84] P. Mastrolia, E. Mirabella, G. Ossola, and T. Peraro. *Scattering Amplitudes from Multivariate Polynomial Division*. Phys.Lett., B718:173–177, 2012.
- [85] P. Mastrolia, E. Mirabella, and T. Peraro. *Integrand reduction of one-loop scattering amplitudes through Laurent series expansion*. JHEP, 1206:095, 2012.

- [86] R. G. Stuart and A. Gongora. *Algebraic Reduction of One Loop Feynman Diagrams to Scalar Integrals. 2*. Comput.Phys.Commun., 56:337–350, 1990.
- [87] G. Ossola, C. G. Papadopoulos, and R. Pittau. *CutTools: A Program implementing the OPP reduction method to compute one-loop amplitudes*. JHEP, 0803:042, 2008.
- [88] P. Nogueira. *Automatic Feynman graph generation*. J.Comput.Phys., 105:279–289, 1993.
- [89] J. Vermaseren. *New features of FORM*. 2000.
- [90] J. Kuipers, T. Ueda, J. Vermaseren, and J. Vollinga. *FORM version 4.0*. Comput.Phys.Commun., 184:1453–1467, 2013.
- [91] G. Cullen, M. Koch-Janusz, and T. Reiter. *Spinney: A Form Library for Helicity Spinors*. Comput.Phys.Commun., 182:2368–2387, 2011.
- [92] T. Reiter. *Optimising Code Generation with haggies*. Comput.Phys.Commun., 181:1301–1331, 2010.
- [93] A. van Hameren. *OneLOop: For the evaluation of one-loop scalar functions*. Comput.Phys.Commun., 182:2427–2438, 2011.
- [94] R. K. Ellis and G. Zanderighi. *Scalar one-loop integrals for QCD*. JHEP, 0802:002, 2008.
- [95] T. Hahn and M. Perez-Victoria. *Automatized one loop calculations in four-dimensions and D-dimensions*. Comput.Phys.Commun., 118:153–165, 1999.
- [96] T. Hahn. *Feynman Diagram Calculations with FeynArts, FormCalc, and LoopTools*. PoS, ACAT2010:078, 2010.
- [97] J. Fleischer, T. Riemann, and V. Yundin. *New developments in PjFry*. PoS, LL2012:020, 2012.
- [98] S. Actis, A. Denner, L. Hofer, A. Scharf, and S. Uccirati. *EW and QCD One-Loop Amplitudes with RECOLA*. PoS, RADCOR2013:034, 2013.
- [99] Y. Zhang. *Integrand-Level Reduction of Loop Amplitudes by Computational Algebraic Geometry Methods*. JHEP, 1209:042, 2012.
- [100] S. Badger. *Direct Extraction Of One Loop Rational Terms*. JHEP, 0901:049, 2009.
- [101] A. van Hameren, C. Papadopoulos, and R. Pittau. *Automated one-loop calculations: A Proof of concept*. JHEP, 0909:106, 2009.
- [102] N. Greiner, G. Heinrich, P. Mastrolia, G. Ossola, T. Reiter, et al. *NLO QCD corrections to the production of $W^+ W^-$ plus two jets at the LHC*. Phys.Lett., B713:277–283, 2012.
- [103] G. Luisoni, P. Nason, C. Oleari, and F. Tramontano. *$HW^\pm/HZ + 0$ and 1 jet at NLO with the POWHEG BOX interfaced to GoSam and their merging within MiNLO*. JHEP, 1310:083, 2013.
- [104] S. Hoeche, J. Huang, G. Luisoni, M. Schoenherr, and J. Winter. *Zero and one jet combined next-to-leading order analysis of the top quark forward-backward asymmetry*. Phys.Rev., D88(1):014040, 2013.

-
- [105] T. Gehrmann, N. Greiner, and G. Heinrich. *Precise QCD predictions for the production of a photon pair in association with two jets*. Phys.Rev.Lett., 111:222002, 2013.
- [106] M. J. Dolan, C. Englert, N. Greiner, and M. Spannowsky. *Further on up the road: $hhjj$ production at the LHC*. Phys.Rev.Lett., 112:101802, 2014.
- [107] G. Heinrich, A. Maier, R. Nisius, J. Schlenk, and J. Winter. *NLO QCD corrections to $W^+W^-b\bar{b}$ production with leptonic decays in the light of top quark mass and asymmetry measurements*. JHEP, 1406:158, 2014.
- [108] N. Greiner, A. Guffanti, T. Reiter, and J. Reuter. *NLO QCD corrections to the production of two bottom-antibottom pairs at the LHC*. Phys.Rev.Lett., 107:102002, 2011.
- [109] N. Greiner, G. Heinrich, J. Reichel, and J. F. von Soden-Fraunhofen. *NLO QCD Corrections to Diphoton Plus Jet Production through Graviton Exchange*. JHEP, 1311:028, 2013.
- [110] T. Gehrmann, N. Greiner, and G. Heinrich. *Photon isolation effects at NLO in $\gamma\gamma + jet$ final states in hadronic collisions*. JHEP, 1306:058, 2013.
- [111] G. Cullen, N. Greiner, and G. Heinrich. *Susy-QCD corrections to neutralino pair production in association with a jet*. Eur.Phys.J., C73(4):2388, 2013.
- [112] A. Denner, S. Dittmaier, M. Roth, and L. Wieders. *Electroweak corrections to charged-current $e^+e^- \rightarrow 4$ fermion processes: Technical details and further results*. Nucl.Phys., B724:247–294, 2005.
- [113] S. Catani, S. Dittmaier, and Z. Trocsanyi. *One loop singular behavior of QCD and SUSY QCD amplitudes with massive partons*. Phys.Lett., B500:149–160, 2001.
- [114] S. Badger, B. Biedermann, and P. Uwer. *NGluon: A Package to Calculate One-loop Multi-gluon Amplitudes*. Comput.Phys.Commun., 182:1674–1692, 2011.
- [115] S. Badger, B. Biedermann, P. Uwer, and V. Yundin. *Numerical evaluation of virtual corrections to multi-jet production in massless QCD*. Comput.Phys.Commun., 184:1981–1998, 2013.
- [116] J. Alwall, M. Herquet, F. Maltoni, O. Mattelaer, and T. Stelzer. *MadGraph 5 : Going Beyond*. JHEP, 1106:128, 2011.
- [117] R. Frederix, S. Frixione, V. Hirschi, F. Maltoni, R. Pittau, et al. *Scalar and pseudoscalar Higgs production in association with a top-antitop pair*. Phys.Lett., B701:427–433, 2011.
- [118] S. Alioli, P. Nason, C. Oleari, and E. Re. *A general framework for implementing NLO calculations in shower Monte Carlo programs: the POWHEG BOX*. JHEP, 1006:043, 2010.
- [119] M. Bahr, S. Gieseke, M. Gigg, D. Grellscheid, K. Hamilton, et al. *Herwig++ Physics and Manual*. Eur.Phys.J., C58:639–707, 2008.
- [120] T. Sjöstrand, S. Ask, J. R. Christiansen, R. Corke, N. Desai, et al. *An Introduction to PYTHIA 8.2*. 2014.
- [121] P. Bolzoni, F. Maltoni, S.-O. Moch, and M. Zaro. *Vector boson fusion at NNLO in QCD: SM Higgs and beyond*. Phys.Rev., D85:035002, 2012.

- [122] T. Han and S. Willenbrock. *QCD correction to the $p p \rightarrow W H$ and $Z H$ total cross-sections*. Phys.Lett., B273:167–172, 1991.
- [123] T. Figy, C. Oleari, and D. Zeppenfeld. *Next-to-leading order jet distributions for Higgs boson production via weak boson fusion*. Phys.Rev., D68:073005, 2003.
- [124] M. Cacciari and G. P. Salam. *Dispelling the N^3 myth for the k_t jet-finder*. Phys.Lett., B641:57–61, 2006.
- [125] M. Cacciari, G. P. Salam, and G. Soyez. *FastJet User Manual*. Eur.Phys.J., C72:1896, 2012.
- [126] J. Pumplin, D. Stump, J. Huston, H. Lai, P. M. Nadolsky, et al. *New generation of parton distributions with uncertainties from global QCD analysis*. JHEP, 0207:012, 2002.
- [127] F. Campanario, T. Figy, S. Plätzer, and M. Sjödahl. *Electroweak Higgs plus Three Jet Production at NLO QCD*. 2013.
- [128] T. Figy, V. Hankele, and D. Zeppenfeld. *Next-to-leading order QCD corrections to Higgs plus three jet production in vector-boson fusion*. JHEP, 0802:076, 2008.
- [129] H. Georgi, S. Glashow, M. Machacek, and D. V. Nanopoulos. *Higgs Bosons from Two Gluon Annihilation in Proton Proton Collisions*. Phys.Rev.Lett., 40:692, 1978.
- [130] S. Dawson. *Radiative corrections to Higgs boson production*. Nucl.Phys., B359:283–300, 1991.
- [131] A. Djouadi, M. Spira, and P. Zerwas. *Production of Higgs bosons in proton colliders: QCD corrections*. Phys.Lett., B264:440–446, 1991.
- [132] D. Graudenz, M. Spira, and P. Zerwas. *QCD corrections to Higgs boson production at proton proton colliders*. Phys.Rev.Lett., 70:1372–1375, 1993.
- [133] M. Spira, A. Djouadi, D. Graudenz, and P. Zerwas. *Higgs boson production at the LHC*. Nucl.Phys., B453:17–82, 1995.
- [134] R. V. Harlander and W. B. Kilgore. *Next-to-next-to-leading order Higgs production at hadron colliders*. Phys.Rev.Lett., 88:201801, 2002.
- [135] C. Anastasiou and K. Melnikov. *Higgs boson production at hadron colliders in NNLO QCD*. Nucl.Phys., B646:220–256, 2002.
- [136] V. Ravindran, J. Smith, and W. L. van Neerven. *NNLO corrections to the total cross-section for Higgs boson production in hadron hadron collisions*. Nucl.Phys., B665:325–366, 2003.
- [137] C. Anastasiou, C. Duhr, F. Dulat, F. Herzog, and B. Mistlberger. *Higgs boson gluon-fusion production in N³LO QCD*. 2015.
- [138] X. Chen, T. Gehrmann, E. Glover, and M. Jaquier. *Precise QCD predictions for the production of Higgs + jet final states*. Phys.Lett., B740:147–150, 2015.
- [139] V. Del Duca, W. Kilgore, C. Oleari, C. Schmidt, and D. Zeppenfeld. *Higgs + 2 jets via gluon fusion*. Phys.Rev.Lett., 87:122001, 2001.

-
- [140] J. M. Campbell, R. K. Ellis, and G. Zanderighi. *Next-to-Leading order Higgs + 2 jet production via gluon fusion*. JHEP, 0610:028, 2006.
- [141] V. Del Duca, W. Kilgore, C. Oleari, C. Schmidt, and D. Zeppenfeld. *Gluon fusion contributions to H + 2 jet production*. Nucl.Phys., B616:367–399, 2001.
- [142] F. Campanario and M. Kubocz. *Higgs boson production in association with three jets via gluon fusion at the LHC: Gluonic contributions*. Phys.Rev., D88(5):054021, 2013.
- [143] F. Wilczek. *Decays of Heavy Vector Mesons Into Higgs Particles*. Phys.Rev.Lett., 39:1304, 1977.
- [144] A. Pak, M. Rogal, and M. Steinhauser. *Finite top quark mass effects in NNLO Higgs boson production at LHC*. JHEP, 1002:025, 2010.
- [145] R. V. Harlander, H. Mantler, S. Marzani, and K. J. Ozeren. *Higgs production in gluon fusion at next-to-next-to-leading order QCD for finite top mass*. Eur.Phys.J., C66:359–372, 2010.
- [146] R. K. Ellis, W. Giele, and G. Zanderighi. *Virtual QCD corrections to Higgs boson plus four parton processes*. Phys.Rev., D72:054018, 2005.
- [147] M. Whalley, D. Bourilkov, and R. Group. *The Les Houches accord PDFs (LHAPDF) and LHAGLUE*. 2005.
- [148] T. Stelzer and W. Long. *Automatic generation of tree level helicity amplitudes*. Comput.Phys.Commun., 81:357–371, 1994.
- [149] J. Alwall, P. Demin, S. de Visscher, R. Frederix, M. Herquet, et al. *MadGraph/MadEvent v4: The New Web Generation*. JHEP, 0709:028, 2007.
- [150] R. Frederix, T. Gehrmann, and N. Greiner. *Automation of the Dipole Subtraction Method in MadGraph/MadEvent*. JHEP, 0809:122, 2008.
- [151] R. Frederix, T. Gehrmann, and N. Greiner. *Integrated dipoles with MadDipole in the MadGraph framework*. JHEP, 1006:086, 2010.
- [152] F. Maltoni and T. Stelzer. *MadEvent: Automatic event generation with MadGraph*. JHEP, 0302:027, 2003.
- [153] K. Hamilton, P. Nason, and G. Zanderighi. *MINLO: Multi-Scale Improved NLO*. JHEP, 1210:155, 2012.
- [154] C. Degrande, J. Gerard, C. Grojean, F. Maltoni, and G. Servant. *Probing Top-Higgs Non-Standard Interactions at the LHC*. JHEP, 1207:036, 2012.
- [155] P. Artoisenet, P. de Aquino, F. Maltoni, and O. Mattelaer. *Unravelling $t\bar{t}h$ via the Matrix Element Method*. Phys.Rev.Lett., 111(9):091802, 2013.
- [156] W. Beenakker, S. Dittmaier, M. Kramer, B. Plumper, M. Spira, et al. *Higgs radiation off top quarks at the Tevatron and the LHC*. Phys.Rev.Lett., 87:201805, 2001.
- [157] W. Beenakker, S. Dittmaier, M. Kramer, B. Plumper, M. Spira, et al. *NLO QCD corrections to t anti-t H production in hadron collisions*. Nucl.Phys., B653:151–203, 2003.

- [158] S. Dawson, L. Orr, L. Reina, and D. Wackerth. *Associated top quark Higgs boson production at the LHC*. Phys.Rev., D67:071503, 2003.
- [159] S. Dawson, C. Jackson, L. Orr, L. Reina, and D. Wackerth. *Associated Higgs production with top quarks at the large hadron collider: NLO QCD corrections*. Phys.Rev., D68:034022, 2003.
- [160] S. Dittmaier, . Kramer, Michael, and M. Spira. *Higgs radiation off bottom quarks at the Tevatron and the CERN LHC*. Phys.Rev., D70:074010, 2004.
- [161] T. Plehn, G. P. Salam, and M. Spannowsky. *Fat Jets for a Light Higgs*. Phys.Rev.Lett., 104:111801, 2010.
- [162] F. Krauss, R. Kuhn, and G. Soff. *AMEGIC++ 1.0: A Matrix element generator in C++*. JHEP, 0202:044, 2002.
- [163] V. Hirschi, R. Frederix, S. Frixione, M. V. Garzelli, F. Maltoni, et al. *Automation of one-loop QCD corrections*. JHEP, 1105:044, 2011.
- [164] J. M. Butterworth, A. R. Davison, M. Rubin, and G. P. Salam. *Jet substructure as a new Higgs search channel at the LHC*. Phys.Rev.Lett., 100:242001, 2008.
- [165] P. Artoisenet, R. Frederix, O. Mattelaer, and R. Rietkerk. *Automatic spin-entangled decays of heavy resonances in Monte Carlo simulations*. JHEP, 1303:015, 2013.
- [166] K. Melnikov, M. Schulze, and A. Scharf. *QCD corrections to top quark pair production in association with a photon at hadron colliders*. Phys.Rev., D83:074013, 2011.
- [167] Z. Bern and A. Morgan. *Massive loop amplitudes from unitarity*. Nucl.Phys., B467:479–509, 1996.
- [168] L. J. Dixon. *Calculating scattering amplitudes efficiently*. 1996.
- [169] M. E. Peskin. *Simplifying Multi-Jet QCD Computation*. 2011.

Acknowledgements

First and foremost, I wish to express my gratitude to my daily supervisor, Pierpaolo Mastrolia. He was always available for guidance and advice and never ceased to show genuine interest in the progressing of my work throughout the years. I would like to thank all the other members of the GOSAM collaboration for their contributions and help. Among them, I would like to especially mention Giovanni Ossola and Gionata Luisoni, who were involved in practically all of the projects discussed in this dissertation, and provided really a lot of help and insights on a broad range of topics.

I am grateful to the Max-Planck Institut für Physik in München (Werner-Heisenberg Institut) for providing everything needed for this work to be a success, including especially the computing facilities, which were employed for some of the projects described in this dissertation. In particular I would like to thank Thomas Hahn for providing excellent and instant support to solve any technology-related problems I encountered during my time at the institute.

I would like to thank the New York City College of Technology for hosting me during my visit. I am also grateful to its Center for Theoretical Physics for providing the computational resources used for some of the projects presented in this work.

Finally, I am most grateful to Niki Klop for her endless support and encouragement, and for the joy of having her company in this shared adventure abroad.

The work presented in this dissertation was supported by the Alexander von Humboldt Foundation, in the framework of the Sofja Kovalevskaja Award Project *Advanced Mathematical Methods for Particle Physics*, endowed by the German Federal Ministry of Education and Research.